ABSTRACT

Title of Document: **CHARACTERIZATION AND MODELLING OF MAGNETO-AUXETICITY, THE MAGNETICALLY INDUCED AUXETIC BEHAVIOR, IN GALFENOL**

Ganesh Raghunath,
Doctor of Philosophy, 2015

Directed By: Professor Alison B. Flatau,
Department of Aerospace Engineering

Iron-Gallium alloy (Galfenol) is a magnetostrictive smart material (λsat ~400 ppm) with potential for robust transduction owing to good magneto-mechanical coupling and useful mechanical properties. In addition, Galfenol exhibits a highly negative Poisson's ratio (denoted by ν) along the <110> crystallographic directions on {100} planes with ν values of as low as -0.7 under tensile loads. Consequently, their samples become wider when elongated and narrower when compressed (aka

auxeticity). This is an anisotropic, in-plane and volume conserving phenomenon with compensating contractions and expansions in the third (out of plane) direction.

Since there is good magneto-elastic coupling in Galfenol, a negative Poisson's ratio is expected to be observed under application of magnetic fields even under zero stress conditions. This work deals with systematically studying the magneto-elastic contributions in Galfenol samples between 12 and 33 atomic percent Ga as a non-synthetic (no artificial linkages, unlike foams) 'structural auxetic' material, capable of bearing loads. This investigation addresses the profound gap in understanding this atypical behavior using empirical data supported by analytical modeling from first principles to predict the Poisson's ratio at magnetic saturation, multi-physics finite element simulations to determine the trends in the strains along the <110> {100} directions and magnetic domain imaging to explain the mechanical response from a magnetic domain perspective.

The outcome of this effort will help comprehend the association between anisotropic magnetic and mechanical energies and hence the magnetic contributions to the atomic level interactions that are the origins of this magneto-auxetic characteristic. Also, it is well established that a number of mechanical properties such as shear resistance and toughness depend on the value of Poisson's ratio. There is a slight increase in these mechanical properties with non-zero ν values, but as we enter the highly auxetic regime ($\nu<-0.5$), these values increase by magnitudes. Hence, the possibility of ν values approaching -1.0 under applied magnetic fields at zero stress is

extremely intriguing, as these properties can be much larger than is possible in conventional materials. This has potential for several novel applications where the value of Poisson's ratio can be magnetically tuned to keep it near -1 under applied stresses.

CHARACTERIZATION AND MODELLING OF MAGNETO-AUXETICITY, THE MAGNETICALLY INDUCED AUXETIC BEHAVIOR, IN GALFENOL

By

Ganesh Raghunath

Dissertation submitted to the Faculty of the Graduate School of the
University of Maryland, College Park, in partial fulfillment
of the requirements for the degree of
Doctor of Philosophy
2015

Advisory Committee:
Professor Alison B. Flatau, Chair
Professor Norman M. Wereley
Professor Sung W. Lee
Professor Ichiro Takeuchi
Professor Manfred Wuttig

But of what use is the education that does not benefit society?
- Ancient Tamil saying

Dedicated to my grandparents:

Thandankorai Umamaheshwaran Venkatasubramanian
Shantha Venkatasubramanian

Acknowledgements

My family has been the backbone of my work at Maryland and I would like to thank them for their unconditional love and support. Without their sacrifice my work would have been extremely hard to accomplish. Personally, my grandparents have played an important role in the development of my identity and shaping the individual that I am today. I must mention that my grandfather is the primary reason for my interest in science at a very early age and I'm extremely indebted him. The personal contributions of my friends and roommates are monumental and I'm extremely grateful to them for making my stay at Maryland a pleasant and memorable one!

I would also like to thank the office staff at Aerospace Engineering, the folks at the Aero and Physics machine shop and last but not the least, the entire University of Maryland community for creating an environment conducive for research and personal development.

Table of Contents

List of Tables

List of Figures

List of Conventions

1. < > indicates a family of crystallographic directions.

2. [ ] represents a particular crystallographic direction.

For example, in a cubic crystal <100> represents [100], [-100], [010], [0-10], [001] and [00-1].

3. { } indicates a family of crystallographic planes.

4. ( ) represents a particular crystallographic plane.

For example, in a cubic crystal {100} represents (100), (-100), (010), (0-10), (001) and (00-1).

5. Fe81Ga19 also written as 19 at. % Ga, FeGa alloy is used to indicate that the FeGa alloy contains 19 atoms of Gallium for every 81 atoms of Iron, i.e. the Ga content is denoted by percentage of atoms and NOT by percentage mass of Ga.

Commonly used Symbols

H : Magnetic field

B : Magnetic induction

M : Magnetization

λ : Magnetostriction

σ : Stress

ε : Strain

μ_r : Relative permeability

μ_0 : Permeability of free-space

E : Young's Modulus (also used for Electric Field)

$E_{\text{"subscript"}}$: Energy terms

S : Compliance

d_{33} : Piezo-magnetic coefficient

d^*_{33} : Inverse Piezo-magnetic coefficient, sensitivity

Note: All direction cosines are with respect to the <100> directions of a cubic crystal

$(\alpha_1, \alpha_2, \alpha_3)$: Direction cosines for orientation of magnetic moment

$(\beta_1, \beta_2, \beta_3)$: Direction cosines of magnetic field

Chapter 1: Introduction

The goal of the research presented in this dissertation is to discern the magneto-auxetic effect observed in iron-gallium alloys called Galfenol along certain crystallographic directions under applied magnetic fields and zero mechanical stress conditions. The interaction of magnetic fields with the elasticity of atomic bonds in the crystal lattice of Galfenol leads to a negative Poisson's ratio (aka auxeticity). The combination of inherent magneto-elastic coupling and good structural attributes in Galfenol along with its magneto-auxetic behavior is very interesting and holds immense potential for novel applications.

The introduction chapter attempts to provide the reader with sufficient background to help understand and appreciate the contributions of this work. This chapter begins with a statement of research objectives and the motivation behind this effort. Three major concepts: physics of magnetism, magnetostriction and auxeticity; essential to the investigation will be discussed in detail in this chapter.

Section 1.2 will present a detailed discussion of the fundamentals of magnetism which is essential to comprehend the magnetic contributions to the magneto-elastic phenomena. This will also include a brief introduction to magnetic domains and their imaging. The subsequent section deals with the magneto-elastic effect and its governing equations. An overview of magnetostrictive materials with special attention to Galfenol will follow. Finally, a general background to auxetic

materials and their development over the years will be provided. This will include a discussion on previous works on auxeticity in Galfenol.

1.1: Objectives and motivation

Galfenol ($Fe_{100-x}Ga_x$ with ~12 < x < ~33) is a unique smart material with extremely useful properties such as high tensile strength [6, 7] and good magneto-mechanical coupling properties [7, 8]. Consequently, significant research [7-11] has been directed towards understanding the origin and developing potential applications based on these properties. Apart from these characteristics, it is also one of very few structural materials that exhibit a large negative Poisson's ratio. It is only recently that studies towards understanding this auxetic behavior of Galfenol along the <110> {100} direction has begun [3, 9, 12-15].

Analysis of the auxetic magneto-elastic response of Galfenol to applied magnetic fields at zero mechanical stress, which has not previously been explored, is the main focus of the research presented here. A magnetic field is applied along one of the <110> {100} crystallographic directions and the longitudinal and transverse <110> strains on the same (100) plane are systematically studied for a broad spectrum of compositions with special emphasis to quantifying the magneto-auxetic phenomenon and comparison of the results obtained from this study with previously published auxeticity data from other protocols including tensile testing and resonant ultrasound testing methods. A theoretical anisotropy model from first principles that

2

uses elastic, magneto-elastic and mechanical work energies to describe the change in magnetization and the corresponding magnetostriction in the material due to applied magnetic fields is also derived. The experimental results for Poisson's ratio at magnetic saturation are used to validate the predicted values from this model. The trends in the strains observed from the experiments are compared to those obtained from finite element multi-physics simulations formulated by modifying the well-established energy based model called, 'Armstrong model' **[8, 16]**. Images of magnetic domain evolution on the surface of single crystal Galfenol {100} samples recorded using Magneto-Optic Kerr Effect (MOKE) microscopy under applied magnetic fields along the <100> direction are used to understand the micromagnetic domain contribution to the magneto-elastic auxetic effect. The results from these tasks will be used to understand the atomic level interactions in Galfenol which is the origin of the auxetic behavior.

This effort is directed towards aiding scientists and engineers to understand and exploit the unique properties of this alloy to develop novel applications.

1.2: Physics of magnetism

This section begins with a brief history of magnetism and a definition of magnetic quantities. This will set the stage for atomic basis for magnetism, followed by a discussion of magnetism in solids. Subsequently, a brief overview of magnetic domains and their evolution through domain wall motion will be presented as it

serves as a meso level bridge between atomic origin of magnetism and macro-scale magnetization of bulk materials.

The underlying physics behind magnetism and specific information on ferromagnetic materials is essential to understand the behavior of magnetostrictive materials like Galfenol, and is discussed in Section 1.3.

1.2.1: History of magnetism

The knowledge of magnetism dates back to the 6th century when the Greek philosopher Thales of Miletus in Magnesia observed that a loadstone (Fe_3O_4) always points along the same direction.

The earth is conceptualized as a huge permanent magnet with its magnetic north pole facing nearly towards the geographical South Pole and its magnetic south pole facing nearly towards the geographical North Pole. Magnetic theory in materials developed over the years with the earth's poles as a reference. Unlike mechanical forces, forces of magnetism are non-contact forces that are manifested in the form of dipoles (known as the north and south poles), where like poles repel each other and unlike poles attract each other.

1.2.2: Fundamental magnetic quantities

Hans Christian Oersted (1820) observed that a current carrying conductor produces a magnetic field and attributed it to the motion of charges that constitute an electric current. The "magnetic field strength" ($\vec{H}$) is defined as the magnetic vector quantity at a point in a magnetic field which measures the ability of electric currents or magnetized bodies to produce magnetic induction at that point [17]. Magnetic field strength is measured in Oersted (cgs) or Ampere per meter (SI), where 1 A/m=79.57747 Oe.

Equation (1.1) is called the Biot-Savart law and it gives us the elemental field strength $d\vec{H}$ at a point at a distance $\vec{r}$ from a conductor of elemental length $d\vec{l}$ that carries a current i.

$$dH = \frac{\mu_o}{4\pi} i \frac{d\vec{l} \times \vec{r}}{r^2} \tag{1.1}$$

Ampere derived Eq. (1.2), which is the integral form of this law, where $\vec{H}$ is the magnetic field produced by N number of current elements with current i in each of them in a closed circuit of a fixed length.

$$N_i = \oint \vec{H}.d\vec{l} \tag{1.2}$$

The field generated at the center of an infinitely long solenoid can be calculated using Ampere's Law. The magnetic field at the center of a solenoid of finite length l is computed as shown in Eq. (1.3).

$$H = \frac{Ni}{l} \qquad\qquad (1.3)$$

Magnetic force is visualized using imaginary streamlines known as lines of magnetic flux (ϕ). The units of magnetic flux are maxwell (cgs) or weber (SI) where 1 Wb = 108 Mx. These magnetic field lines have the following properties:

(1)   The lines of flux are continuous, starting from the North Pole and ending in the South Pole.

(2)   These lines can never intersect each other and the tangent to a line of force at a point gives the direction of the magnetic induction.

(3)   The density of the flux lines determines the strength of the magnetic induction.

The "magnetic induction" or "magnetic flux density" is denoted by $(\vec{B})$ and gives a measure of the strength of magnetic flux induced in a material due to the application of an external magnetic field. Magnetic induction is measured in gauss (cgs) or tesla (SI) where 1 T = 1 Wbm^{-2} = 10^4 G.

The magnetic flux (ϕ) through a material of area $\vec{A}$ can be related to the magnetic induction using Equation (1.4).

$$\phi = \vec{B} \times \vec{A} \tag{1.4}$$

The amount of flux entering and leaving any closed surface is always equal. Hence, the lines of induction always form a closed path (also known as Gauss's Law) [17] and can be expressed by Eq. (1.5). Note that the elemental area ($d\vec{A}$) is a vector whose direction is normal to the surface.

$$\int \vec{B}.d\vec{A} = 0 \tag{1.5}$$

Magnetic induction and magnetic field can be related using the linear constitutive Equation (1.6).

$$\vec{B} = \mu\vec{H} \tag{1.6}$$

Here, μ is known as the magnetic permeability of the material. The magnetic permeability of vacuum (μ_0) has a constant value of $4\pi \times 10^{-7}$ Hm^{-1} (SI) or 1 (cgs).

The SI unit of permeability is Henry per meter and is derived from the concept of inductance. Permeability is a material property and is usually a complex function of magnetic field, material temperature, thermal history, stress etc. Usually materials

are characterized by their relative permeability (μ_r), which is defined by Equation (1.7).

$$\mu_r = \frac{\mu}{\mu_0} \tag{1.7}$$

Magnetization ($\vec{M}$) of a material indicates the amount of magnetic moment ($\vec{m}$) per unit volume, aligned in the material due to an externally applied field $\vec{H}$. Volume magnetization is denoted by $4\pi\vec{M}$ in the cgs unit system and is measured in Gauss (G). In the SI system magnetization is measured in Am^{-1}. Hence the total magnetic induction in a material is given in the SI system by Eq. (1.8) and in the cgs system by Eq. (1.9).

$$\vec{B} = \mu_o\left(\vec{H} + \vec{M}\right) \tag{1.8}$$

$$\vec{B} = \vec{H} + 4\pi\vec{M} \tag{1.9}$$

A property of the magnetic material called magnetic susceptibility (χ_m) relates the magnetization in the material to the applied magnetic field. This linear constitutive equation is shown in Eq. (1.10).

$$\vec{M} = \chi_m\vec{H} \tag{1.10}$$

Using Equations (1.6) to (1.10), a relationship between permeability and susceptibility can be derived as shown in Equation (1.11).

$$\chi_m = \mu_r - 1 \tag{1.11}$$

Susceptibility is a measure of the magnetic moments that will be aligned in the magnetic material by the externally applied magnetic field. Permeability gives a measure of the extent of magnetic flux that will pass through a material when it is exposed to a magnetic field.

The $\vec{B}$ (or $\vec{M}$) vs. $\vec{H}$ curve represents the magnetic behavior of a material. These are also known as 'hysteresis' plots and were first observed in iron by Warburg [18] and named such by Ewing [19] to emphasize on the fact that the $\vec{B}$ or $\vec{M}$ of the materials lags behind the $\vec{H}$ in response.

Equations 1.12-1.15 are collectively known as Maxwell's equations which are used to describe an electromagnetic field in classical physics [17]. They summarize the relationship between electric and magnetic parameters in ferromagnetic media.

$$\vec{\nabla} \times \vec{H} = \vec{J_f} + \frac{\partial \vec{D}}{\partial t} \quad \text{(Ampere's Law)} \tag{1.12}$$

$$\vec{\nabla} \times \vec{E} = -\frac{\partial \vec{B}}{\partial t} \quad \text{(Faraday's Law)} \tag{1.13}$$

$$\vec{\nabla}.\vec{B} = 0 \quad \text{(No monopoles)} \tag{1.14}$$

$$\vec{\nabla}.\vec{D} = \rho_f \quad \text{(Gauss's Law)} \tag{1.15}$$

Here, $\vec{\nabla}$ is the gradient operator, defined as $\vec{\nabla} = \frac{\partial}{\partial x}\hat{\imath} + \frac{\partial}{\partial y}\hat{\jmath} + \frac{\partial}{\partial z}\hat{k}$ and $\vec{J_f}$ is the free current density (unit: Am^{-2}) or the current per unit are perpendicular to the flow due to motion of charges. $\vec{D}$ is the electric displacement (unit: Cm^{-2}), $\vec{E}$ is the electric field (unit Vm^{-1}) and ρ_f is the free charge density (unit: Cm^{-3}).

1.2.3: Magnetism at the atomic scale

The magnetic moment of the atom arises due to the angular momentum of the electrons. The current that develops when an electron of charge e ($=1.603 \times 10^{-19}$ C) rotates around the nucleus in an orbit of radius r at an angular velocity of $\dot{\theta}$ as shown in Fig. 1.1 is given by $i = \frac{-e\dot{\theta}}{2\pi}$.
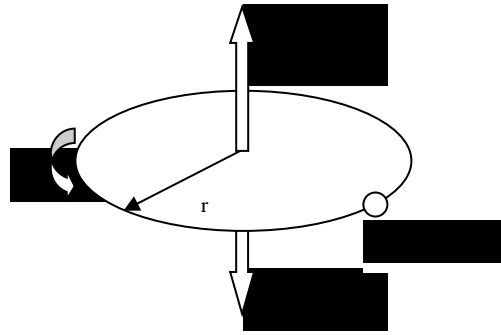
Figure 1.1: Electron in an orbit visualized as a current carrying loop.

Equation (1.16) defines the orbital magnetic moment μ_{mm} generated by this electric current.

$$\mu_{mm} = -\frac{1}{2}e\dot{\theta}r^2 \qquad (1.16)$$

10

Since the angular momentum of the moving electron is $P = m\dot{\theta}r^2$, the magnetic moment can be expressed as shown in Equation (1.17).

$$\mu_{mm} = -\frac{1}{2}\left(\frac{e}{m}P\right) \qquad (1.17)$$

The magnetic moment is thus proportional to the angular momentum of the electron and is in the opposite direction.

Quantum mechanics teaches that the orbital motion of the electron in a coulombic potential is characterized by the three integer quantum numbers (principal, azimuthal and spin quantum numbers). The total angular momentum (J) is the sum of the orbital angular momentum (L) and the intrinsic spin angular momentum (S). While the orbital angular momentum is explained by the classical mechanics approach, the spin angular momentum is a completely quantum mechanical effect.

The magnetic moment associated with orbital angular momentum is

$$\mu_L = -L\mu_B \qquad (1.18 \text{ a})$$

and that with spin angular momentum is

$$\mu_S = -2\mu_B S \qquad (1.18 \text{ b}).$$

Here, $\mu_B = \dfrac{e\hbar}{2m}$ is called the Bohr magneton and represents the atomic unit of

orbital magnetic moment.

Hence, $J = \hbar\left(\sqrt{l(l+1)} + \sqrt{s(s+1)}\right)$ $\qquad$ (1.18c),

where, l and s are the orbital and spin quantum numbers respectively. The allowed

values for l are integers and s are $\pm\dfrac{1}{2}$ (up and down spin states).

Pauli's exclusion principle states that no two electrons can coexist in the same

quantum state. As a consequence, electrons pair up, i.e. the electrons are stacked such

that within the same orbit if one electron has spin up ($s = +1/2$) then the other will

have spin down ($s = -1/2$). This leads to the cancellation of the magnetic moments

resulting in a net zero magnetic moment. Therefore, an atom has a magnetic moment

only when there are unpaired electrons.

The minimum energy state is observed while the electrons fill up the shells

which complies with Hund's rule states that:

(1) S takes the minimal value that is consistent with Pauli's exclusion principle.

(2) L takes the maximum value that is consistent with Pauli's exclusion

         principle.

(3) J assumes the value of $L - S$ if the shell is less than half filled and $L + S$

         otherwise.

As a consequence of Hund's rule which is described in detail in **[4]**, some of the elements with 3d and 4f shell electrons have more than one unpaired electrons leading to strong atomic moments.

1.2.4: Magnetism at the macroscale

The best way to introduce the different types of magnetism is to describe how materials respond to magnetic fields. This may be surprising to some, but all matter is magnetic; albeit from the perspective of having electron spins about atoms. It's just that at the macro scale, some materials are much more magnetic than others. The main distinction is that in some materials there is no collective interaction of atomic magnetic moments, whereas in other materials there is a very strong interaction between atomic moments. This section deals with bulk materials where there is a large interaction of atomic moments with applied magnetic fields.

1.2.4.1: Diamagnetism

Diamagnetism occurs in those materials in which all the electrons are paired up (i.e. zero atomic magnetic moments). The susceptibility of these materials is small and negative, typically $\chi_d \approx -10^{-5}$. The induced magnetization is proportional to the external magnetic field but is opposite in direction (as suggested by the negative sign). These materials tend to oppose the action of the magnetic field in accordance with Lenz's law.

1.2.4.2: Paramagnetism

Paramagnetism appears in elements that have unpaired electrons. Similar to diamagnetic materials, the negative magnetic moment is induced even in paramagnetic materials with a linear dependence of the magnetization with the applied magnetic field. However, the alignment of the atomic moments with the magnetic field dominates, resulting in a positive magnetic moment. Paramagnetic materials exhibit positive susceptibility of the order of $\chi_d \approx 10^{-5}$ to 10^{-2}.

1.2.4.2: Ferromagnetism

Ferromagnetism is characterized by a strong magnetic behavior. Susceptibility of ferromagnetic materials is much higher than those of paramagnetic materials and can be as high as $\chi_f \approx 1000$. The origin of such a strong magnetism is not only the strong atomic moment from the unpaired electrons but also the spontaneous magnetization produced due to the alignment of all atomic moments parallel to each other. The behavior of ferromagnetic substances such as Fe which exhibit a paramagnetic behavior at higher temperatures (but display a larger magnetization) is described by Eq. (1.19).

$$\chi_p = \frac{C}{T}\left(\frac{T}{T-T_c}\right)\frac{1}{\gamma} \approx \frac{C}{T-\Theta_p} \quad \text{when } T \gg T_c \quad (1.19),$$

where, T_c is the Curie temperature, C is the Curie Constant and $T_c < \Theta_P = \gamma T_c$.

At 0 K, in a saturated ferromagnetic single crystal, all elementary magnetic moments are parallel and upon heating the material, the thermal agitation tends to misorient the moments and the magnetization decreases and eventually vanishes at the Curie Temperature, T_C. At lower temperatures, the response of ferromagnetic materials is essentially nonlinear and exhibits a certain extent of hysteresis.

In 1928, Heisenberg [20] proposed a different approach to explain this behavior. He defined the quantum mechanical exchange interaction energy between atoms of spin S_i and S_j as $w_{ij} = -2JS_iS_j$, where J is the exchange integral that is the source of the molecular field. If J is positive, then the spins are arranged parallel and we have ferromagnetism. Else, the spins align antiparallel to each other resulting in antiferromagnetism.

The physical origins of the exchange interaction energy can be understood from Pauli's exclusion principle and Coulomb interaction. Suppose two atoms with unpaired electrons are close to each other, then the electrons will share one molecular orbital if the spins of the two atoms are antiparallel. This increases the Coulomb energy. If this increase in the Coulomb energy is less than the energy minimization due to spin cancellation then the electrons maintain antiparallel spin. Such antiparallel alignment of spin is called antiferromagnetism. If the electrons maintain parallel spins and form separate molecular orbitals, according to Pauli's exclusion principle, then

the opposite happens and the Coulomb energy decreases. Such parallel alignment of spin is known as ferromagnetism.

1.2.5: Magnetic domain theory

The quantum mechanical exchange interaction energy described in Section 1.2.3 causes spontaneous magnetization of the ferromagnetic materials which results in parallel alignment of the atomic spins. However, the overall magnetization of the sample need not be to the extent of complete saturation. An alignment of all the dipoles along the same direction would lead to a drastic increase in the magnetostatic energy of the system due to the formation of free poles. Hence, a balance has to be reached between the exchange and magnetostatic energies such that the overall energy in the system is at a minimum. To attain such a state, the material splits into domains, within which all the spins are aligned along a particular direction. But the spins in the different domains are along different directions.

For explaining these features of a ferromagnet, in 1906 Weiss **[21]** proposed a theory that bridges the atomic origins of magnetism with magnetism in bulk materials. This approach assumed that a molecular field exists in the magnetic matter which aligns all the elementary moments in a given volume called the 'Weiss Domain'. For an applied field at angle between 0 and 90°, the evolution of the Weiss domains is as shown in Fig. 1.2.
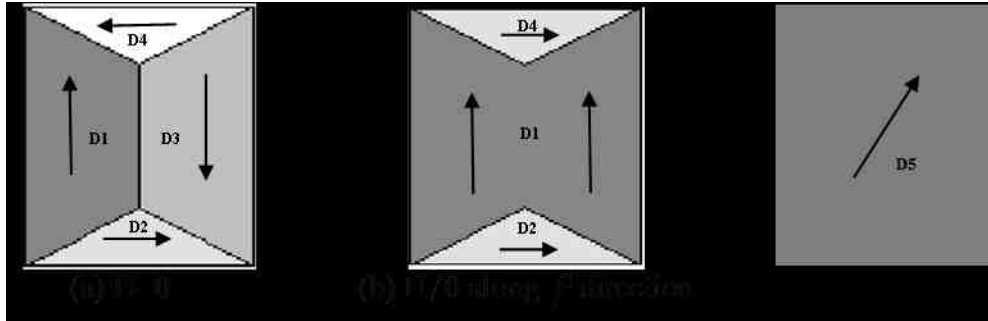
Figure 1.2: Division of a ferromagnet into Weiss domains (a) prior to an applied field (b) in the presence of an applied field oriented toward the upper right corner of the sample and (c) at magnetic saturation in the presence of an applied field oriented toward the upper right corner of the sample (↗).

In general, the magnetization will orient itself along an 'easy axis'. The energy that describes this directional preference in orientation of the magnetization is called the magnetic anisotropy energy. Figure 1.2 (a) shows this energy-minimized state with four domains. The domains align with magnetic easy axis of this material in antiparallel pairs, and with tips to tips and tails to tails so as to minimize the internal energy of the region. When a field is applied, the magnetization in the direction that is closest to the applied magnetic field grows at the expense of the one which is least preferred. In this case, D1 grows and D3 shrinks as shown in Fig. 1.2 (b). If a stronger field is applied, the direction of magnetization jumps from the easy axes directions that minimize energy to the align with easy axis most favorably aligned with applied field direction (here, D2 and D4 jump to D1), which then rotates to align with D5) and we are left with one single domain at magnetic saturation as shown in Fig. 1.2 (c). This process increases the internal energy in the system.

According to Weiss theory, when a magnetic field is applied in any direction, different processes occur. The magnetization flips the domain of maximum misorientation with respect to the applied field (180° domain walls nucleation and displacement). Figure 1.2 (b) shows the growth of D1 at the expense of D3 through the displacement of a 'Bloch wall' which separated domains D1 and D3 in Fig. 1.2 (a) upon application of a magnetic field. Additionally, the magnetization in domain D4 reverses in direction further minimizing system internal energy in the presence of the applied field H.

When the material breaks into N domains, the magnetostatic energy reduces by $1/N$ times but the exchange energy increases at the domain boundaries (domain walls). This causes the domains to break down further until equilibrium is reached between the magnetostatic energy and the domain wall energy, as suggested in Fig. 1.3 (a,b). Closure domains are formed at the edges in the case of materials with cubic magnetocrystalline anisotropy which result in zero magnetostatic energy as shown in Fig. 1.3 (c).
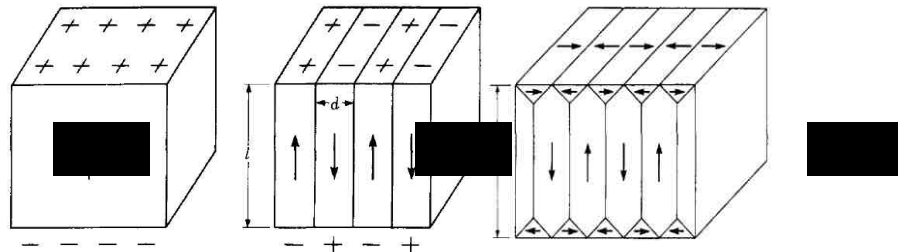
Figure 1.3: (a) Single domain throughout the sample with a high magnetostatic energy. (b) Formation of N domains reduces this energy by $1/N$ times. (c) Closure domains result in zero magnetostatic energy [4].

18

Domain walls are formed due a balance between magnetocrystalline and exchange coupling energy. Large magnetocrystalline anisotropy favors the rotation of moments over fewer lattices, i.e. thin domain wall boundaries, as intermediate orientations result in a large energy penalty. In contrast, large exchange coupling favors a more gradual rotation of moments, so that the difference in orientation between neighboring spins is minimized. This results in thicker domain walls. The moments in the domain wall can rotate/re-orient more easily than the moments within a domain, in response to an applied magnetic field. This results in domain boundary motion, which is an important mechanism for magnetization.

The first attempts to observe the ferromagnetic domain patterns was by Bitter [22] in 1931. He put his sample under a microscope and used a powder-pattern method. The observed domain patterns were maze-like patterns as shown in Fig.1.4 (a), which were misinterpreted as the real domains.
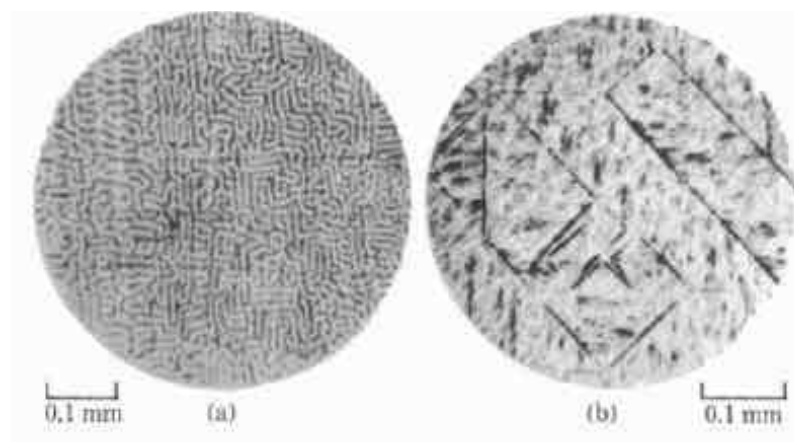
Figure 1.4: Bitter patterns in Fe-Si that is (a) mechanically polished, (b) electrochemically polished or annealed [4].

19

In 1934 Kaya [23] showed that the maze patterns were not the real domains but were caused by stresses introduced during surface polishing. The true domain structure, however, remained elusive. Finally, in 1949 Williams et al. [24] observed well defined domain structures on a precisely cut, stress-free Fe-Si crystal as shown in Figure 1.4 b. Unlike maze domains the true domains are much larger in size and are more geometrical.

In cubic materials such as Fe, Fe-Si, Fe-Al etc. there are two kinds of magnetic domain walls – the 180° walls separating two domains of anti-parallel magnetization with respect to each other and the 90° walls separating two domains of magnetizations that are perpendicular to each other [4]. Fig. 1.5 shows the surface domains on Fe-Si, a cubic material obtain using Magneto Optic Kerr Effect (MOKE) microscopy.
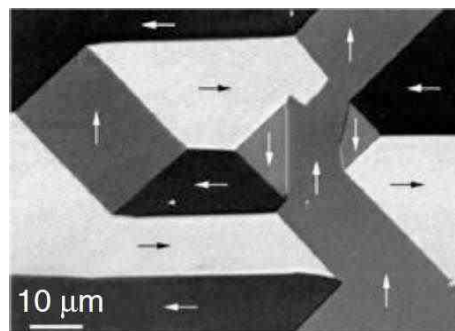
Figure 1.5: Magnetic domains on (100) surface plane $Fe_{97}Si_3$ single crystal alloy showing 180° domain walls separating $[100]/[\bar{1}00]$ - type domains and 90° domain walls separating $[100]/[010]$ - type domains [25].

The 180° walls in cubic materials on the surface parallel to any of the 6 faces of the cube are always straight **[4, 26]**. If the walls are curved, to maintain the anti-parallel orientation of the magnetization, magnetic free poles will tend to appear along the walls, which give rise to a demagnetizing field in the opposite direction to that of the magnetization in the domains. Thus, the magnetostatic energy of the system increases which is not desired. This is depicted in Fig. 1.6.
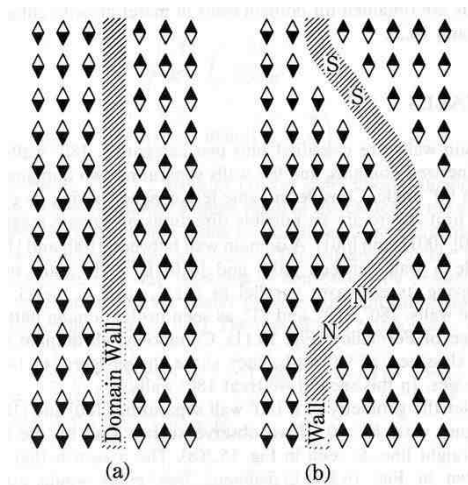
Figure 1.6: (a) A Straight 180◦ domain wall has minimal magnetostatic energy (b) A curved 180◦ domain wall costs magnetostatic energy [4].

However, when the 180° domain wall is observed as shown in Fig. 1.7, it might appear curved because in this case, free poles are absent. But the total surface area of the domains is increased, hence increasing the total wall energy. Additional energy is required to sustain such a curved domain wall which can be attributed to the presence of voids, irregular distribution of internal residual stresses and the dependence of wall energies on the crystallographic directions.
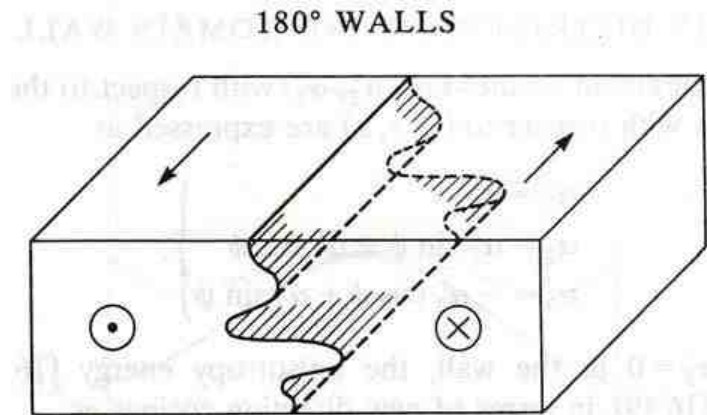
Figure 1.7: Possible curvature of a 180° domain wall in a material with uniaxial anisotropy **[4]**.

Further discussions on magnetic domains and their observation using MOKE microscopy are provided in Chapter 5.

1.3: Magnetostriction

All ferromagnetic materials display a change in shape due to a change in magnetization. This phenomenon of magneto elastic coupling which arises due to the interaction between the magnetic moments of neighboring atoms is called magnetostriction. It was first discovered in Nickel samples by James Joule in 1842 **[27]**.

1.3.1: Magneto-elastic effect

The *Joule effect* **[28]** describes the change in length due to a change in the magnetization state of the material. This is also known as linear magnetostriction and assumes that the volume of the material remains constant. This phenomenon is

described in Fig. 1.8 where the application of an external magnetic field to a demagnetized ferromagnetic sample leads to a change in the dimension due to flipping of the magnetic moments. Magneto-elastic coupling arises from the shifting of the positions of neighboring atoms that make up the magnetic material (with partially filled outer orbits and unbalanced electron populations) in response to the rotation of their magnetic moments and the rigidly attached anisotropic charge clouds. The electron spins of these atoms re-orient from an initial configuration that is attributed to a randomized energy minimization state to being aligned with the external field so as to minimize the overall energy in the system.
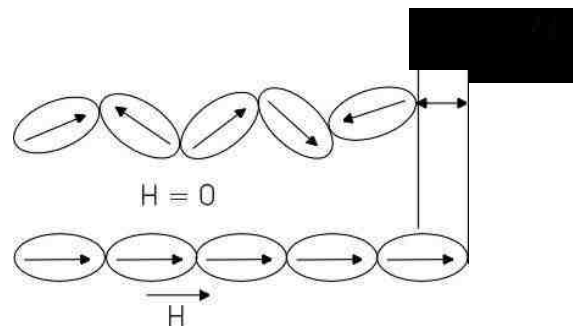
Figure 1.8: Magnetization change in Joule Effect [29].

The *Villari effect* (1865) **[30]** is the mechanical stress-induced change in magnetization as shown in Fig. 1.9. A material with positive magnetostriction (e.g. iron) shows an increase in magnetization with an increase in stress whereas a material with negative magnetostriction (e.g. nickel) exhibits an increase in magnetization with a decrease in stress. Conventionally, a tensile stress is considered positive whereas a compressive stress is considered negative.

23
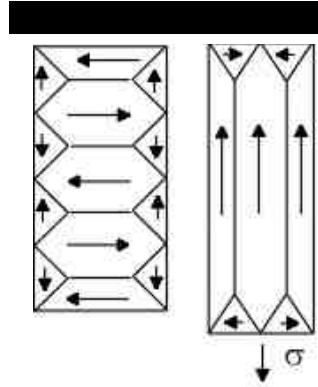
Figure 1.9: Magnetization change in Villari Effect (a) no stress; (b) tensile stress.

The *Wiedemann effect* (1858) **[31]** describes a twist in the material due to a helical field produced by passing a current through the material (e.g. wire). The *Matteucci effect* **[32]** describes the change in magnetization in the helical direction when a ferromagnetic material is twisted.

Barrett (1882) **[33]** observed a change in volume of ferromagnetic materials under the influence of magnetic field and termed it as *volume magnetostriction*. The term *forced magnetostriction* **[34]** describes an increase in the magnetostriction that can be obtained in a magnetically saturated material by increasing the temperature so that further increase in magnetic field reorders the magnetic moments which got disordered due to thermal agitation. Such an increase in magnetostriction is extremely small and to date has no practical application.

A similar phenomenon of a change in the volume of a ferromagnetic material is also observed when the external magnetic field applied is increased beyond

saturation along the easy axis where the moments move away from the easy axis to align with the direction of applied field. This was observed in Terfenol-D by Calkins **[35]**.

Conventionally, the *Joule* and *Wiedemann* effects are used for actuation purposes while the *Villari* and *Matteucci* effects are used for sensing purposes.

The origin of these macroscopic effects can be traced down to atomic scales. Magnetoelastic coupling arises from strong interaction between electron clouds of adjacent atoms and spin-orbit coupling **[5]**. The orbital motion of the electron which is strongly coupled to the crystal lattice structure resists the efforts of the external magnetic field to orient the electron spin along the field direction **[36]**. The flipping of the orbits towards the direction of field which leads to a corresponding distortion of the crystal lattice manifests as magnetostriction.

Mechanical force acting on a material produces mechanical strain as the atomic bonds are stretched or twisted. This causes the displacement of the overlapping electron clouds in a bond thus affecting the electromagnetic state of the material. The change in the electromagnetic state of the material due to the applied force manifests as the inverse effect (i.e. *Villari* and *Matteucci* effects).

Magnetocrystalline anisotropy is determined by the magnitude of spin-orbit coupling at the atomic level. A smaller spin-orbit coupling and consequently smaller

magnetocrystalline anisotropy enables the orbit to reorient itself to the direction of the electron spin at smaller magnetic fields. The atomic lattice distortions associated with a given spin-orbit reorientation is attributed to be the origin of magnetostriction. Hence, for large magnetostriction, the spin-orbit coupling should produce significant lattice distortions. Since it is also desired that large magnetostriction occurs at low magnetic fields, small magnetocrystalline anisotropy is preferred. A brief review of magnetostrictive materials is provided in Appendix A and an explanation of the actuator and sensing behavior is discussed in Appendix B.

1.3.2: Magneto-elastic modeling in magnetostrictive materials

Various non-linear models have been developed to account for the magneto-mechanical response of ferromagnetic materials over different operating conditions **[37-39]**. This work uses the model developed by Armstrong **[40, 41]** that was able to capture the cubic anisotropy and predict three-dimensional actuation in magnetostrictive materials. The model presented in this section is the basis for analysis used in Chapter 2 where the magneto-auxetic behavior of the magnetostrictive alloy Galfenol is examined for different Galfenol compositions. This section deals with deriving an expression for magnetostrictive strain for applied fields along any direction using energy methods.

1.3.2.1: Gibbs free energy in magnetostrictive materials

The dipole-dipole interaction energy between the atoms shown in Fig. 1.10 can be modeled in terms of the bond length r between them using Eq. (1.20) **[4]** where $[\alpha_1, \alpha_2, \alpha_3]$ are the magnetization direction cosines and are defined as: $\alpha_1 = \sin\theta\cos\varphi$, $\alpha_2 = \sin\theta\sin\varphi$ and $\alpha_3 = \cos\theta$ and $[\beta_1, \beta_2, \beta_3]$ are the direction cosines of the bond direction.
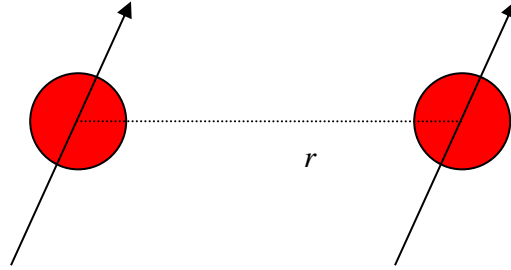
Figure 1.10: Interaction between neighboring dipoles of magnetic moment μ_{mm} and separated by a distance r.

$$w(r,\alpha) = l(r)\left\{ \left(\alpha_1\beta_1 + \alpha_2\beta_2 + \alpha_3\beta_3 \right)^2 - \frac{1}{3} \right\} \qquad (1.20)$$

When the crystal is strained by ε as shown in Eq. (1.21) the equilibrium bond length r changes to $r(1+\varepsilon)$. Calculating the change in the interaction energy Δw and summing it up for all the nearest neighbor pairs in a unit volume of the lattice, one can get the magneto-elastic energy as shown in Eq. (1.22).

$$\varepsilon = \begin{Bmatrix} \varepsilon_{xx} \\ \varepsilon_{yy} \\ \varepsilon_{zz} \\ \varepsilon_{xy} \\ \varepsilon_{yz} \\ \varepsilon_{zx} \end{Bmatrix} \tag{1.21}$$

$$E_{mag-elas} = B_1 \left\{ \varepsilon_{xx} \left(\alpha_1^2 - \frac{1}{3} \right) + \varepsilon_{yy} \left(\alpha_2^2 - \frac{1}{3} \right) + \varepsilon_{zz} \left(\alpha_3^2 - \frac{1}{3} \right) \right\}$$
$$+ B_2 \left\{ \varepsilon_{xy} \alpha_1 \alpha_2 + \varepsilon_{yz} \alpha_2 \alpha_3 + \varepsilon_{zx} \alpha_3 \alpha_1 \right\} \tag{1.22}$$

The coefficients B_1 and B_2 are known as magnetoelastic coupling coefficients. They depend on the number of nearest neighbor pairs, unstrained bond length, the function $l(r)$ and its spatial gradient. The spontaneous magnetostriction or equilibrium strain in a domain in the absence of any external stress or magnetic field can be obtained by minimizing the sum of magnetoelastic and elastic energy with respect to each of the strain components.

To evaluate the expression for magnetostriction, the Gibbs free energy of the system is formulated as the Legendre transformation of the internal energy. Assuming an isothermal and isentropic process, the Gibbs free energy is reduced to the enthalpy of the system. This is expressed as the sum of the magneto-crystalline anisotropy energy $E_{anisotropy}$, the magnetoelastic energy $E_{mag-elas}$, the elastic energy E_{elas}, the

magnetic work (Zeeman Energy) W_{mag}, and the mechanical work W_{mech} as shown in Eq. (1.23).

$$H = E_{anisotropy} + E_{mag-elas} + E_{elas} - W_{mag} - W_{mech} \qquad (1.23)$$

Where, according to definition,

$$E_{anisotropy} = K_1(\alpha_1^2\alpha_2^2 + \alpha_2^2\alpha_3^2 + \alpha_3^2\alpha_1^2) + K_2(\alpha_1^2\alpha_2^2\alpha_3^2) \qquad (1.24)$$

Here, α_i are the direction cosines of the magnetization. K_1 and K_2 are the cubic anisotropy constants [4].

The anisotropy energy in a cubic crystal determines the easy axes for magnetizing the material at each composition and the total energy in the magneto-elastic system is directly proportional to the anisotropy constants K_1 and K_2. Fig. 1.11 is obtained by evaluating the magnetocrystalline anisotropy energy (as shown in Eq. (1.24)), along the <100>, <110> and <111> directions for different values K_1 and K_2.
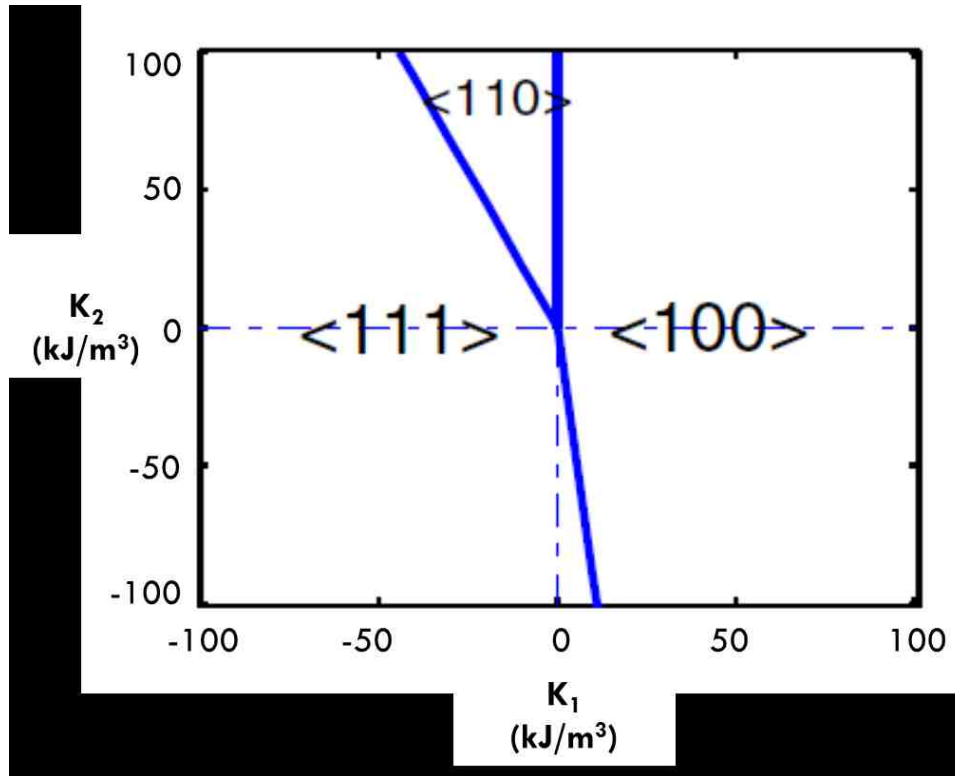
Figure 1.11: Easy axes for different values of cubic magnetocrystalline anisotropy constants K_1 and K_2. Based on [3].

For $K_1 > 0$ and $K_2 > -9\,K_1$, the <100> direction is the easy axis whereas for $K_1 < 0$ and $K_2 > -(9/4)\,K_1$, the <110> direction is easy. For all other cases <111> direction is the easy axis. Thus, for a given value of K_1 and K_2, the easy direction can be determined and this strongly influences the nature of λ-H and B-H curves along a given crystallographic direction. But, the values of the anisotropy constants K_1 and K_2 which describe the dependence of energy distribution on crystallographic direction have to be established empirically. For Galfenol, which has <100> easy axes , there are only a few compositions for which the values of K_1 and K_2 have been determined (discussed further in Section 1.3.4) [42].

$E_{mag-elas}$ has already been defined in Eq. (1.22). Equation (1.25) shows the expression for E_{elas}, where, $\tilde{C}$ is the stiffness matrix of the material.

$$E_{elas} = \frac{1}{2}\varepsilon^T \tilde{C}\varepsilon \qquad (1.25)$$

For cubic materials such as Galfenol, $\tilde{C}$ can be expressed in terms of the elastic constants c_{11}, c_{12} and c_{44} as shown in Eq. (1.26).

$$\tilde{C} = \begin{bmatrix} c_{11} & c_{12} & c_{12} & 0 & 0 & 0 \\ c_{12} & c_{11} & c_{12} & 0 & 0 & 0 \\ c_{12} & c_{12} & c_{11} & 0 & 0 & 0 \\ 0 & 0 & 0 & c_{44} & 0 & 0 \\ 0 & 0 & 0 & 0 & c_{44} & 0 \\ 0 & 0 & 0 & 0 & 0 & c_{44} \end{bmatrix} \qquad (1.26)$$

The expressions for the terms that define the magnetic and mechanical work done in the system are as shown in Eqs. (1.27 and 1.28).

$$W_{mag} = \mu_0 M^T H \qquad (1.27)$$

Here, $M = M_s \begin{bmatrix} \alpha_1 & \alpha_2 & \alpha_3 \end{bmatrix}^T$, M_S is the saturation magnetization.

$$W_{mech} = \sigma^T \varepsilon \qquad (1.28)$$

Where, σ is the externally applied stress.

Hence,

$$H = K_1(\alpha_1^2\alpha_2^2 + \alpha_2^2\alpha_3^2 + \alpha_3^2\alpha_1^2) + K_2(\alpha_1^2\alpha_2^2\alpha_3^2) + B_1\left\{\varepsilon_{xx}\left(\alpha_1^2 - \tfrac{1}{3}\right) + \right.$$

$$\left. \varepsilon_{yy}\left(\alpha_2^2 - \tfrac{1}{3}\right) + \varepsilon_{zz}\left(\alpha_3^2 - \tfrac{1}{3}\right)\right\} + B_2\{\varepsilon_{xy}\alpha_1\alpha_2 + \varepsilon_{yz}\alpha_2\alpha_3 + \varepsilon_{zx}\alpha_3\alpha_1\} +$$

$$\tfrac{1}{2}\varepsilon^T\tilde{C}\varepsilon + \mu_0 M^T H + \sigma^T\varepsilon \tag{1.29}$$

1.3.2.2: Equilibrium strain in magneto-elastic systems

Early works **[43, 44]** had assumed zero applied stress to determine the equilibrium strain. A different approach of assuming constant 3-D stress has been proposed in a more recent study **[45]** which will be followed here.

The equilibrium states of the system can be calculated by minimizing H with respect to its internal variables α_i and ε. It is assumed that $H(\alpha_i, \varepsilon)$ is a continuous function of α_i and ε and has continuous second order partial derivatives.

Performing the differential in Eq. (1.30), an expression for equilibrium strain can be obtained in Eq. (1.34).

$$\frac{\partial H(\alpha_i, \varepsilon)}{\partial \varepsilon} = 0 \tag{1.30}$$

$$\begin{bmatrix} B_1\left(\alpha_1^2-\dfrac{1}{3}\right) \\[2mm] B_1\left(\alpha_2^2-\dfrac{1}{3}\right) \\[2mm] B_1\left(\alpha_3^2-\dfrac{1}{3}\right) \\[2mm] B_2\alpha_1\alpha_2 \\[2mm] B_2\alpha_2\alpha_3 \\[2mm] B_2\alpha_3\alpha \end{bmatrix} + \tilde{C}\varepsilon - \sigma = 0 \tag{1.31}$$

For convenience, let us call

$$\left[B_1\left(\alpha_1^2-\frac{1}{3}\right) \quad B_1\left(\alpha_2^2-\frac{1}{3}\right) \quad B_1\left(\alpha_3^2-\frac{1}{3}\right) \quad B_2\alpha_1\alpha_2 \quad B_2\alpha_2\alpha_3 \quad B_2\alpha_3\alpha \right] = b \tag{1.32}$$

Equation (1.31) can be simplified to the expression in Eq. (1.33).

$$b^T + \tilde{C}\varepsilon - \sigma = 0 \tag{1.33}$$

Solving for ε yields,

$$\varepsilon^* = \tilde{C}^{-1}\sigma - \tilde{C}^{-1}b^T \tag{1.34}$$

Since $\tilde{C}^{-1}\sigma$ is the mechanical strain and $-\tilde{C}^{-1}b^T$ is the magnetostriction λ, Eq. (1.34) can be rewritten as

$$\varepsilon^* = \varepsilon_{mech} + \lambda \tag{1.35}$$

Examining Eqs. (1.33-1.35) further, the equilibrium strain derived for zero stress includes only the second part of Eq. (1.35), which is the magnetostrictive strain λ **[43, 44]**. Here, since the stress is non-zero, the equilibrium strain is a superposition of ε_{mech} and λ .

To determine whether ε^* corresponds to a maximum or minimum, the second derivative of H is computed as represented by Eq. (1.36).

$$\frac{\partial^2 H(\alpha_i, \varepsilon)}{\partial \varepsilon^2} = \tilde{C} \tag{1.36}$$

Since $\tilde{C}$ is a positive quantity, ε^* corresponds to a relative minimum of $H(\alpha_i, \varepsilon)$ and is therefore the equilibrium strain.

1.3.2.3: Magnetostrictive Strain

The change in dimension under applied magnetic fields can be calculated from Eq. (1.33-1.35). This magnetostrictive strain is shown in Eq. (1.37).

$$\lambda = -\tilde{C}^{-1} b^T \tag{1.37}$$

Substituting for $\tilde{C}$ in Eq. (1.37), we get

$$\lambda = -\begin{bmatrix} c_{11} & c_{12} & c_{12} & 0 & 0 & 0 \\ c_{12} & c_{11} & c_{12} & 0 & 0 & 0 \\ c_{12} & c_{12} & c_{11} & 0 & 0 & 0 \\ 0 & 0 & 0 & c_{44} & 0 & 0 \\ 0 & 0 & 0 & 0 & c_{44} & 0 \\ 0 & 0 & 0 & 0 & 0 & c_{44} \end{bmatrix}^{-1} \begin{bmatrix} B_1\left(\alpha_1^2 - \dfrac{1}{3}\right) \\ B_1\left(\alpha_2^2 - \dfrac{1}{3}\right) \\ B_1\left(\alpha_3^2 - \dfrac{1}{3}\right) \\ B_2\alpha_1\alpha_2 \\ B_2\alpha_2\alpha_3 \\ B_2\alpha_3\alpha \end{bmatrix} \qquad (1.38)$$

Equation (1.38) upon simplification yields

$$\lambda = -\begin{bmatrix} \dfrac{B_1}{c_{12}-c_{11}}\left(\alpha_1^2 - \dfrac{1}{3}\right) \\[4pt] \dfrac{B_1}{c_{12}-c_{11}}\left(\alpha_2^2 - \dfrac{1}{3}\right) \\[4pt] \dfrac{B_1}{c_{12}-c_{11}}\left(\alpha_3^2 - \dfrac{1}{3}\right) \\[4pt] \dfrac{B_2}{c_{44}}\alpha_1\alpha_2 \\[4pt] \dfrac{B_2}{c_{44}}\alpha_2\alpha_3 \\[4pt] \dfrac{B_2}{c_{44}}\alpha_3\alpha_1 \end{bmatrix} \qquad (1.39)$$

Therefore, the elongation due to magnetostriction along any direction (represented by the direction cosines $\gamma_1, \gamma_2, \gamma_3$) can be evaluated using the expression

$$\frac{\delta l}{l} = \lambda_{xx}\gamma_1^2 + \lambda_{yy}\gamma_2^2 + \lambda_{zz}\gamma_3^2 + \lambda_{xy}\gamma_1\gamma_2 + \lambda_{yz}\gamma_2\gamma_3 + \lambda_{zx}\gamma_3\gamma_1 \qquad (1.40)$$

35

where, λ_{ii} are the magnetostrictive strains.

Upon substituting the values of λ_{ii} from Eq. (1.39),

$$\frac{\delta l}{l} = -\frac{B_1}{c_{12} - c_{11}}\left(\gamma_1^2\alpha_1^2 + \gamma_2^2\alpha_2^2 + \gamma_3^2\alpha_3^2 - \frac{1}{3}\right)$$
$$-\frac{B_2}{c_{44}}\left(\gamma_1\gamma_2\alpha_1\alpha_2 + \gamma_2\gamma_3\alpha_2\alpha_3 + \gamma_3\gamma_1\alpha_3\alpha_1\right)$$

(1.41)

The magnetostriction along [100] direction can be calculated by substituting the corresponding values for γ_1, γ_2 and γ_3 as well as α_1, α_2 and α_3.

When $\alpha_1 = \gamma_1 = 1$ and $\alpha_2 = \alpha_3 = \gamma_2 = \gamma_3 = 0$,

$$\lambda_{100} = \Delta l_{100} = -\frac{2}{3}\frac{B_1}{c_{11} - c_{12}}$$

(1.42)

Similarly, the magnetostriction along the [111] direction can also be calculated. Here, γ_1, γ_2, γ_3 and α_1, α_2, $\alpha_3 = \dfrac{1}{\sqrt{3}}$.

$$\lambda_{111} = \Delta l_{111} = -\frac{1}{3}\frac{B_2}{c_{44}}$$

(1.43)

Using Equations (1.42) and (1.43), the magneto-elastic coupling constants can be represented in terms of the magnetostriction constants and elastic constants [44] as

36

$$B_1 = -\frac{3}{2}\lambda_{100}(c_{11} - c_{12})$$

$$B_2 = -3\lambda_{111}c_{44} \qquad \text{(1.44 a,b)}$$

Hence, upon substituting for B_1 and B_2 from Eq. (1.44 a,b) into Eq. (1.39) and Eq. (1.41), we get Eq. (1.45) and Eq. (1.46) respectively.

$$\lambda = \begin{bmatrix} \frac{3}{2}\lambda_{100}\left(\alpha_1^2 - \frac{1}{3}\right) \\ \frac{3}{2}\lambda_{100}\left(\alpha_2^2 - \frac{1}{3}\right) \\ \frac{3}{2}\lambda_{100}\left(\alpha_3^2 - \frac{1}{3}\right) \\ 3\lambda_{111}\alpha_1\alpha_2 \\ 3\lambda_{111}\alpha_2\alpha_3 \\ 3\lambda_{111}\alpha_3\alpha_1 \end{bmatrix} \qquad \text{(1.45)}$$

$$\frac{\delta l}{l} = \frac{3}{2}\lambda_{100}\left(\gamma_1^2\alpha_1^2 + \gamma_2^2\alpha_2^2 + \gamma_3^2\alpha_3^2 - \frac{1}{3}\right)$$
$$+ 3\lambda_{111}\left(\gamma_1\gamma_2\alpha_1\alpha_2 + \gamma_2\gamma_3\alpha_2\alpha_3 + \gamma_3\gamma_1\alpha_3\alpha_1\right) \qquad \text{(1.46)}$$

This magnetostriction where the overall volume was conserved (which arises from Eq. (1.46), where the higher order terms are ignored) $\frac{\partial v}{v} = \lambda_{xx} + \lambda_{yy} + \lambda_{zz} = 0$ is called Joule's Magnetostriction. This is shown in Fig. 1.11. However all magnetostrictive materials exhibit volume magnetostriction to some extent [46].

(a) λ_{100} (b) λ_{111}
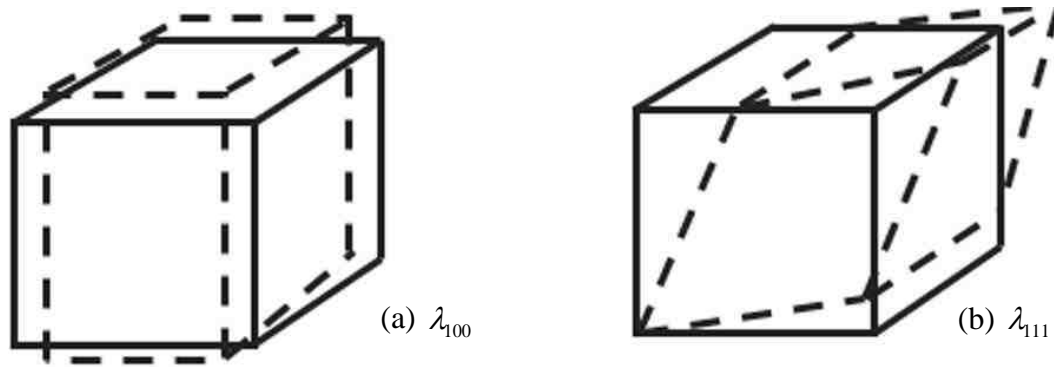
Figure 1.11: Volume conserving magnetostriction [5] along (a) <100> and (b) <111> crystallographic directions.

Joule's magnetostriction also leads to an additional anisotropy which is called magnetostriction induced anisotropy. Hence the overall anisotropy is the sum of magneto-crystalline anisotropy and magnetostriction induced anisotropy. As expected, if the magnetostriction is constrained (with the constraint at scales less than the exchange length), the magnetostriction induced anisotropy becomes zero **[45]**. This has also been empirically verified **[47]**.

1.3.3: Crystallography

The magneto-elastic characteristics bear a direct relationship to the changes in the crystal lattice. This section will give a brief overview of the crystal structure of Fe-Ga and the corresponding Miller Indices which will aid subsequent discussions.

Both the magnetostriction and the auxetic behavior of Galfenol are enhanced in the case of single crystal samples. A single crystal material is one in which the periodic and repeated atomic pattern extends throughout its entirety without

38

interruption. The Galfenol samples studied here all possess a body centered cubic (BCC) crystal lattice, shown schematically in Fig. 1.12. The lattice is assumed to be comprised of iron atoms with randomly distributed gallium atoms taking the place of iron atoms.
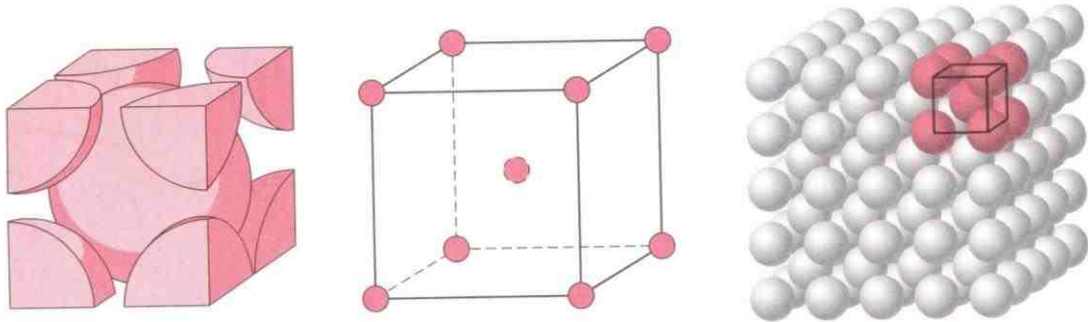
Figure 1.12: Body centered cubic lattice: (a) Hard sphere unit cell representation (b) Reduced-sphere unit cell representation (c) Array of unit cells [48].

The iron crystal lattice is BCC in structure and as Gallium is added to obtain Galfenol of different compositions, various phases are obtained which are shown in Fig. 1.13. The significance of the phase distribution which depends on the energy required for the Ga atoms to occupy certain points in the crystal lattice will be discussed in detail in Section 1.3.4.
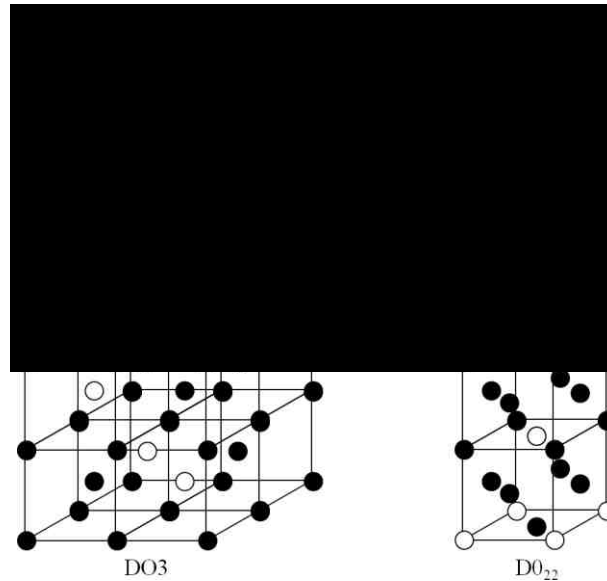
Figure 1.13: Structure of different phases in Fe–Ga [26]. (a) A_2 phase which is usually formed at low compositions where the Ga atoms are equally likely to occupy any of the 9 locations in the BCC crystal lattice of α-Fe. (b) B_2 phase where the Ga atom occupies the center of the BCC lattice. (c) $L1_2$ phase where Galfenol exists in a FCC structure with Ga atoms occupying the corners of the cube and Fe atoms occupying the center of the faces. (d) $D0_3$ phase where Ga atoms occupy the center of alternating unit cells in the BCC crystal. (e) $D0_{22}$ phase where the Ga atoms occupy corners and face center of alternating faces of a FCC structure with Fe atoms occupying the remaining locations in the lattice.

Miller Indices which were developed in the year 1839 have been used to describe a vector in a particular direction [u v w] or a plane (u v w) of any lattice. Fig. 1.14 shows a BCC cell with the Miller indices of the various primary directions as well as the (001) plane marked. Here, the atom at the bottom far-left corner of the cube is assumed to be the origin for the indices.

40
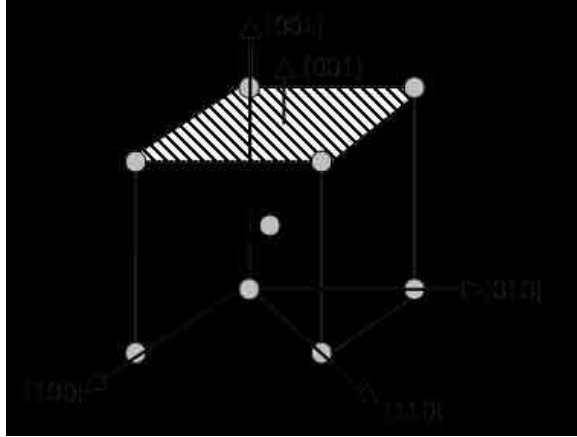
Figure 1.14: BCC cell with Miller indices with shaded (100) plane.

In the case of Galfenol, maximum magnetostriction is observed along the [100] direction when a stress is applied along the same direction **[8, 11, 26]**. This will be discussed in detail in Section 1.3.4. In addition, an auxetic response (i.e. a negative Poisson's ratio) is observed along the <110> direction. This will be discussed in Section 1.4.

The corresponding Poisson's ratios are written as $\nu_{(100,\ 010)}$ and $\nu_{(110,\ 1\ \bar{1}0)}$, where the first subscript represents the load direction and the second identifies the direction transverse to the load. We shall leave off the first subscript in the remainder of this dissertation for ease of representation.

1.3.4: Iron-Gallium alloys

In this section, the metallurgical and magnetostrictive properties of Iron-Gallium alloys (Galfenol) will be discussed with special attention to works pertinent

to this research. For a more extensive discussion on Galfenol the dissertations of Kellogg, Atulasimha and Datta **[8, 11, 15]** may be consulted.

When Fe-Ga alloys were developed at the Naval Surface Warfare Center by Clark and team around 2001 **[7, 49]**, it was observed that the alloy exhibited a peak magnetostriction of $\sim 400\,\mu\varepsilon$ **[7]** (much larger than Fe-Al $\sim 140\,\mu\varepsilon$ **[50]**) under magnetic fields of as low as about 100 Oe along the <100> easy axes. The Fe-Ga alloy system also exhibits high tensile strengths (about 400 MPa **[6, 7]**), ductile-like behavior **[15]**, low saturation **[15]** and low hysteresis **[51]**; all useful properties for device applications. Additionally, there is limited dependence of magnetomechanical properties on temperatures between -20°C and 80°C **[15]**

Galfenol can also be easily rolled **[52, 53]**, machined **[54]** and welded **[55]**, making it easy to manufacture in different shapes and sizes and unlike Terfenol-D, these alloys can also be bent **[11, 56]**.

The variation of the magnetostrictive constants λ_{100} and λ_{111} as a function of the composition of Gallium (in percentage) is shown in Fig. 1.15.
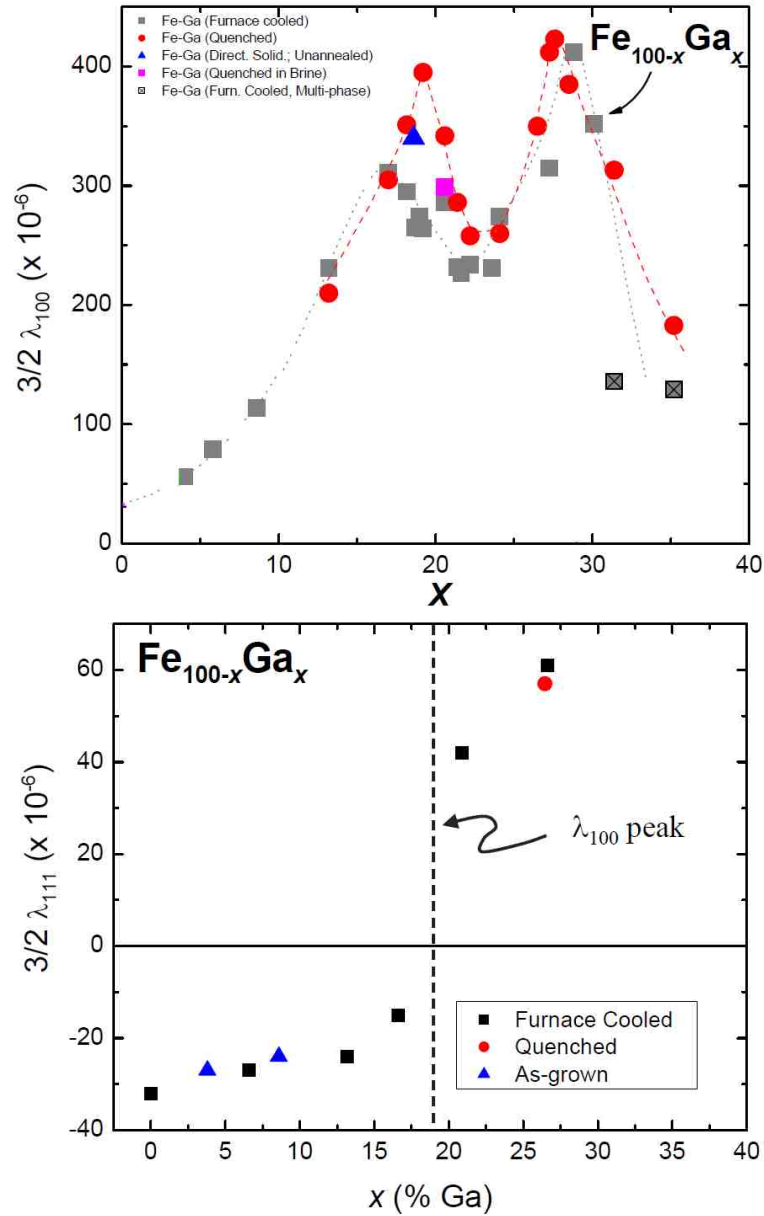
Figure 1.15: Magnetostrictive constants (λ100 -top and λ111 -bottom) for single crystal samples of Fe–Ga alloys for different at% Gallium [49].

Magnetostriction ($3/2\,\lambda_{100}$) of α -Fe increases monotonically from 36 $\mu\varepsilon$ [44] to 300 $\mu\varepsilon$ with a gradual addition of nonmagnetic Ga, for concentration up to 17 at% Ga. Beyond this, the magnetostriction is thermal history dependent up to 25 at% Ga. While quenching the alloy from a high temperature sustains the monotonic increase

up to 20 at% Ga, slow-cooling decreases the magnetostriction beyond 17 at% Ga. Past 25 at% Ga, the magnetostriction increases again with a second peak at 28 at% Ga. The reasons for the peak values of magnetostriction have been extensively studied [7, 49, 57].

Figure 1.16 shows the equilibrium phase diagram of Fe-Ga [58, 59]. At room temperature, α-Fe has a body-centered cubic (BCC) or A2 crystal structure. Up to 12% of Ga, a solid-solution of Fe and Ga is formed, beyond which Fe–Ga alloy forms a mixture of two phases, A2 and $L1_2$ up to 25 at%. At higher temperatures, phases like $D0_3$, B2, $D0_{19}$ exist. Galfenol with compositions of as high as ~35% Ga that are quenched from high temperatures will retain an α-Fe, a body-centered cubic (BCC) or A2 crystal structure. The unit cells of these structures were shown in Fig 1.13. The melting point of Galfenol can also be obtained from the equilibrium phase diagram.
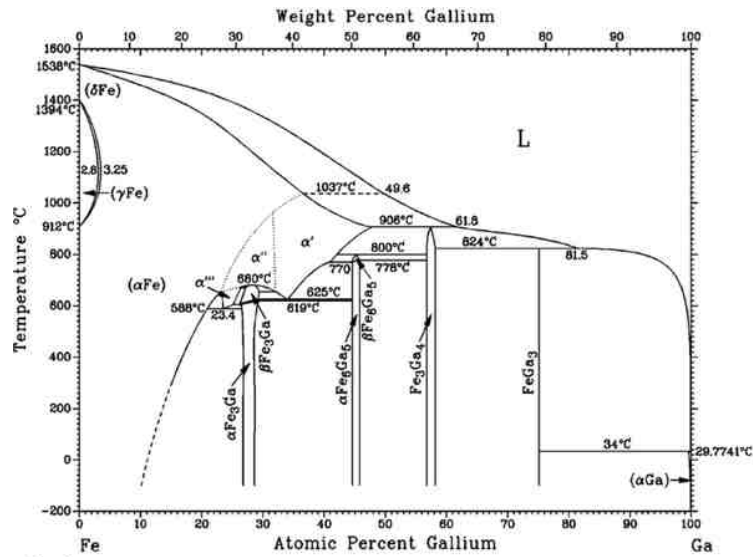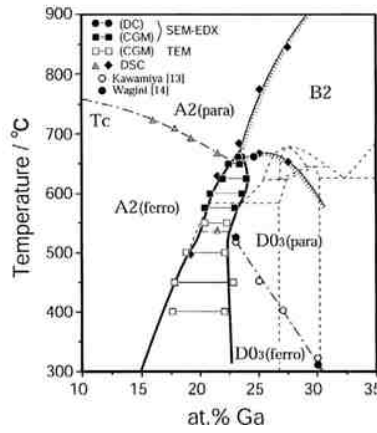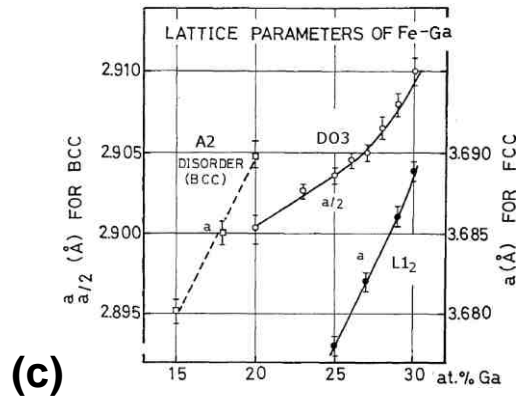
Figure 1.16: (a) Equilibrium phase diagram of Fe-Ga. (b) Metastable phase diagram of Fe-Ga. (c) Lattice parameters measured used XRD in Fe-Ga [60].

Note that there are two peaks in magnetostriction that correspond to about 19 at% Ga and about 28 at% respectively. This may be explained qualitatively using the pairing model suggested by Cullen [57]. The Ga atoms are large relative to Fe and randomly substitute for Fe atoms by fitting into α-Fe BCC lattice sites forming Ga-pairs along the edges of the cubic lattice as illustrated by a 2-D schematic in Fig. 1.17 (a). The Ga pairs may facilitate short term order leading to anisotropic condition, resulting in magnetostriction in the <100> direction. As the Ga content increases beyond 17 at. % Ga (in furnace cooled and 19 at. % Ga in quenched FeGa alloys), an increased formation of $D0_3$ and B_2 crystallographic structure results as shown in Fig. 1.17 (b).
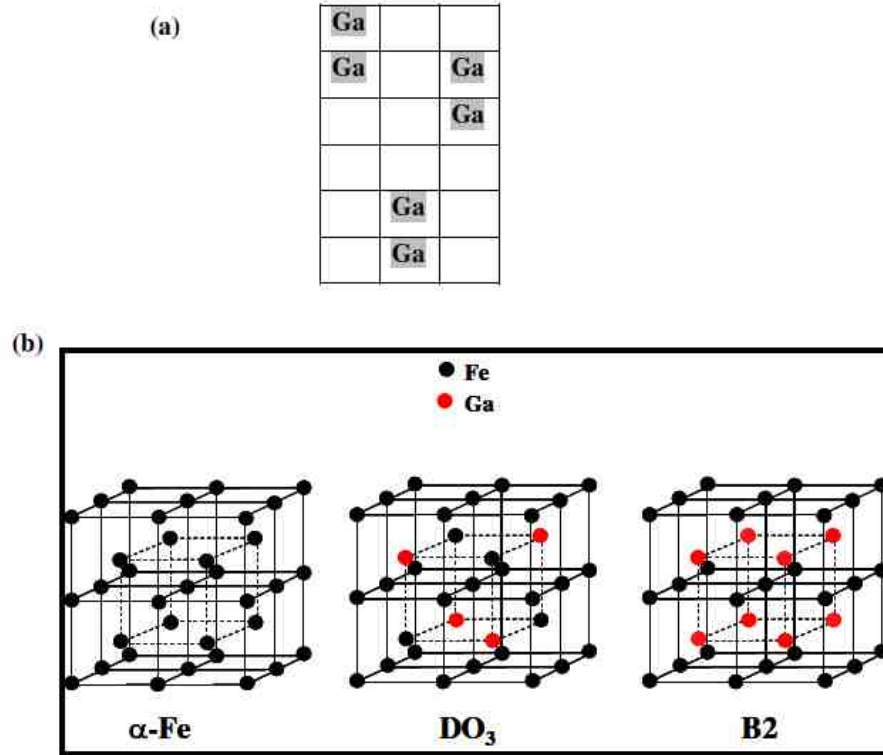
Figure 1.17: (a) Schematic of Ga-Ga pairs Fe-lattice randomly substituted with Ga atoms (disordered A2 phase).
(b) Crystallographic structure of ordered phases D03 and B2 of FeGa. (Based on presentation by Arthur E. Clark at Galfenol Workshop at University of Maryland, College Park, 2005)

Modeling of the magnetostriction produced by various structures from first principles using quantum mechanics and a density functional approach by Wu et al. **[61]** may help resolve some of the ambiguities encountered in the current qualitative theories on magnetostriction in Galfenol.

The magnetic anisotropy in the crystal which determines the preference for a particular direction is defined by Eq. 1.24. The magnetic anisotropy as a function of Ga concentration was measured by Rafique et al. **[42]**. As shown in Fig. 1.18 the

anisotropy constant K_1 decreases to almost zero as the first peak in magnetostriction is approached. The anisotropy constant K_2 which has a negative value for low Ga compositions, increases with Ga content such that is also becomes almost zero near the first peak at about 20% Ga content.
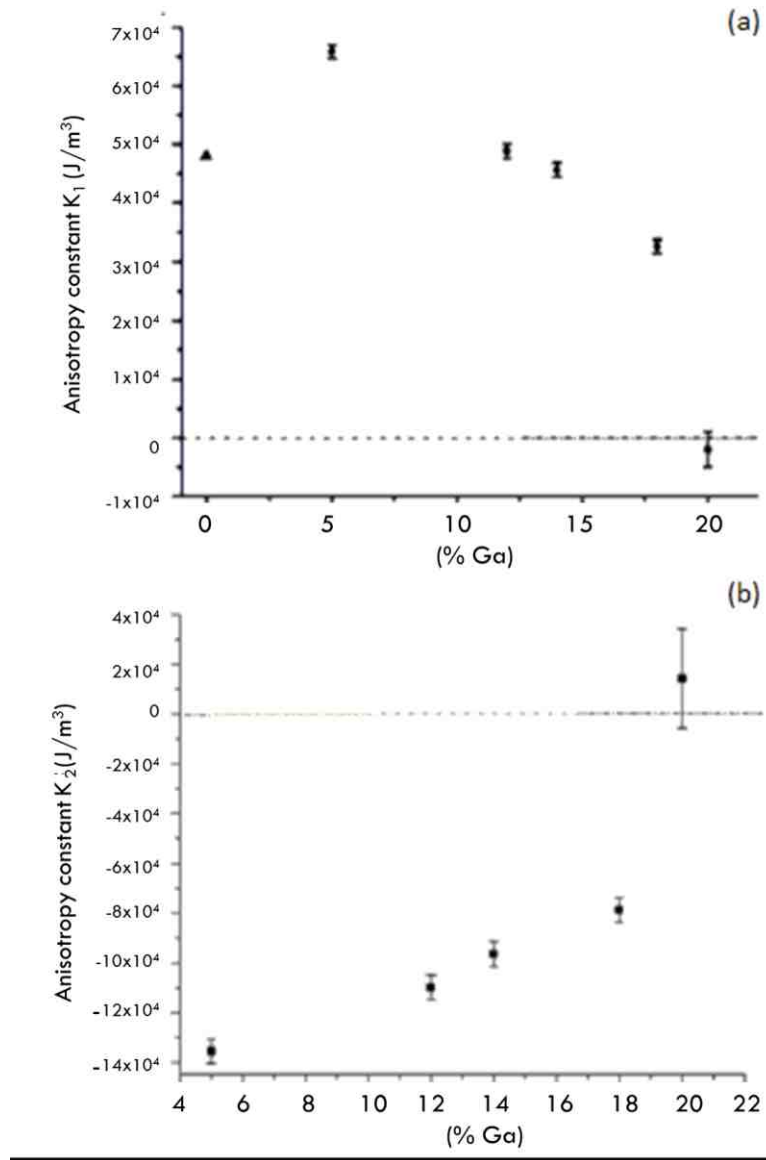
Figure 1.18: Magnetic anisotropy constants (a) K_1 and (b) K_2 as a function of Ga at. % in Galfenol.

K_1 is of particular importance in alloys with <100> easy axes like Galfenol, owing to the direct correlation between K_1 being positive and the <100> axes being the easy axes (illustrated in Fig. 1.11). The influence of K_1 on the easy axis and Poisson's ratio at each composition <20% Ga will be discussed in detail for Galfenol under applied stresses in Chapter 2 and for applied magnetic fields in Chapter 4.

The elastic constants were measured by Wuttig et al. [62] and Clark et al. [49] as shown in Fig. 1.19. Based on Equations (1.25 and 1.26), the tetragonal shear modulus $c' = (c_{11} - c_{12})/2$ linearly softens with increasing Ga at%, whereas the diagonal shear modulus c_{44} remains more or less unchanged. Clark et al. [40] also show a linear increase in the magnetoelastic constant B_1 with the increase in Ga at% leading to the first peak. Since the magnetostriction constant $\lambda_{100} = -B_1/3c'$, the dependence of magnetostriction on Ga at% leading to the first peak is quadratic. It is believed that the second peak is purely due to the softening of shear modulus.
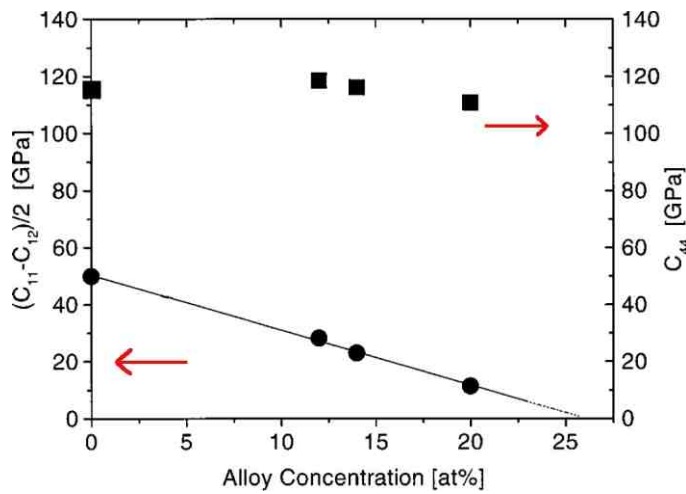
Figure 1.19: Shear constants c' and c_{44} as a function of Ga at. % in Galfenol.

49

1.4: Negative Poisson's ratio (Auxeticity)

Virtually all common materials undergo a transverse contraction when stretched in one direction and a transverse expansion when compressed. The magnitude of this transverse deformation is governed by a material property called Poisson's ratio (ν). It is defined as the negative ratio of a transverse and longitudinal strain in a material which is developed due to a longitudinal extension or compression.

According to thermodynamics, the Poisson's ratio of a stable isotropic, linear elastic material cannot be less than -1.0 or greater than 0.5 due to the requirement that Young's modulus, shear modulus and bulk modulus must have positive values. Conventional materials have a positive Poisson's ratio and have been extensively studied and documented over the years. A perfectly incompressible material (like rubber) deformed elastically at small strains will have $\nu=0.5$ while those that exhibit very little lateral strain like corks have $\nu \sim 0$. Most metals like aluminum, copper, iron etc. have a Poisson's ratio between 0.2 and 0.4.

Although materials with negative Poisson's ratio are theoretically permissible, its occurrence in real materials is limited **[63]**. This type of material can be found naturally occurring in some rocks, minerals and even biological tissues such as the skin covering a cow's teats. People have known about such materials for over 100 years **[64]**, but have not given them much attention because the magnitude of auxeticity was quite small ($\nu \sim$ -0.1).

One of the largest examples of auxetic structures is the graphite core found in some nuclear reactors. These cores were developed in the late 1950s **[65]** and so pre-date the bulk of auxetic materials research by some 30 years or so. These structures were not designed specifically to have auxetic properties. Instead, they were designed to withstand the horizontal shear forces generated during earthquakes, while also having low resistance to changes in volume caused by exposure to radiation and thermal variations.

Large-scale negative Poisson's ratio was first realized in 1982 in the form of two-dimensional silicone rubber **[66]**. Interest in this field peaked in 1987 when Lakes developed the first auxetic polyurethane foam with a re-entrant structure **[63, 67]** which had a Poisson's ratio value of ~ -0.7. Since then, a wide variety of auxetic materials have been fabricated, including polymeric and metallic foams, microporous polymers, carbon fiber laminates and honeycomb structures. Typical examples are polymer-ploytetrafluorothylene (PTFE), ultra-high molecular weight polyethylene (UHMWPE), polypropylene (PP) **[68-70]**. These materials were named auxetics by Evans **[71]**, which, in contrast to conventional materials (like rubber, glass, metals, etc.), expand transversely when pulled longitudinally and contract transversely when pushed longitudinally. "Auxetics" comes from the Greek word auxetos, meaning "that which may be increased".

Although these synthetic materials such as auxetic polymers have large negative values for Poisson's ratio (as low as -12 **[72]**), they are structurally weak due to inherent porosity **[73]**. As such, they are not useful in load bearing applications **[74]**. When their structural properties are engineered to improve stiffness, the auxetic behavior tends to be reduced **[73]**.

There is considerable fundamental and practical interest in structural auxetic materials which apart from having a negative Poisson's ratio are also capable of bearing loads **[75]**. Such materials have potential for several novel engineering applications such as improving fatigue life, sound and vibration damping, limiting crack propagation, ultrasonic energy absorption, indentation resistance and fiber pullout mitigation in composites etc. In recent times, the biomedical industry is exploring the use of such materials for micro filters and valves in drug delivery systems and synclastic (doubly curved) structures for bandages.

Analysis of the elastic constants of anisotropic metallic systems with a cubic crystallographic structure have suggested that their Poisson ratio value might attain a negative value along some directions **[66]**. The calculation of Poisson's ratio is complicated for directions oblique to the crystal axes, because the elastic tensor for general orientations involves as many as 21 interrelated components in the cubic phase **[76]**. Galfenol, a magnetostrictive alloy of Iron and Gallium is one such cubic material which has been shown to exhibit Poisson's ratio values as low as -0.7 **[12]** along the <110> {100} crystallographic direction under tensile loads.

The hypothesis that will be investigated in this study is the possibility of a magneto-auxetic response, i.e. an auxetic response under applied magnetic fields and zero stresses, that exploits the inherent magneto-mechanical coupling in the alloy. Quantifying the Poisson's ratio response to magnetic fields rather than to mechanical stress at various compositions of Gallium in the alloy will be the primary focus of this work along with understanding the associations between the anisotropic magnetic and mechanical energies that are the origins of this phenomenon.

A recent work by Tan et al. **[77]** established an auxetic behavior under electrical loads in electric-field-induced ferroelectric phase of an antiferroelectric ceramic. This is similar to the hypothesis of this work where a magnetic field will be used to induce an auxetic response in Galfenol. It was shown that structural changes (de-tilting of oxygen ocatahedra) in the lattice induced in the ferroelectric phase are the microscopic origins of this effect in PNZST43/6/2. The current work will attempt to provide an atomic level mechanism in Galfenol based on structural changes in the lattice on the same lines as Tan et al.

1.4.1: Materials with a negative Poisson's ratio their classification

Auxetic materials are interesting both because of their novel behavior and because of enhancements in other material properties that are related to Poisson's

ratio. For this reason, they can be considered as both functional materials as well as structural materials **[75]**.

The magnitude of auxetic response is determined by the internal structure of the material. Based on the architecture of its internal structure, auxetic materials are classified as geometric auxetics and molecular auxetics. Their distinction will be discussed in detail in Sections 1.4.1 and 1.4.2. Various models have also been proposed in an attempt to explain the auxetic phenomenon in the different types of auxetic materials **[78, 79]**.

Another way of classifying auxetic materials is based on whether they are artificially manufactured or freely occurring in nature, as synthetic auxetics and natural auxetics respectively. Examples of naturally occurring auxetics include catskin and load-bearing cancellous (spongy) bone found in human shins **[67]**. Most of the man-made auxetics were developed after Rod Lakes developed an auxetic polymeric foam at the University of Iowa **[63]** by converting an ordinary foam using a relatively simple process of heating and squashing. A whole range of synthetic auxetic materials have been produced since then, including carbon fiber composites **[80]**, honeycomb structures **[81]** and microporous polymers **[68]**. Early three-dimensional auxetic metamaterials with anisotropic Poisson's ratios have also recently been presented **[82]**.

Auxetic response itself is categorized into two major groups, volume conserving in-plane auxetic materials, where there are compensating contractions or expansions in the third out of plane direction to maintain volume conservation, and non-volume conserving auxetic materials where the volume of the material is not conserved whilst exhibiting an auxetic mechanical response.

Another interesting feature of this response is that it is scale independent! Deformation can take place at the macro-, micro- or even molecular level (see Fig.1.20).
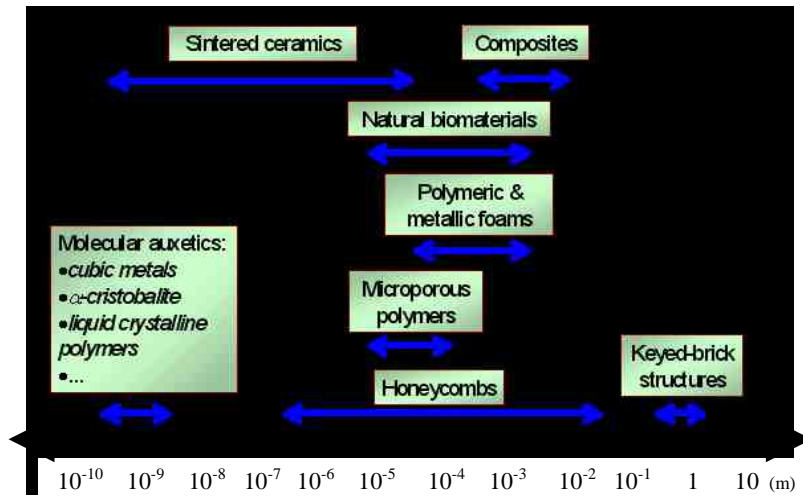
Figure 1.20: Order of strain along the transverse direction owing to auxetic response in different auxetic structures (taken from [67]).

1.4.1.1: Geometric auxetics

A large auxetic response with $v < -10$ can be achieved in geometric auxetics by engineering the internal structure such that hinges that connect the unit cells that

make up the material or twisted-chain like hierarchies embedded in the structure (usually macroscopic) cause a large transverse deformation due to concurrent stretching when pulled.

Examples of such materials include foams and honeycombs with a tradeoff on strength (especially along specific directions). Figure 1.21 shows the internal structure of some geometric auxetic materials.
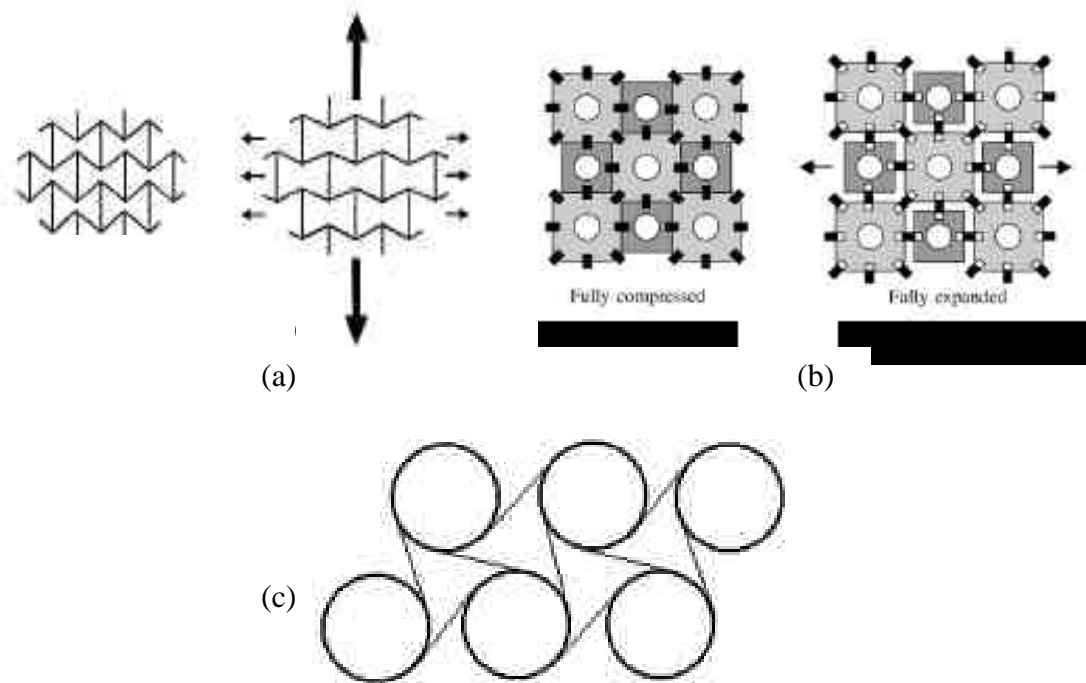
Figure 1.21: Examples of geometric auxetic materials: (a) 2D representation of an auxetic honeycomb reentrant structure, (b) Auxetic keyed-brick structure of a Magnox reactor core and (c) Auxetic chiral (noncentrosymmetic) structure [75].

Geometric auxetic materials are also usually synthetic auxetic materials that are manufactured with appropriate internal structures such that a large negative Poisson's ratio can be achieved.

1.4.1.2: Molecular auxetics

Molecular auxetics are those materials which exhibit a negative Poisson's ratio by virtue of their intrinsic atomic/molecular structure and the way in which the atoms that make up the material interact with one and other under the influence of an external stimulus. The magnitude of the Poisson's ratio is usually smaller than that of geometric auxetics and is of the order of -0.1. Most molecular auxetics are found in nature (usually cubic metal systems) but recently, such materials have been synthesized in labs [83].

An auxetic response has also been observed in some naturally occurring single crystal materials such as arsenic [84] and cadmium [85]. Studies in 1979 revealed the existence of a negative Poisson's ratio in face centered crystals (FCC) [86]. This work presented a compilation of experimental values of elastic moduli of FCC metals and rare-gas solids and the calculated Poisson ratio values along the <100> and <110> crystallographic directions. Analysis in 1990 by Jain and Verma [1] suggested that the role of conduction electrons in metals may be vital in determining whether or not a particular metal will have negative values of v along the <110> crystallographic directions. Some of these values of both FCC and body centered cubic (BCC) are shown in Table 1.1.

The auxetic response in cubic metal systems (which may be found in certain single crystal and highly textured polycrystalline materials) is usually in-plane and reflects a high degree of elastic anisotropy. The schematic of Fig 1.22 depicts this

response for the [110] loading of a (001) plane. This loading direction and plane was shown to have maximum auxeticity for cubic materials by Rovati **[87]**.
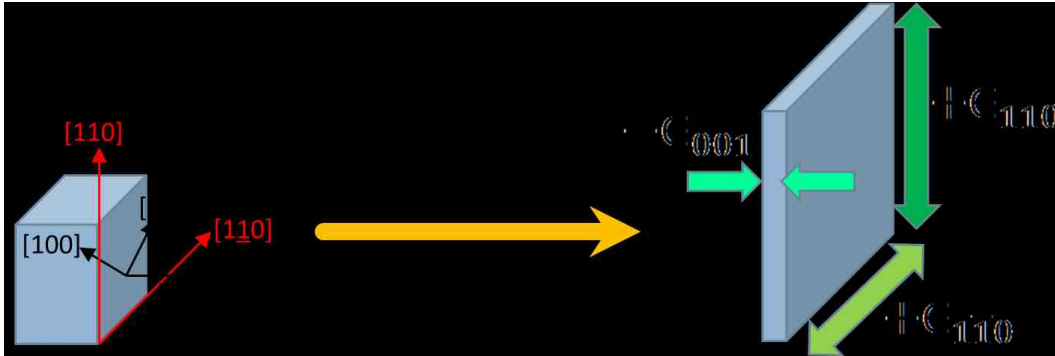
Figure 1.22: Schematic of in-plane auxetic response to uniaxial tensile loading.

In 1998, Ray Baughman and team at AlliedSignal revealed that contrary to popular belief, 69% of the cubic elemental metals and some rare-gas solids are auxetic when stretched along the <110> crystallographic direction. This work also proposed an explanation for the auxetic response based on atomic behavior as shown in Fig. 1.23 where the pulling apart of atoms labeled 2 and 4 causes the atoms labeled 1 and 3 to move closer to each other, thus pushing atoms 5 and 6 outwards.
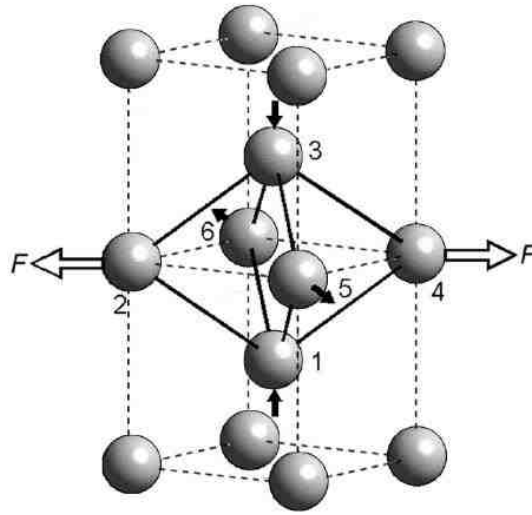
Figure 1.23: Atomic basis for auxetic behavior [78].

In 1991, Ledbetter found evidence of auxetic behavior in $YBa_2Cu_3O_7$ and suggested that this behavior is expected in some superconducting compounds at the molecular level **[88]**.

Table 1.1: Poisson's ratio of some auxetic materials [1, 2].

Material	Crystal structure	ν (110, 1 $\bar{1}$0)	Young's Modulus (110, 010) (GPa)	ν (110, 010)
Lithium	bcc	-0.5498	4.9	0.36
Iron	bcc	-0.0587	190-210	0.29
Nickel	fcc	-0.0676	200	0.31
Copper	fcc	-0.1358	110-128	0.34
Galfenol[1]	bcc	$\geq$ -0.75	131	0.58
Anisotropic materials	-	$\leq$ -1	-	-

---

[1] Values obtained from this work and previous works **[13, 20, 23]**

More recently, in 2005 Ting showed that Poisson's ratio for anisotropic elastic materials can have an arbitrarily large positive or negative value under the prerequisite of positive definiteness of strain energy density. The large Poisson's ratio values in cubic materials is physically realistic because the strains are bounded **[2]**.

1.4.2: Auxeticity in Galfenol

Ever since it was discovered that addition of Gallium to Iron could result in a tenfold amplification of the magnetostrictive effect of Iron by researchers at the U.S. Navy in 1998, several efforts have been made to characterize the properties and understand the working of the alloy **[3, 8, 11, 14, 15, 42, 49, 53, 61, 89-91]**.

While characterizing slip planes in this material **[92]** to understand the material and develop applications, Rick Kellogg observed that his 17 at. % Ga Galfenol sample exhibited a negative Poisson's ratio ~ -0.37 along the [110] direction on the (100) plane under tensile loads as shown in Fig. 1.24. He documented an increase in the auxetic response along the [110] (100) with increases in Gallium content in the alloy using published values of elastic constants, noting that values of lower than -0.7 occur in 28 at% Ga Galfenol samples **[15]**. This is opposite to the trend observed for Poisson's ratio along the [100] (100) direction where the positive values increase in magnitude with increases in Gallium content in the alloy as shown in Fig. 1.25.
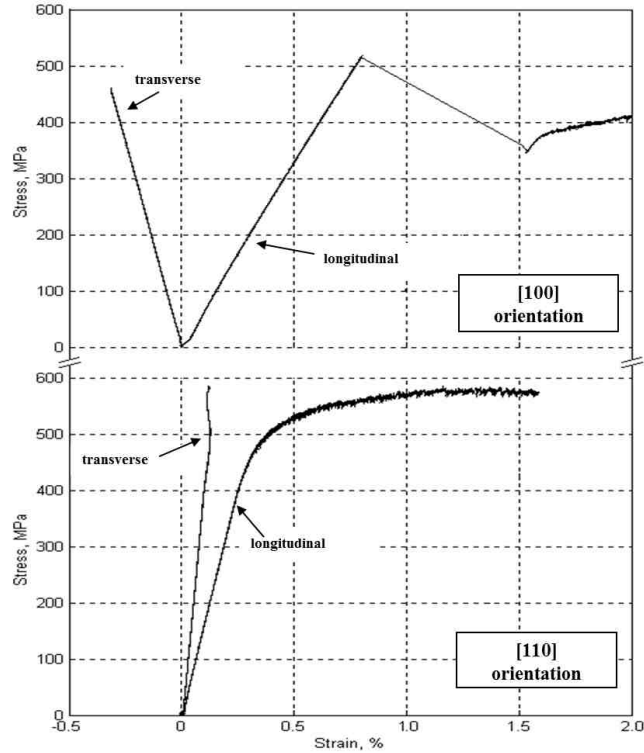
Figure 1.24: Strains documented along the longitudinal and transverse <100> and <110> on the (100) plane by Kellogg in a 17 at. % Ga Galfenol sample under tensile loads showing auxetic response along the <110> direction (from **[23]**).
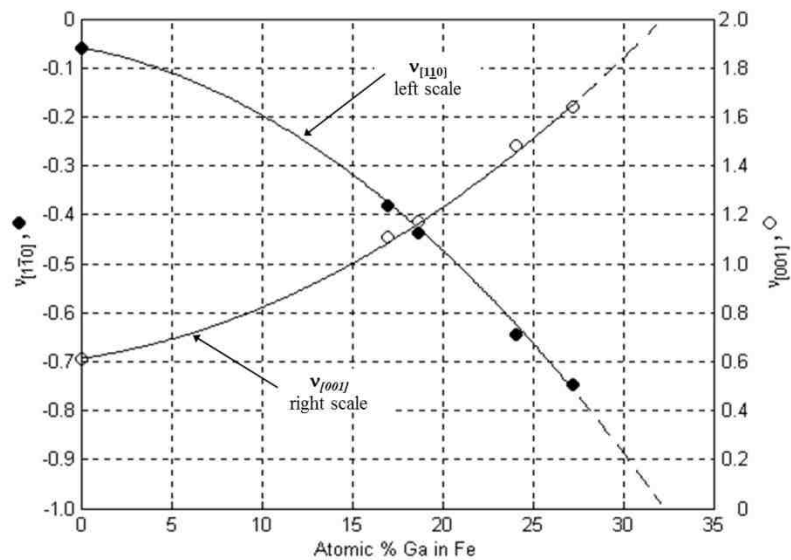
Figure 1.25: Variation of Poisson's ratio along the [100] and [110] on the (100) plane with increasing Gallium content in Galfenol (from **[23]**).

61

Since Kellogg, several researchers have looked at this in-plane auxetic behavior in Galfenol using different protocols. Yoo *et al.* **[93]** measured the elastic modulus of Galfenol at compositions of 18 at. %, 29 at. % and 33 at. % Ga by applying a constant external magnetic field in a closed loop and simultaneously mechanically loading the samples. The Poisson's ratio was computed from the strains recorded along the [110] (100) directions. The application of a magnetic field reduced auxeticity in some but not all of Yoo's samples, and thus no claims regarding trends in response were made **[93]**.

Schurter **[3]** in her thesis experimentally determined the elastic properties of Fe-Ga samples of compositions between 12% Ga and 25% Ga through tensile testing of single-crystal dogbone-shaped specimens along the auxetic <110> {100} direction The samples of Galfenol were subjected to a tensile load of up to about 150MPa using a Hydraulic MTS machine. Schurter also conducted Resonant Ultrasound Spectroscopy (RUS) of small parallelepiped samples cut from the dog bone samples and confirmed the increase in the auxetic response with increasing Gallium content observed and/or predicted by Kellogg.

Zhang *et al.* **[12]** developed a model based on the elastic constants derived using density functional theory (DFT) to predict the value of Poisson's ratio at mechanical saturation for the three Galfenol samples. Working with Schurter, the model predictions were validated in Iron Gallium alloys of compositions 12 at. %, 18

at. % and 25 at. % Ga with experimental data gathered under mechanical stresses at zero magnetic field.

Figure 1.26 shows a comparison of results from this work with previously published data. These include modeling of Poisson's ratio along the <110> direction under applied stresses by McLean [94] in α-Fe, RUS studies by Schurter to determine the value of Poisson's ratio [3], experimental data from tensile testing Kellogg and Clark [15, 49] and tensile testing data under applied DC magnetic fields by Yoo [93].
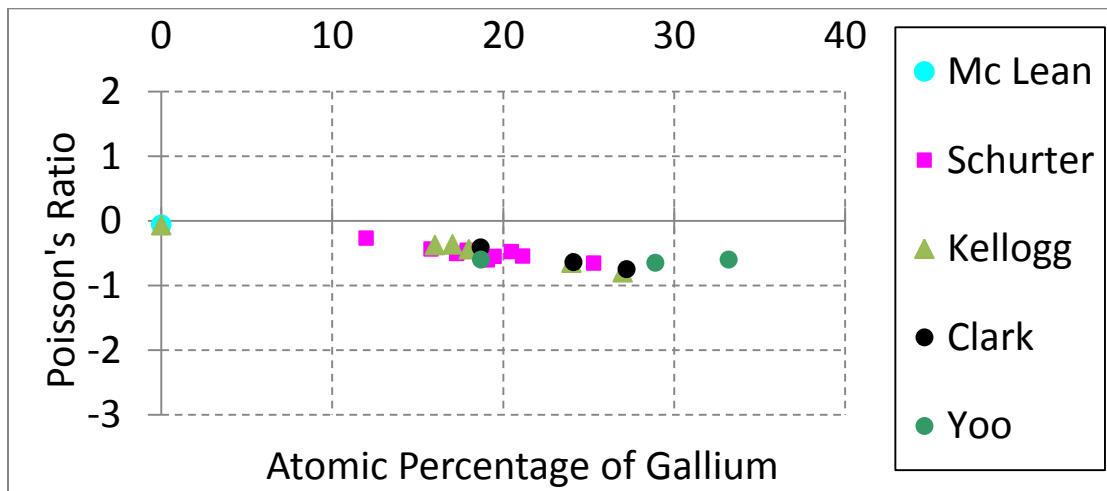
Figure 1.26: Poisson's ratio values of Galfenol along the <110> auxetic direction from previously published works.

In 2013, Paes and Mosca [95] showed that the strain induced by magnetization rotation contributes significantly in the linear regime of the stress-strain curve and is partly the reason for auxetic behavior in Galfenol under applied tensile loads. They also showed that the elastic response becomes predominant only after magnetostrictive saturation has been achieved.

63

All previous works on auxeticity in Galfenol have considered the alloy as yet another material that exhibits a negative Poisson's ratio when mechanically stretched along a particular crystallographic direction. But Galfenol is a magnetostrictive material with inherent magneto-elastic coupling (discussed in Section 1.3). This implies that a magnetization change always accompanies mechanical stresses in the material and vice versa. The current work explores the possibility of obtaining an auxetic behavior under magnetic fields and zero mechanical stresses. Such a response opens up new avenues for potential applications, some of which shall be discussed in Appendix C.

1.4: Introduction to the rest of the dissertation

This section will present an overview of the subsequent chapters in this dissertation. Chapter 2 begins with the formulation of an energy based theoretical model that can predict the value of Poisson's ratio at magnetic saturation for the different compositions of Galfenol. This model is based on the magneto-mechanical model developed by Armstrong **[40]** to model actuation in Terfenol-D. The subsequent sections will deal with the implementation of this formulation into COMSOL Multiphysics 3.5 to obtain a 3D electromagnetic finite element simulation that is capable of predicting the trends in strain along the <110> {100} directions as a magnetic field is applied to the sample at zero mechanical stress.

The goal of Chapter 3 is to experimentally quantify the magnitude of strains obtained along the auxetic <110> {100} crystallographic direction in Galfenol under

applied magnetic fields and zero stress conditions. The chapter begins with a section that discusses the background of the samples used in this study. An explanation on the specimen preparation technique and sample analysis will follow. The next section elucidates the experimental procedure with special focus on the data acquisition technique, repeatability issues and the data reduction method used here.

Discussion of the results obtained from the experiments to determine the Poisson's ratio is presented in Chapter 4. The validity of the predictions made by the mathematical model and the multiphysics simulations is also examined. The focus of this chapter is to provide a possible mechanism for auxetic response in Galfenol samples of different compositions.

The reminder of this dissertation deals with imaging magnetic domains and understanding their correlation to the auxetic mechanical response observed when a magnetic field is applied along the <110> {100} direction in single crystal Galfenol specimens. The first section in Chapter 5 presents a background to optical domain observation techniques with special attention to the MOKE (Magneto-Elastic Kerr Effect) microscope. The experimental procedure and the domain images at remanence follow this section. Since optical techniques require high standards of surface finish, issues with polishing the Galfenol samples is also discussed. Domain images under changing magnetic fields are presented in the subsequent section to understand how the domains react to external magnetic fields.

Finally Chapter 6 presents a summary of the research presented in this dissertation, highlighting the contributions of this work and make recommendations for future work.

Chapter 2: Analytical modeling and simulations

This chapter builds on the development of a complete non-linear model of the material from first principles based on the Armstrong model given in Section 1.3.2. This will be followed by application of the model to compute strains along the <110> crystallographic directions under applied magnetic fields and zero stress conditions. Magnetostriction values at magnetic saturation are used to calculate the Poisson's ratio for a range of Galfenol compositions. In the last section of the chapter the Armstrong model is implemented using COMSOL Multiphysics 3.5 to simulate field dependent magnetostriction along the auxetic crystallographic directions for a range of Galfenol compositions. For a detailed review of other modeling methods, readers can refer to the works of Dapino, Atulasimha and Datta **[8, 11, 96]** .

2.1: Analytical computation of Poisson' s ratio

This section deals with calculation of Poisson's ratio along the auxetic <110> directions at magnetic saturation. Based on the fundamental relations in magnetostriction that were derived in Section 1.3 based on an energy-based mathematical approach, Eq. (2.1) is obtained.

$$
\begin{aligned}
\frac{\delta l}{l} &= \frac{3}{2}\lambda_{100}\left(\gamma_1^2\alpha_1^2 + \gamma_2^2\alpha_2^2 + \gamma_3^2\alpha_3^2 - \frac{1}{3}\right) \\
&+ 3\lambda_{111}\left(\gamma_1\gamma_2\alpha_1\alpha_2 + \gamma_2\gamma_3\alpha_2\alpha_3 + \gamma_3\gamma_1\alpha_3\alpha_1\right)
\end{aligned}
\tag{2.1}
$$

Since the auxetic behavior in the response is observed along the <110> crystallographic direction, the values of $\alpha_1, \alpha_2, \alpha_3$ and $\gamma_1, \gamma_2, \gamma_3$ are chosen to accommodate this. The ratio of the strains obtained along the [110] and [   ] directions from Eq. (2.1) is used to calculate the value of the Poisson's ratio at each compositions based on the values of λ_{100} and λ_{111}.

Along the longitudinal [110] direction, the values of the direction cosines of the applied field and magnetostrictive strains are $\alpha_1 = \dfrac{1}{\sqrt{2}}, \alpha_2 = \dfrac{1}{\sqrt{2}}, \alpha_3 = 0$ and

$\gamma_1 = \dfrac{1}{\sqrt{2}}, \gamma_2 = \dfrac{1}{\sqrt{2}}, \gamma_3 = 0$ respectively.

Similarly, along the transverse [$1\bar{1}0$] direction, the direction cosines are given by $\alpha_1 = \dfrac{1}{\sqrt{2}}, \alpha_2 = \dfrac{1}{\sqrt{2}}, \alpha_3 = 0$ and $\gamma_1 = \dfrac{1}{\sqrt{2}}, \gamma_2 = -\dfrac{1}{\sqrt{2}}, \gamma_3 = 0$.

The magnetostrictive strains along the longitudinal and transverse <110> directions are obtained by substituting these values separately into Eq. (2.1) as shown below.

$$\left(\frac{\delta l}{l}\right)_{longitudinal} = \frac{1}{4}\lambda_{100} + \frac{3}{4}\lambda_{111} \qquad (2.2\ a)$$

$$\left(\frac{\delta l}{l}\right)_{transverse} = \frac{1}{4}\lambda_{100} - \frac{3}{4}\lambda_{111} \qquad (2.2\ b)$$

68

The ratio of these strains from Eq. (2.2 a,b) yields the Poisson's ratio as shown in Eq. (2.3).

$$\nu = -\frac{\left(\dfrac{1}{4}\lambda_{100} - \dfrac{3}{4}\lambda_{111}\right)}{\left(\dfrac{1}{4}\lambda_{100} + \dfrac{3}{4}\lambda_{111}\right)} \tag{2.3}$$

The values for the fundamental magnetostrictive constants are picked from readily available literature [26, 49, 92]. Some of these values are shown in Fig. 1.15. The exact values of λ_{100} and λ_{111} for the compositions used in this study are interpolated using the data from Fig. 1.15 and are listed in Table 2.1.

Table 2.1: Values of λ_{100} and λ_{111} obtained from interpolation.

Ga content (at %)	$3/2\lambda_{100}$	λ_{100}	$3/2\lambda_{111}$	λ_{111}
0	31	20.70	-31.5	-21
12	180	120	-25	-16. 67
15.8	365	163.33	-20	-13.33
17.8	400	226.67	-15	-10
20.5	225	216.67	20	13.33
25.3	190	213.33	52	34.67

The values of λ_{100} and λ_{111} from Table 2.1 were used in Eq. (2.3) to compute the Poisson's ratio. Figure 2.1 shows the variation of the transverse strain along $[1\bar{1}0]$ direction (numerator of Eq. (2.30)) and longitudinal strain along [110] direction (denominator of Eq. (2.30)) at magnetic saturation for the different Ga content in Galfenol.
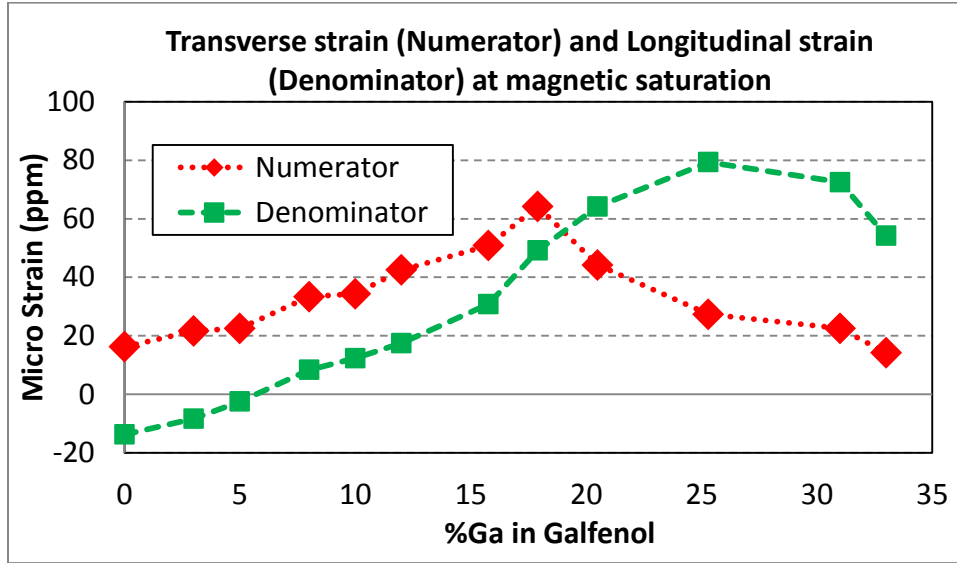
Figure 2.1: Predicted variation of the transverse strain (numerator) and longitudinal strain (denominator) along <110>{100} crystallographic direction at magnetic saturation for the different Ga content in Galfenol.

The values of Poisson's ratio obtained from the model (as the negative ratio of the numerator and denominator in Fig. 2.1) are listed in Table 2.2 for the different Ga compositions.

Table 2.2: Values of Poisson's ratio at magnetic saturation obtained from the energy model using λ_{100} and λ_{111} values from Table 2.1.

Ga Content (at %)	Saturation strain along longitudinal [110] direction (με)	Saturation strain along transverse [1$\bar{1}$0] direction (με)	Poisson's ratio at saturation <110> direction
0	-10.58	20.93	1.9787234
3	-8.33	21.67	2.6
5	-2.50	22.50	9
8	7.50	33.33	-4.333333
10	12.33	34.33	-2.783784
12	17.50	42.50	-2.428571
15.8	48.33	73.33	-1.517241
17.8	66.08	70.58	-1.068096
20.5	67.00	7.50	-0.111111
25.3	76.67	-13.33	0.173913
31	72.50	22.50	-0.310345

These predictions from the analytical solution of the energy model are very exciting because for the first time, Galfenol samples are expected to show values of Poisson's ratio as low as -4.3 at magnetic saturation and zero stress at a composition of 8 at% Ga. There is an increasing trend in the value of Poisson's ratio at magnetic saturation from the model for increasing Ga content, higher than 8% Ga (beginning of partially ordered phases) in the alloy as shown in Fig. 2.2.
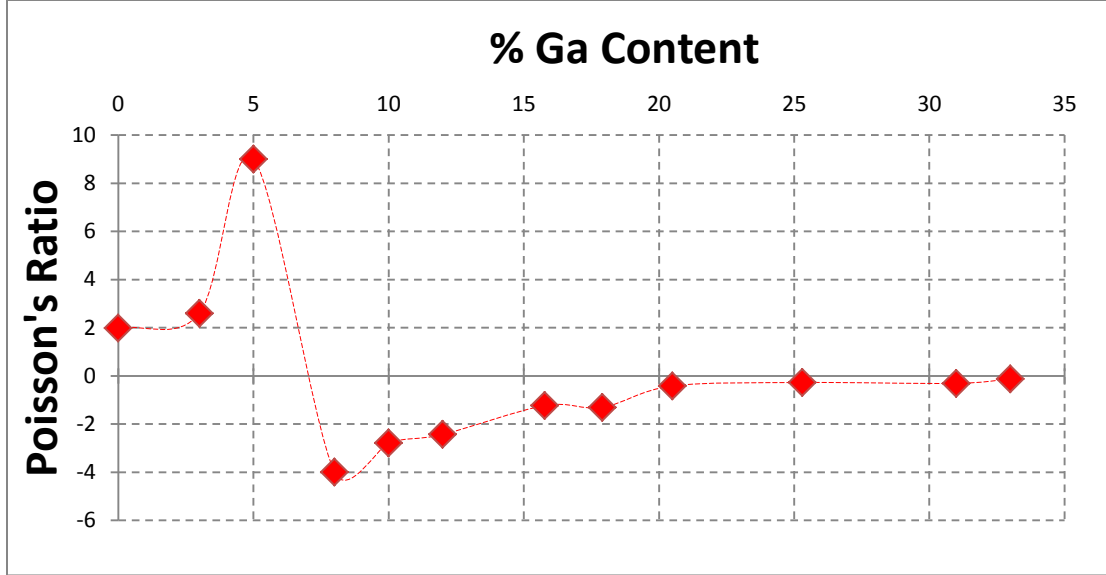
Figure 2.2: Values of Poisson's ratio at magnetic saturation predicted by the analytical model at different Ga compositions in Galfenol.

The trend in Fig. 2.2 is opposite to what was observed under tensile loads at zero magnetic fields along the same auxetic <110> {100} crystallographic directions (shown in Fig. 1.25). An initial thought for explaining this trend was to determine if the trends in magnetic anisotropy constants correlated to the trend in Fig. 2.2.

Figure 2.3 shows that for compositions at which the magnetic anisotropy coefficients have been determined, the Poisson's ratio obtained from the analytical model for applied tensile stresses (from **[15]**) at zero magnetic fields scales in a manner proportional to K_1. This is because along the <110> direction, upon substituting for the values of the direction cosines α_1 α_2 and α_3 the anisotropy energy shown in Eq. (1.24) reduces to

$$E_{anisotropy<110>} = K_1\left(\frac{1}{4}\right) \tag{2.4}.$$
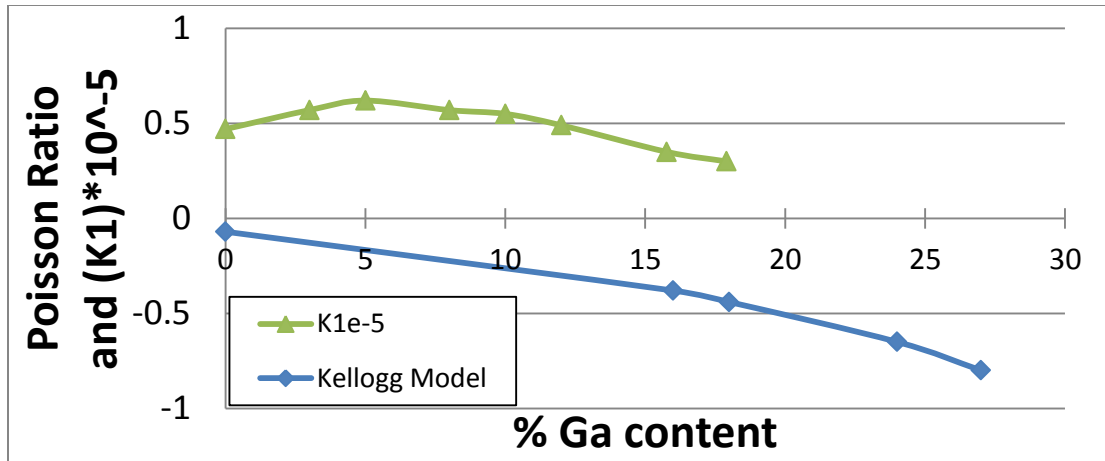
Figure 2.3: Variation of Poisson's ratio predicted by the model from Kellogg under applied stress and zero stress and a scaled value of K_1 as a function of the composition of Ga in Galfenol.

This suggests that as the anisotropy decreases, there is lattice softening due to an increase in magneto-elastic energy which leads to larger strains under applied stresses (Refer Eq. (1.23)) which causes a decrease in the value of Poisson's ratio with increasing Ga content in the alloy. The reason for the lattice softening from a metallurgical perspective has been attributed to the addition of larger Ga atoms which form weaker bonds at high compositions leading to the formation of a metaolloid-like (a mixture of metals instead of an alloy) material [12].

Figure 2.4 shows that the variation of Poisson's ratio at magnetic saturation obtained from the analytical model for applied magnetic fields and zero stresses is scaled in a manner proportional to $1/K_1$ with increasing Ga composition. This is opposite to the trend obtained in Fig. 2.3. From Eq. (2.4-2.5) it can be observed that a decrease in the anisotropy with increasing Ga content leads to an increase in the magnetic energy in the system under applied magnetic fields and zero stresses. This

causes an increase in the magnetic interaction between the atoms that constitute the lattice which restricts lattice softening with increasing Ga content.
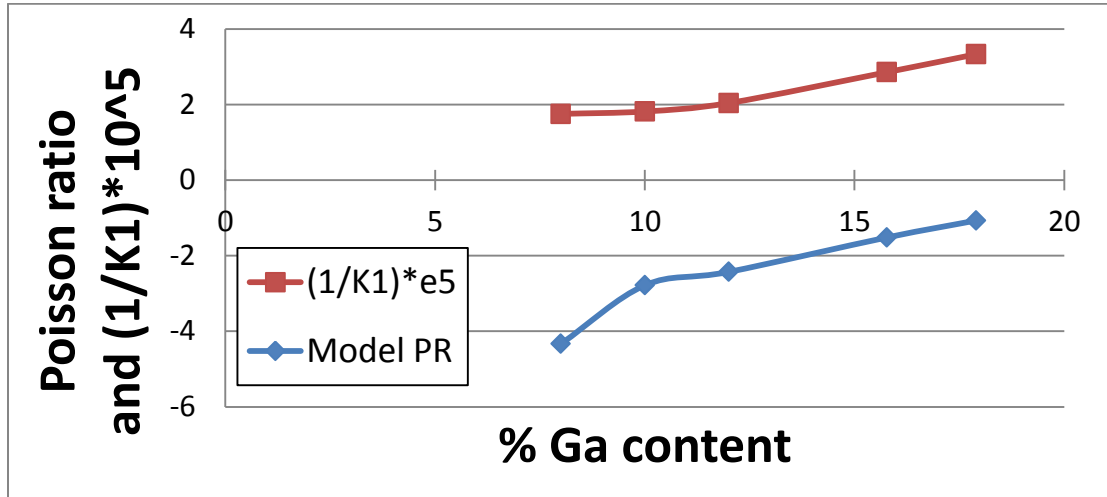
Figure 2.4: Variation of Poisson's ratio at magnetic saturation predicted by the analytical model from this study and a scaled value of $1/K_1$ as a function of the composition of Ga in Galfenol.

It is also important to note that this model does not provide any information about the trends in the strain as the magnetic field is being applied to the samples, rather only information for once they have attained magnetic saturation.

The next section deals with the development of an algorithm which incorporates the features of an energy based model as developed by Armstrong **[8, 10, 16, 26, 97-99]** with modifications to incorporate the <110> direction and zero external stress conditions to predict the trends in the strain as the magnetic field is applied in the auxetic directions. These results from the analytical model will be benchmarked against the experimental data in Chapter 4.

The energy terms which affect both strain and magnetization in a material were introduced in Section 1.3. These terms are: exchange energy, magnetocrystalline anisotropy energy, magnetostatic energy, elastic energy, magnetoelastic energy, Zeeman energy and mechanical work done.

Since, in this work we are only interested in modeling the magnetization and strain response of a bulk material, we can ignore the effect of exchange energy. The magnetization vectors within each domain move cooperatively with no expense in exchange energy. An expense in exchange energy is encountered only at the domain boundaries, which is a small fraction of the total volume. Consequently, the total exchange energy at the boundaries is small compared to the sum total of all the other energy terms considered over the entire system. Therefore, to predict the macroscopic behavior of the sample, without worrying about the precise description of the domain structure, the Armstrong model **[100]**, which uses only the magnetocrystalline, magnetoelastic and magnetic energies is employed. It is important to note that this phenomenological probabilistic approach to modeling the magneto-elastic effect in Galfenol is anhysteretic. The formulation of this model is described in detail in this section.

Considering a magnetic field (H) applied in a direction defined by the direction cosines β_{1F}, β_{2F} and β_{3F} and an applied stress (σ) with direction cosines β_{1s},

β_{2s} and β_{3s}, the energy corresponding to the magnetization oriented in the direction given by α_1, α_2 and α_3 is given by:

$$E(\sigma, H) = E_{magnetocrystalline} + \gamma_\sigma * E_{magnetoelastic} + E_{magnetic} \qquad (2.4)$$

$$E(\sigma, H) = K_1(\alpha_1^2\alpha_2^2 + \alpha_2^2\alpha_3^2 + \alpha_3^2\alpha_1^2) + K_2(\alpha_1^2\alpha_2^2\alpha_3^2) + \sigma * \gamma_\sigma \left\{ -\frac{3}{2}\lambda_{100}(\alpha_1^2\beta_{1s}^2 + \right.$$

$$\alpha_2^2\beta_{2s}^2 + \alpha_3^2\beta_{3s}^2) - 3\lambda_{111}(\alpha_1\alpha_2\beta_{1s}\beta_{2s} + \alpha_2\alpha_3\beta_{2s}\beta_{3s} + \alpha_3\alpha_1\beta_{3s}\beta_{1s}) \Big\} -$$

$$\mu_o M_s H(\alpha_1\beta_{1F} + \alpha_2\beta_{2F} + \alpha_3\beta_{3F}) \qquad (2.5)$$

In this work we use the saturation magnetization (M_s), the magnetostrictive constants (λ_{100} and λ_{111}) and the 4th and 6th order anisotropy constants (K_1 and K_2 respectively) to calculate the Zeeman, stress-induced anisotropy and magnetocrystalline anisotropy energies per unit volume due to a constant zero stress and a magnetic field (H) applied along the [110](100) direction with the assumption that we start from a perfectly demagnetized state with an equal probability of magnetization along all the easy axes available, which is determined by the anisotropy constants.

The following material constants are employed in the model: cubic magnetocrystalline anisotropy constants K_1 and K_2 (Joules/m^3), cubic magnetostriction constants λ_{100} and λ_{111} (μstrain), and saturation magnetization M_s (Ampere/m). A 6th dimensionless factor Υ_σ had to be introduced in Eq. (2.5) to

76

slightly scale the magnetoelastic energy in order to fine-tune the variation in magnetic behavior with stresses. Because this simulation operates with the assumption of zero applied stresses, the effect of the choice of the values of Y_σ are negligible. The direction cosines (β_{1s}, β_{2s}, β_{3s}) and (β_{1F}, β_{2F}, β_{3F}) are respectively determined by the direction of the stress or field applied. For example, a stress and magnetic field applied along the [110] direction is represented by direction cosines ($1/\sqrt{2}$, $1/\sqrt{2}$, 0).

Thus, given a stress and field, the free-energy for various orientations of the magnetic moment (α_1, α_2 and α_3) are evaluated using Eq. (2.5). Numerically the α_1, α_2 and α_3 are chosen to correspond to the azimuthal angle (φ) varying between 0 and 180° and polar angle (ψ) varying between 0 and 360° in spherical coordinates in intervals of 5° (to get converged solutions in reasonable computation time) such that $\alpha_1= \sin\psi \cos\varphi$, $\alpha_2= \sin\psi \sin\varphi$ and $\alpha_3= \cos\psi$. It should be noted that Eq. (2.5) is only appropriate for a single crystal samples. An appropriate method for adapting this energy formulation for polycrystalline materials by incorporating the volume fraction of grains with different orientations has been shown by Atulasimha et al. **[101]**.

Figure 2.5 (a) shows the distribution of energy at zero applied stress and zero field while Fig. 2.5 (b) illustrates the effect of compressive stress and field, both applied along the z-axis, on the energy distribution. Values for model parameters were chosen to emphasize certain effects rather than for a particular alloy.
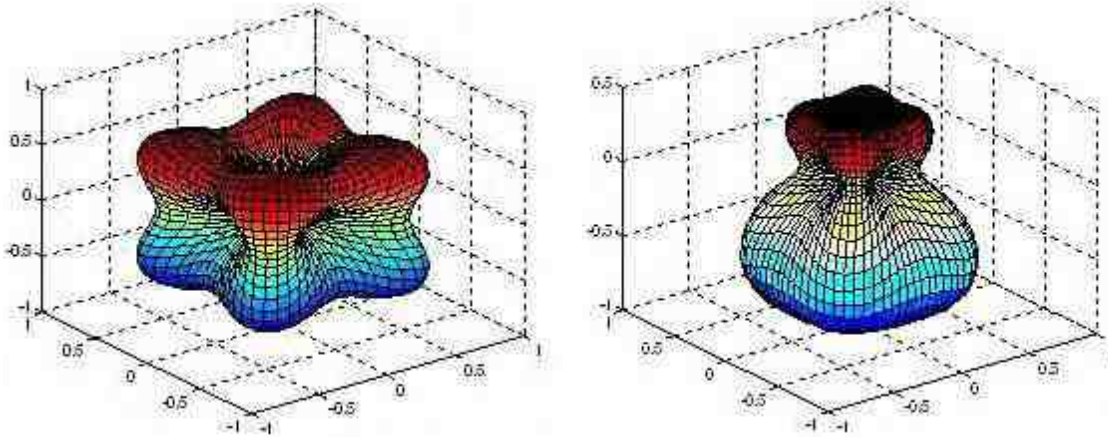
Figure 2.5: Visualization of dependence of energy on orientation of magnetic moment generated by plotting radius proportional to the energy [normalized] in different directions. Energy plot at (a) 0 stress and magnetic field (b) Compressive stress and typical field at which domains flip [8].

The bulk magnetic material is assumed to be composed of a number of non-interacting magnetization units. The volume fraction of the number of such units oriented in a particular direction is chosen such that the overall energy of the system is minimized. A normalizing factor is calculated from the definition of a probability density function. A more detailed explanation of this probabilistic approach is available in Supratik Datta's dissertation [11].

A 7th model parameter, Ω (units: J/m^3) called an empirical scaling factor is employed to obtain the desired smoothness in the *B-H* and *λ-H* curves. Physically, a low Ω produces less smooth distributions and results in steeper gradients and sharper corners in *B-H* and *λ-H* curves, suggesting fewer imperfections in the crystalline structure. Conversely a large Ω leads to smooth characteristics suggestive of greater

imperfections in the material. The values of Ω chosen in this study were based on their effectiveness in predicting the experimental magnetostriction and magetization responses for a given composition of Galfenol along the <100> direction in Atulasimha's work [8].

Using the formulation in Eq. (2.32) for the total energy, an ensemble average of all possible orientations of the magnetization vector is calculated to evaluate magnetization and magnetostriction. Equation (2.33) shows the average value of a physical quantity (say magnetization along the [100] direction, denoted by M_{100}) obtained from this formulation.

$$M_{100} = \frac{\sum_{\varphi=0}^{2\pi} \sum_{\psi=0}^{\pi} M_s\, \alpha_1 |sin\psi|\, \Delta\psi\, \Delta\varphi\, e^{\frac{-E(\sigma,H)}{\Omega}}}{\sum_{\varphi=0}^{2\pi} \sum_{\psi=0}^{\pi} |sin\psi|\, \Delta\psi\, \Delta\varphi\, e^{\frac{-E(\sigma,H)}{\Omega}}} \qquad (2.33)$$

The magnetic induction is calculated using Eq. (1.8), $B = \mu_o(M + H)$. The same formulation can be extended to obtain an expression for the magnetostriction along the [100] direction as shown in Eq. (2.34).

$$\lambda = \frac{\sum_{\varphi=0}^{2\pi} \sum_{\psi=0}^{\pi} \frac{3}{2}\lambda_{100}\left(\alpha_1^2 - \frac{1}{3}\right)|sin\psi|\Delta\psi\, \Delta\varphi\, e^{\frac{-E(\sigma,H)}{\Omega}}}{\sum_{\varphi=0}^{2\pi} \sum_{\psi=0}^{\pi} |sin\psi|\, \Delta\psi\, \Delta\varphi\, e^{\frac{-E(\sigma,H)}{\Omega}}} \qquad (2.34)$$

The total strain can be described by Eq. (2.34) where E_S is the purely mechanical Young's modulus of the material and is also known as the modulus at magnetic saturation. This is the modulus measured when all the magnetic moments are oriented either parallel or anti-parallel.

$$\varepsilon = \frac{\sigma}{E_S} + \lambda \tag{2.35}$$

In this study, we are interested in the strains obtained along the [110] direction under zero mechanicalstress. Hence the mechanical component in Eq. (2.35) vanishes and we compute only the magnetostriction along the auxetic direction.

Although model parameters such as M_s and λ_{100}, λ_{111} can be easily obtained from magnetomechanical actuator characterization, the parameters K_1, K_2, and Ω have to be obtained empirically in order to get the best fit of the curves obtained experimentally. The values of K_1 and K_2 from Fig. 1.15 for quenched iron-gallium alloys [42] are used as a starting estimate for determining these empirical values. A detailed study of the effect of the model parameters on the model prediction can be found in the work of Atulasimha et al. [101]. The model parameters used for the different samples in this chapter are shown in Table 2.3.

Table 2.3: Model parameters used in energy-based simulation

% Ga content	M_s (kA/m)	λ_{100} (με)	λ_{111} (με)	K_1 (kJ/m^3)	K_2 (kJ/m^3)	Ω (J/m^3)	E_s (GPa)
0%	1752	20.7	-21	47	-150	400	90
12%	1600	120	-17	49	-110	550	76
15.8%	1456	163	-13	13	-90	600	76
17.8%	1420	226	-3	16	-80	630	65
20.5%	1321	216	13	-5	10	707	60
25.3%	1036	213	35	-15	40	725	55
31%	982	193	37			733	52
33%	872	133	40			750	52

2.2.1: Finite element formulation

Using this formulation, the elastic and magnetic boundary value problems were derived as shown in Eq. (2.36) and Eq. (2.37) respectively. The elastic boundary value problem (BVP) is formulated and solved using the finite element method:

$$\int_\Omega \delta\tilde{\varepsilon}^T \tilde{\sigma}\,dV - \int_\Omega \delta\tilde{u}^T \tilde{F}_b\,dV - \int_\Omega \delta\tilde{u}^T \tilde{F}_s\,dS = 0 \qquad (2.36)$$

Here, $\tilde{\varepsilon} = \{\varepsilon_{11} \quad \varepsilon_{22} \quad \varepsilon_{33} \quad \gamma_{12} \quad \gamma_{23} \quad \gamma_{31}\}^T$ and $\tilde{\sigma} = \tilde{\mathbf{C}}(\tilde{\varepsilon} - \tilde{\lambda}(\tilde{\sigma}, \tilde{H}))$.

The magnetic boundary value problem is expressed as:

$$\int_\Omega \delta\tilde{H}^T \tilde{B}\,dV = 0 \qquad (2.37)$$

where, $\tilde{B} = \tilde{\mu}(\tilde{\sigma}, \tilde{H})\tilde{H} + \tilde{B}_r$ and $\tilde{\mu}(\tilde{\sigma}, \tilde{H} \neq 0) = \frac{\mu_0(\tilde{M}(\tilde{\sigma}, \tilde{H}) + \tilde{H})}{\tilde{H}}$

The elastic and magnetic boundary value problems were solved iteratively, with the elastic BVP first solved under an assumption of a zero applied stresses, $\tilde{\sigma} = \tilde{0}$. With the resulting stress distribution, the magnetization, $\tilde{M}(\tilde{\sigma}, \tilde{H})$, is calculated using

the energy-based model. The simulations received an input of a local magnetic field ($H_{3\times1}$) and stress ($\sigma_{6\times1}$), and produced an output of local magnetic induction ($B_{3\times1}$) and magnetostriction ($\lambda_{6\times1}$). The magnetic boundary value problem can then be solved to obtain the magnetostriction, $\tilde{\lambda}(\tilde{\sigma}, \tilde{H})$, which is fed back into the elastic boundary value problem. The iterations continue until a convergence criterion is achieved, such as $\Delta B < 0.5\%$ and $\Delta \varepsilon < 0.5\%$.

Using these calculations, a database was created with a range of expected σ_x and H_x values. For each combination of every σ_x and H_x, values were calculated for λ_x and B_x. This database of stress, magnetic field, magnetostriction, and magnetic induction values was called during execution of the algorithm in COMSOL Multiphysics software using Matlab LiveLink. The results from these simulations will be compared with experimental data and discussed in Chapter 4. The Matlab code/script used for this is provided in Appendix H. The effect of varying the values of anisotropy constants K_1 and K_2 in the simulations is discussed in Appendix G.

2.2.2 Limitations of energy based model

For given experimental λ-H and B-H characteristics the model parameters λ_{100}, λ_{110} and M_s are fixed and there is no flexibility in the choice of these parameters. The parameter Υ_σ, used to scale the effect of stress determined by $\sigma * \lambda$, does not affect this simulation since the applied stress is zero. However, there is greater flexibility in the choice of the other three parameters Ω, K_1 and K_2 which significantly influence

82

the nature of the λ-H and B-H curves as explained in the previous section. Hence, the results obtained from the model have a strong dependence on the input values of the 7 parameters discussed in Section 2.3. This section deals with how these parameters affect the accuracy of the model presented.

There are only a few compositions of slow-cooled samples for which the values of K_1 and K_2 have been determined [42]. The values of K_1 and K_2 used in thus study were obtained using linear interpolation. Since the specimens used in the experiments were quenched, the values used in the simulations are a source of error. At around 20 at. % Ga content in Galfenol, both K_1 and K_2 are close to zero. There is no data available for higher compositions of Ga in Galfenol. Given that Clark's data in Fig 1.15 [46] indicates the easy axis for Galfenol is along the <100> axes for compositions of up to 35 at% Ga, we use only combinations of K_1 and K_2 values that meet the prescribed criteria in the simulations.

The value of the smoothing function Ω which defines the imperfections in the material has been empirically verified only for the 15.8% Ga single crystal Galfenol sample from Datta's dissertation [11]. Extrapolation of the data available in this work has been used to obtain the values for the remaining compositions.

Similarly, the values of saturation magnetization, M_s are unavailable for some compositions and have been estimated by extrapolating the available data. The values

of λ_{100} and λ_{111} have been obtained by linear interpolation for this study and could be a source of error in the simulations.

The magnetic ordering in a magnetic material is strongly affected by its thermal history and ambient temperature which determines spontaneous magnetization. The model presented in this chapter was directed towards capturing the magnetization and strain response of a bulk material and did not incorporate exchange energy which accounts for the ordering of magnetization vectors within each domain by calculating the interaction between spins in the lattice. A model that includes the effects of temperature has been discussed in Atulasimha's dissertation **[8]**.

Chapter 3: Experimental methods for characterization of magnetically induced auxetic behavior

This chapter describes the experiments conducted to study the variation of Poisson's ratio with applied magnetic field and zero mechanical stress for samples over a wide range of compositions (12 to 33 at% Ga) in Galfenol along the <110> {100} crystallographic direction. It begins with a section on the sample preparation and analysis. This is followed by a description of the experimental procedure including an overview of the equipment, data acquisition technique, factors affecting repeatability and finally data reduction.

3.1: Specimen background

Since the elastic properties of single-crystal Galfenol are dependent on composition, crystal orientation and heat treatment as discussed in Chapter 1, an overview of the history of the samples used in this study is presented here.

3.1.1: Material manufacture

The specimens were prepared at the DOE Ames Laboratory as follows. A single crystal of $Fe_{100-x}Ga_x$ was grown in an alumina crucible by the modified Bridgman technique. The starting ingot for single crystal growth was prepared by arc-melting appropriate quantities of Fe (99.99% purity) and Ga (99.999% purity) metal several times under an Argon atmosphere. The button was then re-melted, and the

alloy was drop-cast into a copper chill cast-mold to ensure compositional homogeneity throughout the ingot. The alloy was heated in a vacuum of 1.3 x 10-4 Pa up to 1075 K to degas the crucible and charge. The chamber was then backfilled to a pressure of 275 kPa with high purity argon. The ingot was then further heated to the growth temperature and held for 1 hour to allow thorough mixing before withdrawing the sample from the heat zone at a rate of 4 mm/h. Following growth, ingots were annealed at 1000 ºC for 168 hours and slow cooled. Ingots of compositions approaching the first peak of Fig. 1.15, i.e. the 17, 19 and 21 at.% Ga ingots, underwent an additional anneal at 800 ºC for 1 hour under flowing Argon and then were water quenched. This was done to enhance magnetostriction by retaining a more ordered α-iron structure at room temperature (see Fig. 1.13).

3.1.2: Specimen preparation

The single crystal's orientation was determined within 0.25º using Laue X-ray back reflection and then cut into tensile specimens of dimensions as shown in Fig. 3.1 by electro-discharge machining. A picture of the specimen with the strain gages installed is shown in Fig. 3.2. After machining, the orientation of each specimen was again checked by Laue X-ray back reflection.
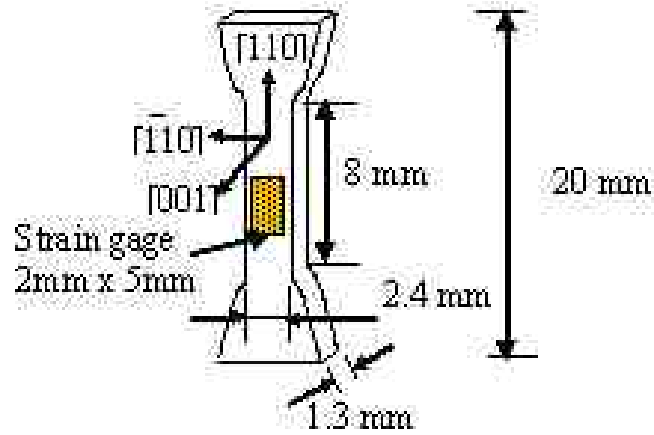
Figure 3.1: Schematic of the [110] Fe-Ga dogbone samples used in this study.

Figure 3.2: Photo of typical Fe-Ga dogbone samples and a sketch depicting crystallographic axes and strain gauge placement on a sample.

3.1.3: Specimen analysis

Energy dispersive X-ray spectroscopy (EDS) and wavelength dispersive X-ray spectroscopy (WDS) were used to determine the composition of each specimen by Schurter [3] in 2007. A sample of known composition of $Fe_{35}Ga_{65}$ was used with each specimen as a calibration standard. Three points were chosen along the surface of each sample, and the composition at each point was measured to an accuracy of 0.21 percent or better. The composition of each sample was given by Ames Laboratory when the samples were first manufactured, however, no specific information about precision or accuracy was provided. In addition, most of the samples were produced prior to the work done by Schurter in 2007, and re-measuring the composition was an opportunity to ensure that the gallium had not depleted over time. Since the results suggested that most of the sample compositions were close to their specified nominal values, the compositions of the samples in this study were not re-measured and have been assumed to be the same as presented in [3]. Table 3.1 summarizes the results.

Table 3.1: Composition analysis of the Fe-Ga dogbones [3].

Orientation	Nominal Ga content (at%)	Measured Ga content (at%)	Change	Relative change
[110]	12.5	12.0 ± 0.2	- 0.5	- 4.0%
[110]	17	17.3 ± 0.3	+ 0.3	+ 1.8%
[110]	19	19.1 ± 0.5	+ 0.1	+ 0.53%
[110]	21	21.1 ± 0.2	+ 0.1	+ 0.48%
[110]	25	25.3 ± 0.3	+0.3	+ 1.2%
[110]	31	-	-	-
[110]	33	-	-	-

Two additional samples at 31% Ga and 33% Ga content were purchased from

Etrema Products, Inc. Their compositions were checked just after production in situ

and their nominal compositions were prescribed already. These two samples

underwent no heat treatment and the prescribed composition values were also used in

the studies by **[93]**.

The anneal-quench performed to enhance magnetostriction in the 17, 19 and

21 at% Ga samples was expected to cause some gallium depletion. For this reason,

the compositions of those three samples were measured using WDS before and after

heat treatment and the results are presented in Table 3.2.

Table 3.2: Composition analysis of the Fe-Ga samples before and after heat treatment
at 800° C for one hour [3].

Orientation	Original Ga content (at %)	Final Ga content (at %)	Change	Relative change
[110]	17.3	15.8 ± 1.3	-1.5	- 8.7%
[110]	19.1	17.9 ± 0.5	-1.1	- 5.8%
[110]	21.1	20.4 ± 0.3	-0.7	- 3.3%

3.2: Experimental procedure

A coordinate system was chosen such that the x- and y-axes correspond to

[110] and [1$\bar{1}$0] directions in the (100) plane of the samples respectively. An

electromagnet was used to apply magnetic field up to 400 mT along the length of the

dogbone specimens. The dogbones were fixed on a stand located between the pole

faces of the electromagnet with double sided sticky tape, such that the nominal air gap between the sample and the pole faces was less than 20 mm. Two resistive strain gage rosettes were attached to either faces of the dogbone to measure strain along x- and y-directions (longitudinal and transverse directions). The field was ramped up from ~ 0.1 mT (remanent field) to 400 mT and then down to ~ 0.1 mT at a rate of ~ ±10 mT/s. It is important to note that the experiments were performed at room temperature. The change in the magnetic field over one test cycle is shown in Figure 3.3.
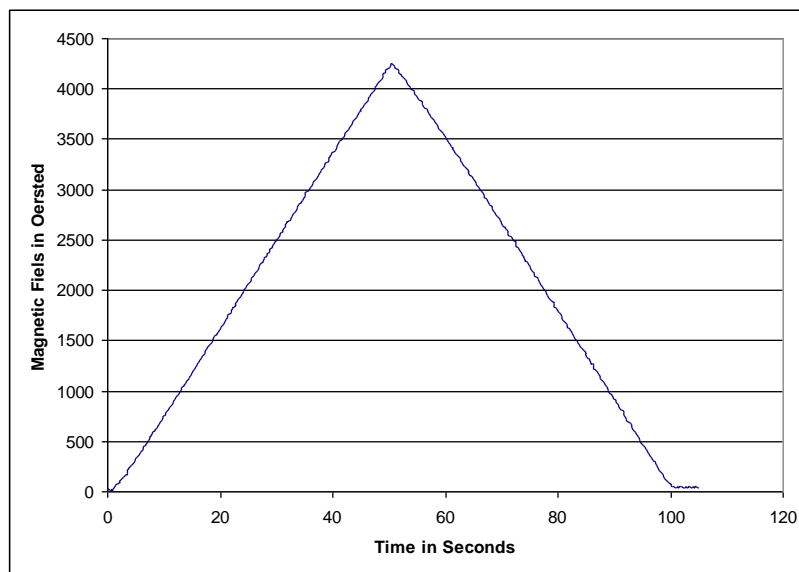
Figure 3.3: Change in magnetic field of ~ ±10 mT/s ramp over one cycle.

3.2.1: Equipment used

The magnetic field was applied using the Walker Scientific LE USA Inc. HF-9H Laboratory electromagnet and the field produced was measured using the LakeShore 425 Gauss meter. The time-varying field depicted in Fig. 3.3 was achieved

with a feedback control algorithm implemented using LabVIEW to adjust the signal to the electromagnet based on data from a Gauss meter located between the electromagnet pole pieces. An overview of this experimental setup is shown in Fig. 3.4.
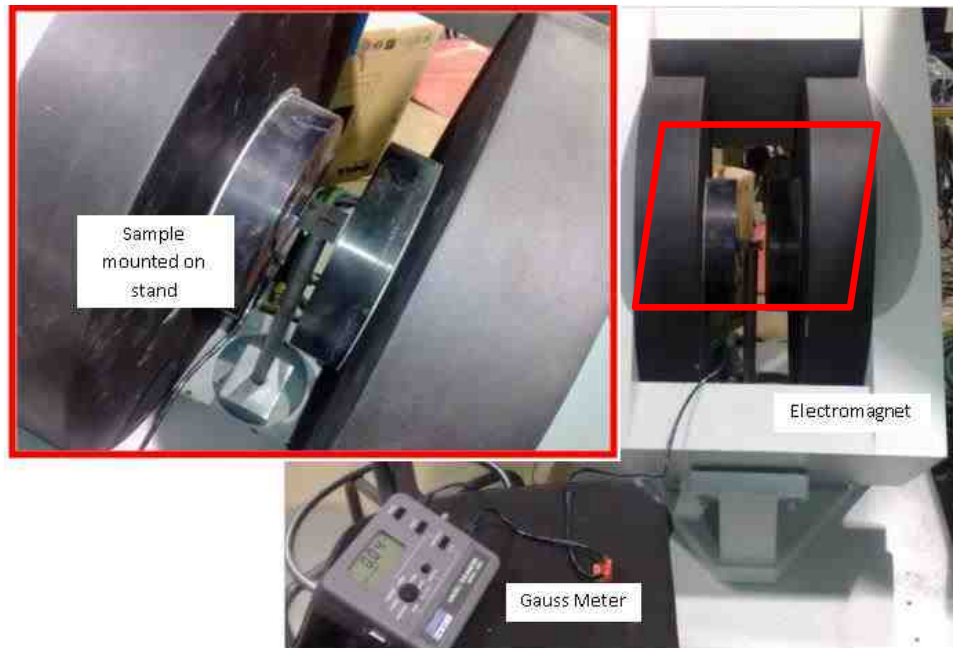
Figure 3.4: Setup for experimental characterization of strains under magnetic fields and zero applied stresses.

3.2.2: Data acquisition

Each specimen had two strain gages attached to it. One strain gage measured strain in the longitudinal direction (Vishay MicroMeasurements (EA-06-031DE-350) and the other measured the strain in the transverse direction (EA-06-031EC-350). Because of the small size of the specimens, there was space only for one strain gage on each side. Each strain gage was connected to a strain indicator (Vishay 3800), which were connected to the PC-based NI LabVIEW data acquisition system through

the National Instruments DAQ board. The magnetic field was measured by a Gauss meter (LakeShore 425), which was also connected to the PC-based data acquisition system.

3.2.3: Errors and repeatability issues

To check for avoidable errors and to compensate for unavoidable errors, the results reported in this study were measured numerous times. Each of the [110] dogbone specimens was tested with one set of strain gages (over multiple cycles), and then retested with a different set of strain gages because they showed some variation in the results. Each sample underwent a trial with one set of strain gages over at least 5 cycles. Each cycle consisted of two ramps in the magnetic field: 0mT to +400mT to 0mT and 0mT to -400mT to 0mT. The number of trials that each sample was subjected to is listed in Table 3.3. More trials were performed if there were inconsistencies in the data, until there was good confidence in the data. This was done by neglecting erroneous cycles and testing the samples over multiple trials.

Repeatability was an issue as the strain gages reported drift (of up to 10 $\mu\varepsilon$ over the time span needed for gathering data from 5 load cycles) and in some cases inconsistency due to noise arose in the electronics. To improve confidence in the data, the experiments were first performed with manual data acquisition and later tested again using the NI LabVIEW data acquisition systems. When compared, there was less than 10% variation in the results. The strain data at very low fields (<5mT) have

not been used in the calculations for steady state, high field Poisson's ratio. The errors in these experiments were of the order of $\sim \pm 5\mu\varepsilon$.

Table 3.3: Number of trials for which each specimen exhibited consistent results.

Composition of Galfenol (at % of Ga)	Number of Trials
12%	4
15.8%	4
17.9%	4
20.5%	3
25.3%	3
31%	2
33%	2

3.2.4: Data reduction and analysis

An algorithm was developed in Matlab to analyze the data from each test. The raw data consisted of the magnetic field, the longitudinal strain and the transverse strain. From this, a field vs. strains plot, a field vs. Poisson's ratio plot and a lateral strain vs. longitudinal strain were created for each sample. Many of the samples showed considerable noise in the field-strain plot at low field values (generally the first 5% of the data) before the dependence became linear. The Poisson's ratio was calculated as the average of the negative ratio of transverse strain to longitudinal strain, using data from the linear portion of the strain-strain curve using a script that determines the slope of the curve.

Poisson's ratio is calculated at every data point by using Eq. (3.1) to plot the trend of change in Poisson's ratio with applied magnetic field. Equation (3.2)

93

computes the Poisson's ratio once the magnetostrictions along both the longitudinal and transverse directions reach steady state (by neglecting the first 'a' data points).

$$v_{110} = \frac{\varepsilon_{1\bar{1}0}}{\varepsilon_{110}} \qquad (3.1)$$

$$v_{110} = \frac{1}{n-a} \sum_{i=a}^{n} \frac{\varepsilon_{1\bar{1}0}}{\varepsilon_{110}} \qquad (3.2)$$

Chapter 4: Results and discussion

Though the magnetostriction along the [110] direction at zero external stress has been studied for a few compositions of Galfenol in previously published works **[8, 46]**, this is the first work that completely documents magnetostriction along $[1\bar{1}0]$ and the variation of Poisson's ratio under varying magnetic fields and zero applied stress. This chapter will include the results from Galfenol samples of compositions between 12% Ga and 33% Ga. Interesting results from some other samples will also be presented. These results will be compared with data from the analytical model and the multiphysics simulation and an attempt will be made to present insights into the magneto-auxetic behavior from a magnetic dipole and a scaled atomic interactions perspective.

Please note that the data set presented in this Chapter for each composition is from a trial where the strain values were closest to the average value from all the trials. The Poisson's ratio value presented for each composition is the average of the values obtained from all the trials. Graphs showing the raw data of all the trials are presented in Appendix D

4.1: Behavior of 15.8 at%. Ga and 17.9 at%. Ga Galfenol

Results from the 15.8 at%. Ga and 17.9 at%. Ga <110> oriented single crystal sample will be discussed in this section. At this composition, the alloy is in the A_2 phase with order $D0_3$ precipitates because of the high temperature (~1000°C) from

which the samples were quenched **[60]** (Refer Fig. 1.13). Based on Fig. 1.15, it can be inferred that <100> are the easy axes for all compositions studied. However for these two compositions, values for the magnetic anisotropy constants K_1 are much larger than for higher compositions, where the magnitude of K_1 decreases toward zero. This may suggest a greater difference in the ease with which the <100> easy axes can be magnetized compared with the ease with which the intermediate <110> axes and the hard <111> axes can be magnetized.

4.1.1: Results from the 15.8 at%. Ga <110> oriented specimen

4.1.1.1 : Experimental data for 15.8% Ga content

The strain data obtained from the 15.8% Ga <110> {100} oriented single crystal Galfenol sample is shown in Fig. 4.1. The blue curve indicates the magnetostriction along the longitudinal [110] direction and the red curve indicates the magnetostriction along the transverse $[1\overline{1}0]$ direction when the field is applied along the longitudinal direction.
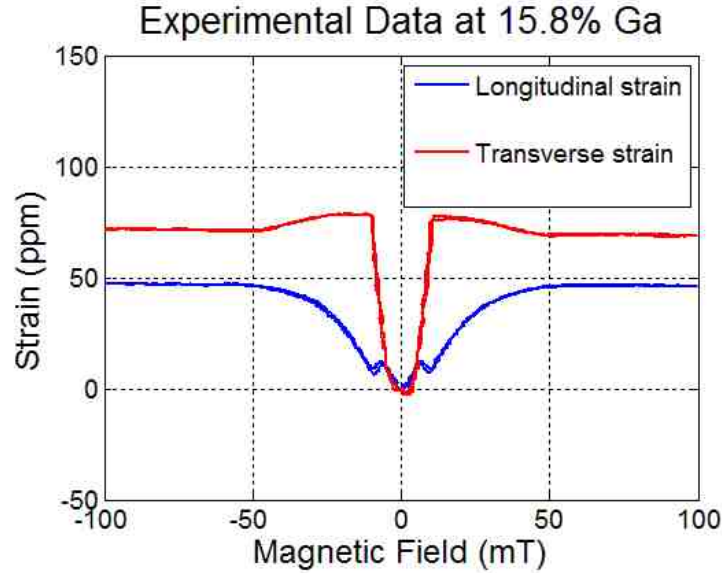
Figure 4.1: Strains along the longitudinal [110] and transverse [1$\bar{1}$0] directions for the 15.8% Ga single crystal Galfenol with applied field along the [110] direction at zero external stress.

The strain values along the transverse and longitudinal <110> directions at magnetic saturation and zero stress were found to be about 70με and about 46με respectively. The sample exhibits an unusual response where the longitudinal strain which increases initially with applied field to 11με experiences a dip between ±5mT and ±10 mT of about 3με before increasing again to reach saturation past ±50mT. The transverse strain increases and reaches a maximum value of about 80με (at the same field of ~ ±10mT) and then drops from the maximum by 5-10% until just past ±40mT where magnetic saturation is approached.

Fig. 4.2 shows the negative ratio of the transverse and longitudinal <110> strains as the magnetic field induced Poisson's ratio. This data set is quite unique. The Poisson ratio varies with the magnitude of applied field in a non-monotonic manner.

97

Additionally, it is the first the author is aware of in which a structural auxetic material exhibits a Poisson's ratio response that is more negative than -1. This is because the magnetically induced transverse strain is larger than the longitudinal strain produced along the direction of the applied field.

At very low fields, i.e. less than ~ ±5 mT with strain values that are less than ~1με, the accuracy of the Poisson ratio values is uncertain due to a low a signal to noise ratio because strains of ±1με are at the resolution of the equipment. Above ~ ±5mT, the Poisson ratio decreases with increasing field to a minimum value of ~ −10 at ±10 mT and then gradually increases to −1.5 at magnetic saturation.
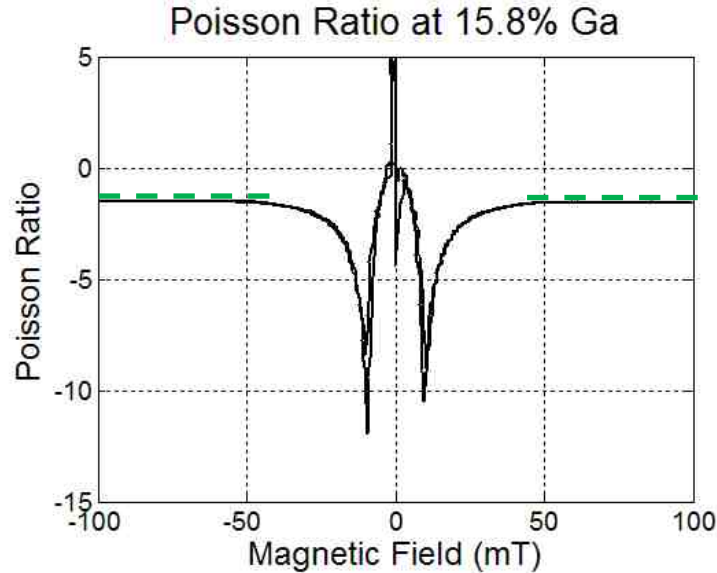
Figure 4.2: Experimental data on variation of the Poisson's ratio with applied magnetic fields in <110> oriented 15.8% Ga Galfenol at zero applied stress (solid line). Poisson ratio value at magnetic saturation predicted using the energy model (dashed line) shown for fields ≥±40mT. At magnetic saturation (fields of greater than 50mT), the value of Poisson ratio obtained from the experiment is -1.50 ± 0.4 and the value from energy model is -1.52.

4.1.1.2 : Energy model at magnetic saturation for 15.8% Ga content

The value of Poisson's ratio at magnetic saturation predicted by the analytical model is ~ -1.52. This is discussed in Chapter 2 and the value of the analytical solution to the energy model at magnetic saturation is listed in Table 2.2. This is shown with the dashed line in Fig. 4.2, where magnetic saturation of the sample is assumed for fields of greater than ~ ±50 mT. The modeled value of -1.52 is in good accordance with the average experimentally determined value at magnetic saturation of -1.5 ± 0.4.

4.1.1.3: Multiphysics simulations for 15.8% Ga content

The strain results from the multiphysics simulation using the modified 'Armstrong model' derived in Section 2.5 is shown in Fig.4.3 (a). The experimental data is shown in Fig. 4.3 (b). The Poisson ratio determined from FEM simulation and experimental data are shown in Fig.4.4 (a) and (b), respectively
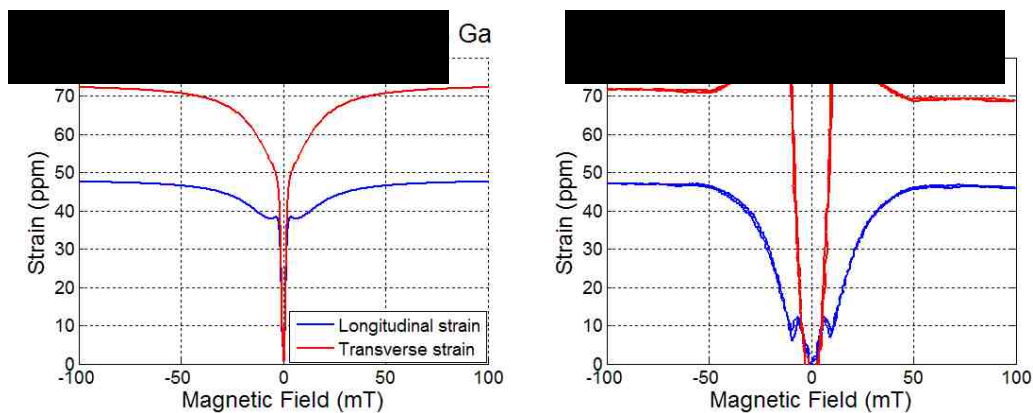
Figure 4.3: Strains along the longitudinal [110] (blue) and transverse [1$\bar{1}$0] (red) directions for the 15.8% Ga Galfenol sample obtained from (a) multiphysics simulation and (b) from experiments.

99
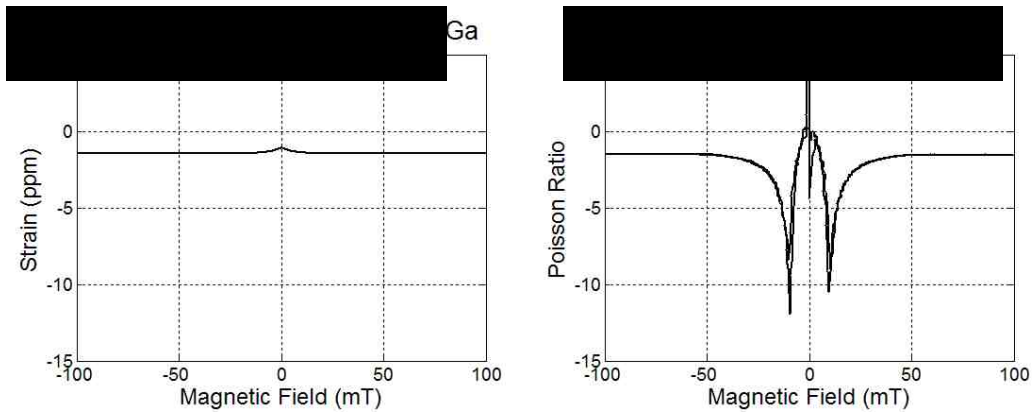
Figure 4.4: Poisson's ratio for the 15.8% Ga Galfenol sample obtained from (a)
multiphysics simulation and (b) from experiments.

The simulation predicts a strain of 72με and 49με along the longitudinal and
transverse <110> directions at magnetic saturation respectively. These values have an
error of about 2% with respect to the values predicted by the mathematical model.
The FEM model captures the non-monotonic increase in longitudinal strain at low
fields in the experimental data, but fails to capture that unusual trend in the transverse
strain. The experimental data appears to reach magnetic saturation at a field of ~50-60
mT, while the FEM simulation appears to just be reaching magnetic saturation at a
field of ~100 mT.

The Poisson's ratio obtained from the simulation monotonically decreases to
reach the steady state value of -1.47. This is lower than the values obtained from the
experiments (-1.5 ± 0.4) and the mathematical model (-1.52).

The simulation was able to predict the 'trends' in the strains with features like the drop in the longitudinal strain occurring at the exact applied field but the magnitude of the strain is off. This could be an attribute of the thermal history of the sample not being considered in the simulations. Other possible sources of errors have been discussed in Section 2.3.2.

4.1.2: Results from the 17.9 at%. Ga <110> oriented specimen

4.1.2.1 : Experimental data for 17.9% Ga content

The strain data obtained from the 17.9% Ga <110> {100} oriented single crystal Galfenol sample is shown in Fig. 4.5. The blue curve indicates the magnetostriction along the longitudinal [110] direction and the red curve indicates the magnetostriction along the transverse $[1\overline{1}0]$ direction when the field is applied along the longitudinal direction.
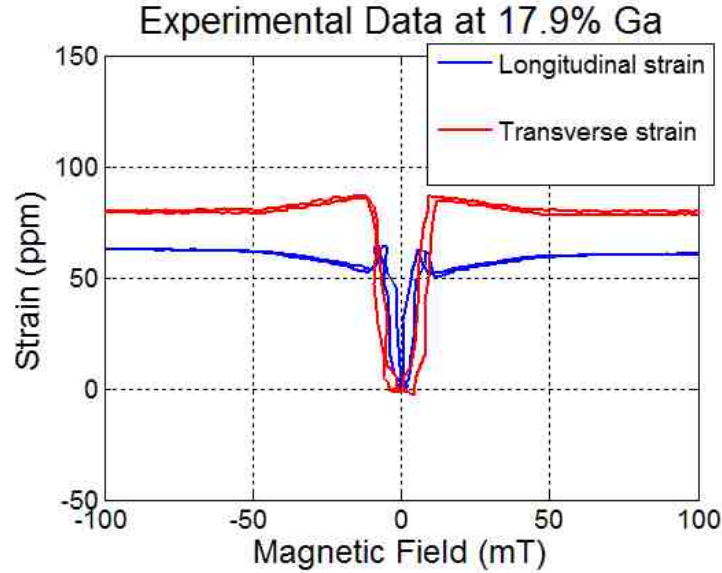
Figure 4.5: Strains along the longitudinal [110] and transverse [1$\bar{1}$0] directions for the 17.9% Ga single crystal Galfenol with applied field along the [110] direction at zero external stress.

The strain values along the transverse and longitudinal <110> directions at magnetic saturation and zero stress were found to be about 79µε and about 62µε respectively. This sample also showed the unusual response exhibited by the 15.8% Ga Galfenol sample (discussed in Section 4.1.1). The longitudinal strain which increases initially with applied field to ~64µε experiences a dip between ±5mT and ±10 mT of about 13µε before increasing again to reach saturation past ±60mT. The transverse strain increases and reaches a maximum value of about 87µε (at the same field of ~ ±10mT) and then drops from the maximum by 5-10% until just past ±50mT where magnetic saturation is approached. The transverse strain is larger than the longitudinal strain along the auxetic <110> direction under applied magnetic fields and zero applied mechanical stress in this sample as well. The negative ratio of

this transverse and longitudinal <110> strains is the magnetic field induced negative Poisson's ratio as shown in Fig. 4.6.

The strain in the longitudinal direction dips from ~ 64με at about ± 4mT to ~ 51με at ±10mT while the strain in the transverse direction which initially increased until ±10mT to reach ~ 87με decreased in magnitude and attained a value of ~79με at magnetic saturation past ±50mT. The negative ratio of this transverse and longitudinal <110> strains is the magnetic field induced negative Poisson's ratio as shown in Fig. 4.6.
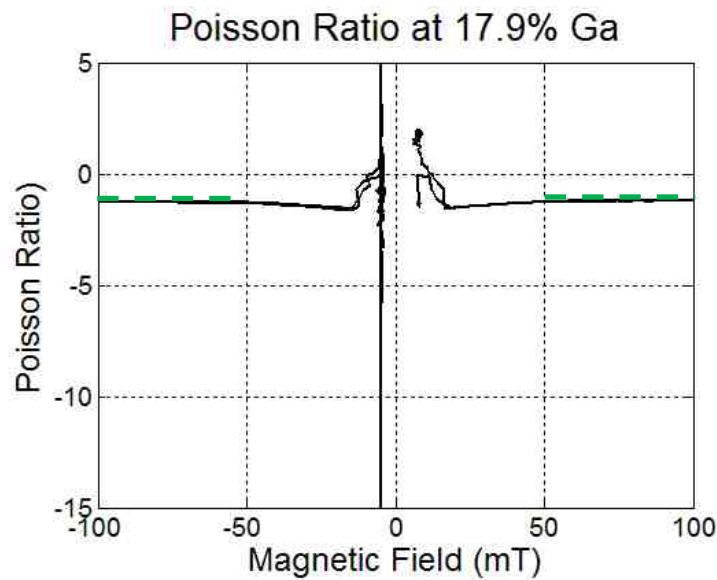
Figure 4.6: Experimental data on variation of the Poisson's ratio with applied magnetic fields in <110> oriented 17.9% Ga Galfenol at zero applied stress (solid line). Poisson ratio value at magnetic saturation predicted using the energy model (dashed line) shown for fields ≥±50mT. At magnetic saturation (fields of greater than 60mT), the value of Poisson ratio obtained from the experiment is -1.27 ± 0.35 and the value from energy model is -1.07.

At very low fields, i.e. less than ~ ±5 mT with strain values that are less than ~1µɛ, the accuracy of the Poisson ratio values is uncertain due to a low a signal to noise ratio because strains of ±1µɛ are at the resolution of the equipment. Above ~ ±5mT, the Poisson ratio decreases with increasing field to a minimum value of ~ −1.7 at ±15 mT and then gradually increases to −1.27 ± 0.35 at magnetic saturation.

It can be observed that the magnitude of the strains is larger in the case of the 17.9% Ga Galfenol sample when compared with the 15.8% Ga sample. This is because the 17.9% Ga composition is close to the first magnetostriction peak along the <100> direction (Refer Fig. 1.15).

4.1.2.2: Energy model at magnetic saturation at 17.9% Ga content

The value of Poisson's ratio at magnetic saturation predicted by the analytical model is ~ -1.07. This is discussed in Chapter 2 and the value of the analytical solution to the energy model at magnetic saturation is listed in Table 2.2. This is shown with the dashed line shown in Fig. 4.2, where magnetic saturation of the sample is assumed for fields of greater than ~ ±60 mT. The modeled value of -1.07 is in good accordance with the experimentally determined value at magnetic saturation of -1.27 ± 0.35.

4.1.2.3: Multiphysics simulations for 17.9% Ga content

The result from the multiphysics simulation using the modified 'Armstrong model' derived in Section 2.5 is shown in Fig.4.7 (a). The experimental data is shown

in Fig. 4.7 (b). The Poisson ratio determined from FEM simulation and experimental

data are shown in Fig.4.8 (a) and (b), respectively.
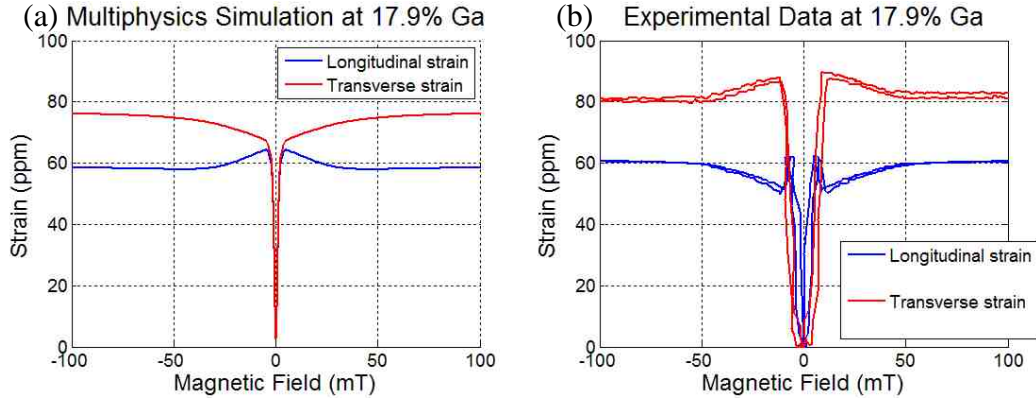
Figure 4.7: Strains along the longitudinal [110] and transverse [1$\bar{1}$0] directions for the 17.9 % Ga Galfenol sample obtained from (a) multiphysics simulation and (b) from experiments.
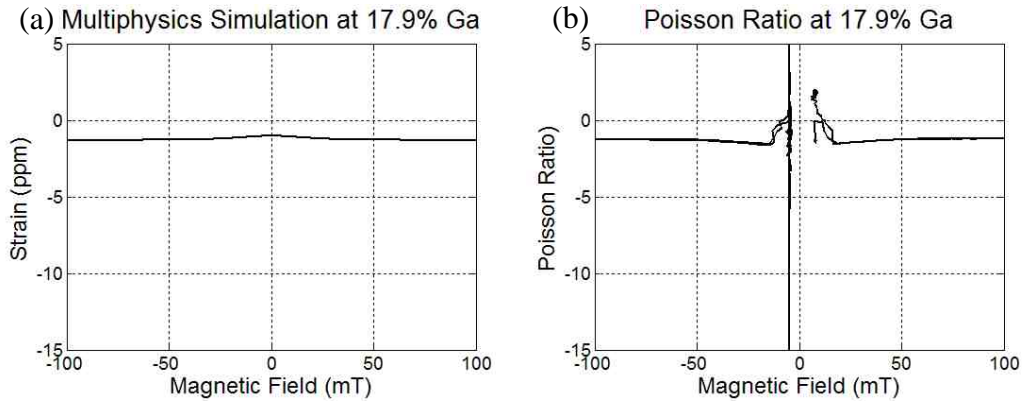
Figure 4.8: Poisson's ratio for the 17.9 % Ga Galfenol sample obtained from (a) multiphysics simulation and (b) from experiments.

The simulation predicts a strain of 59µε and 77µε along the longitudinal and

transverse <110> directions respectively. The experimental values are about 10%

higher than that from the model and the simulation. The thermal history of the

sample, since it was quenched could be a reason for the higher values of strains. The longitudinal strain was about 5% off from the experimental data while the transverse strain was off by 6%. The value of Poisson's ratio at magnetic saturation obtained from the simulation was -1.31 which is lower than the values from the mathematical model and experiments (-1.07 and -1.29 ± 0.35 respectively).

4.1.2.4: Comparison of strain data from 17.9 at%. Ga Galfenol samples with previous data

Previous strain data under applied magnetic fields along the <110> direction and zero applied stresses on an oven cooled, 18% Ga <110> oriented single crystal Galfenol had suggested that saturation magnetostriction along the longitudinal <110> direction would be about 50με [8]. This is also the value predicted by the mathematical model in Table 2.2.

Data from the current experiments showed a larger value (~ 62με) for the longitudinal strain because this sample was quenched. This increased its inherent magnetostriction due to improvements in the ordering of the Ga atoms in the BCC lattice [102]. Figure 4.9 (a) shows magnetostriction data from the current work for the quenched sample and compares it to longitudinal strain from Atulasimha's dissertation shown in Fig. 4.9 (b) [3].
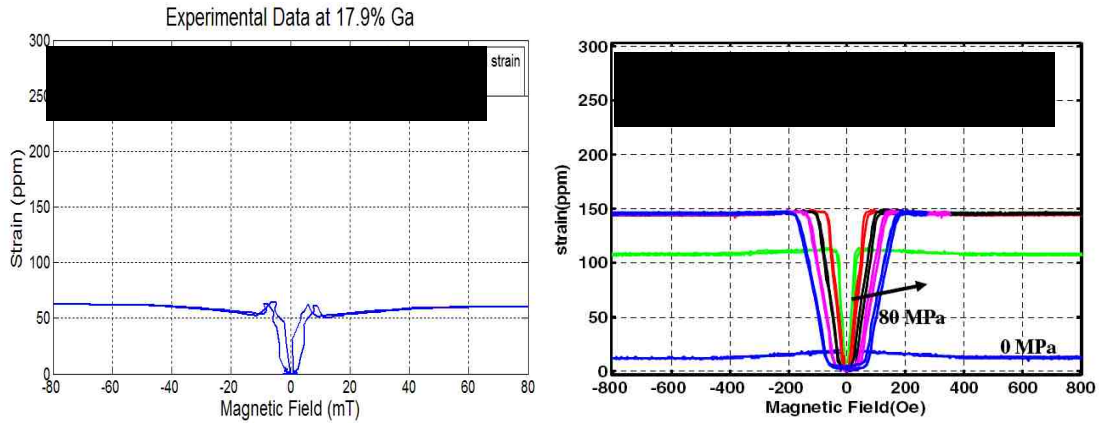
Figure 4.9: Strain along longitudinal <110> direction under applied magnetic fields in ~18 at. % Ga <110> oriented Galfenol from (a) current experiments on a quenched sample and (b) previous experiments by Atulasimha **[8]** on an oven cooled sample.

4.1.3: Proposed mechanism for the magneto-auxetic behavior in 15.8 at%. Ga and 17.9 at %. Ga Galfenol samples

The trends in the strains obtained under applied magnetic fields and zero stress from the 15.8% Ga <110> oriented Galfenol sample is similar to those from the 17.9% Ga <110> Galfenol sample. Both of these samples have a D0$_3$ structure and both have a non-monotonic increase in longitudinal strains with increasing magnetic field. This section presents a possible mechanism to explain the strains observed in the partial D0$_3$ phase using the 15.8% Ga sample as an example. The same mechanism can be used to explain the behavior in the 17.9% Ga sample.

This mechanism is represented by the schematic in Fig. 4.10. The top plot shows the variation of the longitudinal and transverse strains with positive magnetic fields and the variation of the dimensions of the sample. The cartoons below the plot

show the proposed evolution of the orientation of the magnetic dipoles present in the material.

Initially, at zero magnetic fields, all the magnetic moments (denoted by red arrows that indicate their nominal direction; length of arrow indicates relative magnitude in the given direction, but lengths are not to scale) are randomly oriented such that the overall magnetization of the material is zero as shown in Fig. 4.10 (0). When an external magnetic field is applied, the magnetic dipoles rotate to orient themselves along the <100> easy axes available on the (100) plane to attain the lowest energy state as shown in Fig. 4.10 (a), causing an increase in both the transverse and the longitudinal strain up to a field of about 4mT.

As the magnitude of the applied magnetic field increases, a critical field is reached where there is enough energy to start orienting the magnetic dipoles along the <110> directions. At this point, it is unclear if this rotation of the magnetic moments is the reason for a rapid increase in the transverse strain and a small decrease in the longitudinal strain. Most of the dipoles are expected to be completely re-oriented at around 11mT in the 15.8 at. % Ga Galfenol sample.
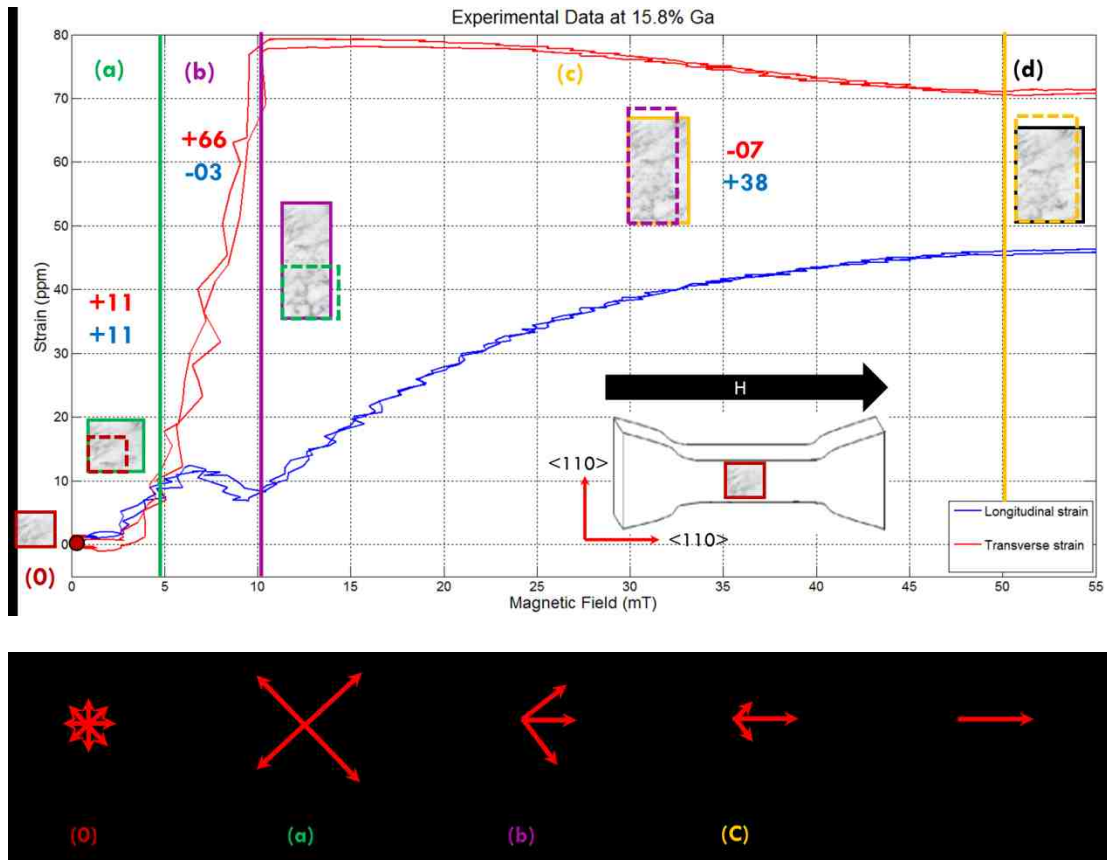
Figure 4.10: Schematic representation of a possible mechanism for magnetostriction along the <110> crystallographic direction for 15.8% Ga Galfenol on the basis of change in orientation of magnetic moments with applied magnetic fields. The grey boxes illustrate change in dimension of the sample (not to scale) at the end of each stage (0-e). The values next to the boxes indicate the change observed along the longitudinal (blue) and transverse (red) directions. Inset: Shows the orientation of the dog bone sample and the direction of applied magnetic field. Sketches (0)-(e) from left to right below graph depict relative strength of magnetization vectors along indicated crystallographic axes at field levels of 0, 2, 8, 30 and 55 mT.

As the applied magnetic field is increased past 11mT, the magnetic energy added to the system aligns all the magnetic dipoles with the applied field direction and the sample reaches magnetic saturation at about 50mT. This is accompanied by an increase in the longitudinal strain and a decrease in the transverse strain.

109

Magnetic domain imaging, discussed in Chapter 5 will be used to improve upon the the proposed mechanism to further understand the magneto-auxetic response of Galfenol under applied magnetic fields along the <110> crystallographic direction from a magnetic domain evolution perspective.

4.1.4: Proposed model of atomic level interactions for magneto-auxetic behavior in 15.8 at%. Ga and 17.9 at%. Ga Galfenol samples

As Ga atoms are added to α-Fe, they start replacing the Fe atoms in the crystal lattice randomly at low Ga concentrations as discussed in Chapter 1. At compositions higher than 12 at. % Ga, an ordered $D0_3$ phase is obtained as shown in Fig. 1.14. These Ga atoms are larger than the Fe atoms and there are differences in the strengths of Fe-Fe bonds, Fe-Ga bonds and Ga-Ga bonds. These factors have been attributed to be the reason for anisotropy in Galfenol [42, 57].

Strains obtained along the auxetic <110> directions under applied tensile loads have been attributed to anisotropic stretching of the bonds between the atoms that make up the crystal lattice of Galfenol [3, 12, 78]. The auxetic response to stress is due to the interaction of the mechanical energy from the applied load and the elastic energy in the atomic bonds.

Under applied magnetic fields, the strains in the auxetic direction occur due to the anisotropic interaction of electron spins of neighboring atoms in the crystal lattice

arising from the applied magnetic energy and the elastic energy in the atomic bonds between the atoms. A 2-D schematic depicting the (100) plane and a possible scenario for the interaction of the 4 in-plane atoms under applied magnetic fields along the auxetic <110> direction is shown in Fig. 4.11. (Note, although this is a 2-D depiction that neglects well-known 3-D interactions, as well as the known differences in atomic bond strengths of Fe-Fe bonds, Fe-Ga bonds and Ga-Ga bonds, it is presented here for illustrative purposes to suggest potential interactions).
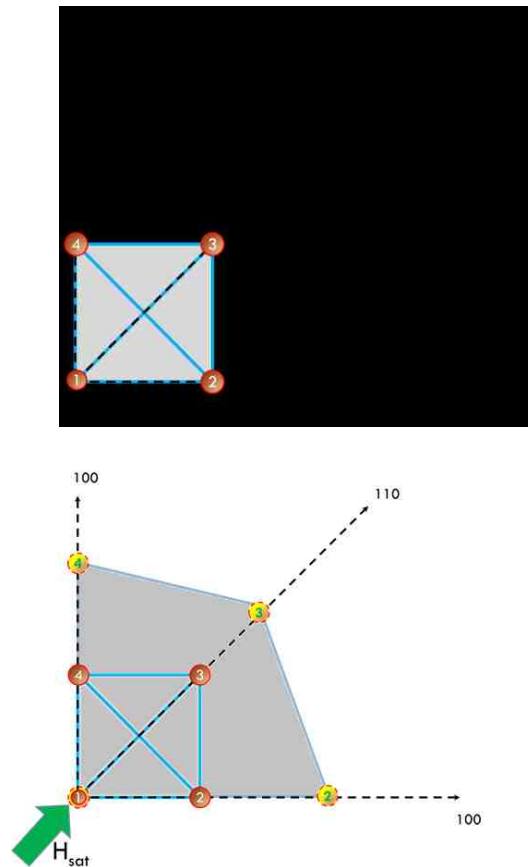
Figure 4.11: Schematic of atomic level strains in a (100) plane of Galfenol. (a) Shows the location of the atoms (brown circles with numbers 1 to 4) on the plane under zero magnetic field and zero stress. (b) Shows the new location of atoms (denoted by the

yellow circles) relative to their original positions at magnetic saturaion for applied field along the [110] directionand zero stress.

Galfenol samples in the A_2-$D0_3$ phase, (at compositions greater than ~12 at. % Ga and lesser than ~20 at. % Ga), have relatively high anisotropy (Fig. 1.18) with <100> being the easy directions (relative to Galfenol alloys with higher Ga content). Hence, the magnetic energy added to the system by the applied magnetic field finds it easier to flow along the <100> directions, moving atoms 2 and 4 from atom 1 due to interaction of the electron spins in these atoms that causes the magnetic dipoles to line up along the <100> directions. Due to this, atom 3 also moves away from atom 1 because of the atomic bonds between atom 3 and atoms 2 and 4 are stronger than the bond between atoms 1 and 3.

As more magnetic energy is added, atoms 2 and 4 move farther away from atom 1 along the <100> directions. Due to this, atom 3 begins to move closer to atom 1 and equilibrium between the elastic energy due to the bond strengths and the applied magnetic energy is attained.

This goes on until the energy from the applied magnetic field overcomes the anisotropy energy penalty. Beyond this critical magnetic field, energy begins to flow along the <110> crystallographic direction along which the magnetic field is applied. This moves atom 3 away from atom 1 as the magnetic dipoles rotate to line up along the favorable <110> direction. Atoms 2 and 4 move slightly closer to atom 1 to reach equilibrium as the specimen reached magnetic saturation along the <110> applied

field direction. Beyond saturation, all the magnetic dipoles have already lined up along the applied field and there are no more changes in the lattice due to atomic level interactions.

4.2: Behavior of 20.5 at%. Ga and 25.3 at%. Ga Galfenol

Results from the 20.5 at%. Ga and 25.3 at%. Ga <110> oriented single crystal sample will be discussed in this section. At this composition, the alloy is in the $D0_3$ phase (partly a mixture of A_2 phase) because of the high temperature (~1000°C) from which the samples were quenched **[60]** (Refer Fig. 1.15). Based on Fig. 1.15, it can be inferred that <100> are the easy axes for all compositions studied. However, for these two compositions, the values of K_1 and K_2 are very close to zero which reduces a strong preference for a particular direction as the easy axis **[61]**. Hence, although the <100> directions are still the easy axes, the 'harder' <110> directions are almost as easy.

4.2.1: Results from the 20.5 at%. Ga <110> oriented specimen

4.2.1.1 : Experimental data for 20.5 % Ga content

The strain data obtained from the 20.5% Ga <110> {100} oriented single crystal Galfenol sample is shown in Fig. 4.12. The blue curve indicates the magnetostriction along the longitudinal [110] direction and the red curve indicates the magnetostriction along the transverse [1$\bar{1}$0] direction when the field is applied along the longitudinal direction.
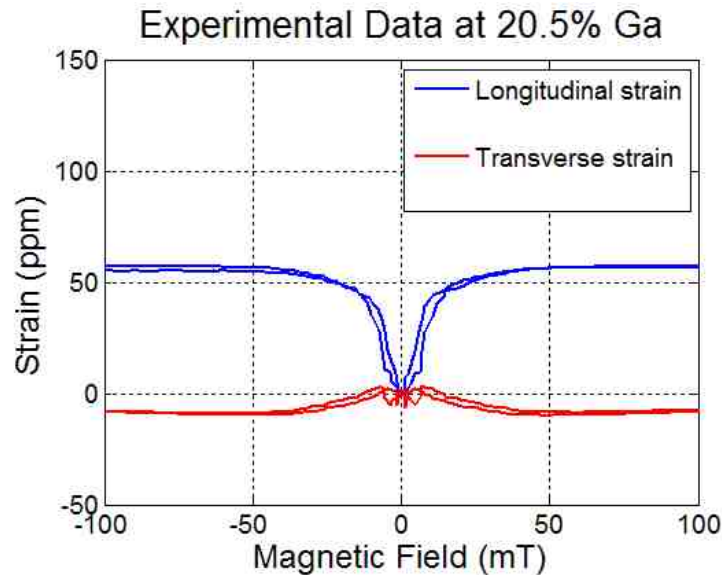
Figure 4.12: Strains along the longitudinal [110] and transverse [1$\bar{1}$0] directions for the 20.5% Ga single crystal Galfenol with applied field along the [110] direction at zero external stress.

The strain values along the longitudinal and transverse <110> directions at magnetic saturation and zero stress were found to be about 57µε and about -8µε respectively. The longitudinal strain increased monotonically and reached magnetic saturation past ±60mT. Though the transverse strain showed a tendency to increase till ~ ±5mT, it quickly turned negative at higher magnetic fields and reached magnetic saturation. The value of transverse strain was very small and close to zero (same order of magnitude as noise from strain gage as discussed in Chapter 3). There were some data sets where the transverse strain at magnetic saturation was very close to zero, sometimes crossing over (due to drift in the strain gauges). These data sets have been ignored in this study. The negative ratio of this transverse and longitudinal

114

<110> strains is the magnetic field induced negative Poisson's ratio as shown in Fig. 4.13.

At very low fields, i.e. less than ~ ±5 mT with strain values that are less than ~1με, the accuracy of the Poisson ratio values is uncertain due to a low a signal to noise ratio because strains of ±1με are at the resolution of the equipment. Above ~ ±5mT, the Poisson ratio decreases with increasing field to a minimum value of ~ −0.2 at ±10 mT and then gradually increases to 0.15 ± 0.6 at magnetic saturation.
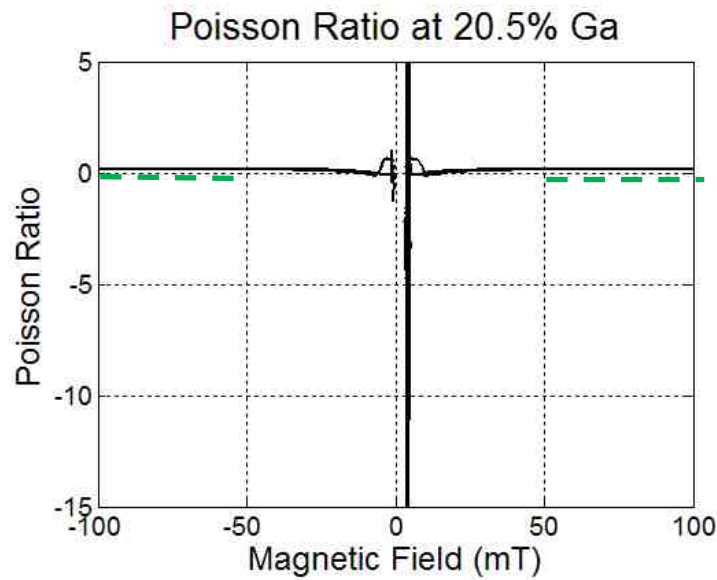
Figure 4.13: Experimental data on variation of the Poisson's ratio with applied magnetic fields in <110> oriented 20.5% Ga Galfenol at zero applied stress (solid line). Poisson ratio value at magnetic saturation predicted using the energy model (dashed line) shown for fields ≥±50mT. At magnetic saturation (fields of greater than 60mT), the value of Poisson ratio obtained from the experiment is 0.15 ± 0.6 and the value from energy model is -0.11.

4.2.1.2 : Energy model at magnetic saturation for 20.5 % Ga content

The value of Poisson's ratio at magnetic saturation predicted by the analytical model is ~ -0.11. This is discussed in Chapter 2 and the value of the analytical solution to the energy model at magnetic saturation is listed in Table 2.2. This is shown with the dashed line shown in Fig. 4.13, where magnetic saturation of the sample is assumed for fields of greater than ~ ±60 mT. The modeled saturation value of -0.11 is lower than the average experimentally determined value at magnetic saturation of 0.15 ± 0.6.

4.2.1.3: Multiphysics simulations for 20.5 % Ga content

The result from the multiphysics simulation using the modified 'Armstrong model' derived in Section 2.5 is shown in Fig.4.14 (a). The experimental data is shown in Fig. 4.14 (b). The Poisson ratio determined from FEM simulation and experimental data are shown in Fig.4.15 (a) and (b), respectively.
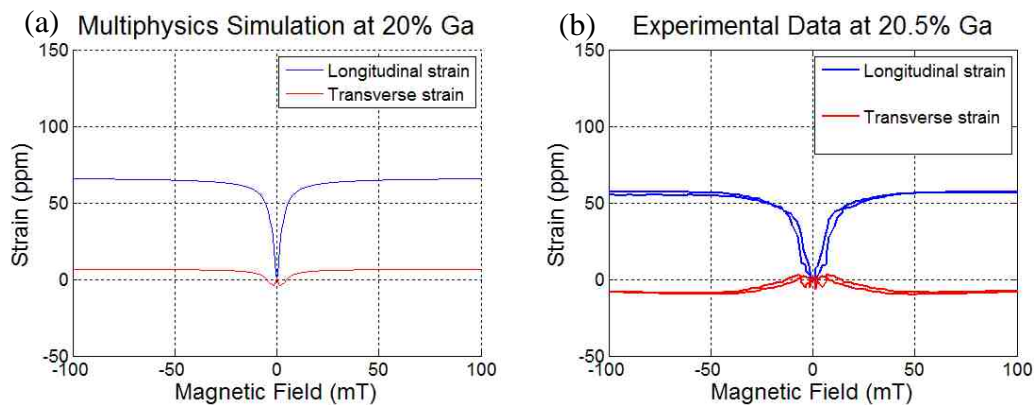
Figure 4.14: Strains along the longitudinal [110] (blue) and transverse [1$\bar{1}$0] (red) directions for the 20.5% Ga Galfenol sample obtained from (a) multiphysics simulation and (b) from experiments.
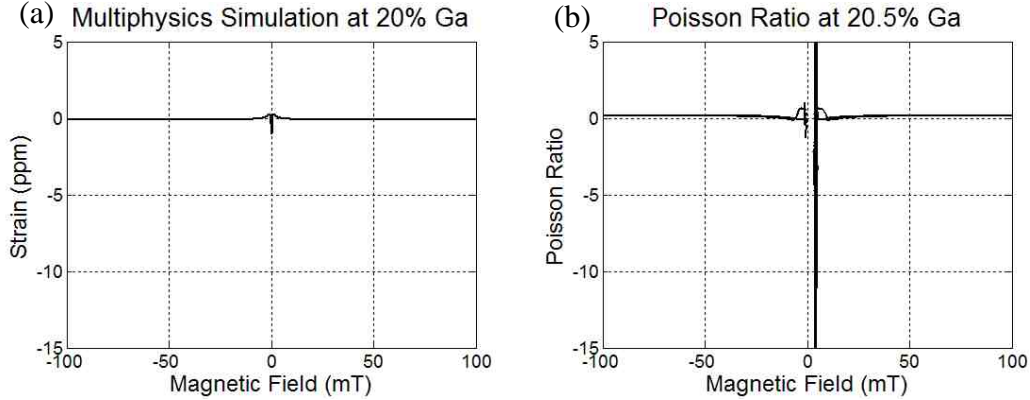
Figure 4.15: Poisson's ratio 20.5% Ga Galfenol sample obtained from (a) multiphysics simulation and (b) from experiments.

The simulation predicts a strain of 66με and 7με along the longitudinal and transverse <110> directions respectively. The simulation and the analytical model predict a negative Poisson's ratio of ~ -0.1 and -0.11 respectively. The simulation was unable to predict the strain values at magnetic saturation that were obtained from the experiments. It is important to note here that as discussed in Section 2.3.2, the modified 'Armstrong model' uses the values of λ_{100} and λ_{111} along with those of K_1 and K_2 to predict the expected magnetostriction trend. At about 20% Ga, λ_{100} reaches a peak while λ_{111} crosses over from being a negative number to a positive number as shown in Fig.1.15. The values of K_1 and K_2 are almost zero (Refer Fig. 1.18) at this composition. Using values of K_1 and K_2 that are less than ±10 kJ/m^3 to lead to numerical convergence problems within the simulation code that were not overcome. Fig. 4.16 shows the result obtained when such low values were used for K_1 and K_2.
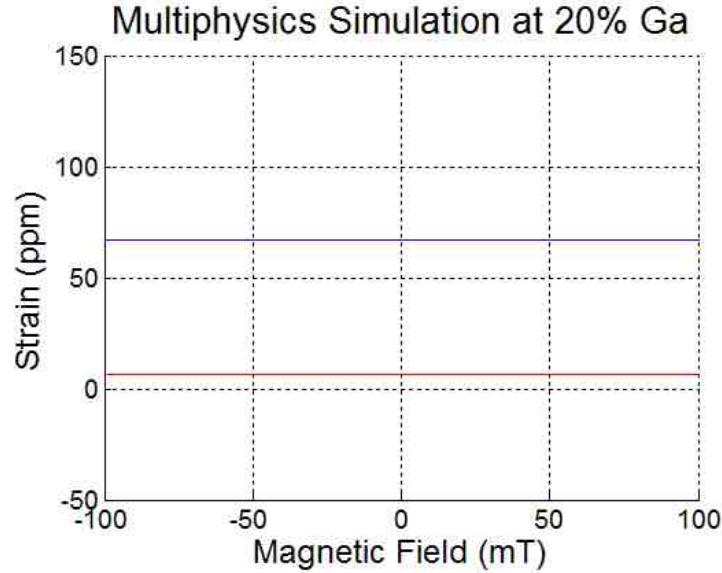
Figure 4.16: Variation of longitudinal (blue) and transverse (red) <110> strains obtained from the simulations for values of K_1 and $K_2 < \pm 1$ kJ/m^3.

Since anisotropy determines the preferred direction for energy to flow in the lattice, the simulation couldn't compute the exact strain values at each applied magnetic field and gave an output with horizontal lines based on the values of λ_{100} and λ_{111}. The values of the parameters used in this simulation are listed in Table 2.3. Thus, the simulation was incapable of predicting the trends observed from the experiments.

4.2.2: Results from the 25.3 at%. Ga <110> oriented specimen

4.2.2.1 : Experimental data for 25.3% Ga content

The strain data obtained from the 25.3% Ga <110> {100} oriented single crystal Galfenol sample is shown in Fig. 4.17. The blue curve indicates the magnetostriction along the longitudinal [110] direction and the red curve indicates the

magnetostriction along the transverse [1$\bar{1}$0] direction when the field is applied along the longitudinal direction.

Figure 4.17: Strains along the longitudinal [110] (blue) and transverse [1$\bar{1}$0] (red) directions for the 25.3% Ga single crystal Galfenol with applied field along the [110] direction at zero external stress.

The strain values along the longitudinal and <110> directions at magnetic saturation and zero stress were found to be about 68με and about -35με respectively. The longitudinal strain monotonically increased with applied magnetic field and reached magnetic saturation at ± 20mT. The transverse strain decreased with applied magnetic field and reach its lowest value at ± 10mT beyond which it increases in magnitude by 6με up to ~15mT and reaches magnetic saturation past ± 20mT. The negative ratio of this transverse and longitudinal <110> strains is the magnetic field induced negative Poisson's ratio as shown in Fig. 4.16. This sample showed a definite positive Poisson's ratio.

At very low fields, i.e. less than ~ ±5 mT with strain values that are less than ~1με, the accuracy of the Poisson ratio values is uncertain due to a low a signal to noise ratio because strains of ±1με are at the resolution of the equipment. There is an initial increase to 1.6 in the Poisson's ratio up to ~ ±5mT. Above ±5mT, the Poisson ratio decreases monotonically with increasing field to 0.52 ± 0.75 at magnetic saturation.
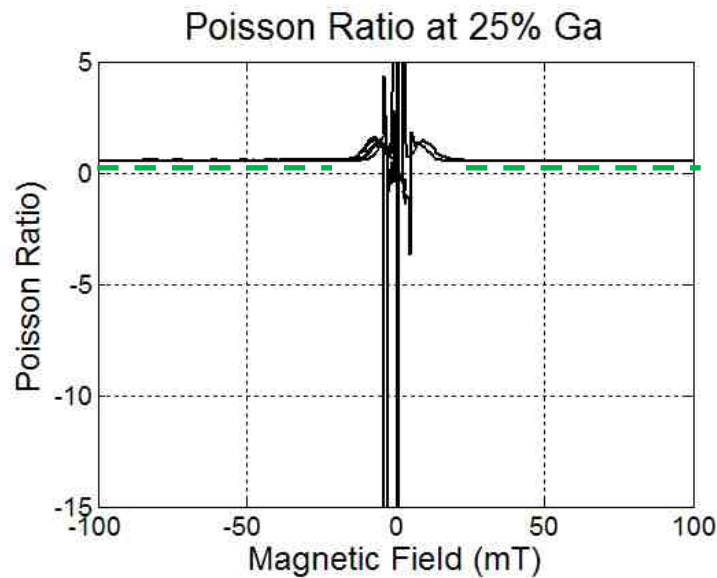
Figure 4.18: Experimental data on variation of the Poisson's ratio with applied magnetic fields in <110> oriented 25.3% Ga Galfenol at zero applied stress (solid line). Poisson ratio value at magnetic saturation predicted using the energy model (dashed line) shown for fields ≥±25mT. At magnetic saturation (fields of greater than 20mT), the value of Poisson ratio obtained from the experiment is 0.52 ± 0.75 and the value from energy model is 0.17.

The value of Poisson's ratio at magnetic saturation predicted by the energy model is +0.17. This is discussed in Chapter 2 and the value of the analytical solution to the energy model at saturation is listed in Table 2.2. This value is shown with the dashed line in Fig. 4.18, where magnetic saturation of the sample is assumed for fields of greater than ~ ±25 mT. The modeled saturation value of +0.17 (discussed in Chapter 2 and values listed in Table 2.1) is smaller than the average experimentally determined value of +0.52 ± 0.75.

4.2.2.3: Multiphysics simulations for 25.3% Ga content

The result from the multiphysics simulation using the modified 'Armstrong model' derived in Section 2.5 is shown in Fig.4.19 (a). The experimental data is shown in Fig. 4.19 (b). The Poisson ratio determined from FEM simulation and experimental data are shown in Fig.4.20 (a) and (b), respectively.
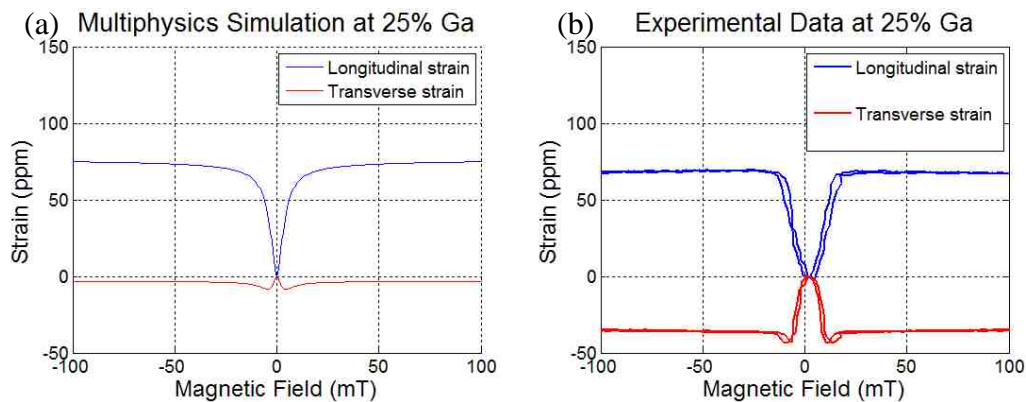
Figure 4.19: Strains along the longitudinal [110] (blue) and transverse (red) [1$\bar{1}$0] directions for the 25.3% Ga Galfenol sample obtained from (a) multiphysics simulation and (b) from experiments.
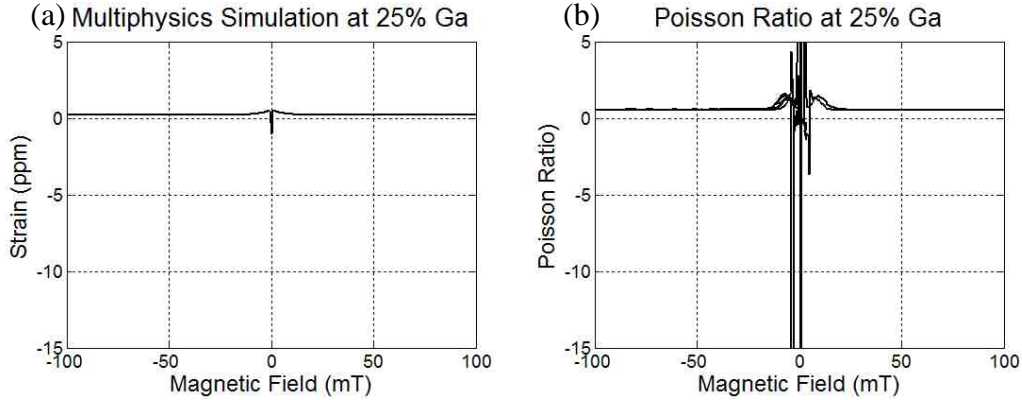
Figure 4.20: Poisson's ratio for the 25.3% Ga Galfenol sample obtained from (a) multiphysics simulation and (b) from experiments.

The simulation predicts a strain of 59µε and 77µε along the longitudinal and transverse <110> directions respectively. The simulation was able to predict that there was contraction in the transverse direction but the value of transverse strain at magnetic saturation was much lower in the experiments than predicted by the simulations. The simulation predicts a strain of 76µε and -9µε along the longitudinal and transverse <110> directions respectively. The simulations also predict a positive value for the Poisson's ratio but the values for transverse strain are much higher than those from the experiments. For this composition, the values of K_1 and K_2 were obtained by extrapolation of the data from Rafique et al [42]. Extrapolation is always a risk factor for introduction of errors. In this case, extrapolation lead to an assumption of a negative value for K_1. However, magnetostriction data show this composition has <100> easy axes, which based on Eq. 1.24 requires that K_1 be positive, not negative. Thus, in spite of the allowing the simulation to produce reasonable strain data, extrapolation has introduced a likely source of error. The other

sources of errors have been discussed in Section 2.3.2. The other sources of errors have been discussed in Section 2.3.2.

4.2.3: Proposed mechanism for the magneto-auxetic behavior in 20.5 at%. Ga and 25.3 at%. Ga Galfenol samples

This section presents a possible mechanism to explain the strains observed in the 20.5% Ga sample. The same mechanism can be used to explain the reason behind the strain response in the 25.3% Ga sample.

In samples of Galfenol between 20% and 25% Ga, the energy required to overcome the anisotropy in the crystal is extremely small. Since the anisotropy penalty is very small, it is overcome at low applied magnetic fields. As the applied magnetic field along the longitudinal <110> direction increases, the magnetic energy stretches the crystal causing a positive longitudinal strain. There is contraction in the transverse direction to compensate for this. This response is similar to the strain behavior along the transverse [010] direction and longitudinal [100] direction for applied magnetic fields along the [100] direction in Galfenol. The mechanism for such a response has been explained using the same argument presented here in previous works **[3, 15]**.

This mechanism is represented by the schematic in Fig. 4.21. The top plot shows the variation of the longitudinal and transverse strains with positive magnetic

fields and the variation of the dimensions of the sample. The cartoons below the plot show the proposed evolution of the orientation of the magnetic dipoles present in the material.

Initially, at zero magnetic fields, all the magnetic moments (denoted by red arrows that indicate their nominal direction; length of arrow indicates relative magnitude in the given direction, but lengths are not to scale) are randomly oriented such that the overall magnetization of the material is zero as shown in Fig. 4.21 (0). When an external magnetic field is applied, the magnetic dipoles rotate to orient themselves along the <100> easy axes available on the (100) plane, along the direction of the applied magnetic field to attain the lowest energy state as shown in Fig. 4.21 (a), causing an increase in both the transverse and the longitudinal strain up to a field of about 5mT.

Beyond 5mT, the energy from the applied magnetic field orients the magnetic dipoles along the <110> directions. As the applied magnetic field is increased, the magnetic energy starts aligning the magnetic dipoles with the applied field direction leading to an increase in the longitudinal strain. In this regime, there is a decrease in the transverse strain to achieve volume conservation and the specimen magnetization saturates at an applied field of about 60mT.
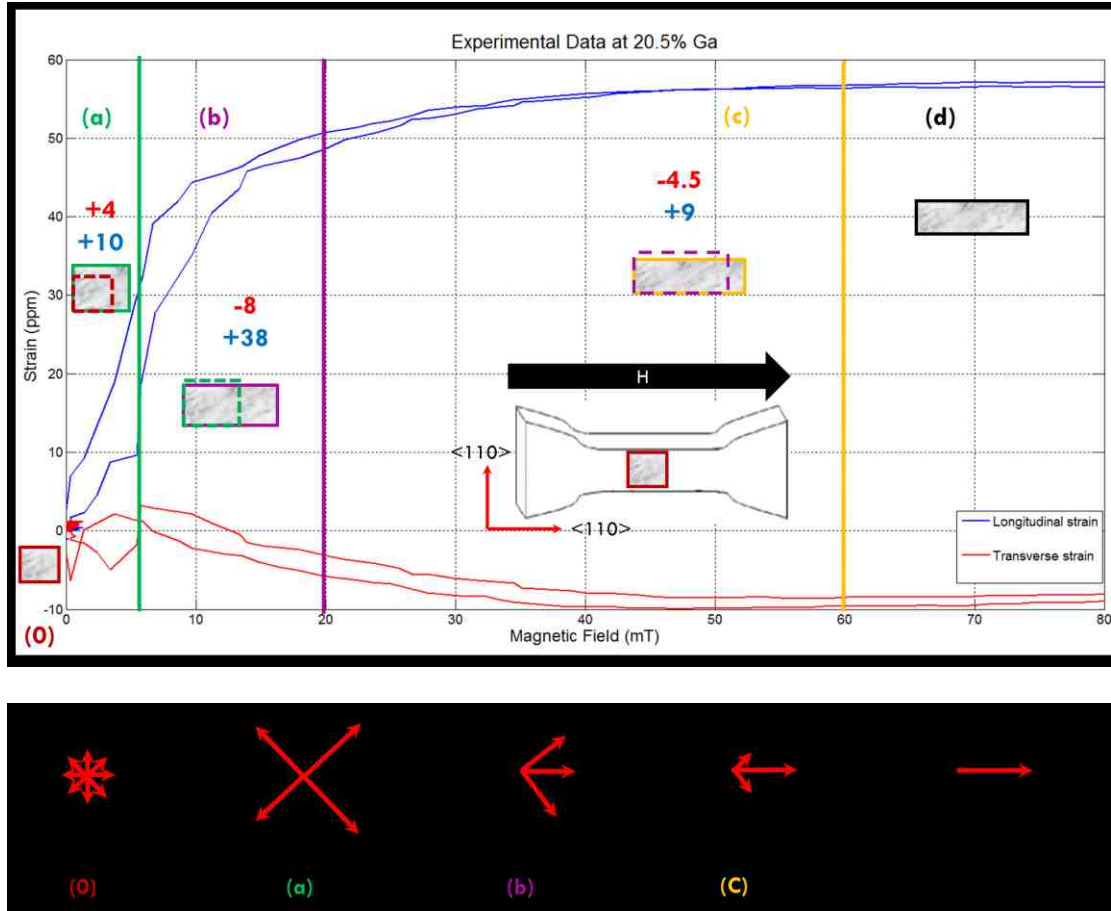
Figure 4.21: Schematic representation of a possible mechanism for magnetostriction along the <110> crystallographic direction for 20.5% Ga Galfenol on the basis of change in orientation of magnetic moments with applied magnetic fields. The grey boxes illustrate change in dimension of the sample (not to scale) at the end of each stage (0-d). The values next to the boxes indicate the change observed along the longitudinal (blue) and transverse (red) directions. Inset: Shows the orientation of the dog bone sample and the direction of applied magnetic field. Sketches (0)-(d) from left to right below graph depict relative strength of magnetization vectors along indicated crystallographic axes at field levels of 0, 5, 20 and 60 mT.

Magnetic domain imaging, discussed in Chapter 5 can be used to improve this

hypothesis.

Results from the 31 at%. Ga and 33 at%. Ga <110> oriented single crystal sample will be discussed in this section. At this composition, the alloy is in the ordered B_2 phase due to quenching from temperatures around 1000^oC **[60]**. At these compositions, the values of K_1 and K_2 are unavailable in literature and as discussed in the previous section, extrapolation of the available data introduces unknown errors. For this reason, this section includes only discussion of the experimental data and the saturation Poisson ratio values obtained from the energy model.

4.3.1: Results from the 31 at%. Ga <110> oriented specimen

4.3.1.1 : Experimental data for 31 % Ga content

The strain data obtained from the 31% Ga <110> {100} oriented single crystal Galfenol sample is shown in Fig. 4.22. The blue curve indicates the magnetostriction along the longitudinal [110] direction and the red curve indicates the magnetostriction along the transverse $[1\bar{1}0]$ direction when the field is applied along the longitudinal direction.
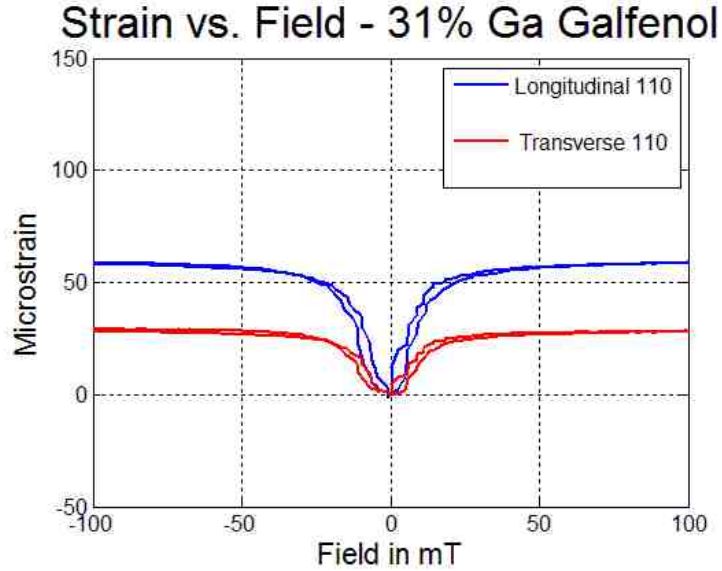
Figure 4.22: Strains along the longitudinal [110] and transverse [1$\bar{1}$0] directions for the 31% Ga single crystal Galfenol with applied field along the [110] direction at zero external stress.

The strain values along the transverse and longitudinal <110> directions at magnetic saturation and zero stress were found to be about 58µε and about 46µε respectively. This sample did not exhibit the unusual response of a dip in the longitudinal strain which was evident in the 15.8% Ga and 17.9% Ga specimens. There is a monotonic increase in both the transverse and the longitudinal strains and the sample reached magnetic saturation past ±60mT.

In this data set, the longitudinal strain was larger than the transverse strain along the auxetic <110> direction under applied magnetic fields and zero stress. The negative ratio of this transverse and longitudinal <110> strains is the magnetic field induced negative Poisson's ratio as shown in Fig. 4.23.
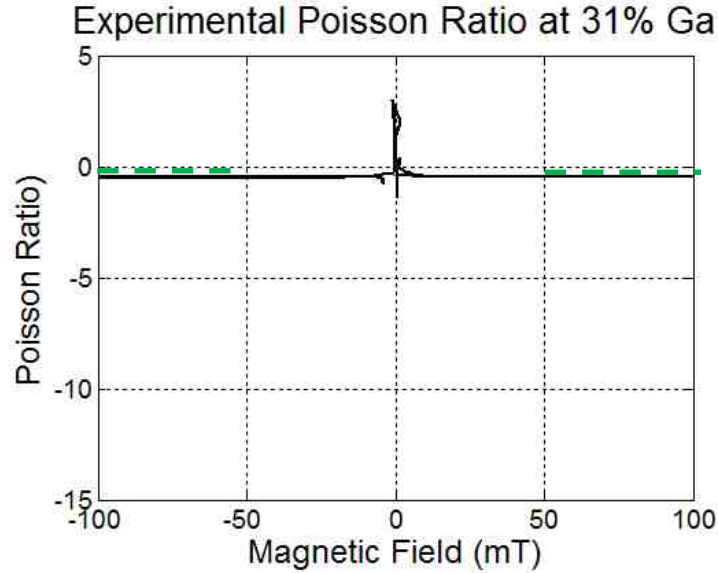
Figure 4.23: The variation of the Poisson's ratio with applied field in 31% Ga Galfenol at zero applied stress. At magnetic saturation (fields of greater than 50mT), the value of Poisson ratio obtained from the experiment is -0.49 ± 0.2 and the value from energy model (dashed line) is -0.31.

At very low fields, i.e. less than ~ ±5mT with strain values that are less than ~1με, the accuracy of the Poisson ratio values is uncertain due to a low a signal to noise ratio because strains of ±1με are at the resolution of the equipment. Above ~ ±5mT, the Poisson ratio decreases with increasing field to −0.49 ± 0.2 at magnetic saturation.

The Poisson's ratio was also computed by calculating the slope of the transverse strain vs. longitudinal strain plot as shown in Fig. 4.24. This method of computing the Poisson's ratio could be employed for this composition because there was monotonic increase in both longitudinal and transverse strains.

128
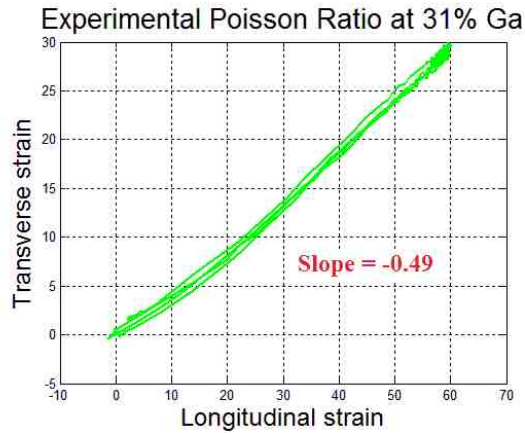
Figure 4.24: Poisson's ratio computed as the slope of the transverse strain vs. longitudinal strain plot.

4.3.1.1: Energy model at magnetic saturation for 31% Ga content

The value of Poisson's ratio at magnetic saturation predicted by the energy model is -0.31. This is discussed in Chapter 2 and the value of the analytical solution to the energy model at saturation is listed in Table 2.2. This value is shown with the dashed line in Fig. 4.23, where magnetic saturation of the sample is assumed for fields of greater than ~ ±60 mT. The modeled saturation value of -0.31 is larger than (less magneto-auxetic than) the average experimental value at magnetic saturation of -0.49 ± 0.2.

4.3.2: Results from the 33 at%. Ga <110> oriented specimen

4.3.2.1: Experimental data for 33% Ga content

The strain data obtained from the 33% Ga <110> {100} oriented single crystal Galfenol sample is shown in Fig. 4.25. The blue curve indicates the magnetostriction along the longitudinal [110] direction and the red curve indicates the magnetostriction

129

along the transverse [1$\overline{1}$0] direction when the field is applied along the longitudinal direction.
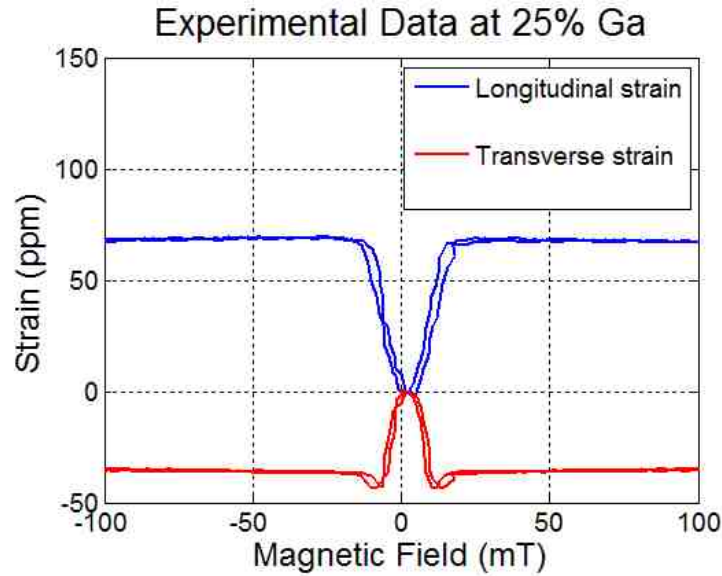

Figure 4.25: Strains along the longitudinal [110] and transverse [1$\overline{1}$0] directions for the 33% Ga single crystal Galfenol with applied field along the [110] direction at zero external stress.

The strain values along the transverse and longitudinal <110> directions at magnetic saturation and zero stress were found to be about $62\mu\varepsilon$ and about $23\mu\varepsilon$ respectively. There is a monotonic increase in both the transverse and the longitudinal strains and the sample reached magnetic saturation past ±40mT.

The longitudinal strain was larger than the transverse strain along the auxetic <110> direction under applied magnetic fields and zero stress in this sample as well. The negative ratio of this transverse and longitudinal <110> strains is the magnetic field induced negative Poisson's ratio as shown in Fig. 4.26.

130

Figure 4.26: The variation of the Poisson's ratio with applied field in 33% Ga
Galfenol at zero applied stress. At magnetic saturation (fields of greater than 40mT),
the value of Poisson ratio obtained from the experiment is -0.37 ± 0.15 and the value
from energy model (dashed line) is -0.23.

At very low fields, i.e. less than ~ ±5mT with strain values that are less than

~1με, the accuracy of the Poisson ratio values is uncertain due to a low a signal to

noise ratio because strains of ±1με are at the resolution of the equipment. Above ~

±5mT, the Poisson ratio decreases with increasing field –0.37 ± 0.15 at magnetic

saturation.

The Poisson's ratio was also computed by calculating the slope of the

transverse strain vs. longitudinal strain plot as shown in Fig. 4.27. This method of

computing the Poisson's ratio could be employed for this composition because there

was monotonic increase in both longitudinal and transverse strains.

131
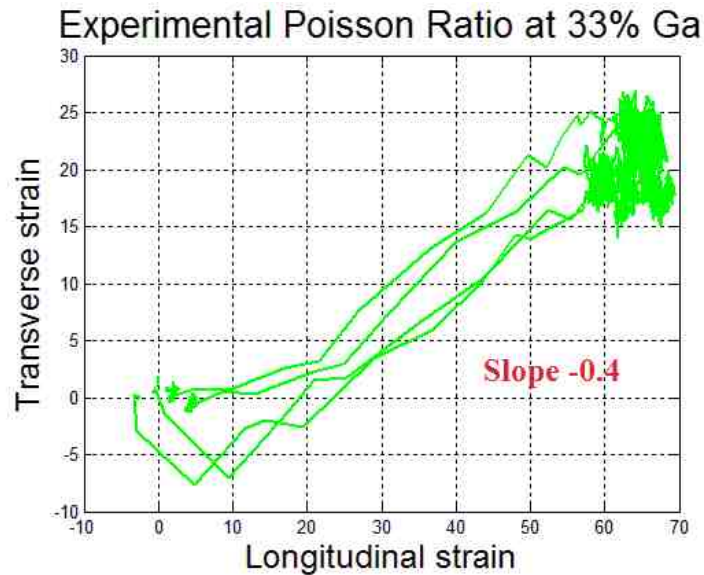
Figure 4.27: Poisson's ratio computed as the slope of the transverse strain vs. longitudinal strain plot.

4.3.2.1: Energy model at magnetic saturation for 33% Ga content

The value of Poisson's ratio at magnetic saturation predicted by the energy model is -0.23. This is discussed in Chapter 2 and the value of the analytical solution to the energy model at saturation is listed in Table 2.2. This value is shown with the dashed line in Fig. 4.26, where magnetic saturation of the sample is assumed for fields of greater than ~ ±40 mT. The modeled saturation value of -0.23 is in fair accordance with the average experimental value at magnetic saturation of -0.37 ± 0.15.

4.3.3: Proposed mechanism for the magneto-auxetic behavior in 31 at%. Ga and 33 at%. Ga Galfenol samples

This section presents a possible mechanism to explain the strains observed in the 31% Ga sample. The same mechanism can be used to explain the reason behind the strain response in the 33% Ga sample.

In samples of Galfenol between 31% and 33% Ga, the extent of anisotropy crystal is not available in literature. From Fig. 4.22 and Fig. 4.25, it is observed that there is monotonic increase in the longitudinal and transverse strains. The mechanism for this is represented by the schematic in Fig. 4.28. The top plot shows the variation of the longitudinal and transverse strains with positive magnetic fields and the variation of the dimensions of the sample. The cartoons below the plot show the proposed evolution of the orientation of the magnetic dipoles present in the material.

Initially, at zero magnetic fields, all the magnetic moments (denoted by red arrows that indicate their nominal direction; length of arrow indicates relative magnitude in the given direction, but lengths are not to scale) are randomly oriented such that the overall magnetization of the material is zero as shown in Fig. 4.28 (0). When an external magnetic field is applied, most of the magnetic dipoles rotate to orient themselves along the <110> axis in the direction of the applied magnetic field to attain the lowest energy state as shown in Fig. 4.28 (a), causing a large increase in both the transverse and the longitudinal strain up to a field of about 20mT.

133

Beyond 20mT, the energy from the applied magnetic field orients more magnetic dipoles along the <110> directions. As the applied magnetic field is increased, the sample reaches magnetic saturation (at ~ 60mT) with a small increase in the longitudinal strain. In this regime, the transverse strain remains almost unchanged.
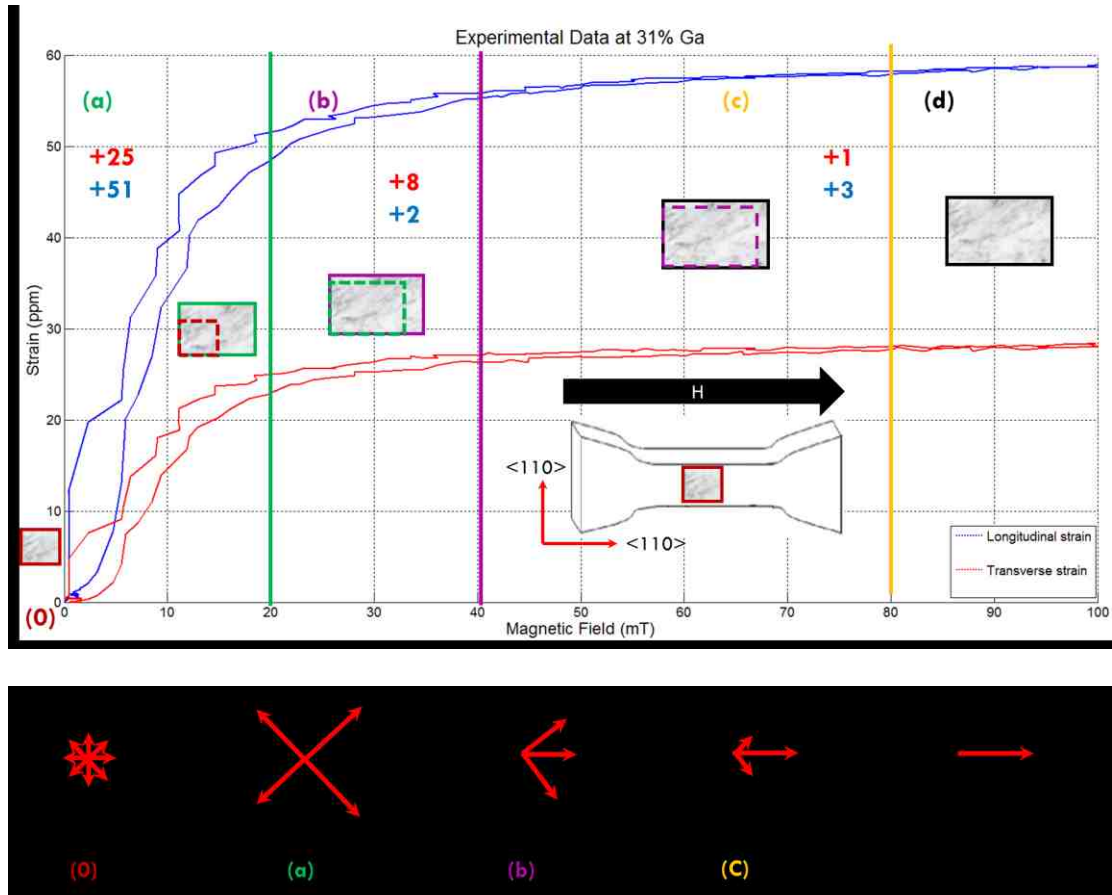
Figure 4.28: Schematic representation of a possible mechanism for magnetostriction along the <110> crystallographic direction for 31% Ga Galfenol on the basis of change in orientation of magnetic moments with applied magnetic fields. The grey boxes illustrate change in dimension of the sample (not to scale) at the end of each stage (0-d). The values next to the boxes indicate the change observed along the longitudinal (blue) and transverse (red) directions. Inset: Shows the orientation of the dog bone sample and the direction of applied magnetic field. Sketches (0)-(d) from

left to right below graph depict relative strength of magnetization vectors along indicated crystallographic axes at field levels of 0, 5, 20 and 60 mT.

Some studies[26, 42] claim that at high compositions of Ga (>25%), the <111> directions are the easy axes (since K_1<0). Since rotation of dipoles from the preferred <111> direction to <110> direction at magnetic saturation would involve only a reduction in the thickness, this could be used to explain the unusual transverse strain which does not decrease as the sample reached magnetic saturation along <110>. Such a response is also consistent with the Baughman's gas dynamic model depicted in Fig. 1.23 which was developed to predict an atomic level mechanism under applied tensile stresses. It hypothesized that the atoms on a (100) plane move farther apart from each other under a tensile stress is applied long the <110> of a BCC crystal. The atoms at the body center of the unit cells above and below the plane experiencing the tensile stress move closer to each other to conserve volume. It is expected that the atoms in samples at these compositions would show this behavior under applied magnetic fields and zero stresses. MOKE imaging can be used to help confirm this mechanism and understand the underlying processes behind the magneto-auxetic response at such high compositions.

4.4: Behavior of Galfenol at other compositions

This section will present simulation results from α-Fe and both experimental results and analytical and multiphysics simulations from the 12 at. % Ga <110>

oriented Galfenol. We did not have access to a single crystal a-Fe sample for obtaining experimental results, so our model results are compared to published data.

4.4.1: Results from <110> oriented α-Fe

4.4.1.1: Published work on magnetic field applied along <110> oriented α-Fe

One of the first modelling works on the effects of application of a magnetic field along the <110> direction were undertaken by E.W. Lee[103]. This study presented magnetostriction data from the model along the [110] at low magnetic fields (up to 3mT) for rectangular samples of varying lengths as shown in Fig 4.29. No published data was found that discusses the concurrent transverse strain, and no published data on the Poisson ratio response to an applied magnetic field was found.
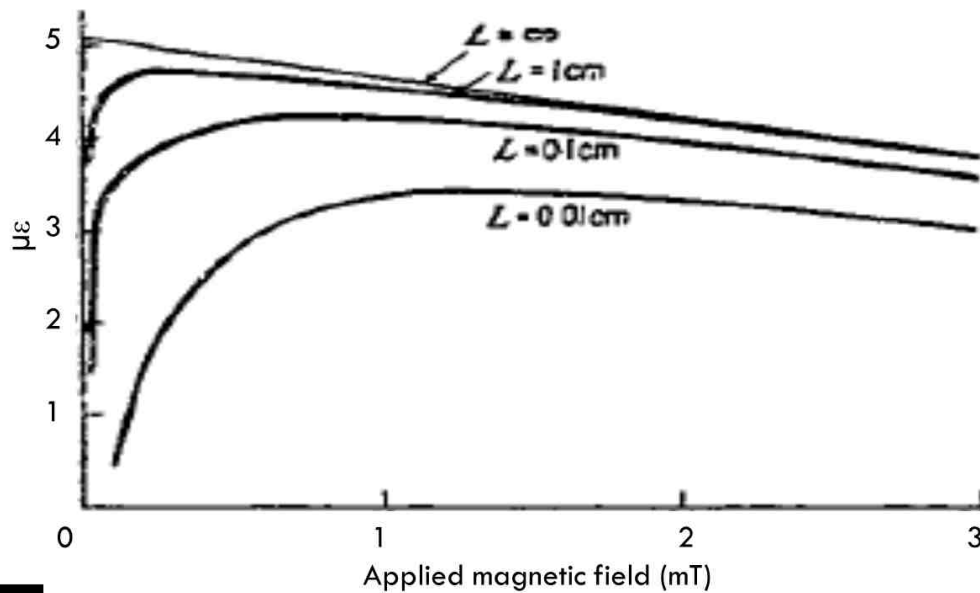
Figure 4.29: (a) λ-H curves for α-Fe (up to 30 Oe ~3mT). Taken from **[103]**.

4.4.1.2: Energy model at magnetic saturation for <110> oriented α-Fe

The value of Poisson's ratio predicted by the energy model is for magnetic saturation along the <110> direction of α-Fe, is +1.98. This is discussed in Chapter 2 and the value of the analytical solution to the energy model at saturation is listed in Table 2.2. This value is shown with the dashed line in Fig. 4.31 along with results from the FEM simulation discussed in the next section, where magnetic saturation of the sample is assumed for fields of greater than ~ ±50 mT.

4.4.1.3: Multi-physics model simulations for <110> oriented α-Fe

Multiphysics simulations were carried out for α-Fe using the formulation derived in Section 2.5. The concentration of Ga was assumed to be zero and the other parameters that were used for the simulations are listed in Table 2.3. Figure 4.30 shows the results from the simulations.
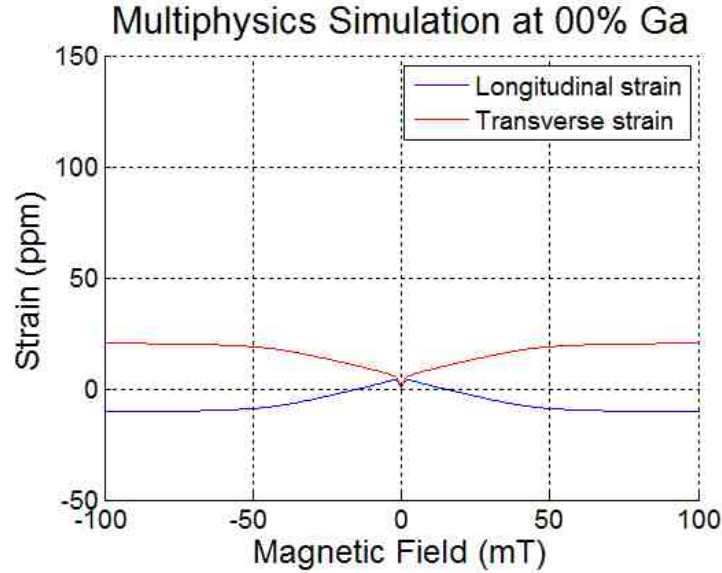
Figure 4.30: Strains along the longitudinal (blue) [110] and transverse (red) [1$\bar{1}$0] directions for α-Fe from the multiphysics simulations.

The values of the strain along the transverse and longitudinal <110> directions at magnetic saturation were 20.5µε and -10.3µε respectively. The variation of Poisson's ratio with applied magnetic field predicted by the simulations are presented in Fig. 4.22. The value of Poisson's ratio from the simulations at magnetic saturation was 1.99 and agreed with the value obtained from the mathematical model (~1.98). The low field longitudinal strain also matches the trend and order of magnitude for the <110> strain response measured by Lee, shown in Fig 4.27. Up to 14.5mT, the Poisson's ratio is negative. Past this field, the value of longitudinal strain becomes negative and a large jump in the value of Poisson's ratio.

138
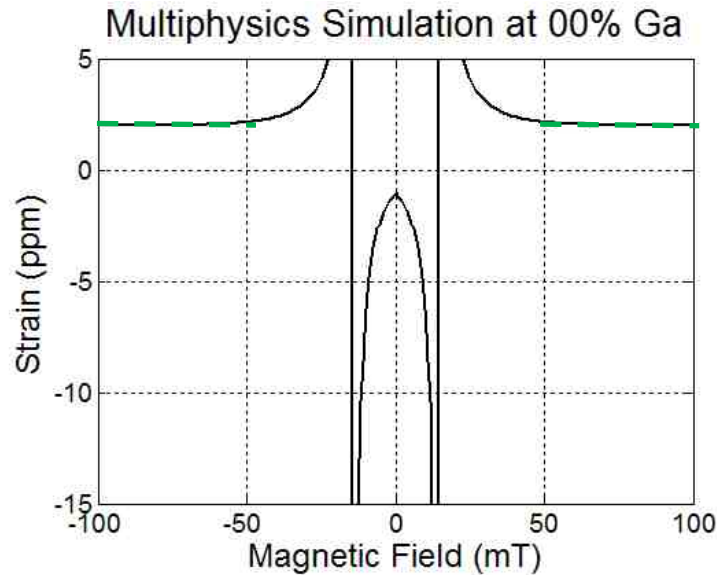
Figure 4.31: Variation of Poisson's ratio with applied magnetic fields along the <110> crystallographic direction at zero stress in α-Fe obtained from multiphysics simulations. At magnetic saturation (fields of greater than 50mT), the value of Poisson ratio obtained from the simulations was -1.99 which is in good agreement with the -1.98 obtained from the energy model (dashed line).

4.4.2: Results from the 12 at%. Ga <110> oriented specimen

Results from the 12% Ga <110> oriented single crystal sample will be discussed in this section. At this composition, the alloy there is a lot of variation in the location that the Ga atoms occupy since it is in the disordered A2 phase **[60]**. From Fig. 2.6, it can be inferred that [100] is the easy axis at this composition.

4.4.2.1 Variation of <110> strains with applied magnetic field

The magnetostriction data obtained from the 12% Ga <110> oriented single crystal Galfenol sample is shown in Fig. 4.32. The blue curve indicates the magnetostriction along the longitudinal [110] direction and the red curve indicates the

magnetostriction along the transverse [1$\overline{1}$0] direction when the field is applied along the longitudinal direction.
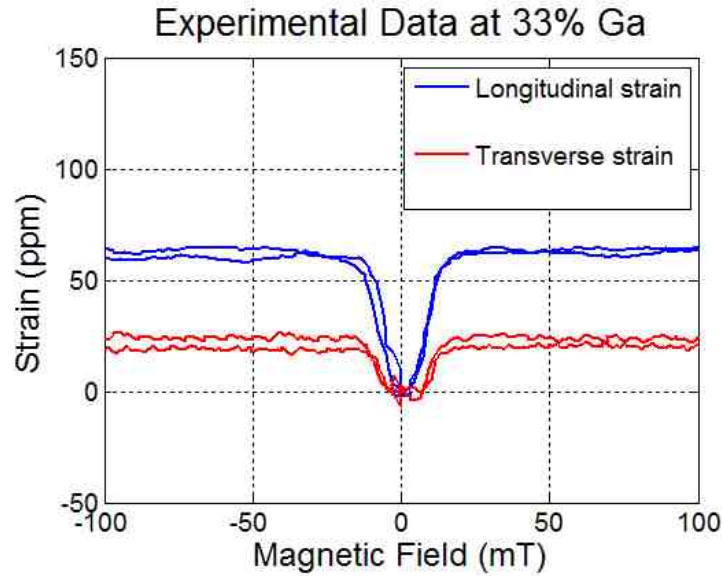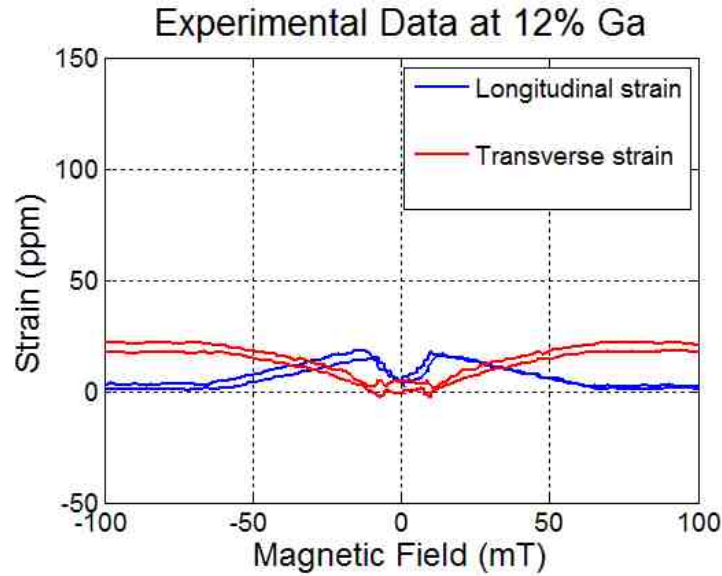

Figure 4.32: Magnetostriction along the longitudinal [110] (blue) and transverse [1$\overline{1}$0] (red) directions for the 12% Ga single crystal Galfenol with applied field along the [110] direction at zero external stress.

The magnetostriction values along the longitudinal and transverse <110> directions at magnetic saturation were found to be about 8με and about 21με respectively. The magnetostriction along the longitudinal direction increased initially up to about ± 20mT to reach a peak strain value of ~20με and later decreased as the sample attained magnetic saturation at about ± 80mT. The strain along the transverse direction increased monotonically as the sample reached saturation. In some of the data sets (Refer Appendix D), the value of longitudinal strain is very close to zero and this caused a sharp increase in the value of Poisson's ratio obtained. The signal to noise ratio is very small in the case of the 12% Ga Galfenol sample because of the

140

low magnitude of strains obtained under applied magnetic fields (maximum strains in either direction were less than 20 $\mu\varepsilon$. The negative ratio of this transverse and longitudinal <110> strains is the magnetic field induced negative Poisson's ratio as shown in Fig. 4.33.
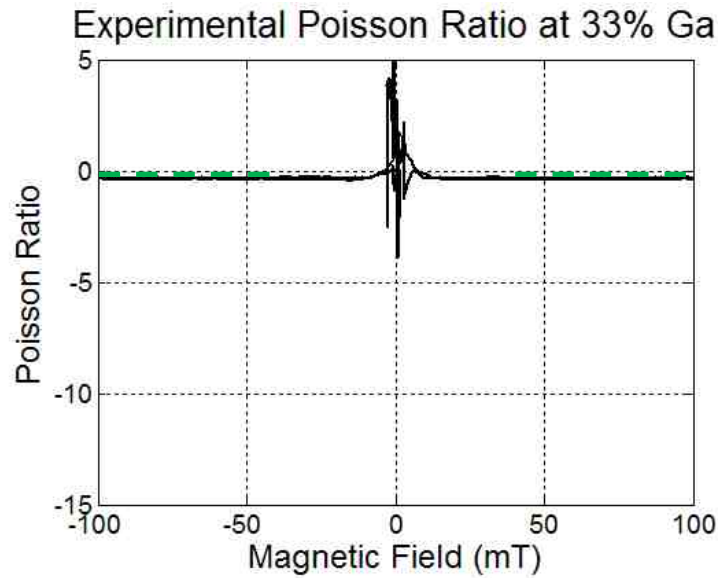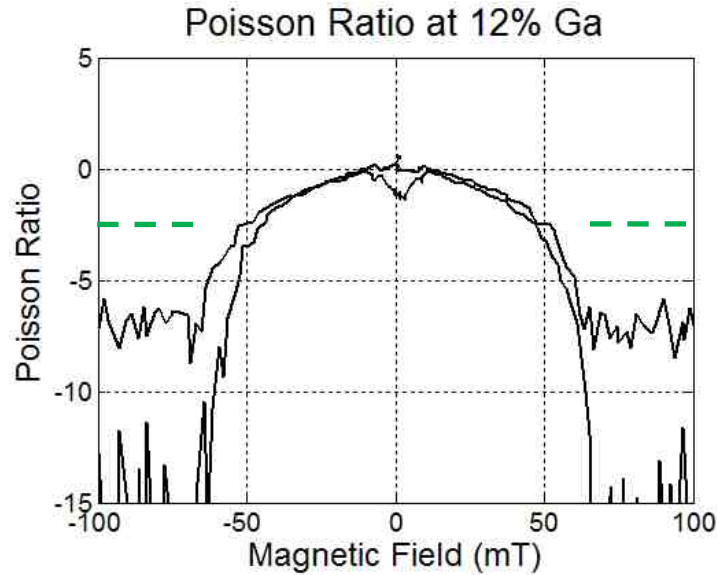

Figure 4.33: The variation of the Poisson's ratio with applied field in 12% Ga Galfenol at zero applied stress. At magnetic saturation (fields of greater than 70mT), the value of Poisson ratio obtained from the experiment is <-5 ± 2 and the value from energy model (dashed line) is -2.43.

The Poisson's ratio value decreases with applied magnetic fields and its value reaches values <-5 ± 2 in this data set because of the uncertainties that arise due to the values of longitudinal strain being relatively close to zero at magnetic fields >50mT. This is much lower than the value predicted by the analytical model shown in Table 2.1. The accuracy of the Poisson ratio values is uncertain due to a low a signal to noise ratio because strains of ±1$\mu\varepsilon$ are at the resolution of the equipment and there

was significant drift in the signals. Above ~ ±5mT, the Poisson ratio decreases with increasing field to <-5 ± 2 at magnetic saturation.

4.4.2.2 Energy model at magnetic saturation for 12% Ga content

The value of Poisson's ratio at magnetic saturation predicted by the energy model is -2.43. This is discussed in Chapter 2 and the value of the analytical solution to the energy model at saturation is listed in Table 2.2. This value is shown with the dashed line in Fig. 4.33, where magnetic saturation of the sample is assumed for fields of greater than ~ ±70 mT. The modeled saturation value of -2.43 is not as low as the average experimental values at magnetic saturation of ~ -3.9 ± 2.

4.4.2.3 Multi-physics model simulations for 12% Ga content

The result from the multiphysics simulation using the modified 'Armstrong model' derived in Section 2.5 is shown in Figure 4.34 (a) and this is compared with experimental data between -100mT and +100mT in (b).
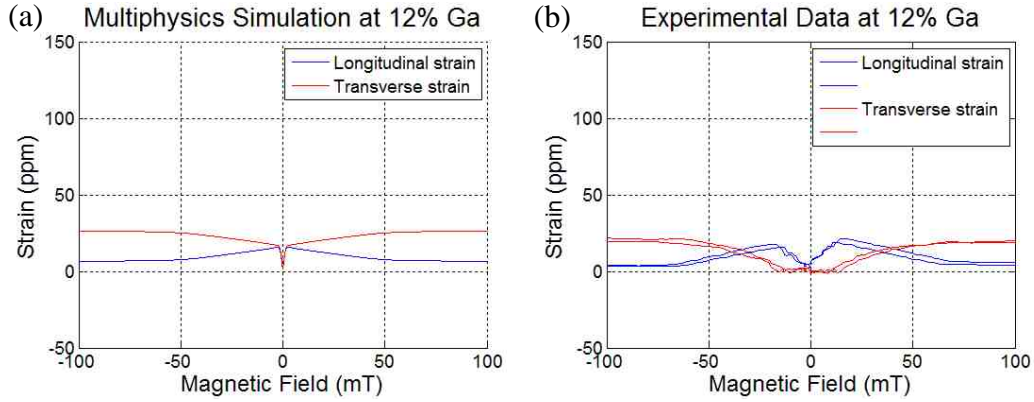
Figure 4.34: Strains along the longitudinal [110] and transverse [1̄10] directions for the 12% Ga Galfenol sample obtained from (a) multiphysics simulation and (b) from experiments.

The simulation predicts a strain of 7με and 26με along the longitudinal and transverse <110> directions respectively. The value of Poisson's ratio at magnetic saturation from the simulation was found to be -3.9 ± 2 which is lower than the values from the experiments (-2.5) and the mathematical model (-2.42). This is because of the really small values of longitudinal strain.

4.5: Conclusions

This section presents the conclusions that can be drawn from the results discussed in this chapter.

4.5.1 Summary of results

The values obtained from analytical modeling, multiphysics simulations and experiments are summarized in Table 4.1.

Table 4.1: Results for saturation 110 strain, saturation 1$\bar{1}$0 strains

% Ga	Expt Long (µε)	Expt Lat (µε)	Model 110 (µε)	Model 1-10 (µε)	Simu 110 (µε)	Simu 1-10 (µε)
0.00			-10.58	20.93	-10.58	20.93
3.00			-8.33	21.67	-8.33	21.67
5.00			-2.50	22.50	-2.50	22.50
8.00			7.50	32.50	7.50	32.50
10.00			12.33	34.33	12.33	34.33
12.00	7.00	21.00	17.50	42.50	17.50	42.50
15.77	46.00	70.00	48.33	73.33	48.33	73.33
17.90	62.00	80.00	66.08	70.58	66.08	70.58
20.50	57.00	-5.00	67.50	7.50	67.50	7.50
25.30	69.00	-34.00	76.67	-13.33	76.67	-13.33
31.00	58.00	28.60				
33.00	62.00	23.30				

Table 4.2 Results for Poisson's ratio values obtained from this study

% Ga	Expt PR	Model PR	Model PR Error (%)	PR Simu	PR Simu Error (%)
0.00		1.98		1.98	
3.00		2.60		2.60	
5.00		9.00		9.00	
8.00		-4.33		-4.33	
10.00		-2.78		-2.78	
12.00	-3.00	-2.43	19.05	-2.43	19.05
15.77	-1.52	-1.52	0.30	-1.52	3.44
17.90	-1.29	-1.07	17.22	-1.07	1.14
20.50	0.09	-0.11	226.7	-0.11	213.9
25.30	0.49	0.17	64.71	0.17	50.00
31.00	-0.49	-0.31	37.06	-0.31	21.33
33.00	-0.38				

A comparison of the experimental data with the Poisson ratio values predicted by the multiphysics simulations and the energy model is shown in Fig. 4.26. A best fit polynomial curve to the means of the experimental data is included in this graph.

A comparison of the experimental data with the values predicted by the multiphysics simulations and the analytical model is shown in Fig. 4.35.
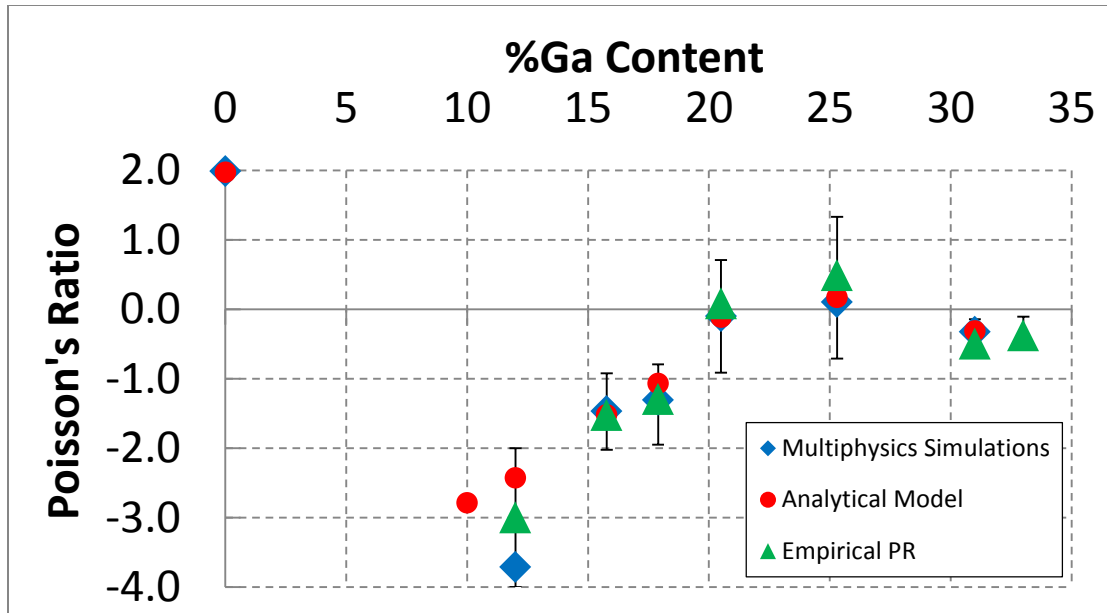
Figure 4.35: Variation of Poisson's ratio at magnetic saturation with Ga content in <110> oriented Galfenol samples obtained from analytical modeling, multiphysics simulations and experiments.

There is a decrease in the magneto-auxetic response as the Ga content in the alloy increases. This decreasing trend in auxetic effect with Ga content is opposite to the trend observed with applied tensile loads along the <110> directions, shown in Fig. 1.26. The reason behind this will be explored in the subsequent paragraphs.

4.5.2 Insights and implications of results

Although no prior studies had examined the Poisson ratio under magnetic fields and zero stress, one published study, the work by Yoo et al. **[93]**, presents data on the effect of simultaneous application of stress and DC magnetic fields to Galfenol samples of three compositions **[93]**. Kellogg **[15]** provides a polynomial fit as a

function of composition to experimental data for <110> Poisson ratio in Galfenol (refer Fig. 1.25). The best fit polynomial to results from the analytical model presented in this research, shown in Fig 2.2 is shown with the three data points from Yoo et al. for combined field and stress, and the polynomial fit to data under only stress from Kellogg et al. in Fig. 4.36. It was observed that the values of Poisson's ratio obtained from tensile testing under applied DC magnetic fields were lower than the values without a magnetic field at 18% Ga content in Galfenol. The values of Poisson's ratio presented in this study at magnetic saturation under applied magnetic fields and zero stress are lower than the values under tensile loads and DC magnetic fields as shown in Fig. 4.36. The values of Poisson ratio obtained by Yoo in samples at 29% Ga and 33% Ga were higher than the values predicted by the best fit polynomial presented by Kellogg but lower than the values obtained from the current work.
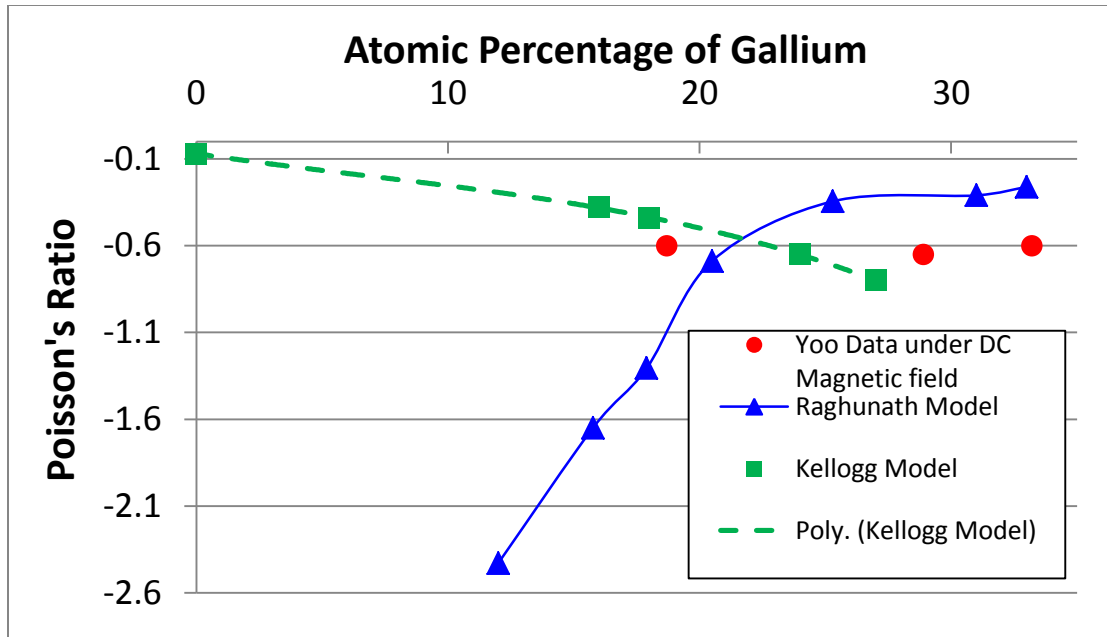
Figure 4.36: Comparison of Poisson's ratio values obtained from tensile loads and zero magnetic fields, tensile loads with a DC magnetic field and magnetic saturation and zero mechanical loads.

Figure 4.36 confirms the theory that the applied magnetic and the mechanical energies compete with each other in magneto-elastic systems and affect the magneto-elastic energy (arising from stretching of atomic bonds) and the magnetocrystalline energy (arising from changes in magnetization in each direction) in the material and the extent of interaction of these energies along each direction is influenced by the anisotropy present in the crystal lattice (defined by K_1 and K_2) as shown in Eq. (2.4-2.5).

It is also observed that in Galfenol samples at compositions <20% Ga, the value of Poisson's ratio is < -1. These samples have <100> easy axes due to the values of K_1 and K_2. A possible mechanism for the magneto-auxetic response has also

been presented for these samples from both a magnetic moment perspective and an atomic interaction perspective. Lattice softening which was attributed to be the reason for large negative Poisson's ratio in Galfenol under applied tensile loads **[12]** is restricted in the case of applied magnetic fields at zero stress because of a decrease in the magnetic anisotropy in the crystal lattice as shown in Fig. 4.37.

In samples of Galfenol at these compositions, most of the strain changes occur as a 'burst' in response to application of low fields. This burst region occurs before field is required to overcome the energy penalty associated with the anisotropy in the crystal lattice where there is instantaneous rotation of magnetic dipoles from the preferred <100> direction to the <110> direction along which magnetic field is applied.

In Galfenol samples at compositions greater than 20% Ga and lesser than 35% Ga, the value of Poisson's ratio is greater than -1. Since the values of transverse strains along the <110> direction under applied magnetic fields are very close to zero, at compositions between 20 and 25 at. % Ga, the values of Poisson's ratio are quite small in magnitude. There is a reduction in the transverse dimension in these samples because there is very little anisotropy in the crystal lattice, making the <110> direction along which magnetic field is applied just as easy as the <100> axis. This is similar to applying a field along the [100] direction where there is a reduction in the transverse [010]. The reason for this has already been explained in literature **[7, 14, 26, 57]**.

At higher compositions (31 and 33% Ga), it can be observed that there is a slight increase in the auxetic response. It was also observed that there was no reduction in the transverse strain and there was a monotonic increase in both <110> strains as the samples reached magnetic saturation. This behavior is similar to the gas dynamics model suggested by Baughman [78] for explaining auxetic response under applied stresses along <110> direction in cubic metals. Latice softening with the increase in Ga content likely is responsible for occurance of this magnetic response at compositions of 31 and 33% Ga but not for compositions of 20 and 25% Ga.

Rearranging the terms in Eq. 2.2 (a and b) which define the longitudinal and transverse strains along the <110> directions under applied magnetic fields and zero stress at magnetic saturation, we can obtain Eq. (4.1 a, b).

$$\lambda_{100} = 2(\varepsilon_{110} + \varepsilon_{1\bar{1}0})$$

$$\lambda_{111} = \frac{2}{3}(\varepsilon_{110} - \varepsilon_{1\bar{1}0}) \hspace{2cm} \text{(4.1 a, b)}$$

Using the experimental values of longitudinal and transverse <110> strains we can compute the values of λ_{100} and λ_{111} as shown in Table 4.3.

Table 4.3: Values of λ_{100} and λ_{111} calculated using average experimental values of longitudinal and transverse <110> strains.

% Ga	Expt ε_{110}	Expt $\varepsilon_{1\bar{1}0}$	λ_{100}	λ_{111}
0.00	-10	21	22	-20.67
12.00	7	21	56	-9.33
15.77	46	70	232	-16.00
17.90	62	80	284	-12.00
20.50	57	-5	104	41.33
25.30	69	-34	70	68.67
31.00	58	28.6	173	19.60
33.00	62	23.3	171	25.80

Figure 4.37 (a) shows the variation of λ_{100} and λ_{111} computed using Eq. (4.1 a, b) as a function of Ga content in the alloy and compares it with data available in literature (refer Fig. 1.15).
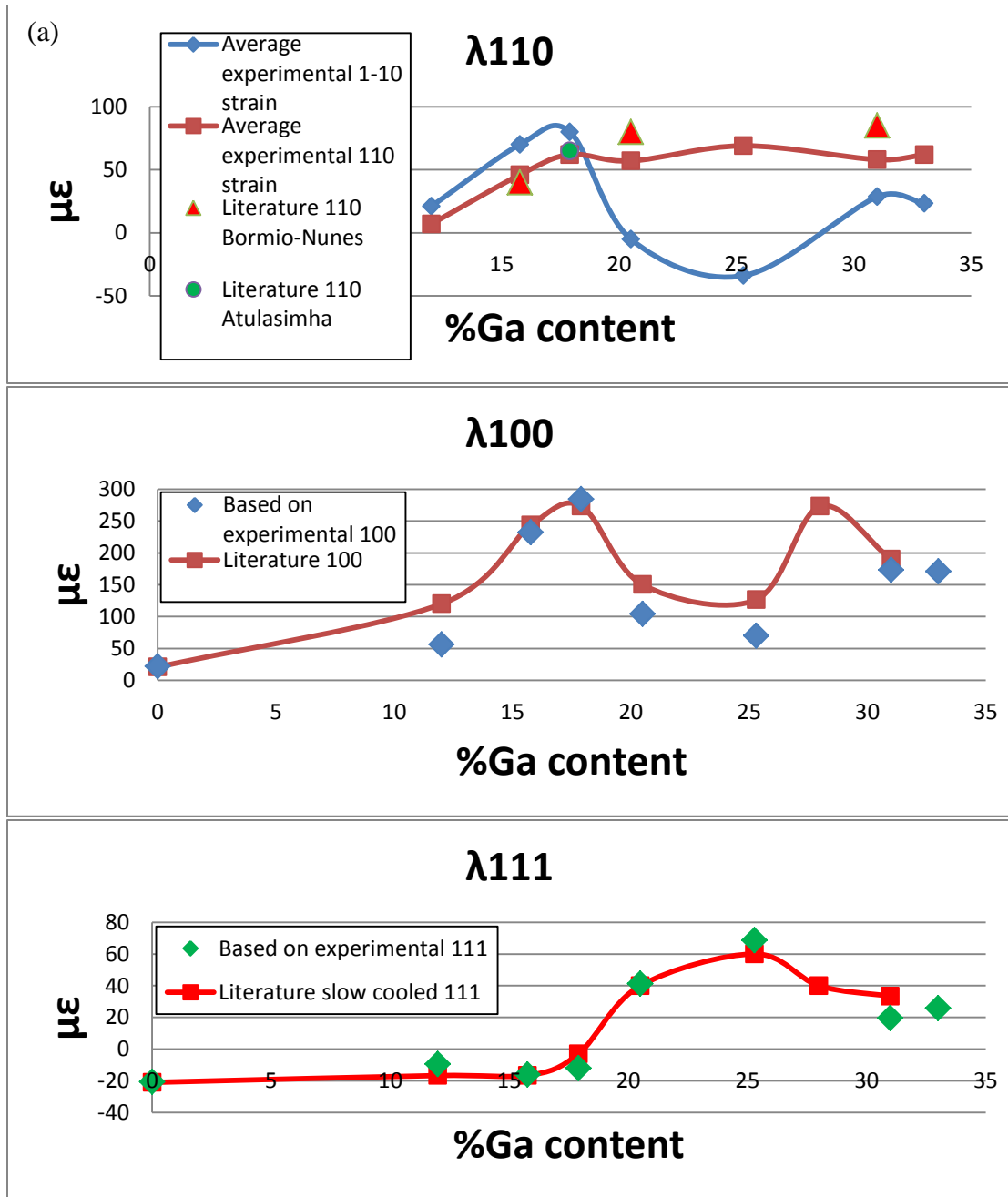
Figure 4.37: Shows the variation of (a) experimental λ_{110}, (b) λ_{100} and (c) λ_{111} as a function of Ga content in the alloy computed using average experimental values of longitudinal and transverse <110> strains under applied magnetic fields and zero stress and comparison with data available in literature [49].

This is one of the first studies to provide data points for λ_{111} in quenched Galfenol samples and this plot provides insights into the values of λ_{100} and λ_{111} at high compositions of Galfenol, past the second magnetostriction peak.

An overview of previously published data measuring Poisson's ratio along the <110> crystallographic direction in Galfenol was presented in Fig. 1.23 and results from the current work was presented in Fig. 4.35 which provide insights on the operation of the alloy under applied mechanical stresses and magnetic fields respectively.

4.6 Mechanical ramifications

The values of Poisson's ratio from applied magnetic fields at zero stress presented in this study are much lower than the values obtained from applied stresses at zero magnetic fields. Another important thing to note is that the values of strains obtained in this study are quite small. But the possibility of obtaining a magneto-auxetic response opens up avenues for novel applications such as coronary stents, corrective actuators (especially in optics), micro pumps etc.

Several mechanical properties such as shear resistance and indentation resistance are expected to improve as Poisson's ratio values approach -1. Equation 4.2 shows the variation of Poisson's ratio along the <110> direction as a function of the elastic stiffness constants in the cubic Fe-Ga crystal.

$$v(110,1\bar{1}0) = \frac{(C_{11}-C_{12})(C_{11}+2C_{12})-2C_{11}C_{44}}{(C_{11}-C_{12})(C_{11}+2C_{12})+2C_{11}C_{44}} \qquad \text{Eq. (4.2)}$$

Based on the Eq. (1.2), the Zener ratio (Z) defined as shown in Eq. (4.3). It is a measure of the anisotropy of the elastic moduli against diagonal and tetragonal distortions represented by c_{44} and $c' = (c_{11} - c_{12})/2$ respectively in cubic structures.

$$Z = \frac{C_{44}}{C'} = \frac{2C_{44}}{C_{11}-C_{12}} \qquad \text{Eq. (4.3)}$$

The bulk modulus (B) is defined as $B = (c_{11} + 2c_{12})/2$. Equation (4.2) can be rewritten in terms of the Zener ratio and the bulk modulus as shown in Eq. (4.4) based on [12].

$$v(110,1\bar{1}0) = \frac{1-Z\frac{C_{11}}{3B}}{1+Z\frac{C_{11}}{3B}} \qquad \text{Eq.(4.4)}$$

Hence, the anisotropic shear resistance is a function of the anisotropic Poisson's ratio as shown in Eq. (4.5).

$$Z \propto \frac{1-\vartheta_{110}}{1+\vartheta_{110}} \qquad \text{Eq. (4.5)}$$

Similarly, the anisotropic indentation resistance or hardness (H) is proportional to the Poisson's ratio as shown in Eq. (4.6) [70].

$$H \propto \left[\frac{1}{(1-\vartheta^2)}\right]^{\gamma} \qquad\qquad \text{Eq. (4.6)}$$

Figure 4.38 shows the variation of mechanical properties as a function of Poisson's ratio.
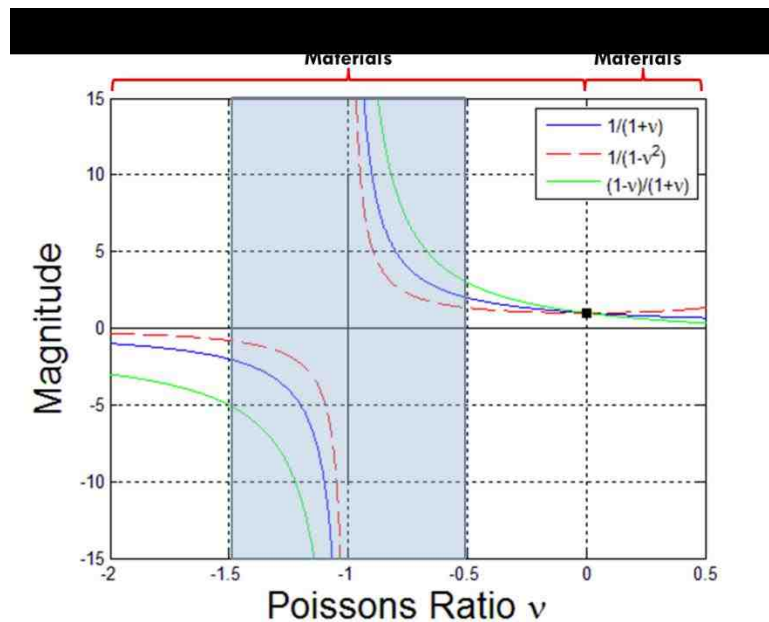
Figure 4.38: Change in magnitude of mechanical properties such as anisotropic shear resistance (green) and anisotropic indentation resistance (red) as a function of Poisson's ratio. . Blue shading is used to draw attention to the region of high impact on mechanical properties.

The possibility of obtaining large mechanical properties by application of magnetic fields and zero stresses enables magnetically tuning (non-contact!) of the mechanical properties of Galfenol which could prove very useful for applications such as additives to magneto rheological fluids to aid with shock absorption.

4.6.1 Indentation testing

To confirm an increase in the mechanical properties of materials as the Poisson's ratio reaches a value close to -1, Vicker's hardness testing was performed on the 17.8% Ga Galfenol sample which has a Poisson ratio ~-1.3 at magnetic saturation using the Hysitron Triboindenter shown in Fig. 4.39. The value of hardness and Young's modulus was collected with a nano indenter that could perform precise nano indents as well as high-resolution surface imaging. The value of penetration hardness was determined from the load-penetration depth curve obtained from this instrument and the effective Young's modulus was calculated from the slope of the unloading curve. The experiment was performed with and without the presence of a permanent magnet of strength 0.3T to compare the values obtained. It is expected that this strength of the magnet is sufficient to magnetically saturate the 1.3mm x 2.0 mm x 2.7mm Galfenol sample which was cut from the dogbones used in the experiments in Chapter 3. The sample is shown in Fig. 4.40.

Figure 4.39: Experimental setup of the nano-indenter experiment. Inset: Sample
mounted on epoxy offset (without permanent magnet).

Figure 4.40: Photo of a dogbone with the rectangular indentation sample cut using
wire electrical discharge machining.

The sample was offset from the magnetic stage using an epoxy mount stuck

using m-bond to the stage. The capacitive transducer in the nano-indenter instrument

had force and displacement measurement sensitivity of 30nN and 0.2nm respectively.

The in-situ scanning probe microscope (SPM) can perform high resolution surface imaging with a repulsive force of 2nN and has a displacement noise floor of <0.02nm. The surface imaging was achieved immediately after the indentations had been formed. In this study, the load applied by the nano indenter was very high, ~1000µN. The loading profile of the tests was a triangle as shown in Fig. 4.41 with a 10s load time and a 10s unload time. The typical testing rate was 100µN/s and the nano indentation tests were repeated at least 3 times under these conditions.
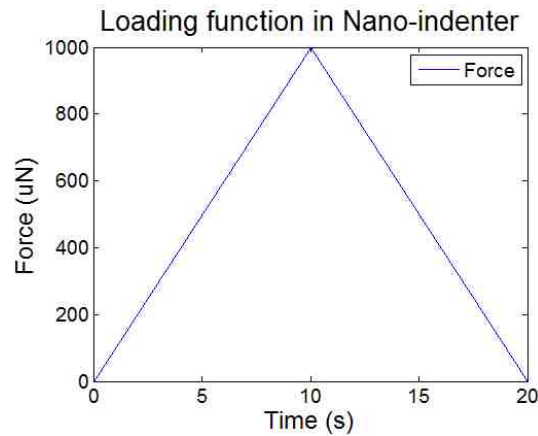
Figure 4.41: Load curve of the nano-indenter probe.

The indenter used was a triangular pyramid-shaped diamond with an edge angle of $\theta=115^o$ (Berkovich indenter). In such cases where the elastic constant of the sample is decided with non-axisymmetric indenters, the contact stiffness is ontained from the slope of the unloading curve. An effective Young's modulus (E*) is presumed by the expression shown in Eq. (4.7).

$$S = C_A E^* A_r^{1/2}$$ <div align="right">Eq. (4.7)</div>

$$\text{Where } \frac{1}{E^*} = \frac{1-v_I^2}{E_I} + \frac{1-v_S^2}{E_S}.$$

Here, $C_A = 2/\pi^{1/2}$, A_r is the projected real contact area between the indenter and the surface, E_I and v_I and E_S and v_S are the Young's modulus and Poisson's ratio for the indenter and sample respectively. The computation of these parameters is performed by the instrument using the indent information.

Figures 4.42 and 4.43 show a typical data set of the load-penetration depth curves obtained from the nano indenter without a permanent magnet and with a 0.3T permanent magnet in contact with the <110> oriented sample of Galfenol respectively.
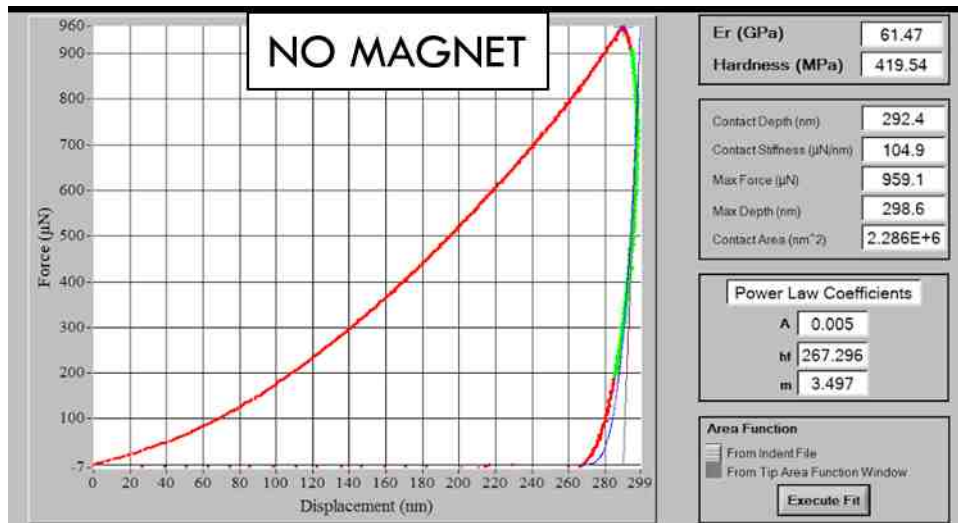
Figure 4.42: Typical load-penetration depth curve obtained from the nano-indenter in the 17.8% Ga <110> oriented Galfenol sample without a permanent magnet.
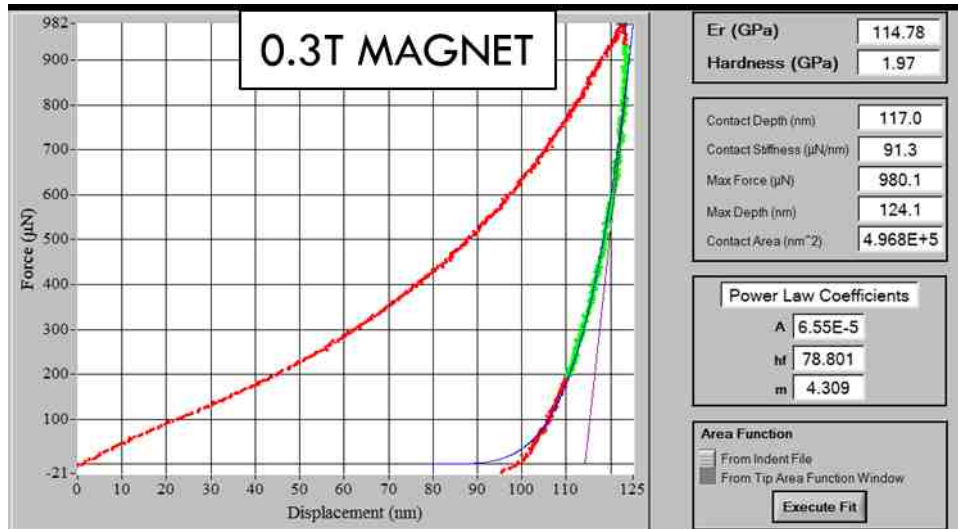
Figure 4.43: Typical load-penetration depth curve obtained from the nano-indenter in the 17.8% Ga <110> oriented Galfenol sample under a 0.3T permanent magnet.

The value of Vicker's hardness of iron available in literature is 608MPa **[104]**. Since Ga is softer than iron, the value of hardness in Galfenol is expected to be lower than that of Iron. The Vicker's hardness of Galfenol obtained from the nano-indenter without a permanent magnet was between 400MPa and 700MPa. The average value was ~550±150MPa. The effective Young's modulus was around 60±25GPa. Under the presence of the 0.3T bias magnet, the hardness value was between 0.95GPa and 4.2GPa. The average value was ~2.5±0.5GPa, about five times larger than the value obtained without magnetic field. The effective Young's modulus values were twice the values obtained without a magnetic field at aroung 120±40GPa.

The nano-indenter experiments confirmed an increase in the hardness value of the 17.8% Ga <110> oriented Galfenol sample under an applied magnetic field of

159

0.3T, where the sample is magnetically saturated and has a Poisson ratio value of -

1.3.

Chapter 5: Magnetic domain imaging

This chapter deals with imaging magnetic domains using Kerr microscopy. Evolution of magnetic domains under applied magnetic fields along the <110> crystallographic direction will be used to understand the magneto-auxetic effect in Galfenol from a magnetic domain perspective. For more imformation about MOKE imaging along other crystallograohic directions, please refer Appendix E.

5.1: Background of MOKE

John Kerr in the year 1877 devised a magneto-optical domain imaging method which was named after him **[25, 105]**. The rotation in the polarization of an incident plane-polarized light beam is defined by introducing an anti-symmetric tensor to the dielectric law ($\vec{D} = \varepsilon\vec{E}$) that connects the electrical vector of the light wave with the induced displacement vector by Eq. (5.1).

$$\vec{D} = \varepsilon(\vec{E} + iQ\vec{m} \times \vec{E}) \qquad\qquad (5.1)$$

$\vec{D}$ is the induced displacement vector, $\vec{E}$ is the electric field vector of the illuminating light, ε is the dielectric constant and Q is a complex material parameter which is proportional to the saturation magnetization and describes the strength of the Kerr effect. A simple representation of this is presented in Fig. 5.1.
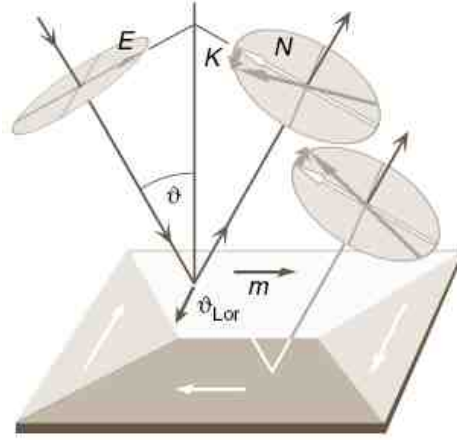
Figure 5.1: Illustration of the elementary magneto-optical interaction
for the longitudinal Kerr effect. The sample with in-plane magnetization is
illuminated using light that is polarized parallel to the plane of incidence **[25]**.

The gyroelectric nature of the Kerr effect is represented by the cross product
in Eq. (5.1) and its symmetry can be derived by the concept of Lorentz force ($\vec{m} \times \vec{E}$)
on the electrons which are set into vibration by the incident light. This force results in
the Lorentz movement v_{Lor} which is mutually perpendicular to the magnetization and
the electric field which when projected on the plane normal to the direction of
propagation of light yields $\vec{K}$, the magneto-optic light amplitude (also called Kerr
amplitude).

This Kerr amplitude is polarized perpendicular to the regular reflected light
amplitude, $\vec{N}$ which is in the same plane as that of the incident light beam. Upon
interference between $\vec{K}$ and $\vec{N}$ (the effective light amplitudes after they pass through
the analyzer), the polarization angle of the reflected light is rotated by the small angle
defined by Eq. (5.2).

$$\Phi_K = KN^{-1} \qquad\qquad (5.2)$$

For domains with opposite magnetization, the sign of this angle changes since the Lorentz force acts in the opposite direction. For contrast, the light reflected from one domain type is almost blocked by the analyzer which converts the rotation of polarization into a change in the intensity.

Based on the various geometries that result in being sensitive to different directions of magnetizations, there are different configurations of Kerr microscopes. An appropriate direction of the incident light is chosen to obtain a Lorentz displacement which can be measured as a Kerr rotation at the analyzer which is proportional to the magnetization component parallel to the reflected beam of light. This indicates that domains that are magnetized parallel to the sample surface require oblique incidence.

When the polarizer is set either parallel or orthogonal to the plane of incidence and $v \neq 0$, the configuration is called *longitudinal* Kerr effect and in such cases, the Kerr angle Φ_K is proportional to $\sin(v)$ and hence disappears for perpendicular incidence. Longitudinal Kerr effect with oblique incidence is used to image the domains [25] as shown in Fig. 5.2 (a). At perpendicular incidence, maximum rotation is exhibited by domains that are magnetized perpendicular to the sample surface. This configuration is called *polar* Kerr effect and $v = 0$. The in-plane magnetic domains do

not cause any Kerr amplitude. A schematic of polar Kerr effect is shown in Fig. 5.2

(b). In *transverse* Kerr effect, the in-plane magnetization is perpendicular to the plane

of incidence as shown in Fig. 5.2 (c). If the polarization of the incident light is at 45°

to the plane of incidence, then the component perpendicular to the plane of incidence

is not affected but the parallel component is modulated in its amplitude upon

reflection. By superposition, this results in the rotation of the polarization leading to

the in-plane magnetization sensitivity.
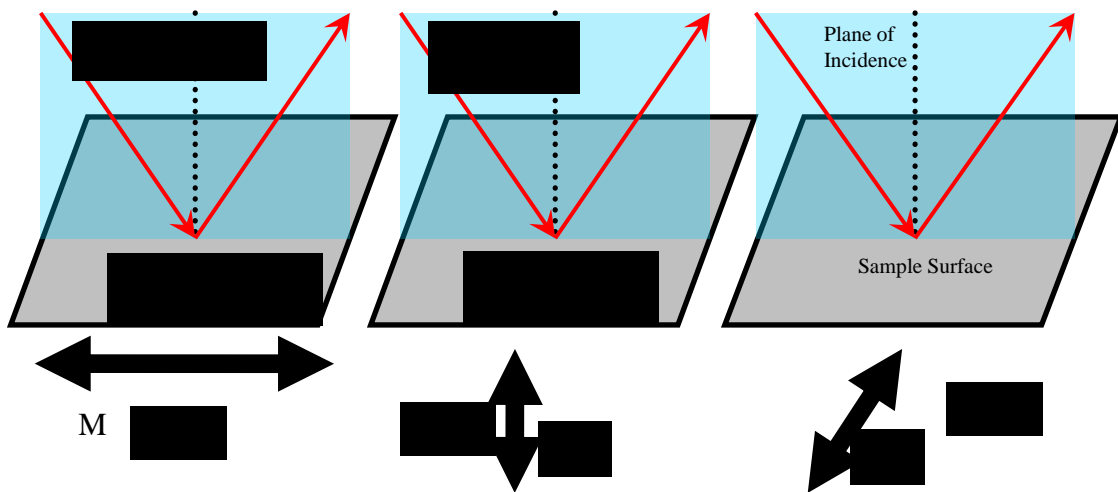
Figure 5.2: (a) Longitudinal MOKE geometry, (b) Polar MOKE geometry and (c) Transverse MOKE geometry.

5.1.1: Wide-field Kerr microscopy setup

This is by far the most versatile domain visualization technique due to innate

advantages like real-time imaging and high contrast as explained in Fig. 5.3. Figure

5.4 shows the wide-field Kerr microscope assembled by Evico Magnetics GmbH.

Optical illumination is used and the microscope has a field of view from several *mm*

down to a few μm upon using objective lenses from $5\times$ to $100\times$.
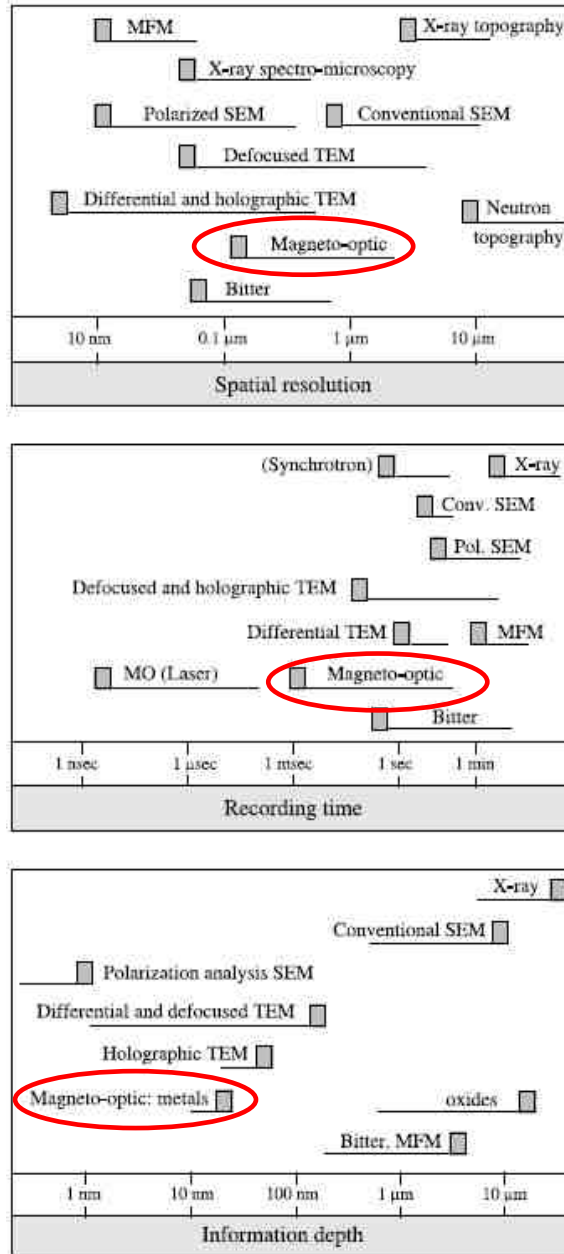
Figure 5.3: Comparison of the various observation techniques. Taken from [25].
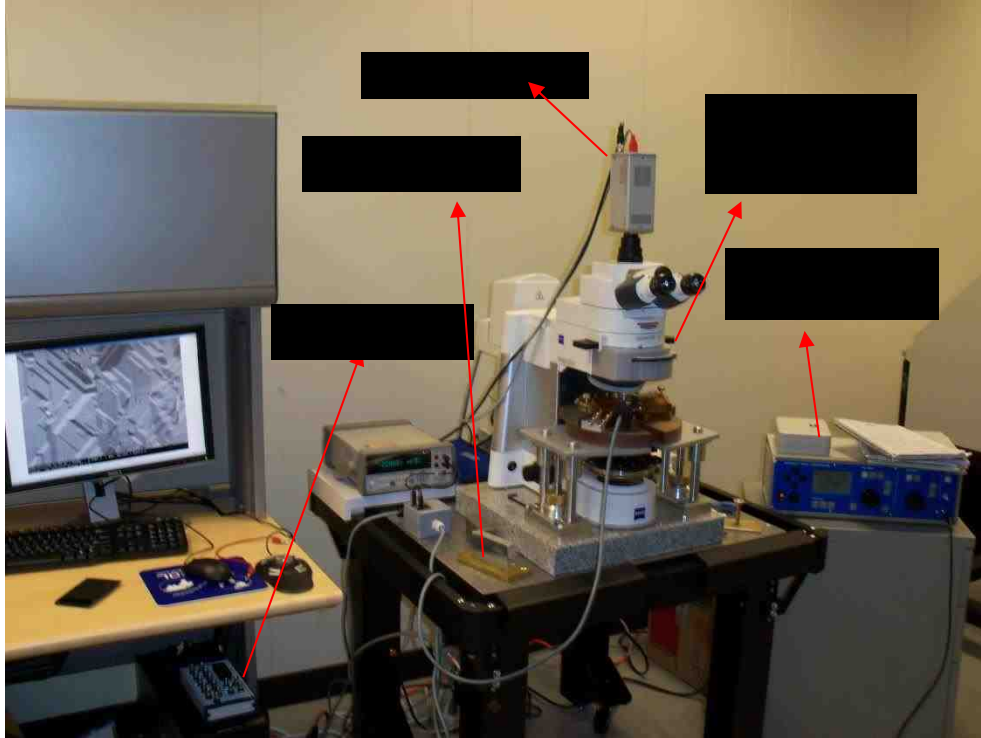
Figure 5.4: Magneto-Optic Kerr microscopy setup.

Magnetic coils capable of applying in-plane magnetic fields of up to 1T on the sample and a digital CCD camera are also incorporated in to the microscope setup.

The image obtained from such a setup contains both magnetic and topographic information. Since Kerr effect is weak, the topographic image dominates an unprocessed image. The magnetic contrast can be enhanced by removing the topographic information from the image. To do so, a domain free image containing only the topographic information is subtracted from the unprocessed image. This is shown in Fig. 5.5. The background image is obtained either at saturation of the sample or by applying an alternating field on the sample and taking an average over a considerable period.
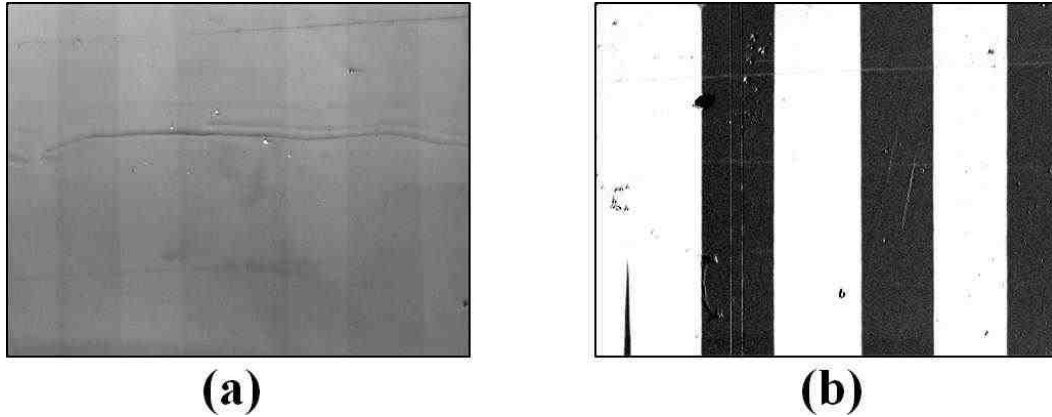
Figure 5.5: Enhancing the contrast by subtracting the background. From [26].

5.1.2: Expected domain patterns in Fe-Ga

The equilibrium magnetic domains are formed to reduce the overall magnetostatic energy as explained in Chapter 2. Details of the domain patterns also depend on the sample shape (thin film or bulk), stress state and surface orientation in the case of bulk samples. If easy anisotropy directions are available on the surface of the sample, simple domains are expected to be formed. Patterns are expected to become increasingly complex as more and more surface misorientations begin to form **[25]**.

In terms of magnetic microstructure, Fe-Ga alloys belong to the class of iron-like materials with a cubic crystallographic structure and a magnetocrystalline anisotropy which favors a <100> crystallographic direction. Hence, one expects domains similar to those that we see in iron samples which are of flux-closing character with regular 180° and 90° domain walls **[25, 26, 106]** as shown in Fig. 1.5.

167

The surface parallel easy <100> family of directions is expected to be preferred with the existence of closure domains.

Based on MFM domain images obtained, Bai *et al.* **[107]** suggested that the domain size in bulk $Fe_{100-x}Ga_x$ single crystals decreased with increasing concentrations of Ga. Typical domain widths for $x = 20$ were reported to be less than $0.4\,\mu m$ with domain lengths less than $2\,\mu m$. It was hypothesized that the increasing nonuniformity of the domains is due to the $D0_3$-like precipitates in the A_2 matrix. This observation was cited in support of theoretical predictions regarding magnetostriction enhancement in Fe–Ga alloys.

Chikazumi *et al.* **[4]** showed that it was possible to image real domains only with stringent surface finish requirements in the case of Fe-Si and suggested that the maze like patterns are only due to the stresses induced by mechanical polishing. This would hold good for any mechanically soft bulk specimens. It is important for the surface to be well polished and free of scratches and stress that might influence the domain structure.

Subsequently , Mudivarthi *et al.* **[26, 89]** determined that the complex maze like patterns observed by Bai *et al.* **[108]** are results of induced surface stresses and are not indicative of domain configurations in bulk samples.

5.1.3: Previous work on magnetic domain imaging to understand strain response in <100> oriented Galfenol samples

Mudivarthi [26] studied the magnetic domain evolution in Galfenol samples for applied magnetic fields and stresses along the <100> direction to explain the strain response obtained. Figure 5.6 shows one such example of magnetic domain imaging under applied magnetic fields along the <100> direction and measuring the longitudinal and transverse <100> strain simultaneously in a <100> oriented quenched 19% Ga Galfenol sample.
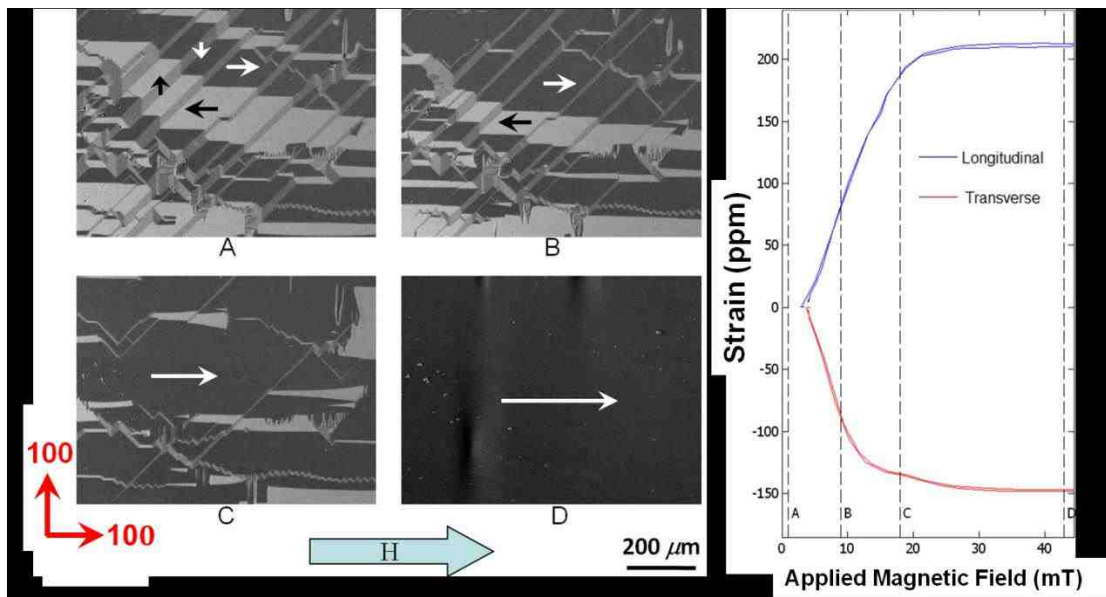
Figure 5.6: Magnetic domain imaging and measurement of strain in a 19% Ga <100> oriented Galfenol sample under applied magnetic field along the <100> direction. Taken from [26].

The current work will use this method to understand the strain response along the <110> auxetic directions in the 15.8% Ga Galfenol sample and explain the anomalous strain behavior observed.

The sample preparation required to optically image the magnetic domains in Galfenol will be elaborated in this section. MOKE imaging requires pristine surface conditions for the sake of good contrast. Since Galfenol is mechanically soft, mechanical polishing can be used to obtain good surface conditions for MOKE imaging.

5.2.1: Polishing issues

Conventional mechanical polishing was used to improve the surface conditions of the samples. Increasingly finer polishing media were used starting with 400grit SiC sheets, down to 1200grit size. Later, alumina suspension was used on the samples up to $0.3 \mu m$.

Mechanical polishing is known to induce a thick, glass-like or amorphous layer with large stress known as Beilby layer due to friction **[109]** . The stress induced anisotropy on this damaged surface overwhelms the stray-field energy resulting in fine out of plane magnetized maze domains which are not representative of the 'true' domains hidden underneath **[4]**. Hence, Silica gel was used on the samples to bring it down to $0.06 \mu m$. This was used to rid the amorphous layer formed from the previous stages of mechanical polishing and to ease out any surface stresses that might have been induced. Fig. 5.7 schematically describes the various stages of mechanical polishing. This aspect is dealt with in detail by Mudivarthi *et al.* **[26, 89]**. But they

had to employ etching in NiTal for about 4 minutes. The current uses the polishing

protocol used by Raghunath and Flatau **[110, 111]** which eliminates the necessity to

etch by employing longer stages of Si gel polishing.
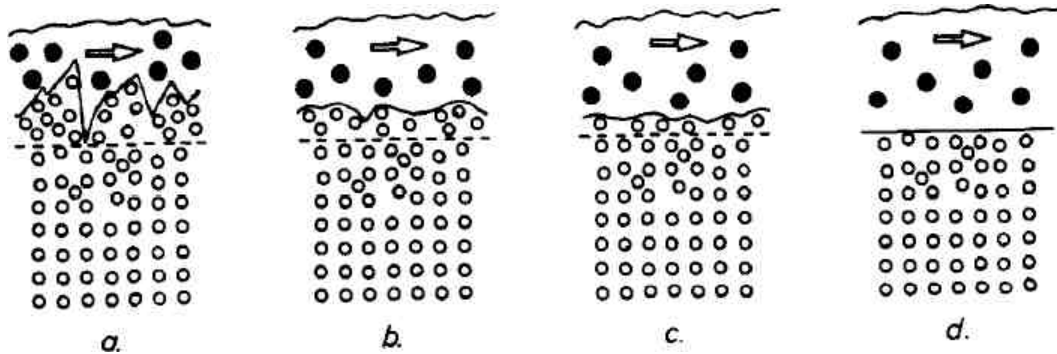
Figure 5.7: (a) Shows the highly stressed layer with fine irregular surface scratches during mechanical polishing using 1200grit. (b) Shows the reduction in the thickness of the highly stressed layer when polished using $1\,\mu m$ Alumina powder solution. (c) Shows further reduction in thickness and smoothening out of irregularities when polished using $0.3\,\mu m$ Alumina powder solution. (d) Finally when polished using $0.06\,\mu m$ Silica Gel, the stressed layer disappears and the true surface layer becomes visible enabling imaging of 'true' domains **[112]**.

Figure 5.8 shows the domain structure evolution of a 17% Ga slow cooled

Galfenol sample with silica gel polishing. It took almost one and a half hours to get

rid of the surface layer and to ease out the stresses that were introduced on the surface

due to polishing, thereby obtaining the surface finish required for obtaining the

domain images at remanence under the MOKE microscope.
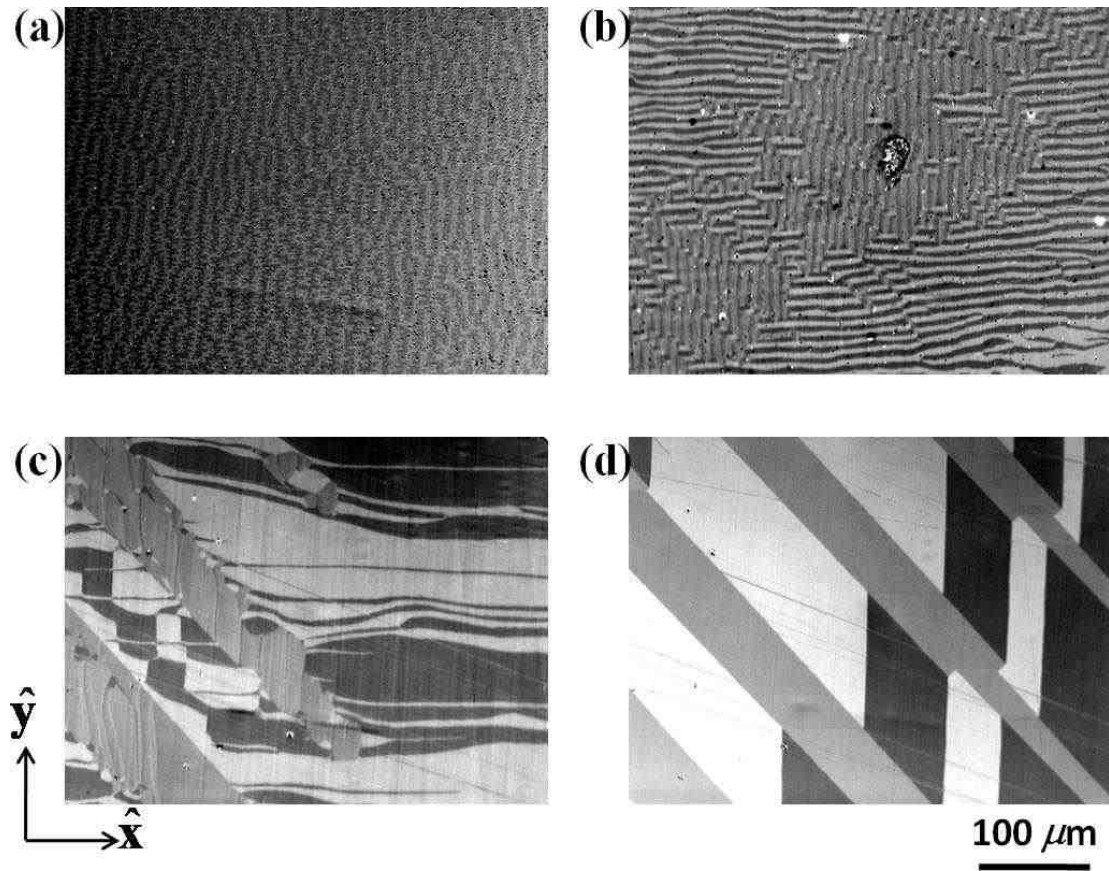
Figure 5.8: Domain structure of 17% Ga slow cooled sample of Galfenol as a function of silica gel polishing time (a) t = 0, (b) t = 20 min, (c) t = 50 min, (d) 75 min (taken from **[26]**).

For studying the auxetic response in Galfenol, the 15.8% Ga <110> oriented Galfenol sample discussed in Chapter 3 is polished using this protocol. A bi-directional strain gage rosette was installed on the back side of the sample. A photo of the sample is presented in Fig. 5.9.
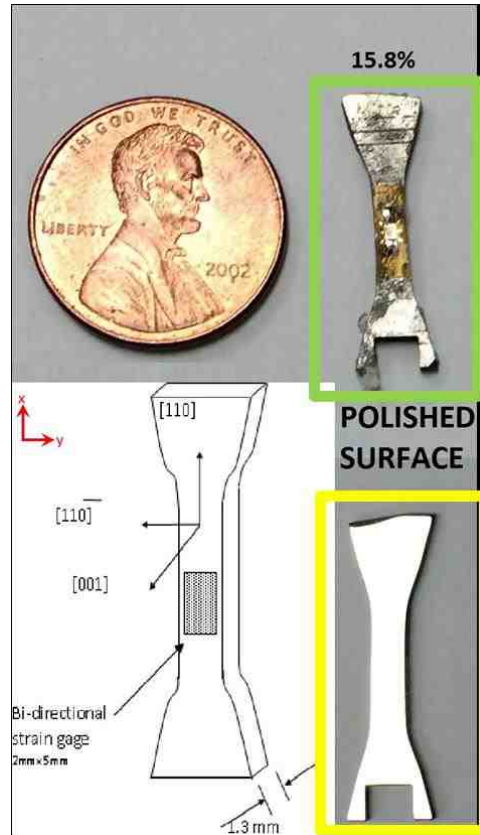
Figure 5.9: Photo of polished 15.8% Ga <110> oriented Galfenol sample (yellow border) and a bi-directional strain gage rosette installed on the back side (green border).

5.3: Experimental setup for Kerr microscopy

Once the samples were polished until desired surface quality was obtained, they were mounted on a stage between the pole pieces of the magnetic coil shown in Fig. 5.10 by means of double sided tape. The magnetic field was applied along the <110> by orienting the stage between the pole pieces (shown in the inset of Fig. 5.10).

173
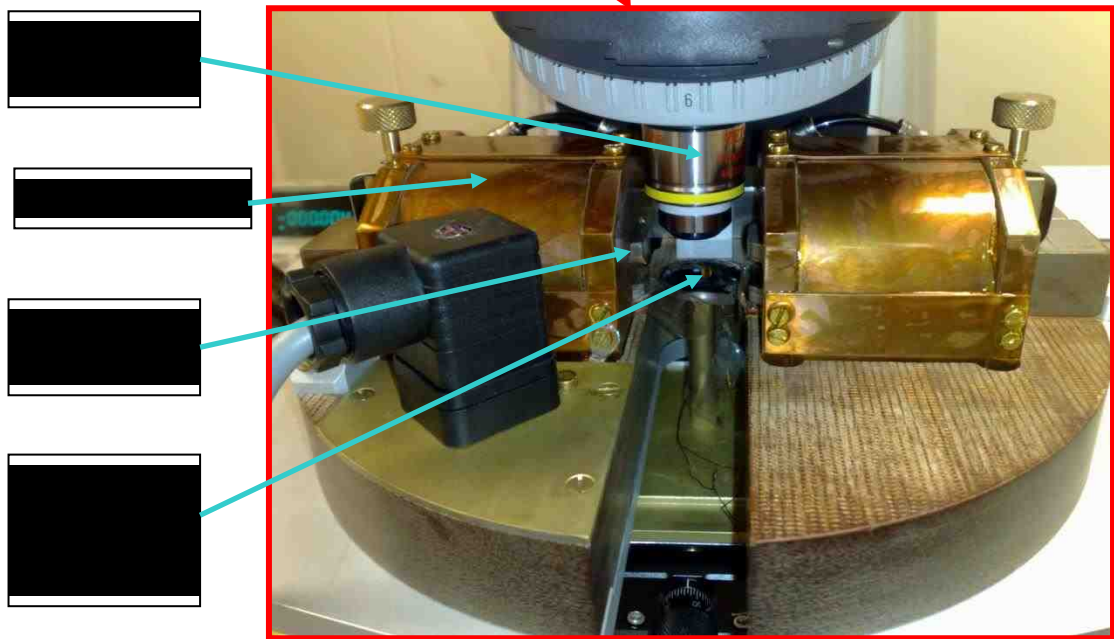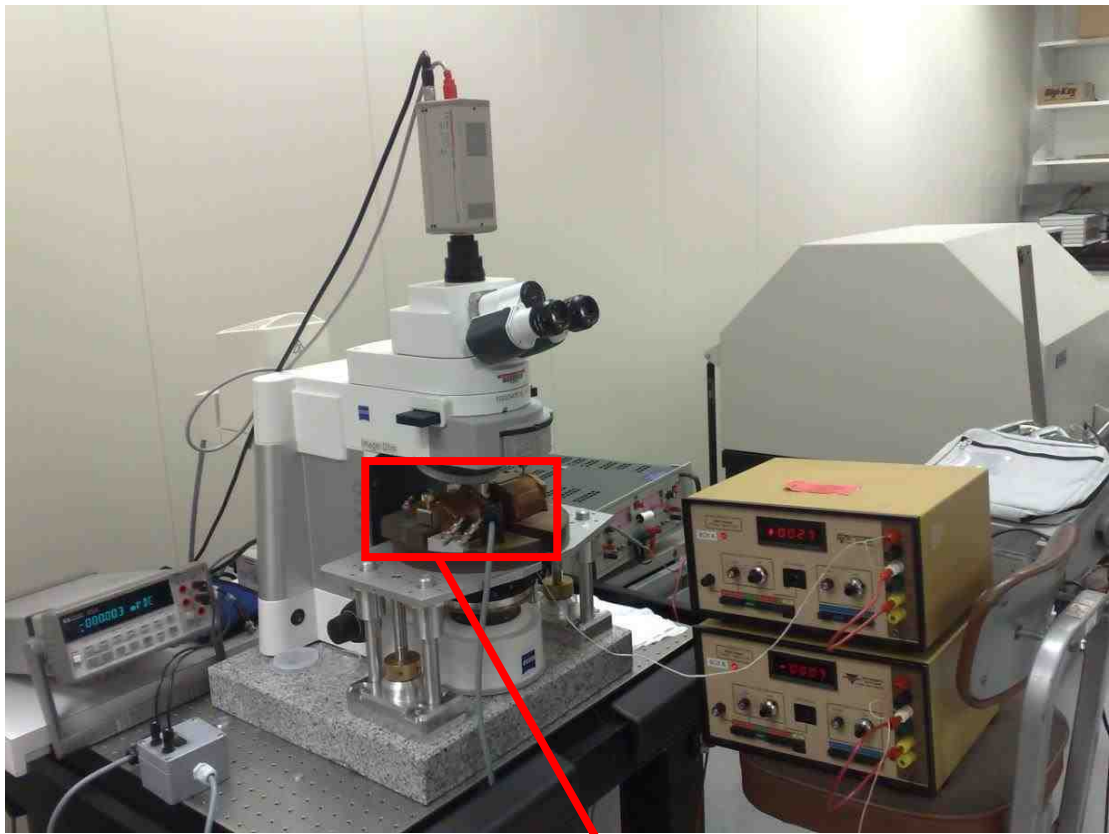
Figure 5.10: Auxeticity experiments done using the strain boxes. Inset: Specimen mounted on the stage under the MOKE microscope.

A coordinate system was chosen such that the x- and y-axes of the dog bone geometry correspond to <110> family of directions in the (100) plane of the sample as shown in Fig. 5.9. An electromagnet with a closed loop control system to maintain its magnetic field was used to apply magnetic field up to 100 mT along the x-axis of the samples.

A resistive T-rosette strain gauge manufactured by Vishay Micro Measurements (EA-06-030TU-120) was attached to the un polished face of the dog bone gauge region to measure strain along x- and y-directions (longitudinal and transverse <110> directions). This strain gage was connected to a strain indicator (Vishay 3800), which was hooked up to a PC-based NI LabVIEW data acquisition system through a National Instruments DAQ board. The magnetic field was ramped up from ∼ 0.1 mT (remnant field) to 100 mT and then down to ∼0.1 mT at a rate of ∼ ±10 mT/s. This field was measured using a LakeShore 425 Gauss meter. The LabVIEW program acted as a feedback loop and the field was controlled by using the computer. Simultaneously, the samples were observed under the MOKE microscope. A video was recorded as the magnetic field was applied and images were captured at critical magnetic fields where anomalous strain was observed.

To check for repeatability, the strain gage was changed for the second round of tests. Several locations on the polished surface were imaged using the MOKE microscope and the strains were recorded. A Matlab script was used to analyze the strain data from each test.

175

5.4: Results and discussions of magnetic domain evolution

This section will present the results from the magnetic domain imaging and also present a discussion on the results to explain the magneto-auxetic behavior exhibited in the 15.8% Ga Galfenol sample with special emphasis to understand the anomalous low field strain response exhibited.

Figure 5.11 shows the variation of strain in the in-plane longitudinal and transverse [110] directions for applied magnetic fields in 15.8 % Ga Galfenol sample. The sample exhibits an unusual response where the longitudinal strain initiallyincreases with applied field but then decreases over a small range of increasing applied field and then resumes an increase with increasing applied field.
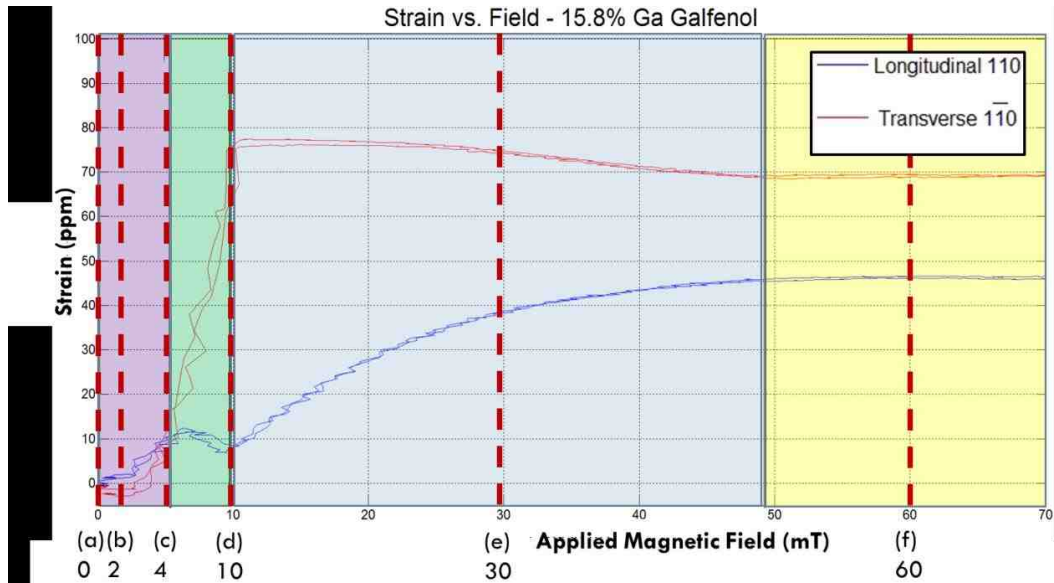
Figure 5.11: Variation of strain along the longitudinal and transverse <110> directions under applied magnetic fields in a <110> oriented 15.8% Ga sample. The red dashed lines define the magnetic field values at which the magnetic domain images were recorded using the MOKE microscope.

176

The strain has been split up into 4 distinct regimes that are denoted by purple, green, blue and yellow in Fig. 5.11. These regions are the regions that were the focus of interest in the discussion of Fig. 4.10. These regions are used to explain the correlation between measure strain and the magnetic domain images. In the first regime, both the longitudinal and the transverse <110> strains increase by about 11$\mu\varepsilon$ up to about 4mT. As the applied magnetic field increases in magnitude, the transverse strain increases in magnitude by about 65$\mu\varepsilon$ and there is a small decrease in the transverse strain of about 3$\mu\varepsilon$. This occurs between 4mT and 10mT, in the green region of Fig. 5.11.

Past 10mT, in the blue region of Fig. 5.11, there is a decrease in the transverse strain of about 7$\mu\varepsilon$ and an increase in the longitudinal strain of about 38$\mu\varepsilon$ and the sample reaches magnetic saturation at about 50mT. Past this field, in the yellow region of Fig. 5.11, the strains are saturated. The mechanism behind these strains have already been discussed in Chapter 4 (Section 4.1.3 and 4.1.4, regarding Figure 4.7 and 4.8) from an atomic and magnetic dipole perspective. Magnetic domain images were recorded at magnetic field magnitudes indicated by the red dashed lines in Fig. 5.11.

The magnetic domain evolution corresponding to the strains in Fig. 5.11 is shown in Fig. 5.12. These images were obtained after subtracting 'domain-free' reference images taken in an alternating magnetic field to enhance contrast.

177
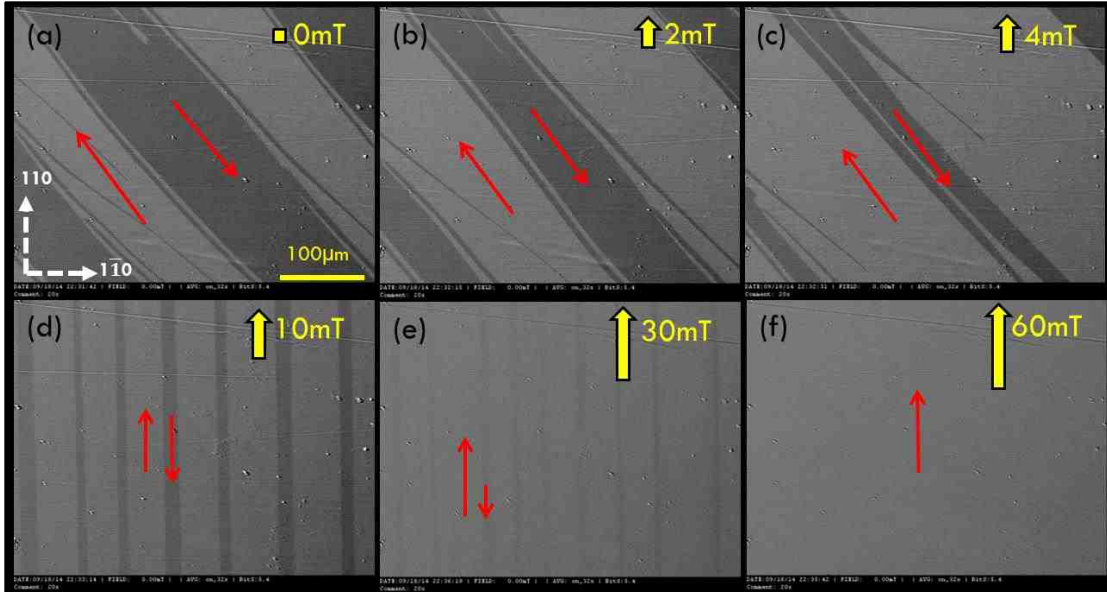
Figure 5.12: Evolution of magnetic domains in the 15.8% Ga Galfenol auxetic dogbone sample for applied magnetic fields along x- axis and zero stress. Images (a)-(f) are domains under fields of 0, 2, 4, 10, 30 and 60 mT respectively. Red arrows indicate the orientation of the magnetic domains.

There exists a superposition of a uniaxial anisotropy on to the cubic anisotropy at zero magnetic field in the sample as suggested by the orientation of the domains along the <100> easy axes present in the (100) plane. For small applied fields (up to ~2mT), there is reversible bulging of the pinned domain walls to increase the favorably oriented domains. The strain curves in the longitudinal and transverse directions increase in this region (between 0-(a) in Fig. 5.11).

At larger fields (up to ~4mT, the purple region of Fig. 5.11, and Fig. 5.12, (a-c)), the domain walls overcome the pinning and wall motion is observed, in which the domains oriented along the <100> direction aligned with the applied field grow. This

causes the small initial increase in both the longitudinal and the transverse <110> directions.

Then, as shown in the green region of Fig. 5.11 and in the transition between Fig 5.12 (c) and (d), for an applied field of ~4mT to ~10 mT the applied field causes the domains to become oriented along the [110] direction by instantaneous wall rotation. In this phase, a decrease in the longitudinal dimension and steep increase in the transverse dimension is observed in the sample. This occurs as a burst in strain as the domains rotate 90 degree from <100> to <110> orientations.

For further increases in the magnitude of the applied field, the blue and yellow regions of Fig. 5.11, the favorable <110> domain (oriented along the direction of applied field) grows by domain wall motion (Fig. 5.12 (d)-(e) until magnetic saturation is attained (Fig. 5.12 (f)). It is interesting to note that the Poisson ratio associated with the dimensional changes in just the yellow region of Fig. 5.11 has a positive value; i.e. it has a decrease in the dimension along the y- axis but an increase in the dimension along the x-axis. These changes in the longitudinal and transverse strains by domain wall motion in the yellow region of Fig. 5.11 are much smaller than the changes from domain rotation in the green region of Fig. 5.11, and this results in the sample having a negative value for the Poisson ratio at magnetic saturation.

Using the information from the MOKE images, the mechanism presented in Chapter 4, Fig. 4.10 (Section 4.1.3) to explain the strains observed can be revised as shown in Fig. 5.13. It is likely that in the middle of the burst region, so between (a)

and (b) of Fig. 5.13, for a field on ~6-8mT, the cartoon from Fig. 4.10 (c) depicts the transition from domain wall motion to domain wall rotation. This revised understanding of the domain mechanisms also applies to Fig. 4.21 in Section 4.2.3 and Fig. 4.28 in Section 4.3.3 of the previous chapter.
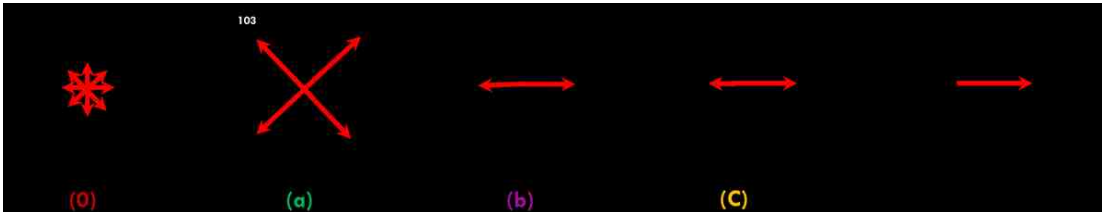
Figure 5.13: Revised magnetic dipole mechanism to explain strains observed in magneto-auxeticity in the 15.8%Ga <110> oriented single crystal Galfenol sample.

The MOKE images confirm magnetic dipole rotation to the <100> direction under low applied fields, prior to aligning with the applied field direction. The magnetic field at which the magnetic domain rotation that causes magneto-auxeticity occurs depends on the magnitude of the anisotropy present in the specimen. Larger the anisotropy, the more difficult it would be to rotate the domains away from the easy <100> axes and higher would be the magnetic field at which rotation takes place.

The evolution of magnetic domains and domain refinement in the closure domains in the 15.8% Ga Galfenol sample is discussed in Appendix F.

Chapter 6: Summary, conclusions and future work

The concluding chapter of this dissertation will focus on summarizing the results and contributions of this research. A section on recommendations for future work will also be presented.

6.1: Summary of research

Auxetic behavior has traditionally been defined as the negative Poisson ratio observed in materials under applied mechanical loads **[63, 67]**. Prior works on auxetic materials have addressed the origins of this negative Poisson's ratio observed under applied mechanical stresses with the intention of developing applications that exploit this trait **[9, 68-71, 75, 78, 80, 81, 83, 86, 113]**.

Since this phenomenon was discovered in Galfenol by Kellogg **[15]** along the <110> crystallographic direction while characterizing slip planes, researchers have confirmed the auxetic behavior in Galfenol under applied mechanical loads **[12, 93]**. The magnitude of the negative Poisson's ratio at various compositions of Ga has been recorded using protocols such as tensile testing and resonant ultrasound spectroscopy **[3, 15]**. Modelling using density functional theory has also been employed to derive its dependence on the materials stiffness properties **[12, 15]**. The modelling concluded that the Poisson's ratio values can be as low as -0.75 under applied tensile loads.

The magnetostrictive effect in Galfenol has already been widely studied and well established **[7, 49, 57, 102]**. As a consequence of inherent magneto-elastic coupling, there is a mechanical response to any changes induced to its magnetic state. The primary objective of this research was to explore the possibility of obtaining an auxetic response to the application of magnetic fields along the auxetic <110> directions and to discern the origin of this behavior. A good understanding of this phenomenon is important to enhance and/or exploit its features to build applications. Galfenol is also very attractive owing to its mechanical properties and load bearing capabilities which is absent in most synthetic auxetic materials.

Following the introduction in Chapter 1, an energy based analytical model of the magneto-mechanical response along the <110> was derived to compute the strains at magnetic saturation in Chapter 2 using the fundamental relations in magneto-elastic systems. This formulation could predict the values of Poisson ratio at magnetic saturation at different compositions of Ga in the alloy. This is followed by a multiphysics simulation to model the strains anticipated in both the longitudinal and transverse <110> directions as the magnitude of the magnetic field along the auxetic <110> direction increases from zero to saturation field at different Ga contents in the alloy. Finally, an overview of a finite element implementation of the modelling which could be used to predict the behavior of any geometry and dimensions, which can also be coupled with other parameters such as passive members to forecast the behavior of devices, is also presented.

Chapter 3 deals with the empirical procedure used to record the strain response to applied magnetic fields along the <110> crystallographic directions. The background of the Galfenol specimens used in this study is presented followed by a description of the equipment used in the experiments. The process for data reductions and issues relating to repeatability are also discussed.

Results from the analytical modelling, multiphysics simulations and the experiments are reported and a comparison is drawn between them in Chapter 4. A discussion of these results along with the description of a possible mechanism to explain the strains observed along the longitudinal and transverse <110> directions are presented at the different compositions of Galfenol. There is good correlation between the values obtained for the Poisson's ratio from analytical modeling, multiphysics simulations and experiments.

A decrease in the auxetic behavior under applied magnetic fields and zero stress is observed with an increase in the Ga content in the alloy. This decrease in auxeticity is predicted by both of the models presented in Chapter 2. This arises both as a result of a decrease in the magnetic anisotropy and increase in the magnetic energy in the magneto-elastic system which restricts lattice softening at high compositions due to increased magnetic interaction between the atoms constituting the lattice. The effect of this on the Poisson ratio is shown in Fig 2.3. This is opposite to the trends observed under applied loads at zero magnetic fields where there is an increase in the auxetic response with increasing Ga content in the alloy. For the stress

only, zero magnetic field case, the reduction in anisotropy and decrease in bond strengths (due to a metalloid- like structure) at high Ga content is shown in Fig. 2.4.

Figure 4.8 shows the variation of λ_{100} and λ_{111} with the composition of Galfenol computed using the experimental results obtained from this study. This could be used to understand the actual behavior of the alloy with increasing Ga content.

The strains obtained under applied magnetic fields in Galfenol are due to the interaction of the magnetic energy with the electron spins of the atoms that make up its lattice. The applied magnetic energy competes with the strength of the bonds between the atoms as the lattice is stretched by the applied magnetic fields due to interplay of the electron spins of the neighboring atoms. This causes an increase in the elastic energy due to stretching of the bonds and also an increase magnetic energy in the material because of the change in its magnetization.

The effect of the magnetic energy added to the magneto-elastic system is dependent on the anisotropy in the crystal. This determines the path of least resistance for energy to influence the atoms in the lattice. In the presence of an easy axis, the applied energy along any direction causes the magnetic moments to orient along this direction first. As more energy is added to the system, a critical point is reached, where the energy penalty for the energy to flow along the direction of application is paid. The extent of anisotropy in Galfenol at each composition determines this critical

magnetic field. Once equilibrium is attained between the atoms, any additional magnetic energy added to the system flows along the applied direction up to magnetic saturation.

In Galfenol samples up to 20% Ga, the value of Poisson's ratio at magnetic saturation is less than (more negative than) -1 since the transverse strain is larger than the longitudinal strain. This is explained as resulting from the presence of strong magnetic anisotropy that favors <100> easy axes in the (100) plane even when a magnetic field is applied along the <110> direction. As the magnetic dipoles rotate from the easy <100> axes to the applied <110> axes, there is a steep increase in the transverse strain accompanied by a small decrease in the longitudinal strain. As the applied magnetic field increase, these dipoles rotate to orient along the favorable <110> direction and attain saturation which causes a small drop in the transverse strain and a large increase in the longitudinal strain.

Past 20% Ga, the value of Poisson's ratio at magnetic saturation is larger than -1. In samples of compositions between 20% and 25% Ga, the anisotropy in the crystal is extremely small. Consequently, the anisotropy penalty is quite small and most of the applied energy interacts with the atoms in the lattice along the <110> direction causing an increase in the longitudinal strain. This is accompanied by very small strains in the transverse direction which are very close to zero (positive or negative).

185

At 31% and 33% Ga, the experimental data did not show rotation of the dipoles from a preferred <100> direction to the <110> applied magnetic field direction. Instead there is a monotonic increase in both the longitudinal and transverse strain as the magnetic field is increase from zero to magnetic saturation. This is consistent with the Baughman gas dynamics model of auxetic behavior in cubic metals.

The results from the multiphysics simulations were able to predict the trends in the strains and the value of strains at magnetic saturation to within 7% for composition of less than 20 at% Ga. But for compositions greater than 20 at % Ga, the error was about 60% owing to the small values of anisotropy constants in the 20.5% Ga and 25.3% Ga samples. The FEM simulations were not accurate in determining the strain values at which rotation of dipoles occurred in the 15.8% Ga and 17.9% Ga Galfenol samples. This could be due to the dependence of the performance of Galfenol on its thermal history. The parameters that are used as inputs to the simulations which greatly influence the results obtained are also dependent on the thermal history. Since these input values were chosen by interpolating and extrapolating the limited data points available in literature, their thermal histories didn't match those of the samples used in this study. This is believed to be the primary source of errors in the simulations. If λ_{100} and λ_{111} and K_1 and K_2 at each composition are measured instead of using values from literature, the errors from the multiphysics simulations are expected to drop significantly.

Chapter 5 focused on understanding the auxetic response in Galfenol from a magnetic domain perspective. A correlation between the magnetic domain images and the strain values recorded confirmed the mechanism presented in Chapter 4. The magnetic domains that were oriented along the easy <100> directions grew initially by domain wall motion once there was enough magnetic field to overcome the pinning of the domains. At a critical magnetic field, the 180° domain walls rotated to orient along the <110> direction. Additional magnetic field lead to the growth of favorable <110> magnetic domains as the sample attained magnetic saturation.

Thus, this study presented a systematic approach to understanding the magnetically induced negative Poisson's ratio in Galfenol from an atomic level perspective, meso scale micro magnetic domain perspective and macro scale magneto-elastic perspective at different Ga compositions.

6.2: Contributions of this research

- First research to observe and characterize the magnetically induced auxetic effect in Galfenol under zero applied mechanical stress.
- This work systematically quantifies the negative Poisson's ratio in a broad spectrum of Galfenol samples between 12 and 31 at. % Ga content.
- Data from samples >20% Ga can be used to yield more information about the second magnetostriction peak in Galfenol including properties such as anisotropy state in the alloy at high compositions.

- Formulation of an energy based analytical model that could predict the values of Poisson's ratio in Galfenol of different compositions along the <110> crystallographic direction at magnetic saturation by using values of λ_{100} and λ_{111} only.

- Development of non-linear multi-physics (magneto-elastic coupled) simulations that could predict the strains along the auxetic <110> directions under applied magnetic fields.

- The trends in Poisson's ratio at magnetic saturation with Ga content in Galfenol obtained from this work can be used to explain the Poisson's ratio values observed by Yoo [93] under tensile testing under DC magnetic fields.

- Presents an understanding of the origin of auxetic strain response under applied magnetic fields from an atomic perspective describing the influence of magnetic fields on the interaction of the electron spins of neighboring atoms in the crystal lattice which causes strains.

- Results from this study confirmed that the applied magnetic and the mechanical energies compete with each other in magneto-elastic systems and affect the strain energy (arising from stretching of atomic bonds) and the magnetocrystalline energy (arising from changes in magnetization) in the material.

- This work also elicits the influence of anisotropy in the crystal lattice in determining the extent of interaction between the magneto-crystalline, magneto-elastic, magnetic energies along each direction in the crystal lattice

and its effect on the Poisson's ratio at the different compositions of Galfenol both experimentally and using simulations.

- A mechanism for the correlating strains obtained from the experiments under applied magnetic fields to the rotation of magnetic dipoles in the material is also presented.

- This is also the first work to investigate the auxetic response in Galfenol from a magnetic domain perspective. A correlation between the evolution of the surface magnetic domains is used to explain the anomalous non-monotonic increase in strain with an increasing magnetic field in 12, 15 and 17 at% Ga Galfenol.

- A new polishing protocol for preparing specimens for Kerr microscopy which eliminated the need for etching was also developed.

6.3: Recommendations and future Work

While this work attempted to address most questions related to characterizing, understanding and modelling the auxetic behavior in Galfenol under applied magnetic fields and zero stresses, some issues merit further works to improve the explanations presented here. Future research will also lead to a more complete picture of the phenomenon of auxeticity in Galfenol and hence improve our understanding of the alloy, provide better predictive capabilities and lead to the development of applications that exploit this behavior.

189

The atomic level changes in dimensions which can be used to confirm the atomic level mechanism presented for understanding the origin of auxetic behavior in Galfenol can be confirmed using Lorentz TEM. A cartoon depicting this experiment where an electron beam is used to image the distance between the atoms in the lattice with and without a magnetic field is shown in Fig. 6.1. The atomic lattice shown in Fig. 6.1 is an exaggerated 2-D projection of the reduced sphere representation of the BCC crystal lattice image before and after the application of a magnetic field.
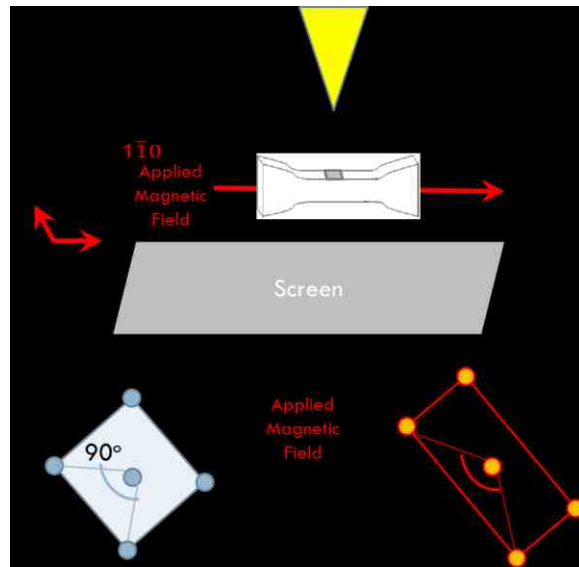
Figure 6.1: An overview of the Lorentz TEM experiment to measure changes in the dimensions of the lattice.

The model presented in Section 4.4 predicts a large improvement in Galfenol's shear strength and hardness as the Poisson's ratio value approaches -1.

This can be verified by shear testing samples of Galfenol with and without a magnetic field. Additional indentation tests on the Galfneol sample along the <110>

direction, such as those presented in Section 4.6, will provide more information about increases in the material hardness.

Density functional theory (DFT) is a computational quantum mechanical modelling method used in physics, chemistry and materials science to investigate the electronic structure (principally the ground state) of many-body systems, in particular atoms, molecules, and the condensed phases. Modelling Galfenol under applied magnetic fields and zero mechanical stresses can be employed to model the auxetic behavior to further understand inter atomic interactions that are attributed to be the origin of the auxetic behavior in Galfenol.

Since the wide field Kerr microscopy technique allows real time visualization of the magnetic domains, studies can be conducted to investigate the magnetic domains under dynamic fields. The results from such a study could be used to develop a dynamic magnetoelastic model.

Imaging the evolution of magnetic domains in Galfenol samples beyond 25 at% Ga content under applied magnetic fields along the <110> auxetic direction will help understand the auxetic response observed in the 31% Ga and 33% Ga Galfenol samples from this study. Also, Kerr images along the <100> directions in these high composition samples of Galfenol could yield more information about the second peak in the magnetostriction.

Previous works on Galfenol have shown that magnetostriction in Galfenol with compositions greater than 20 at. % Ga deviate from the quadratic enhancement observed at lower compositions **[26]**. More data with good confidence intervals will be needed to verify if this is true. These measured values will improve the results from the multiphysics simulations discussed in this work which uses them as input.

As a first step towards the development of applications that use auxeticity in Galfenol, studying the effects of load bearing structural auxetic inclusions in composites can be undertaken. <110> oriented Galfenol additives to magneto rheological fluids can also be studied to investigate potential for performance enhancement.

Finally, the development of magnetically tunable auxetic structures has immense potential for novel applications.

Appendices

Early magnetostrictive materials were mostly ferromagnetic materials like Fe, Ni, Co etc. Their magnetostriction was low (of the order of $10\,\mu\varepsilon$) and hence not many applications could be developed. But all this changed with the development of rare earth-Iron alloy systems that had giant magnetostrictive properties.

One of these breakthrough materials was Terfenol-D which is an alloy of Tb, Dy and Fe that has room temperature magnetostriction close to $2000\,\mu\varepsilon$ **[114]**. This property was conducive for the development of various applications such as active noise and vibration cancellation, servo machining, sonar etc. **[115]**. Table A.1 gives the magnetostrictive constants ($\lambda_{100}, \lambda_{111}$) for various cubic single crystal materials measured at room temperature which define the magnitude of mechanical change that can be obtained from the application of magnetic fields. However, Terfenol-D suffers from low tensile strength (about 30MPa) and brittleness which restricted the applications to only those that involved axial compressive forces.

The discovery of large magnetostriction in Iron Gallium alloys **[7, 49]** has spurred a new wave of research initiatives into magnetostrictive materials. These Fe-Ga alloys are collectively known as Galfenol.

Table A.1 Magnetostrictive constants for various single crystal materials based on [4, 5]

Material	λ_{100} (x10^{-6})	λ_{111} (x10^{-6})
Fe	24	-23
Co	-248	57
Ni	-66	-29
Ni$_{65}$Fe$_{35}$	20	15
Ni$_{65}$Co$_{35}$	40	-35
Fe$_{55}$Co$_{45}$	130	35
Tb [1]	8700	20
Dy [1]	9400	5500
TbFe$_2$ [2]	-	4000
TbFe$_2$	-	3690
DyFe$_2$ [1]	-70	-
DyFe$_2$	-	1890
Tb$_{0.27}$Dy$_{0.73}$Fe$_2$	-	2300
Fe$_{97}$Si$_3$	25	-7
Fe$_{80}$Al$_{20}$	95	5
Fe$_{83}$Ga$_{17}$	208	0

---

[2] Values measured at temperatures close to absolute zero (-273°C).

Appendix B: Actuation and sensing

The actuation and sensing behavior of magnetostrictives can be explained using the Joule and Wiedemann effects and the Villari and Matteucci effects respectively as explained in Section 1.3.1. The mode of operation of magnetostrictive materials is depicted in Fig. B.1 and B.2 for actuation and sensing respectively.

Under no applied magnetic field and no applied stress, a magnetostrictive material is comprised of randomly oriented magnetic moments. If a magnetic field is applied along the longitudinal axis of a magnetostrictive rod, the moments will rotate such that their longitudinal axes are aligned with the magnetic field. If a compressive stress is applied along the longitudinal axis of the rod, the moments will orient themselves so they are perpendicular to the applied stress. The strain resulting from the total length change as the moments rotate from all perpendicular to all parallel is defined as the saturation magnetostriction. This is the phenomenon responsible for Galfenol's actuation behavior, and it is shown schematically in Fig. B.1.
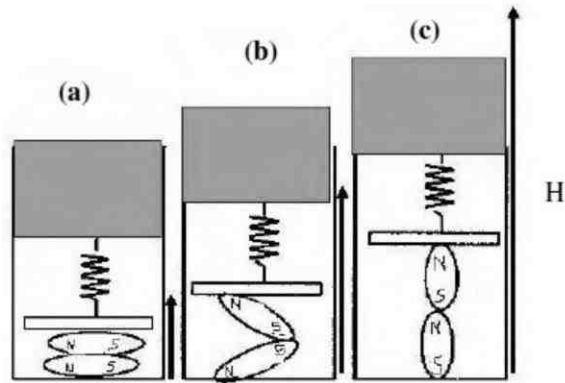
Figure B.1: Galfenol's actuation behavior [8]. The shaded block represents the load and the applied field H increases from (a) to (c).

This process can be reversed to produce a sensing effect. A saturating field initially causes all the moments to align parallel to the rod axis. Increasing the applied compressive stress will cause the moments to rotate such that they are perpendicular to the rod axis. This causes a change in magnetization of the sample, which can be measured. This phenomenon is shown schematically in Fig. B.2.
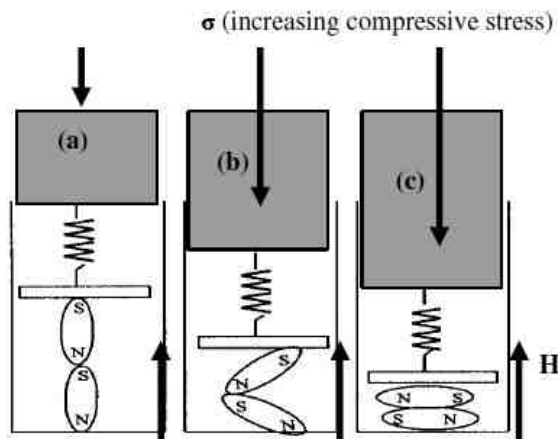
Figure B.2: Schematic of Galfenol's sensing behavior [8]. The applied stress σ increases from (a) to (c) at a constant bias field H.

Appendix C: Applications of auxetic materials

Galfenol is an interesting alloy that has shown great potential for numerous applications. The combination of large negative Poisson's ratio, high strength (~530 MPa yield strength and ~160 MPa [110] Young's modulus **[15]**) and magneto-mechanical coupling makes Fe-Ga a very promising material for novel devices. These special features are very useful in applications such as strain amplifiers, packing materials, energy absorption components, and soundproofing materials **[3, 9]**. However, successfully exploiting the in-plane auxetic properties will require using the proper crystallographic orientation of single crystals and highly textured polycrystalline alloys.

The Poisson's ratio of a material influences the transmission and reflection of stress waves, the decay of stress with distance according to Saint Venant's principle and the distribution of stress around holes and cracks. It has been demonstrated that foams with a negative Poisson's ratio were more difficult to indent than non-auxetic foam materials at low loads (from 10–100 N). In addition, an auxetic foam was less plastic with the most rapid viscoelastic creep recovery of any residual deformation **[70]**. In an auxetic material, there is effective inflow of material to the site of an impact because of lateral contraction, thereby making the location dense. Such materials have potential for use in indentation resistant armor. A schematic of this is shown in Fig. C.1.
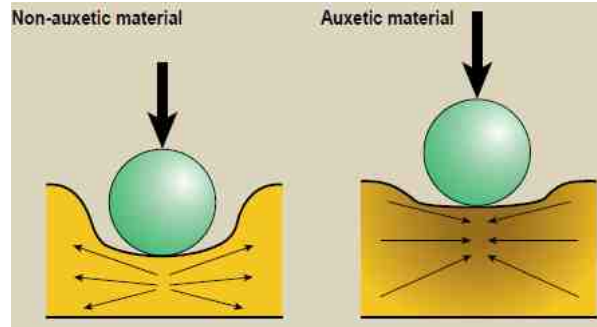
Figure C.1: Comparison of resistance to indentation in a conventional material and an auxetic material.

The lateral deformation of negative Poisson's ratio materials may be of use in new kinds of fasteners like press-fit fastening device suggested by Kellogg **[15]**. If an auxetic fastener is compressed, its width will get narrower, allowing insertion into a holder. When the compressive load is removed, the fastener will widen and thus be stuck in place. Any applied tensile load would cause the fastener to widen even more, making it a nearly perfect fixture. Figure C.2 shows an exaggerated schematic of how this might work where F_C is a compressive force and F_T is a tensile force.
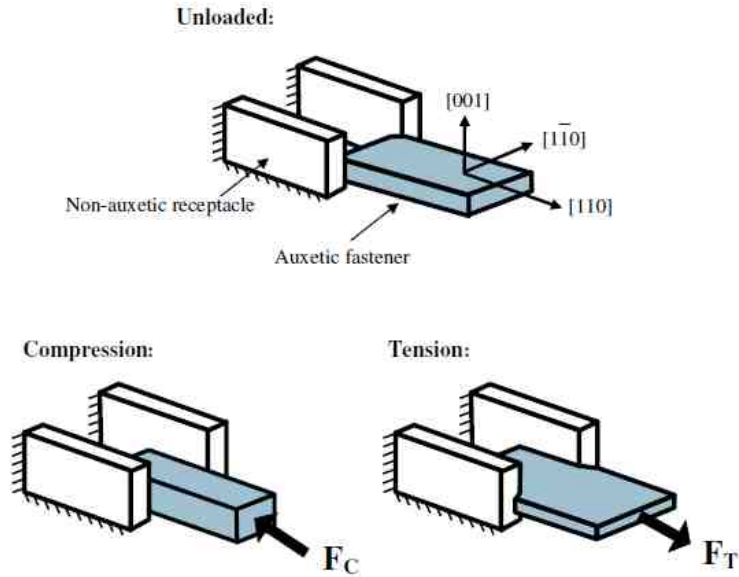
Figure C.2: Press-fit fastening device utilizing auxetic behavior **[15]**.

Auxetic inclusions in composites have been shown to have improved fracture and indentation resistance. It has also shown promise for mitigation of fiber pull-out **[113]**. A cartoon depicting the working of composites made using auxetic fibers is shown in Fig. C.3. High strength, low weight ropes, chords and fishnets have also been made using such fibers.
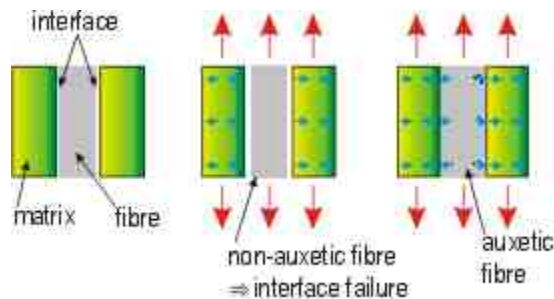
Figure C.3: Composite made form auxetic fibers **[116]**.

'Synclastic' (doubly curved) behavior of auxetic fabrics has been used for medical bandages. But Galfenol which has good load bearing properties can be used as a high strength, low weight structural material in sandwich panels for aircrafts and automobiles [67] as shown in Figure C.4.
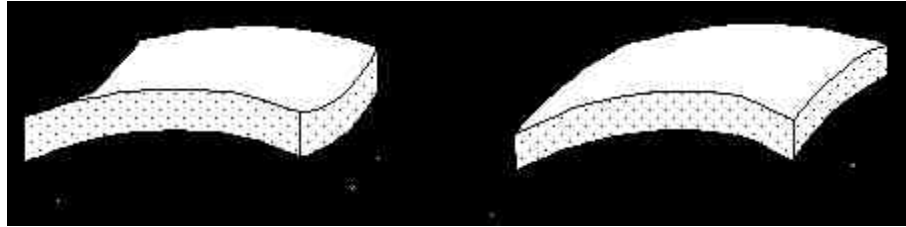
Figure C.4: Doubly curved auxetic sandwich panels [116].

The following section discusses potential applications of Galfenol as an in-plane auxetic material especially under applied magnetic fields at zero stresses.

C.1: Solid state pump

An auxetic tube made from a <110> {100} Fe-Ga sheet as shown in in Fig. C.5 which experiences an increase in the diameter under tensile loads due to auxeticity can be used to build a solid state pump that operates by acting like a diaphragm-like enclosure that can produce volume and pressure changes under applied magnetic fields.
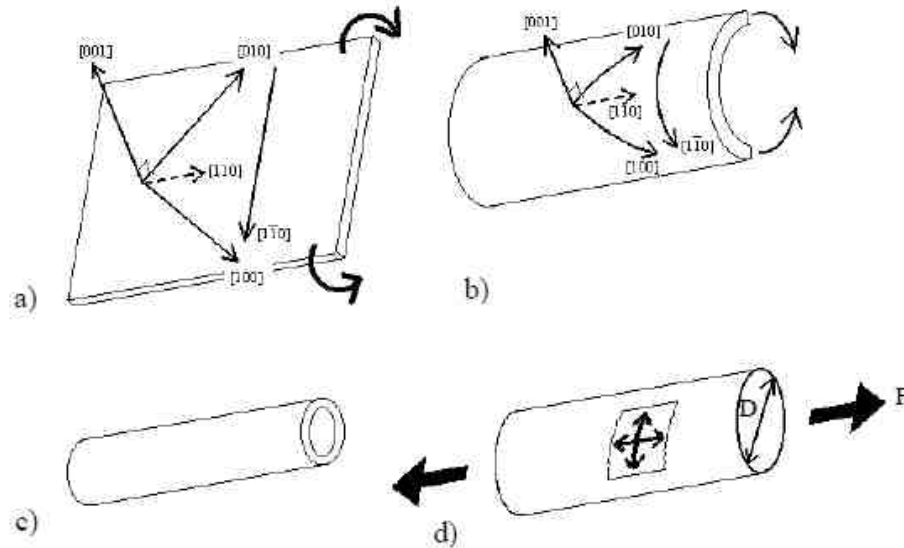
Figure C.5: Auxetic tube formed from bending a thin textured Galfenol sheet. (a) A
<110> {100} oriented sheet. (b) Rolling this sheet over. (c) Auxetic tube formed by
joining the edges of the sheet and possibly even welding them together. (d) A finished
tube under tensile load which causes an increase in its circumference **[15]**.

Directional fluid flow would be generated provided that the ends of the tube
are sealed with one-way check valves as shown in Fig. C.6. To actuate the pump, the
auxetic magnetostrictive tube through which the fluid flows is surrounded by a
solenoid that could be used to magnetically impose a tensile load on the tube. Under a
magnetic field, the tube's length and diameter increase to provide a volume increase
for generating the pump's intake stroke. Removing the applied magnetic field would
allow the tube to contract elastically against the enclosed fluid to produce the output
pressure stroke. This type of pump has the potential to produce high-pressure outputs
and may prove to be extremely robust since there are no moving parts aside from the
check valves.

201
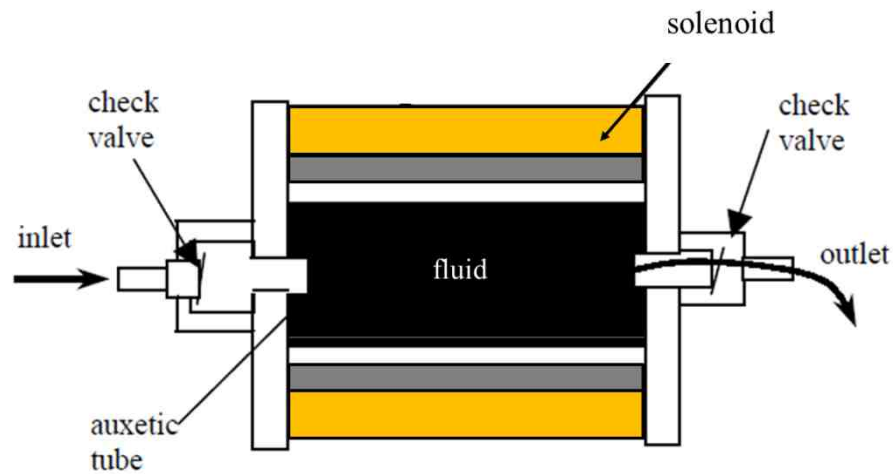
Figure C.6: Cross section of a solid state pump using an auxetic magnetostrictive tube.

It may also be possible to bond the in-plane auxetic sheet to piezoelectric material to form a composite with improved coupling coefficients and enhanced sensing capability. Additionally, if a ferromagnetic inplane auxetic material is used (such as the Fe-Ga alloys), force and pressure changes could be sensed magnetically through changes in the materials' state of magnetization.

C.2: Magnetically activated micro-filters/ Sieve

An auxetic sheet of Galfenol with holes is shown in Fig. C.7. An applied field will cause the diameter of these holes to change. This can be used as a magnetically actuated filter or sieve. The size of the holes can be controlled by the applied magnetic field along the auxetic direction.

Magnetically actuated filters have extensive applications in the bio-medical industry to separate particulate matter of different sizes.
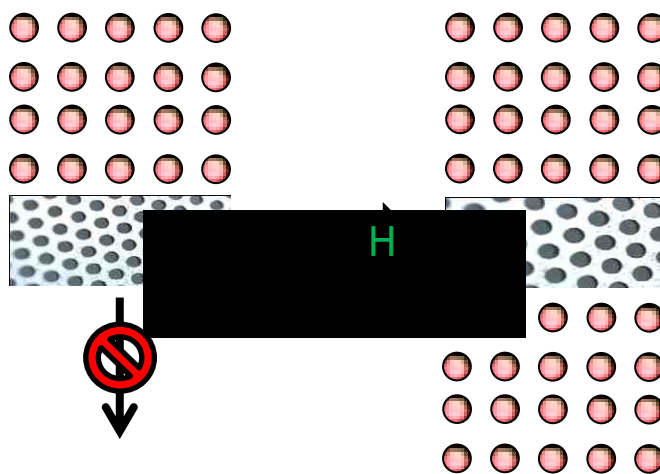
Figure C.7: Schematic of magnetically activated sieve.

This section will present the raw data from all the cycles of data from the trials which were used in the data shown in Chapter 4.

D.1: Raw data from 12% Ga Galfenol

The strain data obtained from the 12% Ga <110> {100} oriented single crystal Galfenol sample is shown in Fig. D.1. The blue curve indicates the magnetostriction along the longitudinal [110] direction and the red curve indicates the magnetostriction along the transverse [1$\bar{1}$0] direction when the field is applied along the longitudinal direction.
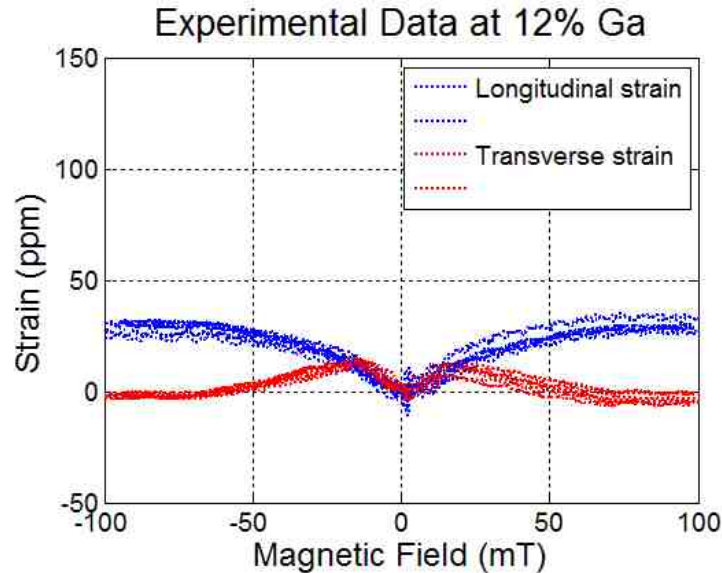
Figure D.1: Strains along the longitudinal [110] and transverse [1$\bar{1}$0] directions for the 12% Ga single crystal Galfenol with applied field along the [110] direction at zero external stress.

D.2: Raw data from 15.8% Ga Galfenol

The strain data obtained from the 15.8% Ga <110> {100} oriented single crystal Galfenol sample is shown in Fig. D.2. The blue curve indicates the magnetostriction along the longitudinal [110] direction and the red curve indicates the magnetostriction along the transverse [1$\bar{1}$0] direction when the field is applied along the longitudinal direction.
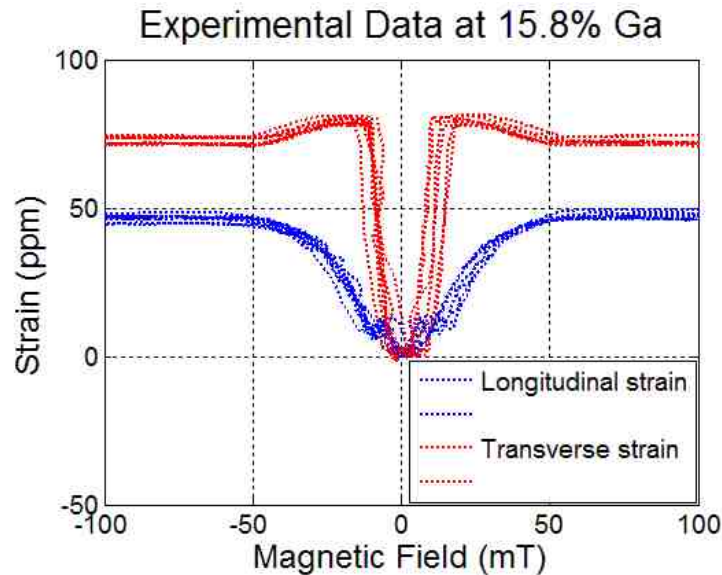
Figure D.2: Strains along the longitudinal [110] and transverse [1$\bar{1}$0] directions for the 15.8% Ga single crystal Galfenol with applied field along the [110] direction at zero external stress.

D.3: Raw data from 17.9% Ga Galfenol

The strain data obtained from the 17.9% Ga <110> {100} oriented single crystal Galfenol sample is shown in Fig. D.3. The blue curve indicates the magnetostriction along the longitudinal [110] direction and the red curve indicates the

magnetostriction along the transverse $[1\bar{1}0]$ direction when the field is applied along

the longitudinal direction.
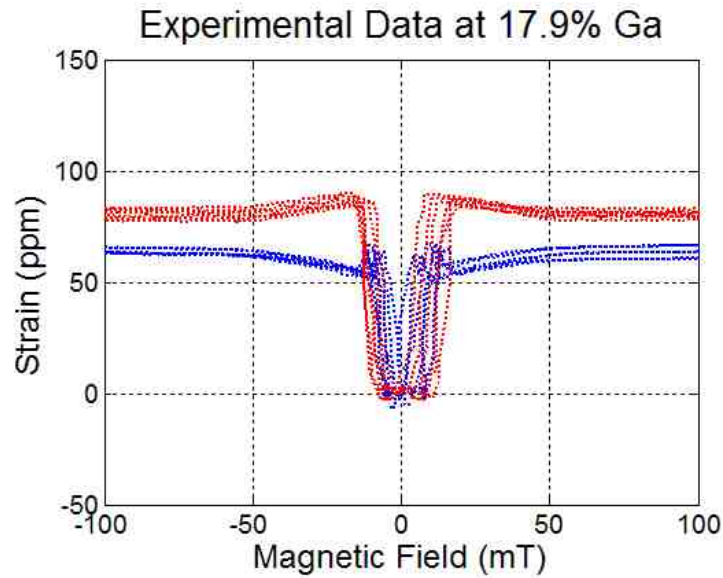
Figure D.3: Strains along the longitudinal [110] and transverse $[1\bar{1}0]$ directions for the 17.9% Ga single crystal Galfenol with applied field along the [110] direction at zero external stress.

D.4: Raw data from 20.5% Ga Galfenol

The strain data obtained from the 20.5% Ga <110> {100} oriented single

crystal Galfenol sample is shown in Fig. D.4. The blue curve indicates the

magnetostriction along the longitudinal [110] direction and the red curve indicates the

magnetostriction along the transverse $[1\bar{1}0]$ direction when the field is applied along

the longitudinal direction.
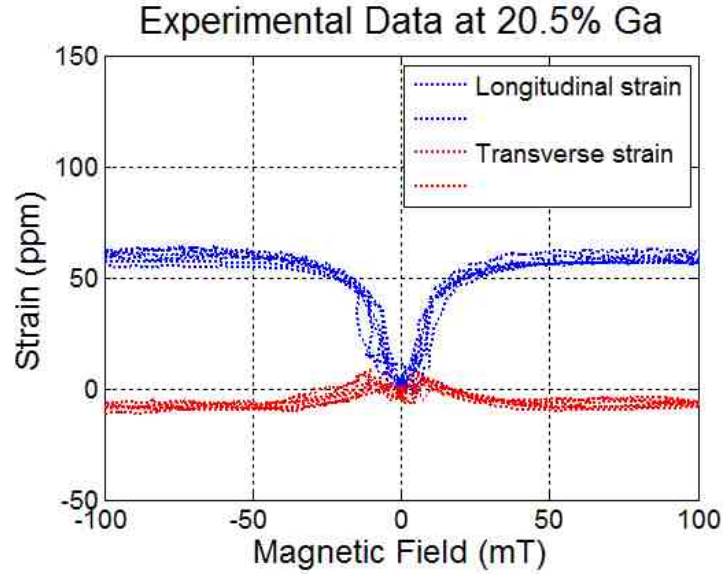
Figure D.4: Strains along the longitudinal [110] and transverse [1$\bar{1}$0] directions for the 20.5% Ga single crystal Galfenol with applied field along the [110] direction at zero external stress.

D.5: Raw data from 25.3% Ga Galfenol

The strain data obtained from the 25.3% Ga <110> {100} oriented single crystal Galfenol sample is shown in Fig. D.5. The blue curve indicates the magnetostriction along the longitudinal [110] direction and the red curve indicates the magnetostriction along the transverse [1$\bar{1}$0] direction when the field is applied along the longitudinal direction.
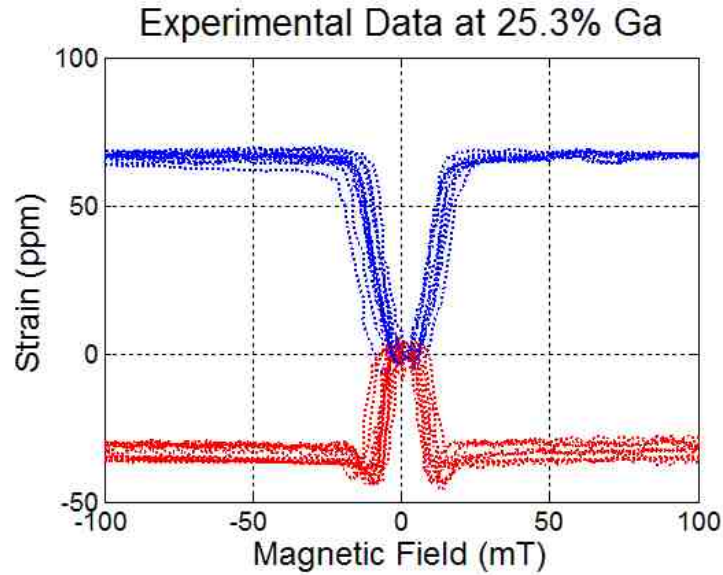
Figure D.5: Strains along the longitudinal [110] and transverse [1$\bar{1}$0] directions for the 25.3% Ga single crystal Galfenol with applied field along the [110] direction at zero external stress.

D.6: Raw data from 31% Ga Galfenol

The strain data obtained from the 31% Ga <110> {100} oriented single crystal Galfenol sample is shown in Fig. D.6. The blue curve indicates the magnetostriction along the longitudinal [110] direction and the red curve indicates the magnetostriction along the transverse [1$\bar{1}$0] direction when the field is applied along the longitudinal direction.
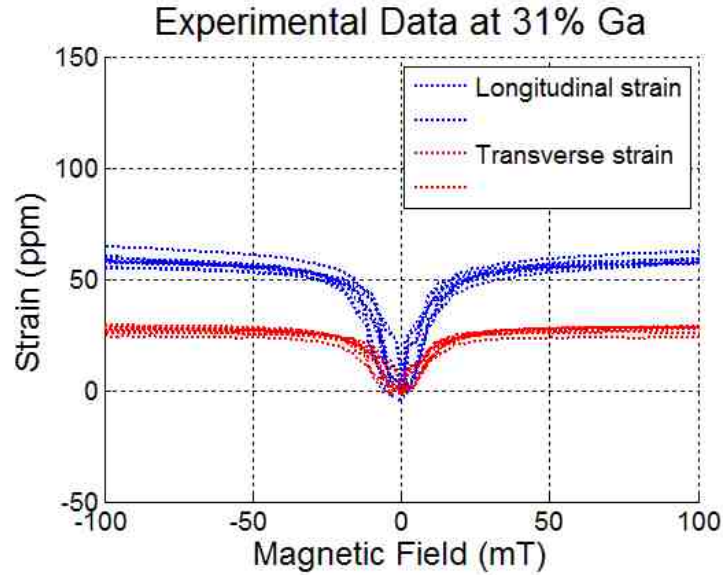
Figure D.6: Strains along the longitudinal [110] and transverse [1$\bar{1}$0] directions for the 31% Ga single crystal Galfenol with applied field along the [110] direction at zero external stress.

D.7: Raw data from 33% Ga Galfenol

The strain data obtained from the 33% Ga <110> {100} oriented single crystal Galfenol sample is shown in Fig. D.7. The blue curve indicates the magnetostriction along the longitudinal [110] direction and the red curve indicates the magnetostriction along the transverse [1$\bar{1}$0] direction when the field is applied along the longitudinal direction.
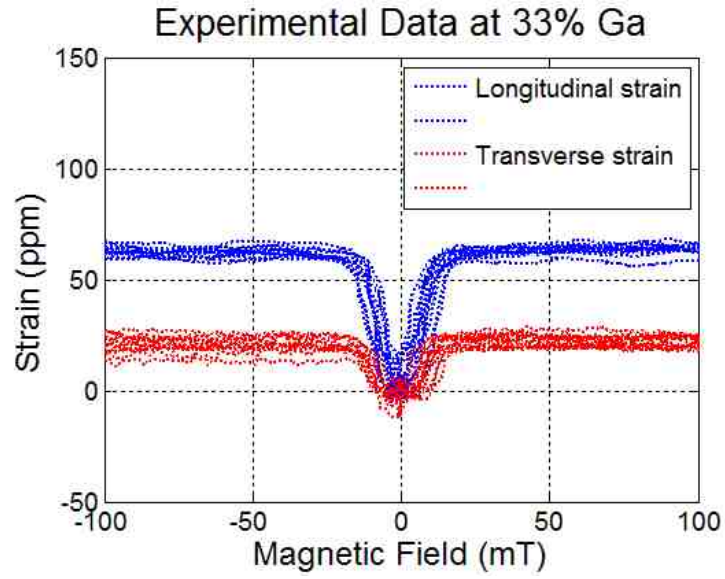
Figure D.7: Strains along the longitudinal [110] and transverse [1$\bar{1}$0] directions for the 33% Ga single crystal Galfenol with applied field along the [110] direction at zero external stress.

Longitudinal mode of the Kerr microscope which was discussed in Chapter 5 was employed to get the images of the Galfenol samples under changing magnetic fields in the <100> oriented 20% Ga slow cooled and quenched samples. The evolution of the magnetic domains under applied magnetic field along the <100> direction will be presented as a baseline case.

Figure E.1: Galfenol single crystal samples 20 at. % Ga composition that were oven cooled and quenched used in kerr microscopy.

Figure E.2 shows the evolution of the domain structure in the 20% Ga Slow-cooled Galfenol sample when the field is applied along [100] direction of the sample (along $-\hat{x}$ of the global axes).
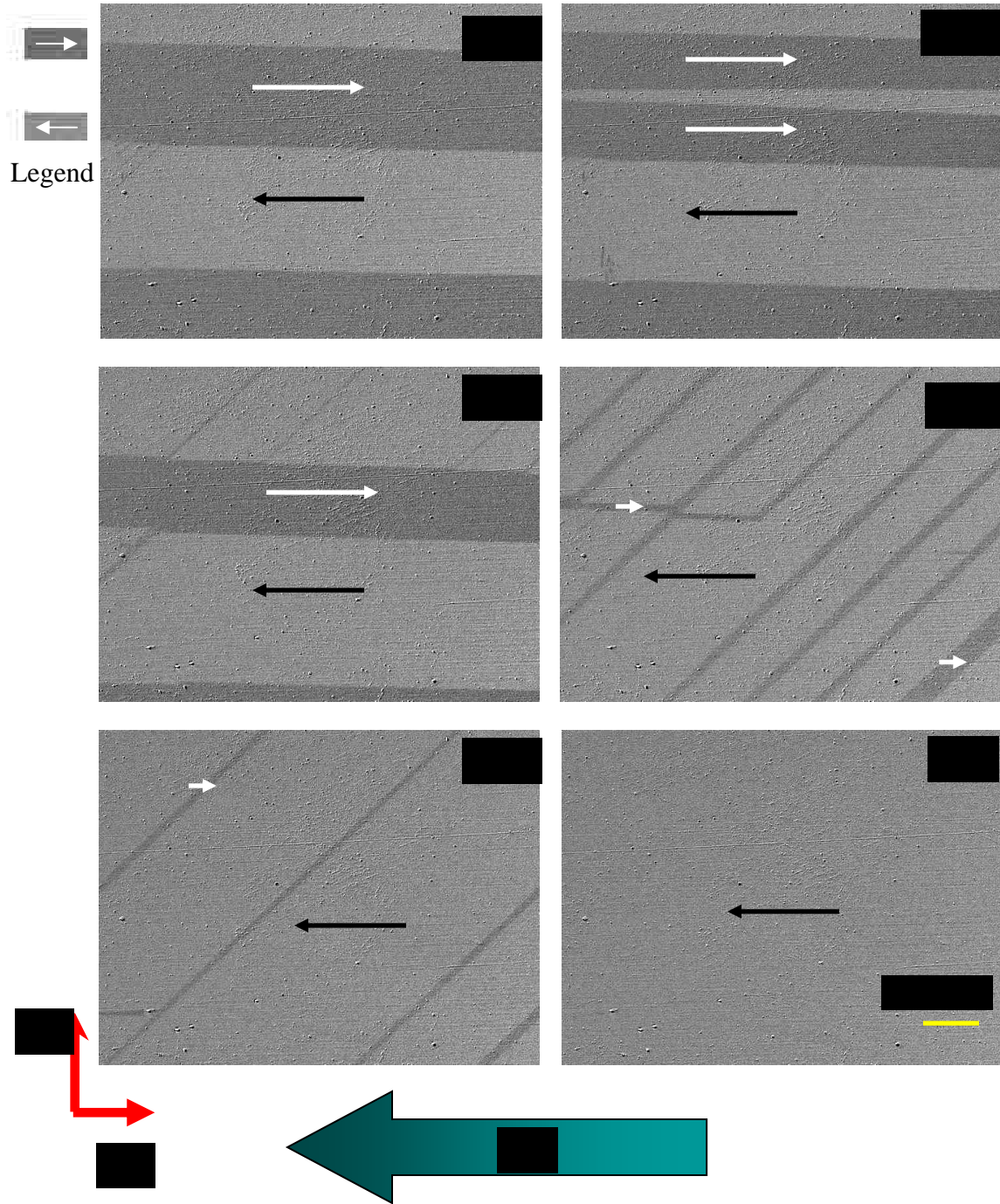
Figure E.2: Evolution of the domain structure in the 20% Ga Slow-cooled Galfenol sample when the field is applied along [100] direction of the sample. (a) at 0 mT (b) at 5 mT (c) at 10 mT (d) at 15 mT (e) at 24 mT (f) at 30mT.

The domains grew by wall motion and eventually saturated at about 30 mT. All the domains at remanence were along the [100] direction only indicating superposition of some uniaxial anisotropy on to the cubic anisotropy.

When the field was applied along the [010] direction (along $\pm\hat{y}$ of the global axes), this uniaxial anisotropy is overcome beyond a certain field (in this case about 20 mT). This leads to nucleation of the domains till 35 mT after which the domains grow by wall motion to eventually saturate completely at about 65mT. This is illustrated in Fig. E.3.
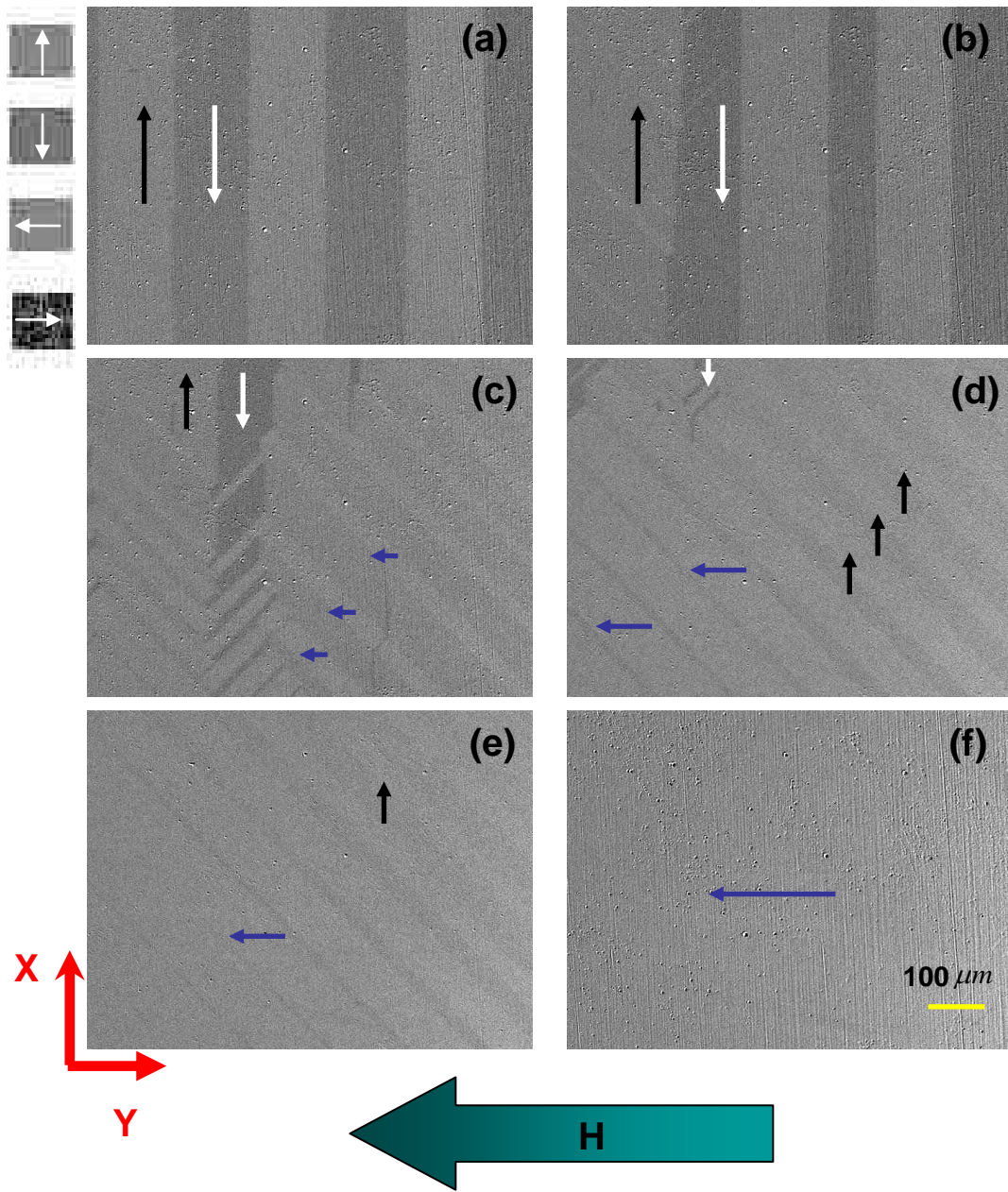
Figure E.3: Evolution of the domain structure in the 20% Ga Slow-cooled Galfenol sample when the field is applied along [010] direction of the sample. (a) at 0 mT (b) at 20 mT (c) at 30 mT (d) at 40 mT (e) at 50 mT (f) at 65mT.

The uniaxial anisotropy is exhibited through out the sample as expected by [26] in the remanent states estimation for this sample. The formation of 90° domain

walls indicates that these domains are just surface domains which do not permeate through the thickness of the specimen due to high energy costs.

A similar set of MOKE images were obtained for the 20% Ga Quenched Galfenol sample as shown in Fig.E.4 and Fig E.5.
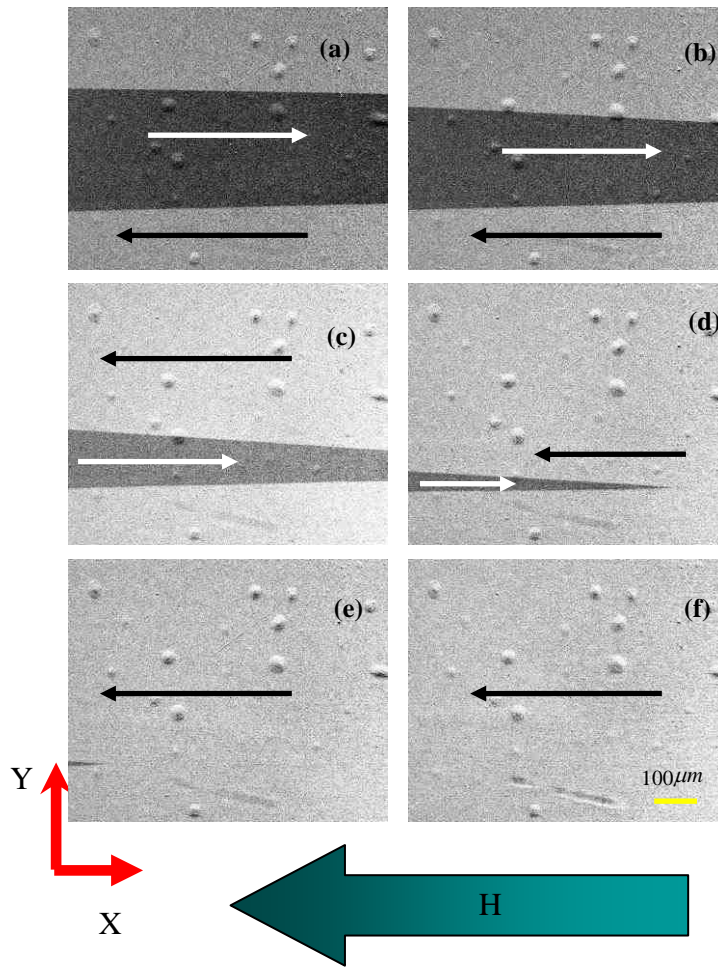
Figure E.4: Evolution of the domain structure in the 20% Ga Quenched Galfenol sample when the field is applied along [100] direction of the sample. (a) at 0 mT (b) at 8 mT (c) at 18 mT (d) at 38 mT (e) at 41 mT (f) at 46mT.
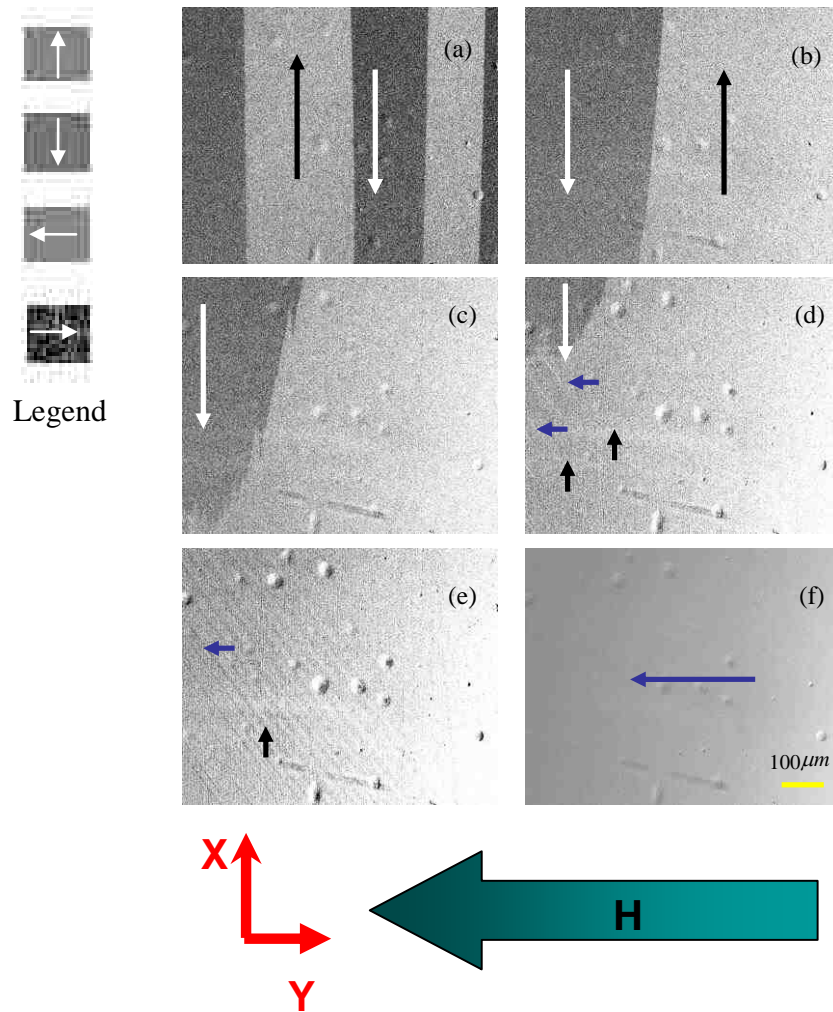
Figure E.5: Evolution of the domain structure in the 20% Ga Quenched Galfenol sample when the field is applied along [010] direction of the sample. (a) at 0 mT (b) at 22 mT (c) at 47 mT (d) at 61 mT (e) at 84 mT (f) at 100 mT.

The Quenched samples of Galfenol saturate at a much later than the quenched samples. The presence of 180° domain walls at remenance confirms the presence of a uniaxial anisotropy for this composition.

This section discusses the domain patterns obtained from the 15.8% Ga Galfenol dogbone sample shown in Fig. 5.9, at a location away from the center of the sample.

F.1: Domain refinement in magnetic domains

This section discusses the domain refinement and closure domains discussed in Chapter1 obtained from the 15.8% Ga Galfenol dogbone sample. The results from Kerr microscopy are shown in Fig. F.1.
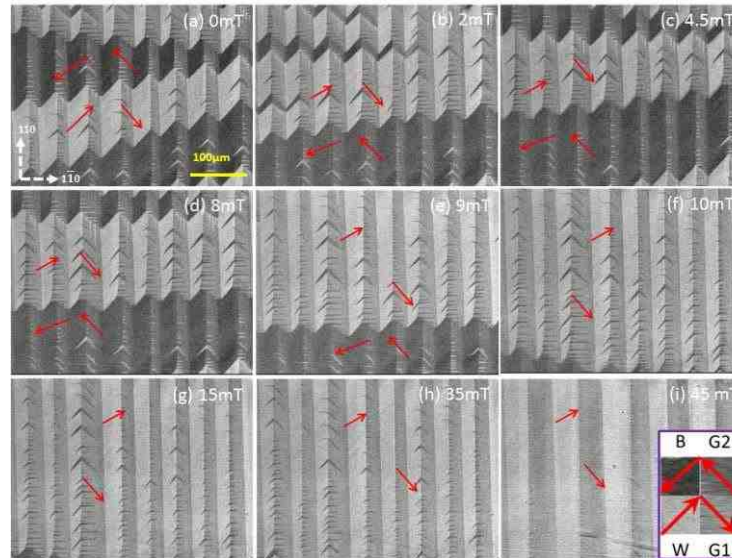
Figure F.1: Evolution of branched domains in 15.8% Ga Galfenol auxetic dogbone sample for applied magnetic fields along x- axis and zero stress at a location away from the center.

Domain refinement to reduce internal stray fields according to echelon pattern in cubic crystals that causes staircase-like edge structures were also observed

in the MOKE images at a location away from the centre of the sample. This four-phase branching reduces the volume of the closure domains as shown in Fig. F.1 (a). The four different grey scales indicate four different domain phases, each of them magnetized along one of the four <100> easy directions within the (001) plane at remanence. It shows in-plane magnetization with 90° and 180° domain walls as expected in cubic alloys such as Galfenol. A fir tree pattern due to a slightly misoriented surface possibly arising from mechanical polishing is also observed.

The evolution of the magnetic domains in this region is presented in Fig F.1. When a magnetic field is applied along the x-axis, the B and G2 shades representing the unfavorable domains decrease in size as shown in Fig. F.1 (b). But at around 4mT, the B and G2 shades reappear and grow in size until about 8mT as illustrated in Fig. F.1 (c) and (d). It is in this field range where there is a decrease in dimension along the x-axis. As the applied magnetic field is increased past 9mT, the magnetic domains represented by W and G1 grow in size as shown in Fig. F.1 (e), (f), (g) and (h). The 90° domains walls along <100> easy directions disappear and the 180° domain wall between W and G1 along the <110> direction in which the magnetic field is applied remains. The sample then reaches the state shown in Fig. F.1 (i) where domains saturate along the <100> direction nominal to the applied field in the <110> direction. Beyond this field, there are no more changes in the strain experienced in both x and y directions for any increase in the applied magnetic field.

The importance of the input parameters to the results obtained from the simulations was discussed in Chapter 2 and 4. This section shows the effect of the values of anisotropy constants K_1 and K_2 on the results obtained from the simulations from Galfenol at 15.8% Ga content. Figure G.1 shows results from choices of K1 and K2 that show: (a) a case with <100> easy axis, (b) a case with <110> easy axis, (c) a case with <111> easy axis and (d) actual simulation (strongest preference for <100> direction).
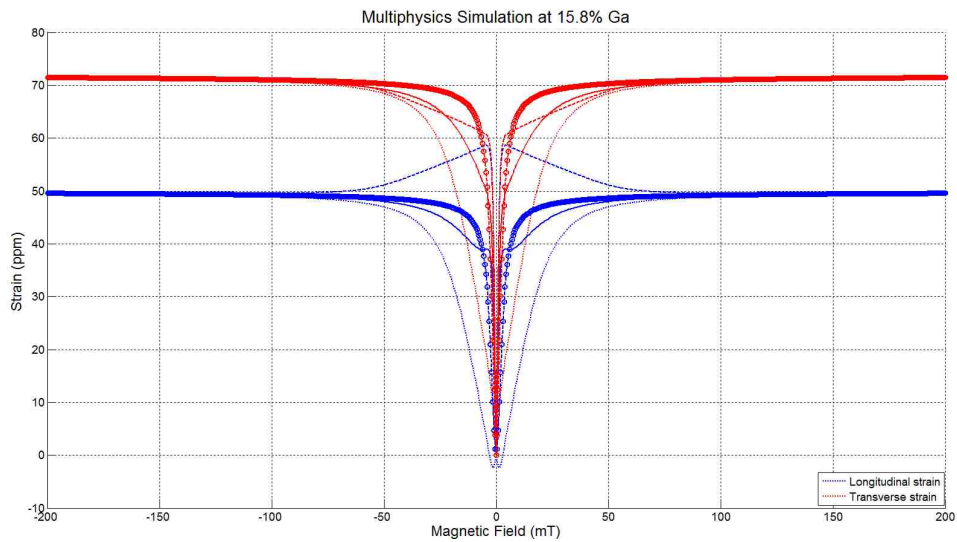
Figure G.1: Simulation results from 15.8% Ga Galfenol showing longitudinal and transverse <110> strains for (a) a case with <100> easy axis (shown using dashes lines), (b) a case with <110> easy axis (shows using dotted lines), (c) a case with <111> easy axis (shown using lines with circles and dashes) and (d) actual simulation with strongest preference for <100> direction (shown using a solid line). Here, Blue indicates longitudinal strain and red indicates transverse strain.

This result can be used understand the easy axes from experimental data at each composition of Galfenol from the trends in the <110> strains observed.

Appendix H: Multiphysics simulation codes

armstrong_optimized_16.m

```matlab
function [B MEStrain]  = armstrong_optimized_16(Hin, Sigmain)
%%%%%%%%%%%%%%%%%%%%%%%%%%%%%%%%%%%%%%%%%%%%%%%%%%%%%%%%%%%%%%%%%%%%%%%%%%%%%
%%
%    Input for the function:
%    Hin and Sigmain must be full 3-D vector/tensor in the form
%    Hin = [Hx Hy Hz]';
%    Sigmain = [Sxx Syy Szz Sxy Syz Sxz]';
%
%    Output from the function:
%    B and magnetostriction in full 3-D form
%    B = [Bx By Bz]';
%    MEStrain = [lxx lyy lzz lxy lyz lxz]';
%
%    Edited on Nov 10th 2008.
%    Changes made:
%    Made changes to Etot2.m that makes it now use stress induced
anisotropy
%    rather than elastic, magnetoelastic, and mechanical work
energies. The
%    stress is resolved into principal stresses & principal
directions and
%    the net stress induced anisotropy due to all the principal
stresses is
%    calculated.
%
%    Edited on Nov 12th 2008
%    Changes made:
%    No more "for loops" to increment theta and phi. Rather, meshgrid
is
%    used which makes the whole program about 70-75 times faster!
%
%    Edited on Nov 14th 2008
%    Changes made:
%    exp(-Etot/omega)*dalpha is now calculated in one step as one
variable,
%    expEtot_dalpha, instead of calculating it in all the steps. The
program
%    now runs more than 155 times faster!
%
%    Time taken for the program to run:
%    Before (10 averages): 0.7921132, 0.7931920, 0.7927836, 0.7947328
%    After (10 averages): 0.0050931, 0.0051732, 0.0051899, 0.0050632
--> 155
%    times faster!
%%%%%%%%%%%%%%%%%%%%%%%%%%%%%%%%%%%%%%%%%%%%%%%%%%%%%%%%%%%%%%%%%%%%%%%%%%%%%
%


%% Global Variables
```

```matlab
global mu_0 K1 K2 Msat MagElas_FCT B1OVERdeltac12c11 negB2OVERc44
c11 c12 c44 B1 B2

%% Constants
% Fundamental
mu_0 = 4*pi*1e-7; % permeability of free space

%Elastic
c11 = 213e9;
c12 = 174e9;
c44 = 120e9;

% Magnetostrictive(MAGNETOELASTIC)
lambda_100 = 2/3*(365e-6); % strain (-2/3*B1/(c11-c12))
lambda_111 = -2/3*(22e-6); % strain (-1/3*B2/(c44)) (-22)
MagElas_FCT = 0.875; % from experimental data
B1 = -3/2*lambda_100*(c11-c12);
B2 = -3*lambda_111*c44;
B1OVERdeltac12c11=B1/(c12-c11);
negB2OVERc44=-B2/c44;


% Magnetocrystalline
K1 =-4e4  %13e3;%actual <100>-50e3%<111>50e3%strong 100 %-50e3%<111>
50e3%strong 100 %  % J/m^3 This is actually K1+dK1 or experimentally
measured K1
K2 =100e3  %-90e3;%actual <100>10e3%<111>-5e3%strong 100  10e3%<111>
-5e3%strong 100  %-90e3;actual <100>% J/m^3

% Saturation magnetization
Msat= 1456e3; % in A/m; number from (B - mu_0*H) from experimental
data

%% VARIABLES

omega = 600; % smoothing function to match with experimental BH plot

%% Angle step size
del_theta = 5; % azimuthal resolution in deg
del_phi = 5; % circular resolution in deg


%% main calculation

% Calculation of principal stresses and their directions
% Sigma_tensor = [Sigmain(1) Sigmain(4) Sigmain(6);
%                 Sigmain(4) Sigmain(2) Sigmain(5);
%                 Sigmain(6) Sigmain(5) Sigmain(3)];

            Sigma_tensor = zeros(3,3);
```

```matlab
[pSdirec, pS] = eig(Sigma_tensor); % pS - principal stresses,
pSdirec - principal stress directions

% Meshgrid of theta and phi
[theta, phi] = meshgrid((0:del_theta:180)*pi/180,
(0:del_phi:359)*pi/180);

% Calculate ALPHA's (direction cosines) from theta and phi
ALPHA1 = sin(theta).*cos(phi);
ALPHA2 = sin(theta).*sin(phi);
ALPHA3 = cos(theta);

% Calculation of energy. It now (Nov. 10th 2008) uses stress induced
anisotropy
Etot = Etot2(ALPHA1,ALPHA2,ALPHA3,Hin,pS,pSdirec);

% Calculation of lambda
% lambdaxx = B1/(c12-c11)*(ALPHA1.^2-1/3);
% lambdayy = B1/(c12-c11)*(ALPHA2.^2-1/3);
% lambdazz = B1/(c12-c11)*(ALPHA3.^2-1/3);
lambdaxx = B1OVERdeltac12c11*(ALPHA1.^2-1/3);
lambdayy = B1OVERdeltac12c11*(ALPHA2.^2-1/3);
lambdazz = B1OVERdeltac12c11*(ALPHA3.^2-1/3);
% lambdaxy = -B2/c44*ALPHA1.*ALPHA2;
% lambdayz = -B2/c44*ALPHA2.*ALPHA3;
% lambdaxz = -B2/c44*ALPHA3.*ALPHA1;
lambdaxy = negB2OVERc44*ALPHA1.*ALPHA2;
lambdayz = negB2OVERc44*ALPHA2.*ALPHA3;
lambdaxz = negB2OVERc44*ALPHA3.*ALPHA1;
% Calculation of Magnetization probability
expEtot_dalpha = (del_theta.*del_phi.*abs(sin(theta))).*exp(-
Etot/omega);
dMxProb = (Msat*ALPHA1).*expEtot_dalpha;
dMyProb = (Msat*ALPHA2).*expEtot_dalpha;
dMzProb = (Msat*ALPHA3).*expEtot_dalpha;
% Calculation of Lambda probability
dLambdaxxProb = (lambdaxx).*expEtot_dalpha;
dLambdayyProb = (lambdayy).*expEtot_dalpha;
dLambdazzProb = (lambdazz).*expEtot_dalpha;
dLambdaxyProb = (lambdaxy).*expEtot_dalpha;
dLambdayzProb = (lambdayz).*expEtot_dalpha;
dLambdaxzProb = (lambdaxz).*expEtot_dalpha;
dProb = expEtot_dalpha;

% Calculation of Magnetization
M = [sum(sum(dMxProb))/sum(sum(dProb));
     sum(sum(dMyProb))/sum(sum(dProb));
     sum(sum(dMzProb))/sum(sum(dProb))];
% Calculation of Magnetostriction
MEStrain = [sum(sum(dLambdaxxProb))/sum(sum(dProb));
            sum(sum(dLambdayyProb))/sum(sum(dProb));
            sum(sum(dLambdazzProb))/sum(sum(dProb));
            sum(sum(dLambdaxyProb))/sum(sum(dProb));
            sum(sum(dLambdayzProb))/sum(sum(dProb));
```

```
                   sum(sum(dLambdaxzProb))/sum(sum(dProb))];
% mu_0
% M
% Hin
B = mu_0*(M + Hin); %induction in Tesla
%----------------------------------------------------------------
```

armstrongDatabaseCreatorActuator110.m

```
% clc; close all; clear all;
tic
%load mu_lamda_gafe16v2.mat
clear B Lamda mew
mu_0=4e-7*pi;
% [HbiasRows HbiasColumns]=size(Hbias);
% [Sigma1Rows Sigma1Columns]=size(Sigma1);

% HbiasMin=-max(Hbias);
% Sigma1Min=-2*max(Sigma1);
% HbiasNew=HbiasMin:2*max(Hbias)/(HbiasColumns-1):max(Hbias);
% Sigma1New=Sigma1Min:max(Sigma1)/(Sigma1Columns-1):2*max(Sigma1);
% Hbias=HbiasNew;
% max(Sigma1)
% Sigma1=Sigma1New;
% max(Sigma1New)

Hbias=-60e3*4:.1e3*4:60e3*4;
Sigma1=0;
% Sigma1=[0 -34e6 -66e6];

[HbiasRows HbiasColumns]=size(Hbias);
[Sigma1Rows Sigma1Columns]=size(Sigma1);

[HbiasRows HbiasColumns]=size(Hbias);
[Sigma1Rows Sigma1Columns]=size(Sigma1);
strainDir1_110=1/sqrt(2);
strainDir2_110=1/sqrt(2);
strainDir3_110=0;
strainDir1_11b0=1/sqrt(2);
strainDir2_11b0=-1/sqrt(2);
strainDir3_11b0=0;

for i=1:HbiasColumns;
    H=[Hbias(i)*1/sqrt(2) Hbias(i)*1/sqrt(2) 0]';
    for j=1:Sigma1Columns;
        sx=[0 0 0 0 0 0]';
        [Bvec Lamdavec]=armstrong_optimized_16(H,sx);
        B(i,j)=Bvec(1);
        Lamda100(i,j)=Lamdavec(1);
        Lamda010(i,j)=Lamdavec(2);
        Lamda001(i,j)=Lamdavec(3);
```

```matlab
        Lamdaxy(i,j)=Lamdavec(4);
        blue=Lamdavec(4)*strainDir1_110*strainDir2_110;
        red=Lamdavec(4)*strainDir1_11b0*strainDir2_11b0;
        display=[blue red];
        Lamda110(i,j)=...
            Lamdavec(1)*strainDir1_110^2+...
            Lamdavec(2)*strainDir2_110^2+...
            Lamdavec(3)*strainDir3_110^2+...
            Lamdavec(4)*strainDir1_110*strainDir2_110+...
            Lamdavec(5)*strainDir2_110*strainDir3_110+...
            Lamdavec(6)*strainDir3_110*strainDir1_110;
        Lamda11b0(i,j)=...
            Lamdavec(1)*strainDir1_11b0^2+...
            Lamdavec(2)*strainDir2_11b0^2+...
            Lamdavec(3)*strainDir3_11b0^2+...
            Lamdavec(4)*strainDir1_11b0*strainDir2_11b0+...
            Lamdavec(5)*strainDir2_11b0*strainDir3_11b0+...
            Lamdavec(6)*strainDir3_11b0*strainDir1_11b0;


        mu(i,j)=B(i,j)/mu_0/Hbias(i); %mu_relative
    end
    i;
end


% for j=1:Sigma1Columns
%       LamdaAdjusted(:,j)=Lamda(:,j)-min(Lamda(:,j));
% end

%One Lambda Line=Lamda(:,constj)
% figure(1)
% plot(Hbias*0.012566371,B) %1 A/m = 0.012566371 Oe
% grid on
% xlabel('Magnetic Field (Oe)')
% ylabel('Magnetic Induction (T)')
figure(1)
hold on
plot(Hbias*0.012566371/10,Lamda110*10^6,'b --o','LineWidth',2)
plot(Hbias*0.012566371/10,Lamda11b0*10^6,'r --o','LineWidth',2)
% plot(Hbias,Lamda010,'g')
% plot(Hbias,Lamda110,'b')
axis([-200 200 -10 80])
% axis([-100 100 -50 150])
% axis([-100 100 -0.00005 .00015])
xlabel('Magnetic Field (mT)','FontSize', 18)
ylabel('Strain (ppm)','FontSize', 18)
title('Multiphysics Simulation at 15.8% Ga','FontSize', 20)
legend('Longitudinal strain','Transverse strain')
set(gca,'FontSize',14)
grid on
hold off


PR=-Lamda11b0./Lamda110;

figure(2)
```

```matlab
% hold on
plot(Hbias*0.012566371/10,PR,'k','LineWidth',2)
% plot(Hbias*0.012566371,Lamda11b0,'r')
% plot(Hbias,Lamda010,'g')
% plot(Hbias,Lamda110,'b')
xlabel('Magnetic Field (mT)','FontSize', 18)
ylabel('Strain (ppm)','FontSize', 18)
grid on
title('Multiphysics Simulation at 16% Ga','FontSize', 20)
axis([-100 100 -15 5])
set(gca,'FontSize',14)
% figure(2)
% plot(Hbias*0.012566371,Lamda110,'g')
% figure(3)
% plot(Hbias*0.012566371,sqrt(Lamda100.^2+Lamda010.^2),'b')
% figure(4)
% plot(Hbias*0.012566371,Lamda110,'k')
% figure(3)
% plot(Hbias*0.012566371,mu)
% grid on
% xlabel('Magnetic Field (Oe)')
% ylabel('Relative Permeability')
% figure(4)
% plot(Sigma1,B)

toc
%-----------------------------------------------------------------
```

Eanisotropy.m

```matlab
function Ean = Eanisotropy(APLHA1,APLHA2,APLHA3)
global K1 K2

Ean =
K1*((APLHA1.^2).*(APLHA2.^2)+(APLHA2.^2).*(APLHA3.^2)+(APLHA3.^2).*(
APLHA1.^2)) + K2*((APLHA1.^2).*(APLHA2.^2).*(APLHA3.^2));
%-----------------------------------------------------------------
```

Eaniso.m

```matlab
function Esan = Esaniso(ALPHA1,ALPHA2,ALPHA3,pS,pSdirec)
global B1OVERdeltac12c11 negB2OVERc44 MagElas_FCT c11 c12 c44 B1 B2

% first principal stress
direc1 = pSdirec(:,1);
BETA1S = direc1(1)/sqrt(sum(direc1.^2));
BETA2S = direc1(2)/sqrt(sum(direc1.^2));
BETA3S = direc1(3)/sqrt(sum(direc1.^2));
Sigma = pS(1,1);
```

225

```matlab
E11 = -
B1OVERdeltac12c11*Sigma*((ALPHA1.^2)*(BETA1S^2)+(ALPHA2.^2)*(BETA2S^
2)+(ALPHA3.^2)*(BETA3S^2)-1/3);
E21 = -negB2OVERc44*Sigma*(ALPHA1.*ALPHA2*BETA1S*BETA2S +
ALPHA2.*ALPHA3*BETA2S*BETA3S + ALPHA3.*ALPHA1*BETA3S*BETA1S);

% second principal stress
direc1 = pSdirec(:,2);
Sigma = pS(2,2);
BETA1S = direc1(1)/sqrt(sum(direc1.^2));
BETA2S = direc1(2)/sqrt(sum(direc1.^2));
BETA3S = direc1(3)/sqrt(sum(direc1.^2));
E12 = -
B1OVERdeltac12c11*Sigma*((ALPHA1.^2)*(BETA1S^2)+(ALPHA2.^2)*(BETA2S^
2)+(ALPHA3.^2)*(BETA3S^2)-1/3);
E22 = -negB2OVERc44*Sigma*(ALPHA1.*ALPHA2*BETA1S*BETA2S +
ALPHA2.*ALPHA3*BETA2S*BETA3S + ALPHA3.*ALPHA1*BETA3S*BETA1S);

% third principal stress
direc1 = pSdirec(:,3);
Sigma = pS(3,3);
BETA1S = direc1(1)/sqrt(sum(direc1.^2));
BETA2S = direc1(2)/sqrt(sum(direc1.^2));
BETA3S = direc1(3)/sqrt(sum(direc1.^2));
E13 = -
B1OVERdeltac12c11*Sigma*((ALPHA1.^2)*(BETA1S^2)+(ALPHA2.^2)*(BETA2S^
2)+(ALPHA3.^2)*(BETA3S^2)-1/3);
E23 = -negB2OVERc44*Sigma*(ALPHA1.*ALPHA2*BETA1S*BETA2S +
ALPHA2.*ALPHA3*BETA2S*BETA3S + ALPHA3.*ALPHA1*BETA3S*BETA1S);

% % first principal stress
% direc1 = pSdirec(:,1);
% BETA1S = direc1(1)/sqrt(sum(direc1.^2));
% BETA2S = direc1(2)/sqrt(sum(direc1.^2));
% BETA3S = direc1(3)/sqrt(sum(direc1.^2));
% Sigma = pS(1,1);
% E11 = B1/(c11-
c12)*Sigma*((ALPHA1.^2)*(BETA1S^2)+(ALPHA2.^2)*(BETA2S^2)+(ALPHA3.^2
)*(BETA3S^2)-1/3);
% E21 = B2/c44*Sigma*(ALPHA1.*ALPHA2*BETA1S*BETA2S +
ALPHA2.*ALPHA3*BETA2S*BETA3S + ALPHA3.*ALPHA1*BETA3S*BETA1S);
%
% % second principal stress
% direc1 = pSdirec(:,2);
% Sigma = pS(2,2);
% BETA1S = direc1(1)/sqrt(sum(direc1.^2));
% BETA2S = direc1(2)/sqrt(sum(direc1.^2));
% BETA3S = direc1(3)/sqrt(sum(direc1.^2));
% E12 = B1/(c11-
c12)*Sigma*((ALPHA1.^2)*(BETA1S^2)+(ALPHA2.^2)*(BETA2S^2)+(ALPHA3.^2
)*(BETA3S^2)-1/3);
% E22 = B2/c44*Sigma*(ALPHA1.*ALPHA2*BETA1S*BETA2S +
ALPHA2.*ALPHA3*BETA2S*BETA3S + ALPHA3.*ALPHA1*BETA3S*BETA1S);
%
```

226

```matlab
% % third principal stress
% direc1 = pSdirec(:,3);
% Sigma = pS(3,3);
% BETA1S = direc1(1)/sqrt(sum(direc1.^2));
% BETA2S = direc1(2)/sqrt(sum(direc1.^2));
% BETA3S = direc1(3)/sqrt(sum(direc1.^2));
% E13 = B1/(c11-
c12)*Sigma*((ALPHA1.^2)*(BETA1S^2)+(ALPHA2.^2)*(BETA2S^2)+(ALPHA3.^2
)*(BETA3S^2)-1/3);
% E23 = B2/c44*Sigma*(ALPHA1.*ALPHA2*BETA1S*BETA2S +
ALPHA2.*ALPHA3*BETA2S*BETA3S + ALPHA3.*ALPHA1*BETA3S*BETA1S);

Esan = MagElas_FCT*(E11+E21+E12+E22+E13+E23);
%-------------------------------------------------------------------
```

Etot2.m

```matlab
function Etot = Etot2(ALPHA1,ALPHA2,ALPHA3,H,pS,pSdirec)

Etot = Eanisotropy(ALPHA1,ALPHA2,ALPHA3) +
Esaniso(ALPHA1,ALPHA2,ALPHA3,pS,pSdirec) +
Wmagnetic(ALPHA1,ALPHA2,ALPHA3,H);
%-------------------------------------------------------------------
```

Wmagnetic.m

```matlab
function Wmg = Wmagnetic(ALPHA1,ALPHA2,ALPHA3,H)
global mu_0 Msat

Wmg = -mu_0*Msat*(ALPHA1*H(1)+ALPHA2*H(2)+ALPHA3*H(3));
%-------------------------------------------------------------------
```

Bibliography

1.   Jain, M. and M.P. Verma, *Poisson's Ratios in Cubic Crystals Corresponding to (110) Loading.* Indian Journal of Pure & Applied Physics, 1990. **28**(4): p. 178-182.

2.   Ting, T.C.T. and Chen, *Poisson's Ratio for Anisotropic Elastic Materials Can Have No Bounds.* Quarterly Journal of Mechanics and Applied Mathematics, 2005. **58**(1): p. 73-82.

3.   Schurter, H.M., *Experimental Investigation of the Mechanical Properties and Auxetic Behavior of Iron-Gallium Alloys*, in *Department of Aerospace Engineering*2009, University of Maryland: College Park, MD.

4.   Chikazumi, S., *Physics of Ferromagnetism, 2nd ed.* 1997, New York: Oxford University Press Inc.

5.   Engdahl, G., *Handbook of Giant Magnetostrictive Materials*2000, San Diego: Academic Press.

6.   Kellogg, R.A., et al., *Tensile properties of magnetostrictive iron-gallium alloys.* Acta Materialia, 2004. **52**(17): p. 5043–5050.

7.   A. E. Clark, et al., *Magnetostrictive properties of body-centered cubic Fe-Ga and Fe-Ga-Al alloys.* IEEE Transactions, 2000. **Magnetics**(5): p. 3238–3240.

8.   Atulasimha, J., *Characterization and Modeling of the Magnetomechanical Behavior of Iron-Gallium alloys*, in *Department of Aerospace Engineering*2006, University of Maryland: College Park , MD.

9.   Evans, K.E. and A. Alderson, *Auxetic materials: Functional materials and structures from lateral thinking!* Adv. Mater., 2000. **12**: p. 617.

10.   Graham, F.C. and et al., *Modeling of a Galfenol transducer using the bidirectionally coupled magnetoelastic model.* Smart Materials and Structures, 2009. **18**(10): p. 104013.

11.   Datta, S., *Quasi-static characterization and modeling of the bending behavior of single crystal galfenol for magnetostrictive sensors and actuators*, in *Aerospace Engineering*2009, University of Maryland: College Park.

12.   Zhang, Y.-n., et al., *Understanding of large auxetic properties of iron-gallium and iron-aluminum alloys Origin of magnetostriction in Fe--Ga.* Journal of Applied Physics, 2010. **108**(2): p. 023513-6.

13.   Atulasimha, J., et al., *Comprehensive three dimensional hysteretic magnetomechanical model and its validation with experimental <110> single-crystal iron-gallium behavior.* Journal of Applied Physics, 2008. **103**(7): p. 07B336-3.

14.   Petculescu, G., et al., *Magnetic field dependence of galfenol elastic properties.* Journal of Applied Physics, 2005. **97**(10): p. 10M315-3.

15.   Kellogg, R.A., *Development and modeling of iron-gallium alloys*, 2003, Iowa State University: Ames.

16.   Mudivarthi, C., et al., *Anisotropy of constrained magnetostrictive materials.* Journal of Magnetism and Magnetic Materials, 2010. **322**(20): p. 3028-3034.

17. Griffiths, D.J., *Introduction to Electrodynamics, 3rd ed.*1999, Upper Saddle River: Pearson Education, Inc.

18. Warburg, E., *Magnetische Untersuchungen.* Annalen der Physik und Chemie, 1881. **249**: p. 141-164.

19. Ewing, J.A., *Magnetic Induction in Iron and other Metals, 3rd ed*1900, London: The Electrician series.

20. Heisenberg, W., *Zur Theorie des Ferromagnetismus.* Zeitschrift fˋur Physik A Hadrons and Nuclei, 1928. **49**(10.1007/BF01328601): p. 619-636.

21. Weiss, P., *Hypothesis of the molecular field and ferromagnetic properties.* J. Phys. Theor. Appl., 1907. **6**(1): p. 661–690.

22. Bitter, F., *On inhomogeneities in the magnetization of ferromagnetic materials.* Phys. Rev., 1931. **38**(10): p. 1903–1905.

23. Kaya, S., *Pulverfiguren des magnetisierten Eisenkristalls.* Zeitschrift für Physik, 1934. **90**(7-8): p. 551-558.

24. H. J. Williams, R.M.B., and W. Shockley, *Magnetic domain patterns on single crystals of silicon iron.* Phys. Rev., 1949. **75**(1): p. 155-178.

25. Hubert, A. and R. Schafer, *Magnetic Domains*1998, Berlin: Springer-Verlag.

26. Mudivarthi, C., *Magnetic and Structural Charecterization of Fe–Ga using Kerr Microscopy and Neutron Scattering*, in *Dept. of Materials Science and Engineering*2010, University of Maryland: College Park, MD.

27. Sturgeon, W., *Annals of Electricity, Magnetism, and Chemistry*, 1842, Sherwood, Gilbert, and Piper.

28. Joule, J.P., *On a new class of magnetic forces.* The Annals of Electricity, Magnetism, and Chemistry, 1842. **8**: p. 219–224.

29. Active Material Laboratory, U.o.C., Los Angeles, *Magnetostriction and Magnetostrictive Materials.*

30. Villari, E., *Change of magnetization by tension and by electric current.* Annalen der Physik und Chemie, 1865. **126**: p. 87–122.

31. Wiedemann, G., *Über die Torsion und die Beziehung derselben zum Magnetismus.* Pogg. Ann., 1860. **106**: p. 161-201.

32. Bozorth, R.M., *Ferromagnetism*1951, New York: Van Nostrand.

33. Barrett, W.F., *On the Alterations in the Dimensions of the Magnetic Metals by the Act of Magnetisation.* Nature, 1882. **26**: p. 585-586.

34. Lacheisserie, E.d.T.d., *Magnetostriction - Theory and Applications of Magnetoelasticity*1993, Boca Raton: CRC Press, Inc.

35. Calkins, F.T., *Design, Analysis, and Modeling of Giant Magnetostrictive Transducers*, 1997, Iowa State University.

36. Cullity, B.D., *Introduction to Magnetic Materials*1972, Reading, MA: Addison Wesley.

37. Bergqvist, A. and G. Engdahl, *A stress-dependent magnetic Preisach hysteresis model.* Magnetics, IEEE Transactions on, 1991. **27**(6): p. 4796-4798.

38. Jiles, D.C., *Theory of the magnetomechanical effect (vol 28, pg 1537, 1995)* JOURNAL OF PHYSICS D-APPLIED PHYSICS 1999. **32**(15): p. 1945.

39. Ghosh, D. and S. Gopalakrishnan, *Role of coupling terms in constitutive relationships of magnetostrictive materials.* CMC-TECH SCIENCE PRESS-, 2004. **1**: p. 213-228.

40. Armstrong, W.D., *Magnetization and magnetostriction processes in Tb(0.27−0.30)Dy(0.73−0.70)Fe(1.9−2.0).* Journal of Applied Physics, 1997. **81**(5): p. 2321-2326.

41. Armstrong, W.D., *An incremental theory of magneto-elastic hysteresis in pseudo-cubic ferro-magnetostrictive alloys.* Journal of Magnetism and Magnetic Materials, 2003. **263**(1–2): p. 208-218.

42. Rafique, S., et al., *Magnetic anisotropy of FeGa alloys.* Journal of Applied Physics, 2004. **95**(11): p. 6939-6941.

43. Kneller, E., *Ferromagnetismus*1962: Springer-Verlag.

44. Kittel, C., *Physical theory of ferromagnetic domains.* Reviews of Modern Physics, 1949. **21**(4): p. 541–583.

45. Mudivarthi, C., et al., *Anisotropy of constrained magnetostrictive materials.* Journal of Magnetism and Magnetic Materials, 2010. **322**(20): p. 3028 – 3034.

46. Bormio-Nunes, C., et al., *Volume magnetostriction and structure of copper mold-cast polycrystalline Fe-Ga alloys.* Journal of Applied Physics, 2005. **97**(3): p. 033901.

47. Kuriki, S., *Strain effects on magnetic anisotropies in (110) Ni films.* Journal of Applied Physics, 1977. **48**(7): p. 2992–2997.

48. Callister, W.D., *Fundamentals of Materials Science and Engineering*2005, Hoboken, NJ: John Wiley & Sons, Inc.

49. Clark, A.E., M.W.-F. K. B. Hathaway, J. B. Restorff, T. A. Lograsso,, and G.P. V. M. Keppens, and R. A. Taylor, *Extraordinary magnetoelasticity and lattice softening in bcc Fe-Ga alloys.* Journal of Applied Physics, 2003. **93**(10): p. 8621–8623.

50. Hall, R.C., *Magnetostriction of aluminum-iron single crystals in the region of 6 to 30 atomic percent aluminum.* Journal of Applied Physics, 1957. **28**(6): p. 707-713.

51. Jayasimha, A. and et al., *Analysis of the effect of gallium content on the magnetomechanical behavior of single-crystal FeGa alloys using an energy-based model.* Smart Materials and Structures, 2008. **17**(2): p. 025027.

52. Na, S.-M. and A.B. Flatau, *Secondary recrystallization, crystallographic texture and magnetostriction in rolled Fe–Ga based alloys.* Journal of Applied Physics, 2007. **101**(9): p. 09N518.

53. H. Chun, et al., *The role of misorientation and coincident site lattice boundaries in goss-textured galfenol rolled sheet.* Journal of Applied Physics, 2010. **107**(9): p. 09A960.

54. Ueno, T., E. Summers, and T. Higuchi, *Machining of iron-gallium alloy for microactuator.* Sensors and Actuators A: Physical, 2007. **137**(1): p. 134 –140.

55. Ueno, T., et al., *Micromagnetostrictive vibrator using iron-gallium alloy.* Sensors and Actuators A:, 2008. **148**(1): p. 280 – 284.

56. Downey, P.R., et al., *Magnetoelastic bending of Galfenol for sensor applications.* Journal of Applied Physics, 2005. **97**(10): p. 10R505-3.

57. Cullen, J.R., et al., *Magnetoelasticity of Fe–Ga and Fe–Al alloys.* Journal of Magnetism and Magnetic Materials, 2001. **226–230, Part 1**(0): p. 948-949.

58. Ikeda, O., K. , and O. R., I., Fukamichi, K., and Ishida, K., *Phase Equilibria and Stability of Ordered b.c.c. Phases in the Fe-rich Portion of the Fe-Ga System.* Journal of Alloys and Compounds, 2002. **347**(1-2): p. 198-205.

59. Massalski, T., *Binary Alloy Phase Diagrams*. 2 ed2002, Materials Park, Ohio, USA: ASM International.

60. Kawamiya, N., K. Adachi, and Y. Nakamura, *Magnetic Properties and Mössabauer Investigations of Fe-Ga Alloys.* Journal of the Physical Society of Japan, 1972. **33**(5): p. 1318-1327.

61. Wu, R., *Origin of large magnetostriction in FeGa alloys.* Journal of Applied Physics, 2002. **91**(10): p. 7358-7360.

62. Wuttig, M., L. Dai, and J. Cullen, *Elasticity and magnetoelasticity of Fe–Ga solid solutions.* Applied Physics Letters, 2002. **80**(7): p. 1135-1137.

63. Lakes, R., *Foam Structures with a Negative Poisson's Ratio.* Science, 1987. **235**(4792): p. 1038-1040.

64. Liu, Q., *Literature review: materials with negative poisson's ratios and potential applications to Aerospace and Defence*, 2005, Defense Science and Technology Organization: Victoria, Australia. p. 36.

65. Bailey, R.W. and H.A. Cox, GEC Journal, 1961. **28**: p. 72-8.

66. Gibson, L.J., et al., *The Mechanics of Two-Dimensional Cellular Materials*. Vol. 382. 1982. 25-42.

67. Lakes, R., *Advances in negative Poisson's ratio materials.* Advanced Materials, 1993. **5**(4): p. 293-296.

68. Caddock, B.D. and K.E. Evans, *Microporous materials with negative Poisson's ratios. I. Microstructure and mechanical properties.* Journal of Physics D: Applied Physics, 1989. **22**(12): p. 1877-1882.

69. Pickles, A.P., K.L. Alderson, and K.E. Evans, *The Effects of Powder Morphology on the Processing of Auxetic Polypropylene (PP of Negative Poisson's Ratio).* Polym. Engng Sci. , 1996. **36**(636).

70. Alderson, K.L., A. Fitzgerald, and K.E. Evans, *The strain dependent indentation resilience of auxetic microporous polyethylene.* Journal of Materials Science, 2000. **35**(16): p. 4039-4047.

71. Evans, K.E., *Tailoring the negative Poisson's ratio.* Chem. Ind, 1990. **20**: p. 654-657.

72. Evans, K.E., *Auxetic polymers.* Membrane Technology, 2001. **2001**(137): p. 9.

73. Prawoto, Y., *SOLID MECHANICS FOR MATERIALS ENGINEERS -- Principles and Applications of Mesomechanics*2013: LULU Press.

74. Konyok, S.S.a.D., *Numerical and Experimental Study of Auxetic Closed-Cell Foams.* Computational Methods in Science and Technology, 2004. **10**(2): p. 197-202.

75. Alderson, A., *A Triumph of Lateral Thought* Chemistry & Industry, 1999. **17**: p. 384-391.

76. Turley, J. and G. Sines, *The anisotropy of Young's modulus, shear modulus and Poisson's ratio in cubic materials.* Journal of Physics D: Applied Physics, 1971. **4**(2): p. 264.

77. Tan, X., et al., *Auxetic behavior under electrical loads in an induced ferroelectric phase.* Applied Physics Letters, 2009. **94**(4): p. 042909.

78. Baughman, R.H., Shacklette, J. M., Zakhidov, A. A., and Stafstrom, S, *Negative Poisson's Ratios as a Common Feature of Cubic Metals.* Nature, 1998. **392**: p. 362-365.

79. Chen, L.Z., et al., *Electrothermal actuation based on carbon nanotube network in silicone elastomer.* Applied Physics Letters, 2008. **92**(26): p. 263104-3.

80. Donoghue, J. and K. Evans, *Composite laminates with enhanced indentation and fracture resistance due to negative Poisson's ratio*, in *8th Int. Conf. Composite Materials, SAMPE*1991: Honolulu, Hawaii.

81. Masters, I.G. and K.E. Evans, *Models for the elastic deformation of honeycombs.* Composite Structures, 1996. **35**(4): p. 403-422.

82. Tiemo, B., et al., *On three-dimensional dilational elastic metamaterials.* New Journal of Physics, 2014. **16**(3): p. 033032.

83. Alderson, A. and K.L. Alderson, *Auxetic materials.* Proceedings of the Institution of Mechanical Engineers, Part G: Journal of Aerospace Engineering, 2007. **221**(4): p. 565-575.

84. Gunton, D.J. and G.A. Saunders, *The Young's modulus and Poisson's ratio of arsenic, antimony and bismuth.* Journal of Materials Science, 1972. **7**(9): p. 1061-1068.

85. Li, Y., *The anisotropic behavior of Poisson's ratio, Young's modulus, and shear modulus in hexagonal materials.* physica status solidi (a), 1976. **38**(1): p. 171-175.

86. Milstein, F. and K. Huang, *Existence of a negative Poisson ratio in fcc crystals.* Physical Review B, 1979. **19**(4): p. 2030-2033.

87. Rovati, M., *On the negative Poisson's ratio of an orthorhombic alloy.* Scripta Materialia, 2003. **48**(3): p. 235-240.

88. Ledbetter, H. and M. Lei, *Monocrystal elastic constants of orthotropic Y1Ba2Cu3O7: An estimate.* Journal of Materials Research, 1991. **6**(11): p. 2253-2255.

89. Mudivarthi, C., et al., *Magnetic domain observations in Fe-Ga alloys.* Journal of Magnetism and Magnetic Materials, 2010. **322**(14): p. 2023-2026.

90. Downey, P.R., *Characterization of Bending Magnetostriction in Iron-Gallium Alloys for Nanowire Sensor Applications*, in *Department of Aerospace Engineering*2008, University of Maryland: College Park.

91. Mudivarthi, C., et al., *Origin of magnetostriction in Fe--Ga.* Journal of Applied Physics, 2010. **107**(9): p. 09A957-3.

92. Kellogg, R.A., et al., *Mechanical properties of magnetostrictive iron-gallium alloys.* SPIE Proceedings, 2003. **Smart Structures and Materials** (Active Materials: Behavior and Mechanics): p. 534-543.

93.   Yoo, J.-H. and A.B. Flatau, *Measurement of field-dependence elastic modulus of iron--gallium alloy using tensile test.* Journal of Applied Physics, 2005. **97**(10): p. 10M318-3.

94.   McLean, K.O. and C.S. Smith, *Ultrasonic parameters in the born model of the lithium halides.* Journal of Physics and Chemistry of Solids, 1972. **33**(2): p. 279-283.

95.   Paes, V.Z.C. and D.H. Mosca, *Magnetostrictive contribution to Poisson ratio of galfenol.* Journal of Applied Physics, 2013. **114**(12): p. 123915.

96.   Dapino, M.J., *Nonlinear and Hysteretic Magnetomechanical Model for Magnetostrictive Transducers*, 1999, Iowa State University.

97.   Atulasima, J., A.B. Flatau, and J.R. Cullen, *Energy-based quasi-static modeling of the actuation and sensing behavior of single-crystal iron-gallium alloys.* Vol. 103. 2008: AIP. 014901.

98.   Evans, P.G. and M.J. Dapino, *State-Space Constitutive Model for Magnetization and Magnetostriction of Galfenol Alloys.* Magnetics, IEEE Transactions on, 2008. **44**(7): p. 1711-1720.

99.   Mudivarthi, C. and et al., *A bidirectionally coupled magnetoelastic model and its validation using a Galfenol unimorph sensor.* Smart Materials and Structures, 2008. **17**(3): p. 035005.

100.   Armstrong, W.D., *A directional magnetization potential based model of magnetoelastic hysteresis.* Journal of Applied Physics, 2002. **91**(4): p. 2202-2210.

101.   Jayasimha, A. and et al., *Characterization and energy-based model of the magnetomechanical behavior of polycrystalline iron–gallium alloys.* Smart Materials and Structures, 2007. **16**(4): p. 1265.

102.   Clark, A.E., et al., *Effect of quenching on the magnetostriction on Fe1-xGa x(0.13<x<0.21).* Magnetics, IEEE Transactions on, 2001. **37**(4): p. 2678-2680.

103.   Lee, E.W., *The [110] Magnetostriction of some Single Crystals of Iron and Silicon-Iron.* Proceedings of the Physical Society. Section A, 1955. **68**(2): p. 65.

104.   Samsonov, G.V., *Mechanical Properties of the Elements*, in *Handbook of the Physicochemical Properties of the Elements*, G.V. Samsonov, Editor 1968, Springer US. p. 387-446.

105.   Kerr, J., *On rotation of the plane of polarization by reflection from the pole of a magnet.* Philosophical Magazine Series 5, 1877. **3**(19): p. 321 – 343.

106.   Tebble, D.J.C.a.R.S., *Magnetic domains.* Reports on Progress in Physics, 1961. **24**(1): p. 116–166.

107.   Bai, F., et al., *Magnetic force microscopy investigation of domain structures in FeGa single crystals* Journal of Applied Physics, 2005. **98**(2): p. 023904-023904-4.

108.   Marana, M., *DEVELOPMENT OF A BIO-INSPIRED MAGNETOSTRICTIVE FLOW AND TACTILE SENSOR*, in *Department of Aerospace Engineering*2012, University of Maryland: College Park , MD.

109. Finch, G.I. and R.T. Spurr, *Surface Changes due to Sliding.* Proceedings of the Royal Society of London. Series A, Mathematical and Physical Sciences, 1952. **212**(1111): p. 462-464.

110. Raghunath, G. and A.B. Flatau, *Study of magnetic domain evolution in an auxetic plane of Galfenol using Kerr microscopy.* Journal of Applied Physics, 2015. **117**(17): p. 17E704.

111. Raghunath, G., et al., *Kerr microscopy studies of the effects of bending stress on galfenol.* Journal of Applied Physics, 2014. **115**(17): p. 17E310-17E310-3.

112. Hoffmann, V., et al., *First domain observations with the magneto-optical Kerr effect on Ti-ferrites in rocks and their synthetic equivalents.* Journal of Magnetism and Magnetic Materials, 1987. **71**(1): p. 90-94.

113. Alderson, K.L., et al., *How to make auxetic fibre reinforced composites.* physica status solidi (b), 2005. **242**(3): p. 509-518.

114. Clark, A.E., *Ferromagnetic Materials*. Vol. 1. 1980, Amsterdam: North-Holland Publishing Company.

115. usa.com/products/terfenol, w.e., *Terfenol-d, Etrema products, inc, Ames, IA, USA.*

116. bolton.ac.uk. *Auxetic Materials Network.* [cited 2011].